Dissertation

submitted to the

Combined Faculties of the Natural Sciences and Mathematics

of the Ruperto-Carola-University of Heidelberg, Germany

for the degree of

Doctor of Natural Sciences

Put forward by

Alexander Philip Stuart Hygate

born in St Mary's, United Kingdom of Great Britain and Northern Ireland

Oral examination: the 30th of January 2020

The Physics of Cloud-scale Star Formation and Feedback Across Cosmic Time

Referees:

Dr. J. M. Diederik Kruijssen

Prof. Dr. Hans-Walter Rix

Abstract

Stars are an important visible and massive constituent of galaxies. They form out of cool, dense molecular gas regions known as molecular clouds and in turn impact this gas by emitting energy and mass known as "stellar feedback". Therefore, understanding the formation of stars and the feedback they generate is crucial for understanding galaxy formation. As a result of modern telescope facilities, high sensitivity, high resolution (cloud-scale) imaging of molecular gas is becoming available in an increasing number of galaxies. Analysis of this data with matched resolution observations of recently-formed, massive stars allows the characterisation of the star formation process on the cloud scale. The "uncertainty principle for star formation" is a statistical method for measuring the relative duration and spatial distribution of evolutionary phases of the star formation process. When applied to observational images that trace molecular clouds and regions of young stars, the method measures the duration of molecular cloud lifetimes, the timescale of their destruction by stellar feedback and the mean separation length between star forming regions. In this thesis, I investigate the physics of star formation and feedback on the cloud scale and present contributions to the development of methods for this analysis. First, I assess the impact of noise, astrometric offsets and diffuse emission on measurements made with the "uncertainty principle for star formation". I present a physically motivated method for separating emission from compact structures and diffuse extended structure in an image. The method separates diffuse and compact emission via filtering in Fourier space, with a filter defined by the mean separation length between star forming regions. This method enables the determination of the molecular cloud lifecycle and the mean separation between star forming regions with the "uncertainty principle for star formation" in data containing a diffuse background component. Second, I present the application of the "uncertainty principle for star formation" to determine the lifecycles of molecular clouds in the nearby flocculent galaxy M33. These measurements indicate that clouds in M33 have lifetimes approximately once or twice the timescale for their collapse due to gravitational freefall. Subsequently clouds are dispersed by stellar feedback over a timescale that could allow the earliest supernovae to explode whilst still embedded in their natal clouds. Third, I present the decomposition of tracer images of the molecular and ionised gas in nine nearby galaxies into compact and diffuse components and thus determine the fraction of emission coming from these components. I then present a correlation analysis between these emission fractions and a number of parameters characterising the galaxies in the sample. Last, I summarise the work of the thesis and present some future prospects for extending analyses such as the work presented in this thesis to other galactic environments in the Nearby Universe and further out into cosmic history.

Zusammenfassung

Sterne sind ein wichtiger, sichtbarer und massereicher Bestandteil von Galaxien. Sie bilden sich aus kühlen, dichten molekularen Gasregionen, die als Molekülwolken bekannt sind und im Gegenzug wirken auf dieses Gas ein, indem sie Energie und Masse abstrahlen. Dieser Vorgang ist als «stellare Rückkopplung» bekannt. Aus diesem Grund ist das Verständnis der Sternentstehung und der von ihr erzeugten Rückkopplung von entscheidender Bedeutung für das Verständnis der Galaxienentstehung. Infolge der Moderne Teleskope wird hochauflösende, hochempfindliche Bildgebung für immer mehr Galaxien verfügbar. Die Analyse dieser Daten mit Beobachtungen passender Auflösung der neugebildete, massereiche Sterne ermöglicht die Beschreibung des Sternentstehungsprozesses auf den Größenskalen der Wolken. Die «Unbestimmtheitsrelation für Sternentstehung» ist eine statistische Methode für die Bestimmung der relativen Dauer und räumlichen Verteilung der Evolutionsphasen des Sternentstehungsprozess. Bei ihrer Anwendung auf Beobachtungsbilder, die Molekülwolken und Regionen junger Sterne verfolgen, misst die Methode die Dauer der Le-

benszeiten der Molekülwolken, die Zeitskala ihrer Zerstörung durch stellare Rückkopplung und den mittleren Abstand zwischen Sternentstehungsregionen. In dieser Arbeit, untersuche ich die Physik der Sternentstehung und stellare Rückkopplung auf den Größenskalen der Wolken und präsentiere Beiträge zur Entwicklung der Methoden für diese Analyse. Erstens beurteile ich die Auswirkungen von Rauschen, astrometrischer versatzen und diffuser Emission auf Messungen, die mit der «Unbestimmtheitsrelation für Sternentstehung» durchgeführt wurden. Ich präsentiere ein physikalisch motiviertes Verfahren zur Trennung der Emission von Kompakten Strukturen und diffuser ausgedehnter Struktur in einem Bild. Das Verfahren trennt diffuse und kompakte Emission durch Filterung im Fourier-Raum, mit einem Filter, der durch den mittleren Abstand zwischen Sternentstehungsregionen definiert ist. Dieses Verfahren ermöglicht die Bestimmung des Lebenszyklus von Molekülwolken und des mittleren Abstands zwischen Sternentstehungsregionen mit der «Unbestimmtheitsrelation für die Sternentstehung» in Daten, die eine diffuse Hintergrundkomponente enthalten. Zweitens präsentiere ich die Anwendung der «Unbestimmtheitsrelation für Sternentstehung» zur Bestimmung des Lebenszyklus von Molekülwolken in der nahen Flocculent-Spiralgalaxie M33. Diese Messungen deuten darauf hin, dass Molekülwolken in M33 eine Lebensdauer haben, die ein- oder zweimal so lang wie die Zeitskala des Gravitationskollaps im freien Fall. Anschließend werden Molekülwolken durch stellare Rückkopplung über einen Zeitraum zerstreut, der es den frühesten Supernovae erlauben könnte, zu explodieren, während diese noch in ihren Geburtswolken eingebettet sind. Drittens präsentiere ich für neun nahegelegenen Galaxien die Zersetzung von Bildern des molekularem und ionisierten Gases in Kompakte und diffuse Komponenten, und bestimm somit den Emissionsanteil der Komponenten. Weiterhin präsentiere ich eine Korrelationsanalyse zwischen diesen Emissionsanteile und einer Reihe von Parametern, die die Galaxien in der Stichprobe Beschreiben. Zuletzt fasse ich diese Arbeit zusammen und präsentiere einige Zukunftsperspektiven für die Ausweitung der Analysen, wie sie in dieser Arbeit durchgeführt wurden, auf andere galaktische Umgebungen im nahen Universum und weiter entfernt in der kosmischen Geschichte.

Contents

List of Figures

List of Tables

1 Introduction

One of the most fundamental questions in modern astronomy is that of how galaxies form and evolve. One of the key processes driving galaxy evolution is star formation. In broad terms, gas in galaxies is transformed into stars, which then in turn impact the gas through the deposition of energy and metals[1] via stellar feedback (such as through supernova explosions).

Stars are luminous objects that emit electromagnetic radiation, shining particularly brightly in the optical wavelength regime, the portion of the electromagnetic spectrum visible to the naked eye. Therefore, stars have been observed from the earliest beginnings of astronomy. Many in the ancient world believed that the celestial bodies they observed were unchanging, with Aristotle declaring: "That there is one heaven, then, only, and that it is ungenerated and eternal, and further that its movement is regular, has now been sufficiently explained" (Aristotle et al., 1922). We now know, however, that astronomical objects are born, change and die through evolutionary processes. It is only recently, historically speaking, that we have been able to observationally constrain the formation process of these stars.

We now know that the stars we observe in the night sky are bound together into the Milky Way galaxy and that many other such galaxies exist. Understanding how these galaxies form and evolve and what drives the differences between them is one of the key questions facing astronomy. Stars are a significant fraction of the mass of galaxies and the radiation and matter that they emit are some of the most readily detectable phenomena in astronomy. Moreover, stellar emission has a large impact on the galaxies hosting the stars, affecting their evolution. Thus a physical understanding of the process of star formation is crucial to the understanding of galaxy evolution.

This thesis is concerned with the development and observational application of methods for probing the physics of star formation and feedback on the cloud-scale. In this chapter (Chapter 1), I briefly introduce some of the key background to this thesis. In Chapter 2, I present a method for filtering diffuse emission from astronomical images in Fourier space. This method allows compact emission within images to be separated from diffuse, large-scale emission, allowing us to constrain the significance of these components and conduct further analysis on them without the other contaminating component. In Chapter 3, I present a characterisation of the lifecycle of molecular clouds in M33. In Chapter 4, I present measurements of diffuse CO and Hα emission fractions in the PHANGS pilot sample of galaxies in the context of the cloud-scale physical properties of these galaxies. Finally, in Chapter 5, I summarise the results of this thesis and provide an outlook on the future of the field.

[1] The term "metals" refers in astronomy and this thesis to chemical elements heavier than hydrogen and helium.

1.1 Galaxies

Galaxies are typically defined as large (hundreds of pc to tens of kpc in size) gravitationally bound collections of massive objects. They consist of a number of different components. Major components of galaxies are: stars, which dominate emission in optical wavelengths; dark matter, which is not luminous, but is a very significant constituent in terms of mass (e.g Rubin et al., 1985); and gas, which provides the fuel for star formation and is most readily observed at radio, milimetre and sub-milimetre wavelengths. In addition, dust, though only constituting a small fraction of the mass of a galaxy, has a large impact on the observed light through absorption and re-radiation of light (dust emits ~ 30 per cent of the Milky Way's luminosity; see e.g. review by Mathis, 1990). Galaxies may also host a central supermassive black hole. Due to their nature, black holes are very hard to detect; see for example Gillessen et al. (2009) who used stellar orbits to infer the presence of a black hole in the Milky Way. When the black hole is in an active mode (i.e. when an active galactic nucleus; AGN), material accreting on to the black hole and can be a significant contributor to its host galaxy's luminosity and can suppress star formation through AGN feedback (see e.g. review by Fabian, 2012). Similarly feedback from stars can impact the galaxy in the form of radiation (see e.g Hopkins et al., 2014a) and cosmic rays (see e.g Chan et al., 2019). In addition to these major observable components, galaxies contain planetary system objects including planets, moons, asteroids and comets that cannot currently be observed in an extragalactic context (however, features in extragalactic gravitational lensing observations can be explained by adding planetary mass objects to these models, see Ingrosso et al. 2009; Dai & Guerras 2018).

Together, the gas and dust are known as the Interstellar Medium (ISM). The ISM makes up ~ 10 - 15 per cent of the total mass of the Milky Way's disc, with the vast majority of this mass being in the form of gas (only ~ 1 per cent of the ISM by mass is dust) (Ferrière, 2001). Whereas its contribution to the total mass of our Galaxy is relatively low, it plays an essential role in shaping its evolution. In particular, stars are formed in clouds of molecular hydrogen in the ISM. I provide further introduction to the ISM and molecular clouds in Section 1.2.

This thesis focusses on the formation of stars from gas and their impact on the ISM through feedback. In order to investigate the star formation process we must be able to trace it observationally. Tracing gas and star formation is, however, not a straightforward process and presents a number of challenges that must be overcome. Figure 1.1 shows a spectral energy distribution (SED) for a typical star-forming, late-type galaxy. A number of features used to trace the formation of stars are indicated. The SED consists of continuum emission, which changes gradually with wavelength and emission lines, which contribute to the luminosity at only specific wavelengths. Both features may be used to trace physical quantities, such as star formation and gas mass, though in order to use emission lines as tracers, one must deal with the additional continuum flux by subtracting it. In particular, common features used to trace star formation are the UV-continuum and Hα emission line and common features used to trace the molecular gas are the dust-continuum and carbon monoxide emission lines. I discuss these different tracer methods and the particular observational issues that must be addressed for molecular gas in Section 1.2.2 and star formation in Section 1.3.1. Observing these different features requires a diverse range of instruments including both ground and space based observatories (see Figure 1.2).

It has long been known that galaxies are an inhomogeneous population with properties that vary markedly from one to another. Probably the most well-known classification scheme for galaxies is the Hubble sequence, developed for the visual classification of galaxies by their morphology (Hubble, 1922, 1926, 1936). An illustration of this sequence is shown in Figure 1.3. Galaxies are distinguished into two main classes, spiral and elliptical, with a transitional class, known as lenticular, and an additional class, not included on the main sequence, for galaxies with an irregular

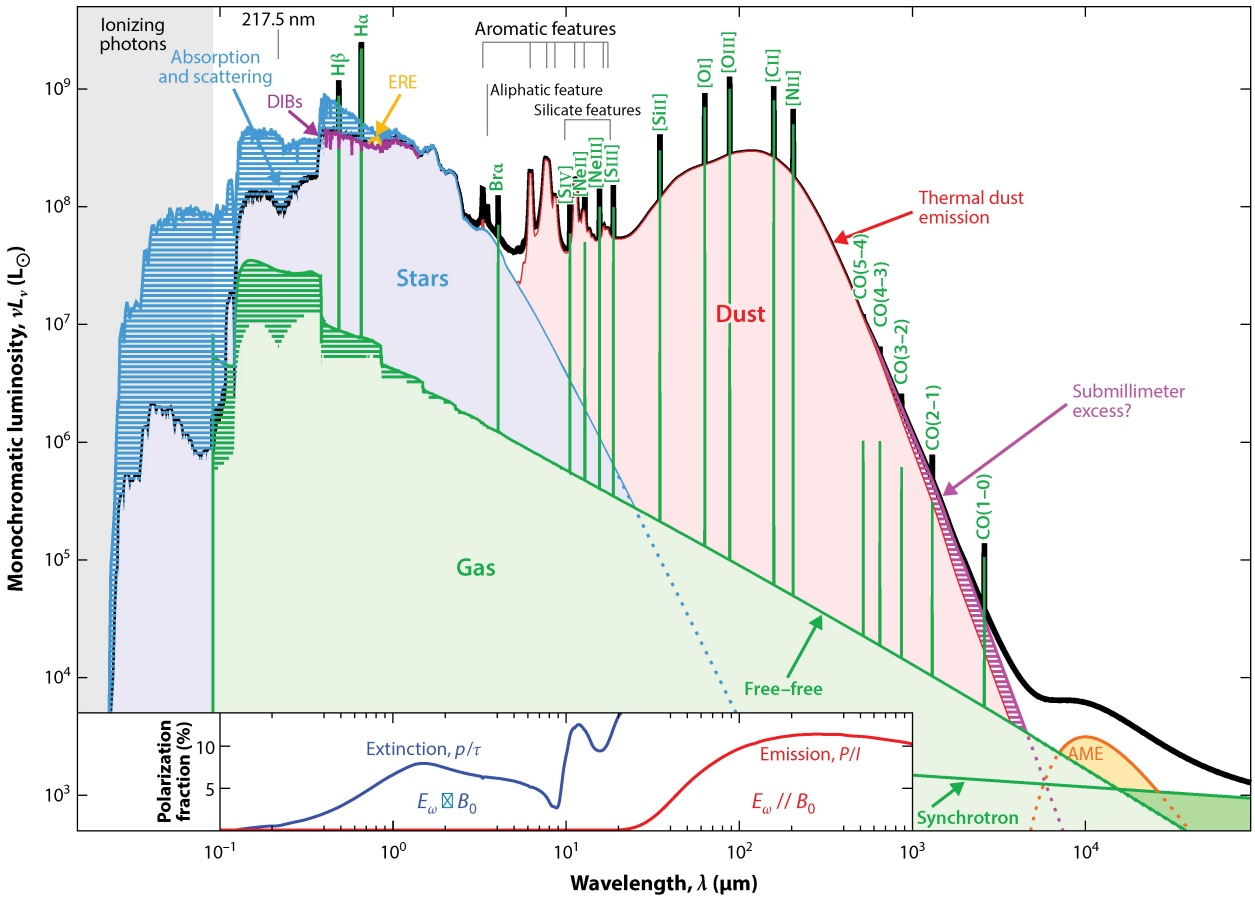

Figure 1.1: Figure taken from Galliano et al. (2018). A spectral energy distribution of a typical star-forming late-type galaxy. The major emitting components (gas, stars and dust) vary in significance with wavelength. The Carbon Monoxide lines emanating from molecular gas are crucial for tracing molecular gas mass. Emission lines from the gas ionised by young, massive stars are used for tracing star formation. Continuum features of the SED are also used as tracers, such as the UV-continuum for star formation and the dust-continuum for dust and molecular gas.

morphology. Figure 1.4 shows an image of an example galaxy from each of these classes.

Elliptical galaxies are colloquially referred to as "red and dead" galaxies. They are red in colour, due to the old stellar populations that they host, which lack massive, blue stars. These old stellar populations result from a lack of recent star formation, hence why they are known as "dead". Detection of molecular gas in ellipticals are rare (5 ± 3 per cent Young et al., 2011) indicating that they lack the necessary fuel for star formation. They have an elliptical shape, with their stellar dynamics dominated by random motions, in contrast to the ordered rotation of spiral discs.

Spiral galaxies are characterised by having a rotationally-supported disc exhibiting spiral structure. This spiral structure ranges from weak flocculent spiral structure to the highly prominent spiral arms of grand design spirals (see Figure 1.5). Spiral galaxies are the sites of ongoing star formation, with the majority of star formation taking place in the Local Universe happening in spiral galaxies (González Delgado et al., 2016). Star-forming galaxies are observed to follow a somewhat tight relationship between their star formation rate (SFR) and stellar mass (Brinchmann et al., 2004), known as the Main Sequence of star forming galaxies.

Understanding what drives the star formation process in spiral galaxies is an active field of

Figure 1.2: Images of the range of different telescope technologies used for observations in this thesis. [Top panel] a subset of the antennas of ALMA, a millimetre/sub-millimetre interferometer consisting of an array of radio telescopes used for observations of CO to trace molecular gas. [Bottom left panel] an artists impression of GALEX in orbit above Earth. GALEX is a space telescope used to trace star formation with UV emission that is strongly attenuated by the Earth's atmosphere. [Bottom right panel] The KPNO 0.6m optical telescope, used for observing Hα, which is another tracer of star formation. Top left image credit: ESO/C. Malin. Bottom left image credit: NASA. Bottom right image credit: NOAO/AURA/NSF

research. Observations indicate that some correlation between morphological features of galaxies and SFR. The presence of spiral arms and their significance is linked to differences in the properties of galaxies; galactic dynamics causes gas to be at higher densities in spiral arms (Elmegreen & Elmegreen, 1986; Foyle et al., 2010). Studies of samples of galaxies, however, indicate that although there is significant star formation in the arms, differences in spiral arm morphology have little impact on the integrated star formation rate of galaxies (Elmegreen & Elmegreen, 1986; Willett et al., 2015). Many ($\sim 40-70$ per cent Eskridge & Frogel, 1999; Oh et al., 2012; Skibba et al., 2012; Ann et al., 2015; Buta et al., 2019) spiral galaxies have a central bar. Such bars are observed to suppress star formation rates which may be explained by the large velocity dispersion of molecular gas situated in bars (Egusa et al., 2018; Maeda et al., 2018). However, bars seem to have little impact on the integrated star formation rate of their galaxies (Willett et al., 2015).

Lenticular galaxies, otherwise known as "S0" galaxies, are an intermediate class between elliptical and spiral galaxies that share characteristics with galaxies from both classes. Like spiral galaxies, they have a prominent disc component, but are without the spiral structure characteristic of spirals. Their spectra are similar to those of elliptical galaxies. They generally have low gas fractions and star formation rates. This leaves them with old stellar populations like elliptical galaxies, although they may have large amounts of dust, like spirals. Lenticular galaxies are often considered to be a transitional stage between star-forming, blue, disc galaxies and "red and dead" elliptical galaxies. Deep imaging of the lenticular galaxy NGC1533 has revealed faint spiral structure along with recent star formation (DeGraaff et al., 2007). More generally, gas infall along with bar-driven secular evolution may trigger rejuvenation of the star formation process in lenticulars (Marino et al., 2011). A reasonable fraction of lenticulars have a detectable molecular gas reservoir, though estimates of this fraction vary significantly, e.g. 78 per cent (Welch & Sage, 2003) verses 28 ± 3 per cent (Young et al., 2011). Indeed, a number of these galaxies have been detected with significant ($\gtrsim 10^9; \mathrm{M}_\odot$ Young et al., 2011) molecular gas reservoirs.

Irregular galaxies are galaxies that do not fit into any of the other classifications, as they are characterised by an irregular morphology. In contrast to spiral galaxies they do not have a defined spiral structure nor, in contrast to elliptical galaxies, do they have a nuclear bulge. They generally contain molecular gas reservoirs and are actively forming stars.

Together, elliptical and lenticular galaxies are referred to as early-type galaxies and spiral and irregular galaxies are known as late-type galaxies. Despite this nomenclature, the Hubble sequence is not an evolutionary sequence from early-type to late-type galaxies. Such an evolution was proposed (see e.g Jeans, 1919), but is not accepted. Indeed, simulations (e.g. Martig et al., 2009) and observations (e.g. van Dokkum, 2005; Schawinski et al., 2014) indicate that events such as mergers may cause galaxies to evolve towards having early-type properties and that there are a number of evolutionary pathways for galaxies. Moreover, significant evolution is observed in galaxies across cosmic time for a number of their properties, including mass (Bundy et al., 2005; Mortlock et al., 2011; Ilbert et al., 2013), star formation rate (Madau & Dickinson, 2014) and molecular gas content (Decarli et al., 2019; Riechers et al., 2019), such that galaxies at high-redshift have many differences to those in the Local Universe. Therefore, the question of how galaxies form and evolve continues to be an active topic of research.

One method of investigating this evolution are numerical simulations of the evolution of isolated galaxies or galaxies in large-scale cosmological boxes through computational modelling of the physical processes driving this evolution. Modern numerical simulations such as Illustris (Vogelsberger et al., 2014), FIRE (Hopkins et al., 2014b), EAGLE (Schaye et al., 2015), FIRE-2 (Hopkins et al., 2018) and IllustrisTNG (Nelson et al., 2018) are able to produce populations of galaxies that agree in terms of many of their properties with Local Universe galaxies. However, the treatment of many of the key processes shaping galaxy evolution by these simulations remains phenomenological and

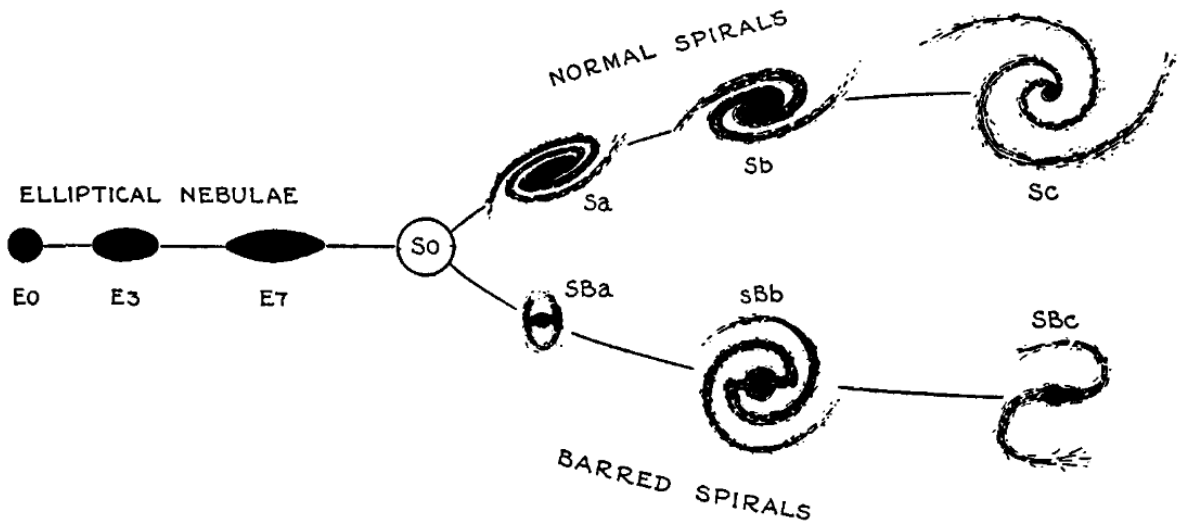

Figure 1.3: The Hubble sequence of galaxies, otherwise known as the Hubble tuning fork. Galaxies are classified into two main types: spiral and elliptical ("E"). Spiral galaxies are subdivided into galaxies with ("SB") and without ("S") a central bar. Lenticular ("S0") galaxies represent a transitional class with some properties of both spiral and elliptical galaxies. Figure taken from (Hubble, 1936).

moreover different models of the same processes are able to produce galaxies with realistic properties (Naab & Ostriker, 2017; Somerville & Davé, 2015). A difficulty of such simulations is that they do not resolve much of the small-scale physics that drives the evolution of galaxies and must use subgrid modelling to simulate these processes. There are a number of different competing models for the same processes. Although, these different models of star formation and feedback physics are able to produce galaxies with the same bulk properties, such as the star formation rate, they produce differing sub-galactic scale distributions of matter (Hopkins et al., 2013; Haas et al., 2013; Scannapieco et al., 2012). Thus observational constraints on the cloud-scale structure of the ISM along with the cloud-scale physics of star formation and feedback that drives this structure are crucial for testing the next generation of galaxy simulations and informing our physical understanding of galaxy evolution.

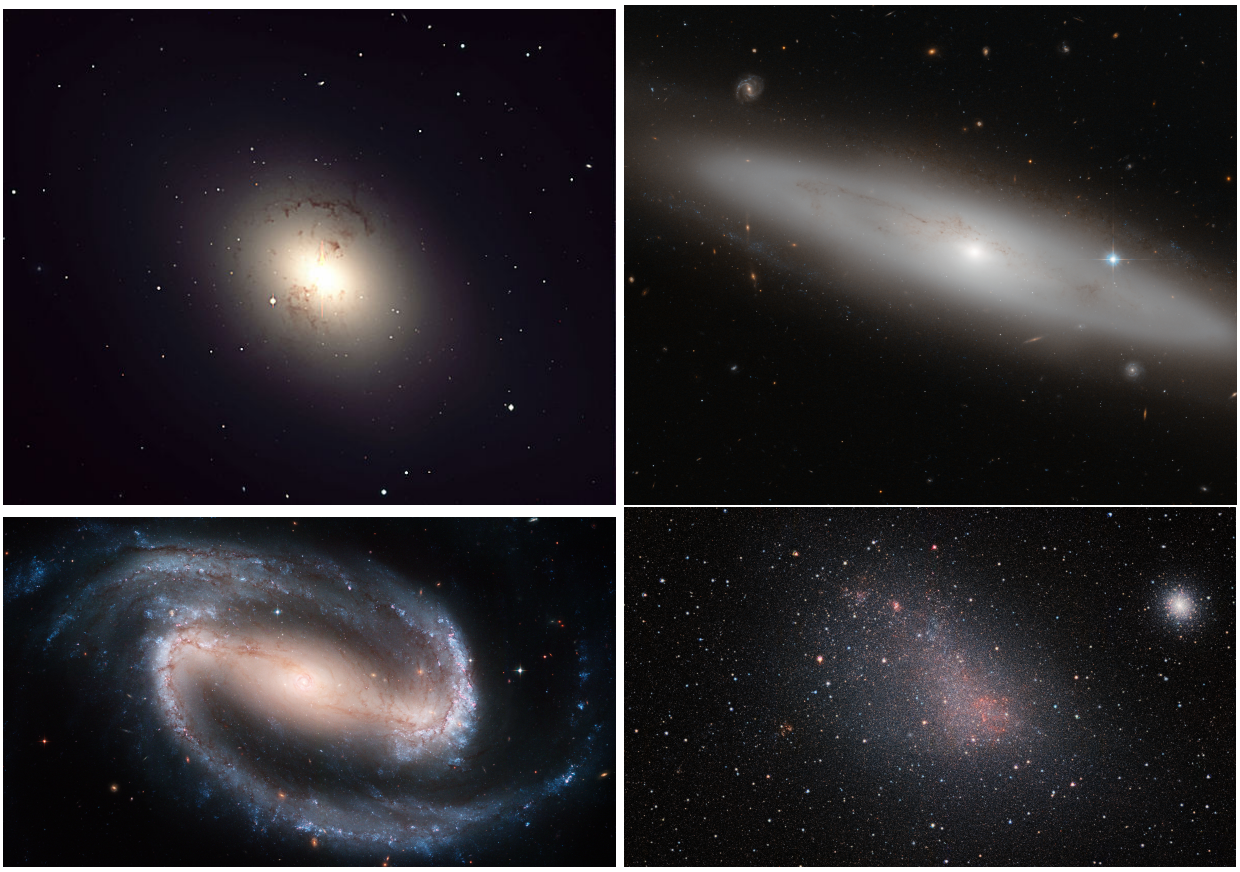

Figure 1.4: Examples of the four different morphological classes of galaxies in the Hubble sequence. [Top left Panel] The elliptical galaxy NGC1316, [Top right Panel] the lenticular galaxy NGC4866, [Bottom left Panel] the spiral galaxy NGC130 and [Bottom right Panel] the Small Magellanic Cloud, an irregular glaaxy. Top left image credit: ESO. Top right image credit: ESA/Hubble, NASA and Gilles Chapdelaine Bottom left image credit: NASA, ESA, and The Hubble Heritage Team (STScI/AURA). Bottom right image credit: ESO/VISTA VMC.

Figure 1.5: Spiral galaxies show a range of different spiral morphologies. One key feature of spiral morphology is the strength of the spiral arms; this strength ranges from weak (flocculent) spiral structure to the strongly pronounced spiral arms of grand design spirals. [Left Panel] The flocculent spiral galaxy M33 and [Right Panel] the grand design spiral galaxy M51. Left image credit: ESO. Right image credit: NASA, ESA, S. Beckwith (STScI) and the Hubble Heritage Team (STScI/AURA).

1.2 The Interstellar Medium (ISM)

The ISM pervades the space in galaxies between stars. It is a significant component of galaxies; in total the ISM comprises $10-15$ per cent of the total mass of the Milky Way's disc (Ferrière, 2001). Moreover, it plays a key role in the evolution of galaxies and it is dynamic and changes over time. Stars form from the densest phase of this ISM (molecular gas) and these stars then alter the ISM through feedback (such as stellar winds and ionisation), which heats the gas, changing its ionisation state and the structure of the ISM.

1.2.1 Components of the ISM

The ISM is primarily comprised of hydrogen (90.8 per cent by number and 70.4 per cent by mass), with a smaller amount of helium (9.1 per cent by number and 28.1 per cent by mass) and metals[2] (only 0.12 per cent by number and 1.5 per cent by mass)(Ferrière, 2001). Almost all of this matter exists as gas; only ~ 1 per cent of the ISM by mass in the form of dust (Ferrière, 2001). The hydrogen in the ISM exists in a number of different phases that are characterised by the state of hydrogen atoms in the phase, i.e. neutral molecular (H_2), neutral atomic (HI) or ionized atomic (HII) hydrogen. These phases are further divided by the temperature and density of the hydrogen, with the temperature of gas in the ISM ranging from $\gtrsim 10^{5.5}$ K in the hottest coronal gas, down to the few tens of K in the cool, dense molecular clouds where stars form. In this section, I provide a brief summary of the physical conditions of the different phases of the ISM. Table 1.1 shows the main components of the ISM and their temperatures and densities.

1.2.1.1 Hot ionised medium (HIM)

The HIM was first proposed to exist by Spitzer (1956). It is the hottest ($\sim 10^6$ K; Ferrière 2001), lowest density ($\sim 0.0065\ n_{\rm H}$ cm^{-3}; Ferrière 2001), phase of the ISM. It is also referred to as coronal gas, or sometimes as the Galactic Corona, due to its similar temperature to the Sun's Corona. It is primarily generated by supernova explosions (see e.g. Spitzer, 1990). The HIM is only a small component of the overall mass of the ISM, however, observations indicate that it pervades the volume of the Milky Way outside of the disc. It cools by adiabatic expansion and X-ray emission (Draine, 2011). The high temperatures of the HIM mean that it is observed in UV and X-ray emission. Diffuse X-ray haloes have been detected in some nearby spiral galaxies and this hot ionised gas appears to be correlated with the warm diffuse ionised gas (Tüllmann et al., 2006).

Table 1.1: A summary of the properties of the phases of ISM in the Milky Way: the temperature, T; the number density of hydrogen nuclei $n_{\rm H}$; the state of hydrogen in the phase $H_{\rm state}$; and common tracers of the phase. Table adapted from Ferrière (2001).

Phase	T [K][a]	$n_{\rm H}$ [cm^{-3}]	$H_{\rm state}$	Common tracers
Hot ionised medium (HIM)	$\sim 10^6$	~ 0.0065	HII	X-ray and UV emission
Warm ionised medium (WIM)	~ 8000	0.2 - 0.5	HII	Hα emission
Warm neutral medium (WNM)	6000 - 10000	0.2 - 0.5	HI	21-cm emission
Cold neutral medium (CNM)	50 - 100	20 - 50	HI	21-cm absorption
Molecular Medium (MM)	10 - 20 K	10^2 - 10^6	H_2	CO line and dust emission

[2] i.e. elements heavier than helium

1.2.1.2 Warm ionised medium (WIM)

In the Milky Way, the majority of the ionised hydrogen (≥ 90 per cent; Haffner et al. 2009) is contained in the diffuse, spatially extended warm ionised medium (WIM). The WIM is also referred to, especially in extragalactic contexts, as Diffuse Ionised Gas (DIG). The gas in this phase is warm ($\sim$ 8000 K; Ferrière 2001) and at low density (0.2 - 0.5 $n_{\rm H}$ cm^{-3}; Ferrière 2001). A number of different sources of the ionising radiation have been proposed, most prominently escaping Lyman continuum radiation from HII regions. The most common tracer of the WIM is the Hα line, which is used as a tracer of star formation (see Section 1.3.1). However, a number of emission lines from hydrogen and other species may be used to trace this phase.

1.2.1.3 HII regions

Ionised gas is also found in denser regions surrounding stars, which are known as HII regions. Radiation with energies above the Lyman limit (i.e. energies of 13.6 eV) are able to ionise the hydrogen in the molecular clouds in which stars are formed. Sufficient quantities of this ionising radiation, known as Lyman continuum, are produced by young, massive stars mostly in the form of UV radiation (see Section 1.3.1.1) in order to create a roughly spherical region of ionised gas around themselves known as a Strömgren sphere. HII regions thus trace young, massive stars and are used as a tracer of recent star formation, being visible along with other ionised hydrogen gas in Hα recombination line emission (see Section 1.3.1.2).

Excess energy from the photons ionising the hydrogen heats the gas, raising its temperature from the tens of Kelvin typical of the molecular medium to temperatures comparable to the WIM ($\sim 10^4$ K). The smallest HII regions known as ultracompact HII have sizes of ~ 0.1 light years across and densities of $\sim 10^4$ cm^3 (Churchwell, 2002). However, ionised regions from multiple stars in each other's vicinity may overlap, creating complex structures of HII gas. Moreover, HII regions can become extremely large, with the density of HII regions in the Milky Way and external galaxies observed to decrease linearly with increasing size (Garay & Lizano, 1999; Kim & Koo, 2001; Hunt & Hirashita, 2009). An example of a giant HII region is NGC604 in M33, which has a size of hundreds of pc (see e.g Relaño & Kennicutt, 2009).

1.2.1.4 Warm neutral medium (WNM)

The WNM is comprised of warm ($6000-10000$ K; Kulkarni & Heiles 1987) HI gas. It is a diffuse phase that is spread out throughout the disc of the Milky Way and exhibits a broad velocity dispersion (~ 9 km s^{-1}; Kulkarni & Heiles 1987). Due to its heat it radiates 21 cm line emission, with which it can be observed. Observations of external galaxies show holes in their HI discs, which are probably the result of feedback from star formation (Deul & den Hartog, 1990; Bagetakos et al., 2011).

1.2.1.5 Cold neutral medium (CNM)

Like the WNM, the CNM consists of neutral atomic hydrogen, however, at much cooler temperatures. In contrast to the diffuse nature of the WNM the CNM is structured into individual clouds, with velocity dispersions significantly lower than the WMN (Kulkarni & Heiles, 1987). These neutral hydrogen clouds have typical densities of $20-50$ cm^{-3} and temperatures of $30-80$ K (Kulkarni & Heiles, 1987). Due to their low temperatures they are observed in 21 cm absorption rather than emission. Studies of external galaxies indicate that molecular clouds form only (or at least most of the time) in filamentary regions with neutral hydrogen surface densities $\gtrsim 10^{21}$ cm^{-2}, but that

such conditions do not by themselves guarantee molecular cloud formation (Engargiola et al., 2003; Wong et al., 2009).

1.2.1.6 Molecular medium (MM)

The Molecular Medium (MM) is the densest, coolest phase of the ISM, in which hydrogen is molecular. Molecular gas is organised into small (tens of pc) molecular clouds, which are the sites of star formation. In addition to these compact structures, there is evidence for a diffuse molecular gas component spread out on large ($\sim$ kpc) scales (see e.g Pety et al., 2013; Caldú-Primo et al., 2013, 2015).

Molecular clouds are dense, cool, assemblages of molecular gas. Milky Way surveys of molecular clouds show they have typical sizes in the tens of pc with radii of $\sim 1-100$ pc, masses of $\sim 10^2-10^6$ $M_\odot$ and densities of $\sim 10^1-10^3$ cm^{-3} (Rathborne et al., 2009). Furthermore, the properties of molecular clouds within the Milky Way are observed to follow a number of relationships know as "Larson's relations".[3] The first relation observed by Larson (1981) is a correlation between the velocity dispersion of the cloud, σ, in km s^{-1} and the cloud's size in pc, L,

$$\sigma = 1.10 L^{0.38}. \tag{1.1}$$

This exponent measured by Larson (1981) is close to the value for subsonic turbulent velocity distributions (the so-called Kolmogorov law $\sigma \propto L^{\frac{1}{3}}$; Kolmogorov 1941.)[4] More recent observations by Solomon et al. (1987) find a power of 0.5, which would indicate supersonic turbulence, however. The second relation observed by Larson (1981) is between the velocity dispersion and the mass of the molecular cloud, M, in units of solar mass,

$$\sigma = 0.42 \frac{M}{\mathrm{M}_\odot}^{0.2}. \tag{1.2}$$

Last, the third Larson relation describes the observed inverse correlation between the size and density of molecular clouds. Larson (1981) relates the cloud size, L, the volume density of hydrogen molecules, $n_{\mathrm{H_2}}$, in units of cm^{-3}, with the relation

$$n_{\mathrm{H_2}} = 3400 L^{-1.1}. \tag{1.3}$$

This implies that the surface density of clouds varies only very weakly with size of the clouds (as $L^{-0.1}$). However, subsequent observations have shown that cloud surface densities vary significantly between and within galaxies (Hughes et al., 2013; Schruba et al., 2019). Additionally, Larson (1981) evaluated the balance between gravitational potential energy and kinetic energy for the sample of clouds considered in their study, finding that $2GM/\sigma^2 L \approx 1$. Thus they concluded that the majority of their sample are gravitationally bound and in virial equilibrium.

Studies of molecular clouds in external galaxies indicate that their properties vary with environment. For example, the average luminous mass of clouds varies between $\sim 1\times10^5$ $M_\odot$ in the LMC to $\sim 3.5\times10^7$ $M_\odot$ in the starburst galaxy NGC 253 (Schruba et al., 2019). In general, molecular clouds appear to be inefficient at converting molecular gas into stars, with typically only ~ 1 per

[3] Also known as "Larson's laws".
[4] Accessed in translation from Kolmogorov (1991).

cent converted into stars per free-fall time (Utomo et al., 2018; Schruba et al., 2019). The dynamical properties of molecular clouds in nearby galaxies are observed to be linked to their galactic environments, with their densities and virial states linked to the ambient pressure. Clouds situated in low-pressure, atomic gas-dominated environments are observed to be pressure confined and have low mass surface densities, whereas clouds in high-pressure molecular-dominated environments have high mass surface densities and appear to be self-gravitating (Schruba et al., 2019).

High-resolution observations of the nearest molecular clouds in the Milky Way show that there are denser structures within molecular clouds. These structures form hierarchically through collapse and are generally categorised into filaments, clumps and cores. Infrared observations of molecular clouds, such as those conducted with the Herschel Space Observatory, show that clouds contain extended filamentary structures of dense gas. These filaments are long thin structures that exhibit a range of lengths up to a few pc and appear to have a typical width of ~ 0.1 pc (Arzoumanian et al., 2019). Clumps are dense subregions within molecular clouds. They have typical sizes of $0.3-3$ pc, masses of $50-500$ $M_\odot$ and densities of $n_{H_2} \sim 10^3 - 10^4$ cm^{-3} (Bergin & Tafalla, 2007) and are capable of forming stellar clusters, i.e. ensembles of stars. Last, cores are very dense ($n_{H_2} \sim 10^5$ cm^{-3}; Williams et al. 2000) compact ($\sim 0.01-0.1$ pc; André et al. 2010; Jessop & Ward-Thompson 2000) regions in which a single star or a multiple-star system (such as a binary star system) will form. High-resolution observations of massive star-forming cores shows further hierarchical structure, with these sources fragmenting into smaller structures (Beuther et al., 2018). Observational estimates of the lifetimes of these cores suggest that they survive for $\sim 1-10$ Myr (e.g Beichman et al., 1986; Lee & Myers, 1999; Jessop & Ward-Thompson, 2000), which is towards the lower end of estimates of the lifetimes for molecular clouds themselves (see Section 1.4.2).

.

Variations in the physical properties of the substructure of molecular clouds may well drive the variation that is observed in the populations of molecular clouds between different galaxies. However, the high resolution observations required to detect such small structures, mean that we are restricted to analysing them in only nearby environments. This thesis is concerned with understanding the physics of star formation in an extragalactic context and I therefore focus on understanding star formation on the cloud-scale. In particular, I discuss the lifecycles of molecular clouds in detail in Section 1.4.

1.2.2 Tracing molecular gas

Although molecular hydrogen, H_2, is the most abundant molecule in the Universe, it was not observed in the ISM until the detection of Lyman-α absorption in 1970 with rocket experiments (Carruthers, 1970). Observing H_2 in emission is, however, very difficult due to its lack of a permanent dipole moment and the high (510 K; Hartquist & Williams, 1998)[5] excitation energy of its lowest permitted rotational transition. It is therefore hard to observe at the low temperatures of molecular clouds (~ 10 K; see Table 1.1). Molecular gas masses can be estimated from H_2 rotational transitions (see Togi & Smith, 2016), however, such measurements are not common. For these reasons emission from other molecules, most notably carbon monoxide (CO), as well as atomic species (such as neutral carbon), ions (most notably the C+ ion) and dust are commonly used to trace the total H_2 mass of galaxies.

The most common isotope of carbon monoxide ($^{12}C^{16}O$, hereafter simply CO) is commonly used as a tracer of the molecular gas due to its rotational transitions having significantly lower energy levels than H_2, which makes them accessible in the temperatures of molecular clouds. Its

[5]The energy of the transition 354.373 cm^{-1} is converted to K with a value of the Boltzmann constant, $k = 0.6950348004$ https://physics.nist.gov/cgi-bin/cuu/Value?k and rounded to the nearest 10 K

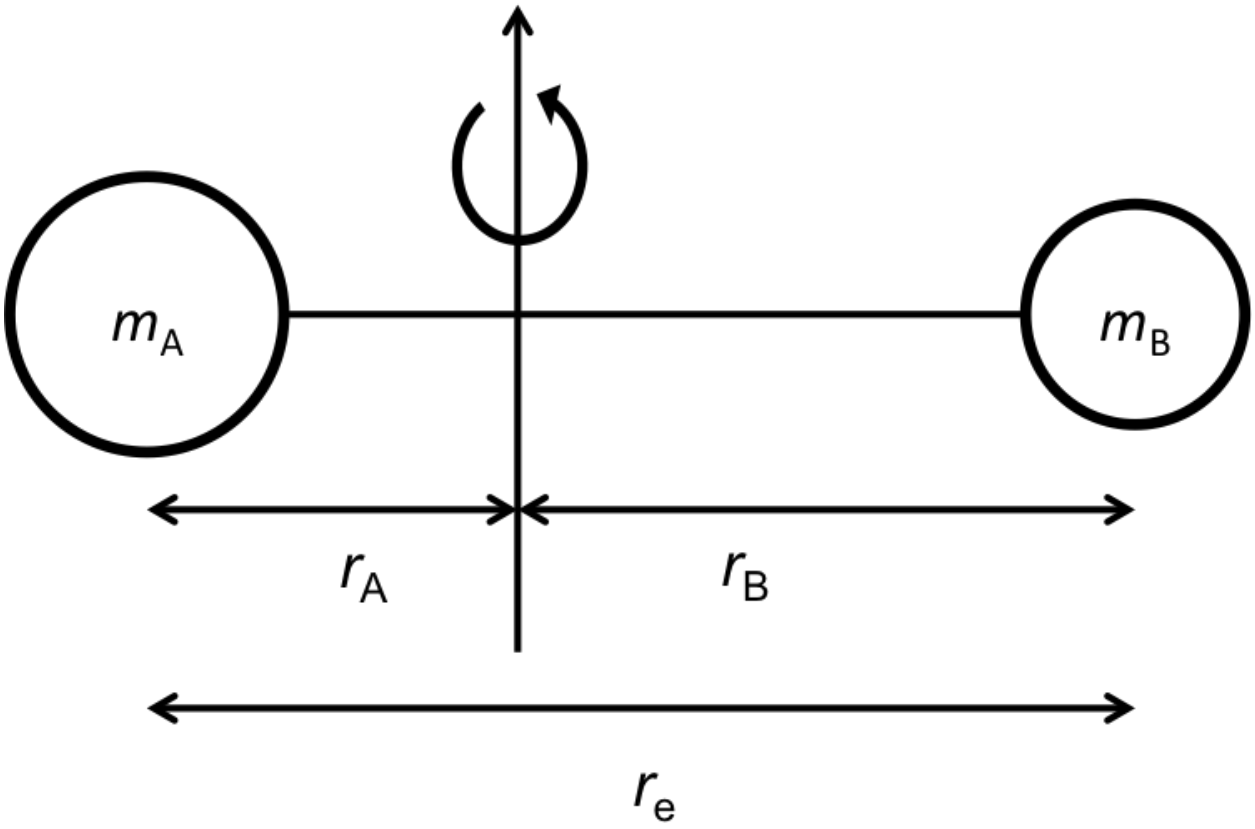

Figure 1.6: An illustration of a rotating diatomic molecule. Two atoms A and B, with masses m_A and m_B, respectively are bound together in a molecule. The molecule rotates about its centre of mass. The equilibrium bond distance, r_e, between the two atoms is the sum of the distance from each atom to the molecules centre of mass, r_A and r_B.

discovery was also reported in 1970, from observations of CO in Orion (Wilson et al., 1970). The "canonical abundance" ratio of CO of to H_2 is 10^{-4} (van Dishoeck et al., 1992). Although direct observations of H_2 with which to compare the CO are limited, they show that this value varies with environment with diffuse clouds having significantly lower CO ratios, whilst those in GMCs are generally consistent with the canonical abundance (van Dishoeck et al., 1992; Sheffer et al., 2008). Two commonly observed CO transitions are the CO(J = 1 → 0) and CO(J = 2 → 1) transition, hereafter, CO(1-0) and CO(2-1). The excitation energy of the CO(1-0) transition is 5.5 K (Hartquist & Williams, 1998)[6] and the excitation energy of the CO(2-1) transition is 17 K (Hartquist & Williams, 1998),[7] with these temperatures comparable to those of molecular clouds.

The rotation energy of molecules is quantised into levels, represented by the angular momentum quantum number $J \in \mathbb{N} \mid 0 \leqslant J$. Figure 1.6 illustrates a diatomic, rigidly-rotating molecule, a good approximation of the CO molecule. For a diatomic, rigidly-rotating molecule, the energy of

[6] The energy of the transition 3.84503 cm^{-1} is converted to K with a value of the Boltzmann constant, $k = 0.6950348004$ https://physics.nist.gov/cgi-bin/cuu/Value?k and rounded to the nearest 0.1 K.

[7] The energy of the transition 11.53495 cm^{-1} is converted to K with a value of the Boltzmann constant, $k = 0.6950348004$ https://physics.nist.gov/cgi-bin/cuu/Value?k and rounded to the nearest 1 K.

a rotational energy level is

$$E(J) = \frac{\hbar^2}{2m_r r_e} J(J+1), \tag{1.4}$$

where m_r is the reduced mass (the effective inertial mass) of the molecule and r_e is the equilibrium bond distance between the two atoms in the molecule (Wilson et al., 2016). For a diatomic heteronuclear molecule "AB" (such as CO) the reduced mass is

$$m_r = \frac{m_\mathrm{A} m_\mathrm{B}}{m_\mathrm{A} + m_\mathrm{B}} \tag{1.5}$$

(Wilson et al., 2016). A photon has a spin, or intrinsic angular momentum, of unity. Thus, for a transition where one photon is emitted or absorbed, allowed transitions may increase or decrease the angular momentum quantum number by unity, due to the conservation of angular momentum. Another way to state this is that the selection rule for allowed transitions is $\Delta J = \pm 1$. For a transition that decreases the energy level, light is emitted, which we may be able to detect. For a transition from energy level J to $J-1$ the change in energy is

$$\Delta E_{J \to J-1} = E(J) - E(J-1) = \frac{\hbar^2}{m_r r_e} J. \tag{1.6}$$

CO molecules are generally excited into higher rotational energies through collisions with the much more abundant $\mathrm{H_2}$ molecules. However, sufficiently energetic collisions with other species will also excite them. $\mathrm{H_2}$ molecules in the ISM have velocities that follow the Maxwell-Boltzmann distribution. Thus at the low temperatures in molecular gas (see Table 1.1), many $\mathrm{H_2}$ molecules have sufficient energy to excite CO from the $J = 0$ state to the $J = 1$ state, as $\Delta E/k = 5.5$ K for this transition. However, far fewer molecules have sufficient energy to excite $\mathrm{H_2}$ by $\Delta E/k = 510$ K. Such a transition results in the emission of a photon whose frequency is set by the relation between the energy and the frequency of a photon, $E = 2\pi\nu\hbar$, giving the relationship

$$\nu_{J \to J-1} = \frac{\hbar J}{2\pi m_r r_e}. \tag{1.7}$$

Thus the transitions form a "ladder" in frequency space whose rungs are set at multiples of the frequency of the transition from the first excited state to the ground state.

Another important consideration with regards to the suitability of a molecular line as a tracer is its critical density n_crit. This is the density at which collisions into the excited state balance transition out of the excited state due to spontaneous emission

$$n_\mathrm{crit} = \frac{A_{J,J+1}}{C_{J,J+1}}. \tag{1.8}$$

where $A_{J,J+1}$ is the Einstein A coefficient, describing the rate of spontaneous emission, which depends on the frequency of the transition and the transition's dipole moment, and $C_{J,J+1}$ is the coefficient of the rate of collisional excitation, which depends on the temperature of the gas and collisional cross section of the particle (Carilli & Walter, 2013). For CO(1-0) in typical cloud

conditions, this equates to $n_{\rm crit} = 2.1 \times 10^3$ cm^{-3} (Carilli & Walter, 2013), which is towards the lower end of the observed densities of molecular gas (see Table 1.1). Thus CO(1-0) is a good tracer of the hydrogen at the typical densities of the molecular medium. Higher J transitions of CO have higher critical densities (e.g. $n_{\rm crit} = 1.1 \times 10^4$ cm^{-3} for CO(2-1); Carilli & Walter 2013) and indeed other molecular species also trace higher densities (for example. the commonly used tracer of dense gas HCN has $n_{\rm crit} = 2.6 \times 10^6$ cm^{-3}; Carilli & Walter 2013). Thus different tracers of the molecular gas may be used together to probe its density structure.

To convert the luminosity of CO line emission to a molecular gas mass, $M_{\rm mol}$, one must apply a conversion factor $\alpha_{\rm CO}$,

$$M_{\rm mol} = \alpha_{\rm CO} L_{\rm CO}, \tag{1.9}$$

where $M_{\rm mol}$ is in units of solar mass and $L_{\rm CO}$ is the observed luminosity of the CO(1-0) line in units of K km s^{-1} pc^2 and $\alpha_{\rm CO}$ is in units of M$_\odot$ $(\mathrm{K\,km\,s^{-1}\,pc^{-2}})^{-1}$ (Bolatto et al., 2013a). The value of $\alpha_{\rm CO}$ has been calibrated with a number of methods and a typical Milky Way value is 4.3 M$_\odot(\mathrm{K\,km\,s^{-1}\,pc^{-2}})^{-1}$ (see Bolatto et al., 2013a). Observational studies show that the value of $\alpha_{\rm CO}$ is not constant across all galaxies, but in fact varies with environment. For example, starburst galaxies are observed to have systematically lower values of $\alpha_{\rm CO}$ (Downes & Solomon, 1998). The value of $\alpha_{\rm CO}$ is also observed to vary with metallicity, with lower metallicity gas requiring the application of a higher value of $\alpha_{\rm CO}$, (see e.g review by Bolatto et al., 2013a).

In addition to the $\alpha_{\rm CO}$ conversion, converting observations of higher-J CO line transitions into gas masses requires the application of an excitation correction factor to obtain the CO(1-0) line luminosity. The luminosity of each transition depends on the temperature and density of the gas from which the photons are being emitted (see e.g. Weiß et al., 2007). This factor can be determined from simulations or from observations of both CO(1-0) and a higher-J CO line either in similar environments as the observation or in a sub-region of the total area of observation (see e.g Gratier et al., 2010b).

The transition frequencies of the $J = 1 \rightarrow 0$ and $J = 2 \rightarrow 1$ transitions are 115.27 GHz and 230.54 GHz, respectively (Carilli & Walter, 2013). Practically, this places them in the regime of millimetre astronomy in the Local Universe, where observations are carried out with radio telescopes. Figure 1.2 shows an example of such a telescope. Fortuitously, they also fall in a region of wavelength-space where observations from the ground are not excluded by the opacity of the atmosphere. However, larger telescopes are required in order to obtain observations at resolutions matched to shorter wavelength observations (such as Hα and UV observations for tracing star formation; see Section 1.3.1). The angular resolution, θ, of a telescope is given by the relation $\theta \approx \lambda/D$, where λ is the wavelength of the observed emission and D is the diameter of the telescope. Engineering limitations fundamentally limit cloud-scale observations at mm-wavelengths with single dish telescopes to the nearest few galaxies. However, interferometry enables observations at better angular resolution without the need to construct larger telescopes. In an interferometer many individual telescopes are operated together to create what is in effect a single telescope whose resolution is set by the distance between the telescopes that comprise the interferometer.

1.3 Star formation

Stars form out of cool, dense, molecular gas within molecular clouds (see Section 1.2.1.6). The masses of these stars are observed to be "sampled" such that stellar populations follow an initial

mass function (Salpeter, 1955). This mass function is often formulated as

$$dN \propto m^{-\alpha} dm, \tag{1.10}$$

where the number dN of stars of a given mass m is defined by a power law with slope, α. For a Salpeter IMF $\alpha = 2.35$ (Salpeter, 1955). Although the exact form of the IMF is debated (Kroupa, 2001; Chabrier, 2003) most evidence shows that the IMF does not vary strongly between different environments (Bastian et al., 2010).

One of the simplest metrics by which one can analyse star formation is the SFR, measured in $M_\odot$ yr^{-1}. The SFR varies significantly between galaxies and understanding this variation is crucial for understanding the evolution of galaxies. As stars form from gas it is natural to relate the SFR to the amount of gas that is available for star formation. One way of characterising the star formation process is through the depletion time, $t_{\rm depl}$, or amount of time that it would take star formation, continuing at the presently observed rate, to totally consume the observed gas reservoir of a galaxy. For nearby spiral galaxies the average value of $t_{\rm depl}$ for molecular gas is observed to be ~ 2 Gyr (Bigiel et al., 2008, 2011).

Spiral galaxies are observed to follow a relatively tight correlation between the SFR surface density, $\Sigma_{\rm SFR}$, and the surface density of gas $\Sigma_{\rm gas}$. This relation is known as the Kennicutt-Schmidt relation (Schmidt, 1959; Kennicutt, 1989, 1998) and its functional form is

$$\Sigma_{\rm SFR} \propto \Sigma_{\rm gas}^{n}, \tag{1.11}$$

where the exponent n is empirically determined and is typically measured to be $\sim 1.3-1.5$ (Kennicutt, 1989, 1998). Other populations of galaxies are also observed to follow a relation of this form, but are offset in terms of their global star formation efficiency. One example is starburst galaxies (galaxies going through an intense phase of star formation) which are found to have a higher global star formation efficiency (see Figure 1.7). In contrast, star-forming early-type galaxies are observed to follow such a relation, but with a lower global star formation efficiency (Davis et al., 2014).

As star formation takes place in clouds of molecular gas, one can ask whether the total amount of hydrogen gas is important for star formation or only the total amount of gas in molecular form. Bigiel et al. (2008) found a tight correlation between $\Sigma_{\rm H_2}$ and the SFR in a sample of 18 nearby galaxies, whereas no significant correlation was observed with $\Sigma_{\rm HI}$. This indicates that although the star formation efficiency (SFE) of the total gas in galaxies is observed to vary between galaxies, there appears to be a roughly constant molecular SFE between and within galaxies. This indicates that the total molecular gas reservoir mostly determines the SFR of local non-starbursting spiral galaxies.

The tight correlation between the gas mass surface density and SFR surface density is observed to break down on small (sub-kpc) scales within galaxies (Bigiel et al., 2008; Onodera et al., 2010; Schruba et al., 2010). Figure 1.8 shows how the scatter in the Kennicutt-Schmidt relation increases as the probed size-scales become smaller. At kpc scales a tight relation is observed, whereas at small (250 pc) scales, a large scatter is observed in the relation. The Kennicutt-Schmidt relation was established with integrated measurements for whole galaxies that average over many molecular clouds and star formation regions at different stages of their evolutionary cycles. In contrast, at small scales, observations probe individual regions at different stages of evolution, i.e. young regions with a high $t_{\rm depl}$ and old regions with a low $t_{\rm depl}$ and thus global averages are not recovered at small scales (Schruba et al., 2010).

Stars, once formed, have a significant impact on their natal molecular clouds (see Figure 1.9 for

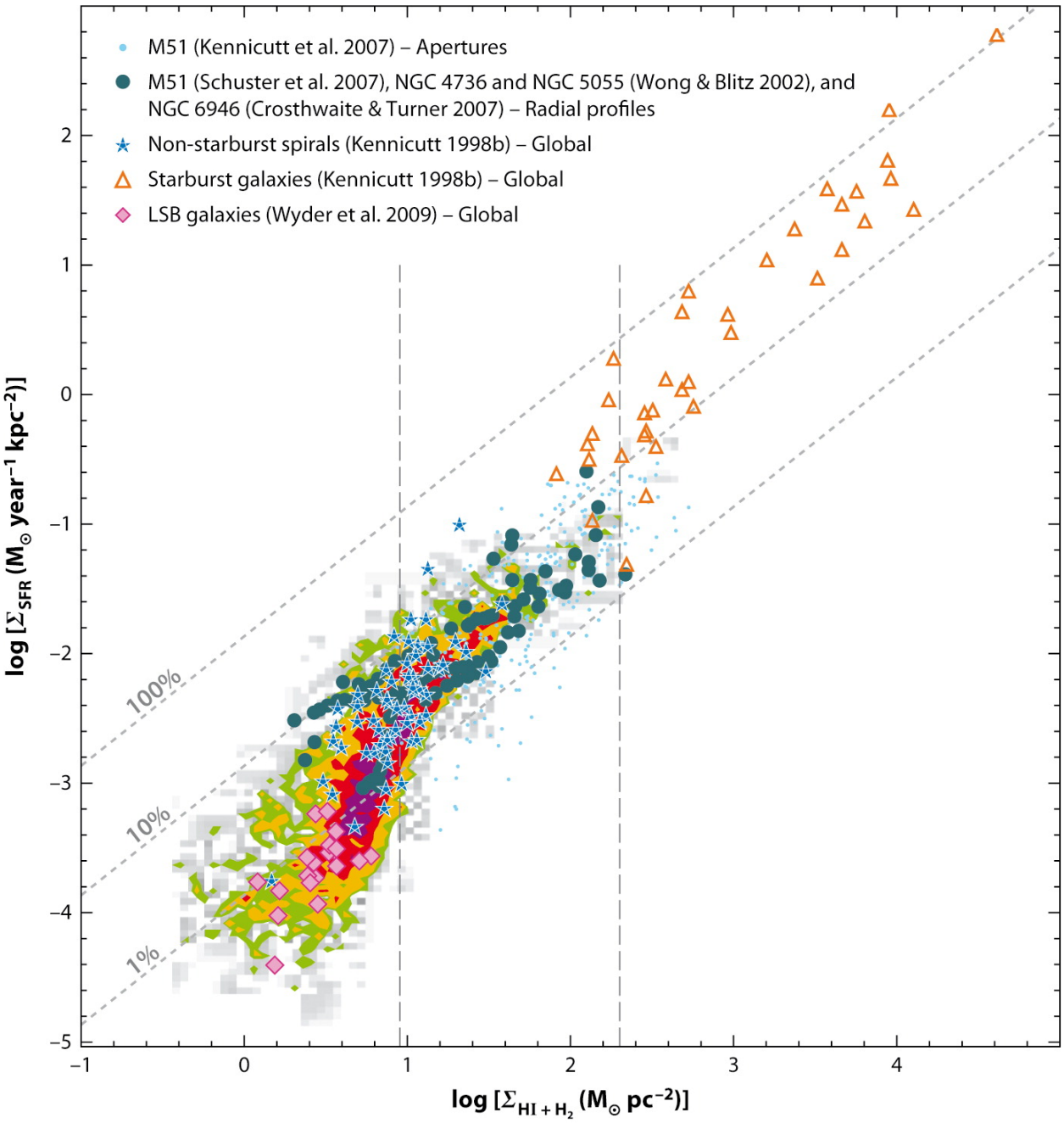

Figure 1.7: The Kennicutt-Schmidt relation between the star formation rate surface density, $\Sigma_{\rm SFR}$, and the total gas mass surface density, $\Sigma_{\rm HI+H_2}$ for a sample of nearby galaxies (coloured areas) individual datasets (points, as indicated in the legend). The dashed grey lines represent lines of constant global star formation efficiency of 1, 10 and 100 per cent. The plot illustrates how for normal star forming galaxies there is a relationship between the two quantities with some scatter around a star formation efficiency of a few per cent. In comparison, starburst galaxies lie above the relation for normal spiral galaxies, whilst low surface brightness galaxies lie below it. Figure taken from Kennicutt & Evans (2012).

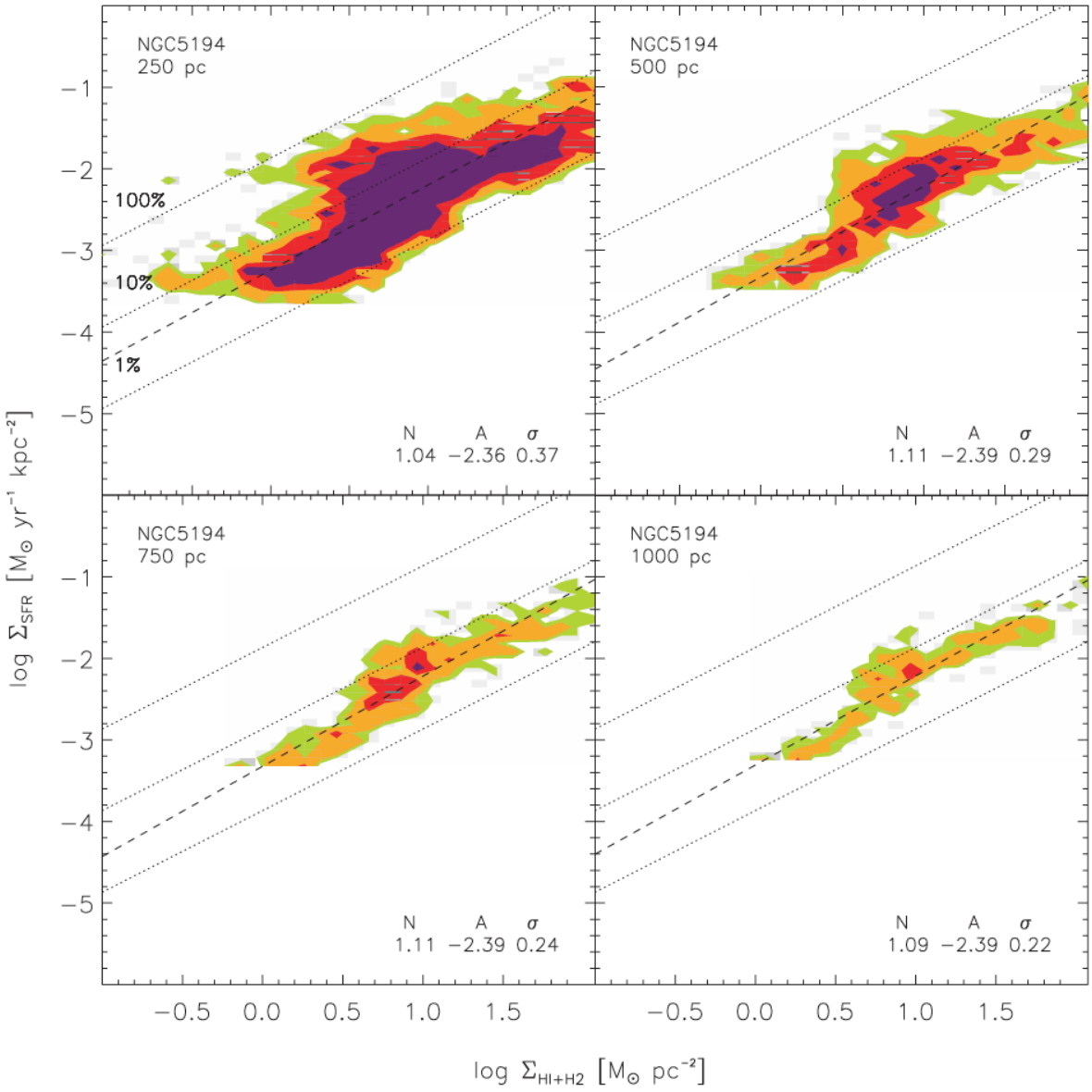

Figure 1.8: The breakdown of the Kennicutt-Schmidt relation on sub-kpc scales in NGC5194. The Kennicutt-Schmidt relation between star formation rate surface density as a function of gas mass surface density was established with integrated measurements of entire galaxies. Within galaxies, the relation holds on large (supra-kpc) scales, but breaks down on small (sub-kpc) scales as galactic structure is increasingly resolved and the correlation between molecular gas and young stars breaks down. Figure taken from Bigiel et al. (2008)

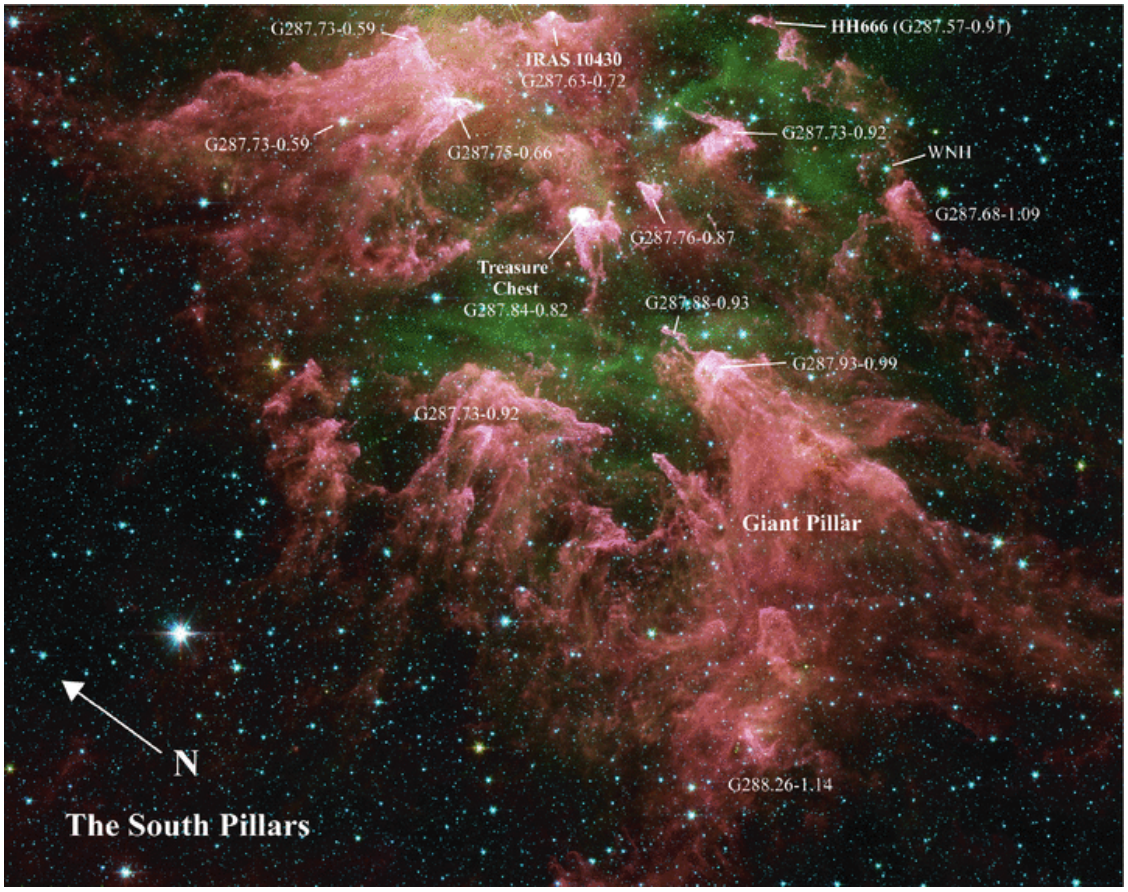

Figure 1.9: Spitzer IRAC observations of the Carina Nebula. This images shows the impact of stellar feedback on a molecular cloud. Figure taken from Smith et al. (2010)

an observational example) and their host galaxies more broadly. Through a number of processes known collectively as "stellar feedback", stars inject energy and matter into the ISM. During their lives, stars emit radiation, which can both photoionise the surrounding gas and exert a pressure on it to mechanically remove it from the vicinity of the star. The photoionising radiation from young, massive stars creates surrounding regions of ionised gas known as HII regions (see Section 1.2.1.3). The Hα line emission from recombining hydrogen atoms in these regions is used as a tracer of star formation (see Section 1.3.1.2). Stars also emit "winds" comprised of matter ejected by the star, which exert a mechanical pressure on the surrounding gas.

The most dramatic form of stellar feedback is that from supernovae. At the end of their hydrogen-fusing phases, stars will obtain their energy from fusing heavier elements until this energy is no longer enough to support them against gravitational collapse. For stars with an inert core mass below the Chandrasekhar limit of ~ 1.4 M$_\odot$, electron degeneracy pressure is sufficient to support them against collapse. Thus low mass stars become white dwarves, stars supported against collapse, but with no source of energy, which therefore slowly cool as they radiate their energy. Sufficiently massive stars ($\gtrsim 8$ M$_\odot$) will instead collapse and end their lives in supernova explosions. The resulting explosions deposit a large amount of energy as well as metals into the ISM, raising its metallicity. These supernovae explosions do not take place for newly formed stars before ~ 3 Myr (Leitherer et al., 2014), when the shortest-lived stars to go supernova explode. This naturally leads to the question of whether clouds are dispersed by quick acting feedback (radiation and winds) before the first supernovae.

1.3.1 Tracing star formation

As the formation of stars proceeds on timescales much greater than a human lifetime, the most direct available method of measuring the SFR is by measuring the ages and masses of currently extant stars. In an ideal situation, one would measure the masses and ages of all the individual stars in a galaxy and compute the SFR directly. However, determining the ages of stars is a highly challenging process (Soderblom, 2010) and thus in practice SFRs calculated in this manner rely on observing only a subset of the total stellar population to which a lifetime can be assigned. An example of such a population is Young Stellar Objects (YSOs) with an IR excess. As resolving individual stars becomes increasingly difficult the further outside of the Milky Way one wishes to observe, such methods are in practice restricted to very nearby galaxies; see for example applications of YSO counting to the LMC (Chen et al., 2010) and counting young stars in the SMC (Hony et al., 2015). We are therefore confined to measuring observable spectral features that are linked to star formation. Such methods rely on the calibration of some observable feature, such as the luminosity of an emission line, to the star formation rate. Table 1.2 gives details of the star formation rate tracers used in this thesis. These methods include both direct methods, that rely on emission from young stars directly, and indirect methods that rely on the impact of young stars on some other population. For each tracer, a prescription must be calibrated. These prescriptions for the SFR take the form

$$\log \mathrm{SFR} = \log L_x - \log C_x, \tag{1.12}$$

where L_x is the luminosity of a tracer "x" and C_x is a calibration constant for said tracer that is determined empirically for each tracer (Kennicutt & Evans, 2012). In this thesis, I utilise both a direct SFR tracer (UV continuum) and an indirect SFR tracer (Hα). As different tracers have different assumptions and are affected differently by observational considerations, the use of multiple tracers helps to form more robust conclusions.

1.3.1.1 UV continuum

Stars emit both continuum emission that varies smoothly with wavelength as well as exhibiting emission and absorption features at wavelengths corresponding to certain quantum transitions. The UV continuum emission that comes from stars is a stellar-emission feature that is used to trace star formation. The continuum emission from stars is well approximated by a blackbody function. Wien's displacement law relates the peak wavelength, λ_{peak}, of a blackbody to the temperature of the body T,

$$\lambda_{\mathrm{peak}} = \frac{b}{T}, \tag{1.13}$$

where b is the Wien displacement law constant $2.897771955 \times 10^{-3}$ m K[8]. Thus, hotter stars emit more radiation at lower wavelengths (i.e. higher energy). For blackbodies, their temperatures are given by the Stefan-Boltzmann law,

$$T \propto L^{\frac{1}{4}}, \tag{1.14}$$

[8] https://physics.nist.gov/cgi-bin/cuu/Value?bwien

and thus more luminous stars have higher temperatures. Furthermore, stars are observed to have greater luminosities the greater their mass,

$$\frac{L}{\mathrm{L}_\odot} = \left(\frac{M}{\mathrm{M}_\odot}\right)^\alpha, \tag{1.15}$$

where the exponent α is measured empirically. For solar metallicity stars of mass $\sim 2-20$ $\mathrm{M}_\odot$, $\alpha \sim 3.5$ (Salaris & Cassisi, 2005). Thus the temperatures of main-sequence stars are set by their masses, with more massive stars having a hotter temperature and UV continuum emission from stars mostly comes from massive stars.

Stars on the main sequence,[9] fuse hydrogen as their fuel and so the main sequence lifetime of a star, τ_{ms}, is determined by the balance between energy available from their hydrogen fuel reservoir, E_{H}, and the energy that they emit, L,

$$\tau_{\mathrm{ms}} = \frac{E_{\mathrm{H}}}{L} \tag{1.16}$$

(Kippenhahn et al., 2012). Taking Equation 1.15 and assuming a constant fraction of the mass of stars is available for hydrogen burning, this gives a relationship for τ_{ms} in terms of the mass of the star, M,

$$\tau_{\mathrm{ms}} \propto \left(\frac{M}{\mathrm{M}_\odot}\right)^{-2.5} \tag{1.17}$$

(Kippenhahn et al., 2012). Therefore the lifetimes of stars on the main sequence decrease sharply with increasing mass. For accurate stellar lifetimes, more detailed modelling must be performed (e.g. Bressan et al., 2012). Even so, this statement remains qualitatively true. Thus, although UV continuum emission traces stars across a large range of ages, in star-forming galaxies it is dominated by young, massive stars (O and B type stars) with ages less than ~ 100 Myr (Hao et al., 2011). Therefore with knowledge of the IMF from which stellar masses are sampled (see Equation 1.10) one can calibrate the observed UV luminosity to an SFR in terms of mass (see e.g. Madau et al., 1998). Due to the high opacity of the atmosphere to UV radiation, UV observations must be carried out at high altitude, either with rockets (e.g Donas et al., 1987), balloons (e.g Sullivan et al., 2000) or space-telescopes. In practice space telescopes are the only method that satisfy the requirements for accurate, cloud-scale extragalactic observations of star formation. GALEX, an example of such a UV space telescope is shown in Figure 1.2.

1.3.1.2 Hα

An alternative to tracing star formation via the direct emission of stars is to measure emission from other components of the galaxy that have been affected by young stars. The most common such method is using emission lines that originate from the gas surrounding young, massive stars that has been ionised by them (HII regions, see Section 1.2.1.3). These lines are readily observed from the ground in optical and IR wavelengths. The most commonly used line is the Hα line, a highly prominent feature of late-type galaxies (see Figure 1.1). In comparison to UV, Hα traces younger, more massive stars and thus traces the star formation across a more recent period of time (see Table 1.2). Although Hα is the most utilised such line, other emission lines are employed to

[9] Not to be confused with the Main Sequence of star formation for galaxies.

Table 1.2: A summary of common methods of tracing star formation. Adapted from Kennicutt & Evans (2012).

Tracer	Wavelength [Å]	t_{median} [a] [Myr]	$t_{90\%}$ [b] [Myr]
FUV	1528 [c]	10	100
NUV	2271 [c]	10	200
Hα	6562.8	3	10

[a] Mean stellar population age of stars contributing emission
[b] Stellar population age below which 90 per cent of emission is contributed
[c] The effective wavelengths of the GALEX FUV and NUV filters (Madore, 2005).

trace star formation. Both other hydrogen emission lines (including H_β and Pa_α) and emission lines from other species are used. These lines are, however, fainter and thus more challenging to observe, which has led to them being less widely applied in the extragalactic context. One key advantage of Hα over UV tracers of star formation is its accessibility from the ground with conventional optical telescopes (see e.g. Figure 1.2). Another advantage is the significantly lower impact of dust extinction, in comparison to UV, which suffers from greater reduction in observed flux and an increased uncertainty of correcting for extinction.

1.4 Molecular cloud lifecycles

Molecular clouds are comprised of dense, cool molecular hydrogen gas and are the sites in which the process of star formation takes place. I give details about their general properties in Section 1.2.1.6 and their observation in Section 1.2.2. Molecular clouds are observed to experience effects, such as from stellar feedback, that must lead to their evolution. Therefore we can ask for how long do molecular clouds live, what processes cause their destruction or dispersal and how long does their dispersal take. Beyond simply giving us a greater understanding of molecular clouds themselves, the answers to these questions have important implications for the understanding of the evolution of the ISM and galaxies in general. In this section, I summarise some of the key of the theory regarding the lifecycles of molecular clouds as well as observational constraints on these lifecycles.

1.4.1 Theories of molecular cloud lifetimes and molecular cloud dispersal by feedback

A simple theoretical timescale linked to the cloud lifetime can be obtained by considering the timescale of gravitational collapse for a molecular cloud under freefall,

$$\tau_{\text{ff}} = \sqrt{\frac{3\pi}{32G\rho}}, \tag{1.18}$$

where ρ is the cloud volume density and G is the gravitational constant. However, the true lifetime of a molecular cloud will be longer if other forces (such as magnetic fields) provide support against collapse. τ_{ff} varies between ~ 1 and ~ 15 Myr for nearby galaxies (Schruba et al., 2019). In the Milky Way a typical value is ~ 10 Myr, though it varies strongly with environment, decreasing to only ~ 0.5 Myr in the Central Molecular Zone of the Milky Way (Schruba et al., 2019).

Another relevant cloud dynamical timescale is the turbulent crossing timescale,

$$\tau_{\text{cr}} = \frac{R}{\sigma}, \tag{1.19}$$

where R is the radius of the cloud and σ is the Gaussian velocity dispersion of the cloud. Observations of nearby galaxies show that τ_{cr} is in general similar to τ_{ff} for their populations of clouds, with values between ~ 1 and ~ 11 Myr (Schruba et al., 2019). With an observed relation between dispersion and cloud size (see Equation 1.1), Larson (1981) estimated that the timescale for internal motion to cause large changes in molecular cloud structure is ~ 15 Myr for a 100 pc cloud, but only 0.2 Myr for a 0.1 pc cloud. This would suggest that the size of molecular clouds plays a role in their lifetimes. Elmegreen (2000) observed that the spread of stellar ages in clusters follows a relationship with the cluster size that matches the relationship between cloud crossing times and cloud sizes and concluded that star formation must take place on a timescale of the order of τ_{cr}.

These cloud dynamical timescales are significantly shorter than the observed molecular gas depletion time (~ 2 Gyr; Bigiel et al. 2008 and Bigiel et al. 2011). The question then arises as to how star formation in molecular clouds translates to globally inefficient star formation. Are molecular clouds long-lived structures that only convert a small fraction of their mass into stars per dynamical time, or are clouds quickly dispersed by feedback from the stars that they form, thus preventing further conversion of their gas into stars? Answering this question requires us to measure the lifetimes of these molecular clouds.

Another important timescale for the lifetimes of molecular clouds is the lifetime of hydrogen molecules. Hydrogen exists in three states within the ISM: H_2, HI and HII. Scoville et al. (1979), Scoville & Hersh (1979) and Scoville & Wilson (2004) observed that a greater fraction of the hydrogen mass in inner regions of galaxies is molecular in form rather than atomic or ionised. From this observation, they concluded that the timescale for hydrogen molecules to cease to be molecular must be greater than the timescale for the conversion of non-molecular hydrogen to molecular hydrogen for a steady state to be preserved between the phases. On this basis they argue that the lifetimes of hydrogen molecules should be greater than 100 Myr by comparison to the dynamical timescale of HI and the spiral arm crossing time. Clouds may have shorter lives than this molecular timescale, however, if they are dispersed without the destruction of the molecules within them. Indeed, determining whether clouds are short or long-lived is important for determining the physical processes that are effective during their lifetimes, with implications for understanding galaxy evolution. For example, Zasov & Khoperskov (2015) calculate that dynamical friction would have a significant impact for the positions of GMCs in M33, but only if they survive for $\gtrsim 100$ Myr.

The lifetimes of molecular clouds are likely governed by the interplay of a number of different processes whose significance varies with environment. Jeffreson & Kruijssen (2018) present an analytic theory for the cloud lifetime that takes into account a number of different timescales. This theory defines a cloud lifetime, τ_{JK18}, in terms of a number of other timescales

$$\tau_{JK18} = \left| \tau_{\kappa}^{-1} + \tau_{\Omega_p}^{-1} + \tau_{ff,g}^{-1} + \tau_{cc}^{-1} - \tau_{\beta}^{-1} \right|^{-1}, \tag{1.20}$$

where τ_{κ} is the timescale of epicyclic perturbations, τ_{Ω_p} is the timescale of perturbations due to the motions of spiral arms through the ISM, $\tau_{ff,g}$ is the gravitational free-fall timescale of the ISM, τ_{cc} is the timescale of cloud-cloud collisions and τ_{β} is the timescale for galactic shear to tear the cloud apart. With the exception of shear (τ_{β}), which acts to disperse the cloud, the processes characterised by these timescales act to compress the clouds and promote star formation (Jeffreson & Kruijssen, 2018). This analytic theory predicts that under different physical conditions, a differing subset of these timescales will determine cloud lifetimes (Jeffreson & Kruijssen, 2018). Testing this prediction requires observing cloud lifetimes in multiple galaxies with a range of different properties.

Another avenue that has been taken to synthesise the competing timescales that act to determine

a cloud's lifetime is the use of numerical simulations, such as the isolated disc galaxy simulations presented by Dobbs et al. (2011), Dobbs et al. (2012) and Dobbs & Pringle (2013). Dobbs & Pringle (2013) find that clouds with masses in excess of 10^5 $M_\odot$ in their simulations live for a minimum of 2 Myr and very few live beyond 40 Myr. They find that in their population of clouds, longer-lived clouds are in general more massive and the majority of clouds live for between 4 and 25 Myr. They also compared their measured cloud lifetimes to τ_{cr}, finding a correlation but with significant scatter.

Other hydrodynamical disc simulations find similar cloud lifetimes, though there is variation between simulations. This variation is driven by differences in the prescriptions used to model various processes, differences in the methods for measuring cloud lifetimes and differences between the galaxies or clouds being simulated. Disentangling these effects is important for making quantitative comparisons between simulations and observations. By way of example, different methods of measuring cloud lifetimes within simulations can produce significantly different results. For example, in simulations of low mass disc galaxies, Richings & Schaye (2016) find a median cloud lifetime of 13 Myr when considering the timescale where greater than or equal to half the particles that comprised the originally identified cloud remained. However, when they instead used a criterion based on cloud mass they found a longer median cloud lifetime of 33 Myr due to gas particles moving into and out of the cloud. Care must therefore be taken when qualitatively comparing the lifetimes of molecular clouds between different simulations and between simulations and observations as a result of differing cloud lifetime definitions. More recently, Fujimoto et al. (2019) compared methods of measuring cloud lifetimes used by simulators and observers. They calculated average lifetimes for their simulated galaxy between ~ 30 and ~ 45 Myr when weighting the lifetimes by number, mass or luminosity. They also applied an observational method (the "uncertainty principle for star formation"; see section 1.4.2.6) to the same simulated galaxy using synthetic observations to determine a cloud lifetime of 36^{+4}_{-6} Myr. Such applications of observational methods to simulations allows a more direct comparison of the results of simulations to observations and will drive understanding of the physical models used.

1.4.2 Observational determinations of molecular cloud lifetimes

A number of different methods have hitherto been used to measure the lifecycles of clouds. These methods have in general been applied to at most a few galaxies and some have only been applied to the Milky Way, due to constraints of resolution and sensitivity. Estimates of the cloud lifetime generally fall between one of two possible estimates: short (~ 10 Myr) lifetimes, approximately the length of a cloud freefall time; and long (~ 100 Myr) lifetimes, on the order of the timescale of galactic rotation. Results in both timescale regimes are found in the same target leading to a tension between the two scenarios. For example, Meidt et al. (2015) find a $20-30$ Myr cloud lifetime for M51 in contrast to Koda et al. (2009), who conclude that clouds live for ~ 100 Myr. A key question therefore is whether molecular clouds are short-lived, transient objects that form stars quickly and are then dispersed or destroyed rapidly by stellar feedback, or whether they are long lived objects that persist for many freefall times.

A common feature of methods for measuring the cloud lifetime is the requirement of multiple observations of different populations (such as molecular clouds and young stars). Many methods require the co-spatiality of these populations to be determined and thus accurately-matched astrometry is an important factor in applying these methods. In the specific case of molecular clouds and young stars, a particular challenge for verifying the astrometry comes from the fact that the two populations are traced by observations at different wavelengths. Catalogues of Milky Way star positions (e.g. GaiaCollaboration et al., 2018) can be employed to ensure a common astrometric solution for images that include foreground stars, which is common for UV and Hα images tracing

SFR. Observations of the molecular gas do not typically include sources within the telescope field of view with a well-determined astrometric precision. Thus the telescope's astrometry must be calibrated by pointing at an object with a well-determined astrometric precision before being pointed towards the actual target. Therefore in order to achieve accurate astrometry with a radio telescope, an accurate model of the pointing of the telescope is required (e.g Greve et al., 1996). The reliability of these models is a fundamental assumption of comparisons between these wavelength regimes.

In the remainder of this section, I summarise a number of methods that have been used to constrain the lifecycles of molecular clouds. Many methods have only been applied in the Milky Way and I detail these first before focussing on those that have been applied extragalactically.

1.4.2.1 Miscellaneous Milky Way methods

The Milky Way is the most extensively studied galaxy in the Universe. Due to the fact that we are located within it, the Milky Way offers a unique regime for observations in terms of resolution and sensitivity. A large number of measurements of the GMC lifetime have been made within our Galaxy. Indeed, a number of methods have thus far exclusively been applied to the Milky Way, because they are highly challenging or currently infeasible at extragalactic distances.

Blitz & Shu (1980) argue that molecular clouds have lifetimes of less than ~ 30 Myr due to the observed clumpyness of the clouds, which they contend would transform into a more centrally condensed distribution were the clouds to live longer. They also argue that sufficient energy is produced by massive stars to render the clouds unbound over this timescale.

The age spreads of stars in associations provides an estimate of the duration over which star formation took place in the progenitor of that association, which can be used as a timescale to calibrate the lives of molecular clouds. Larson (1981) noted that observations placed this age spread at ~ 10 Myr. Based on observations of the maximum age spread of stars in OB associations being about 20 Myr and observations of Milky Way molecular clouds showing that roughly half of clouds that are in self-gravitation are forming stars, Elmegreen (1991) concluded that molecular clouds have lifetimes of ~ 40 Myr.

Murray (2011) observed that a sample of 32 GMCs contained 31 per cent of the star formation in the Milky Way. They then determined the characteristic mass of molecular clouds above which this fraction of star formation occurs and the total number of molecular clouds of this mass or greater present in the Milky Way. Combining the ratio of these numbers with an assumed lifetime of the stellar clusters associated to their GMCs, they determine a cloud lifetime of 27 ± 12 Myr.

Kruijssen et al. (2015) find a ~ 1 Myr cloud lifetime through analysis of the molecular clouds in the Milky Way's Central Molecular Zone (CMZ, the inner few 100 pc of the Galaxy) using an orbital model of gas streams observed in this location of the galaxy. As the physical conditions of the CMZ are somewhat extreme in a Milky Way context, a much shorter cloud lifetime observed in the CMZ is not in contradiction with longer $\gtrsim 10$ Myr cloud lifetimes observed in the disc of the Milky Way and other galaxies. Indeed, molecular gas in the CMZ is denser and hotter than that in the Milky Way's disc, with conditions similar to those in high-redshift galaxies (Kruijssen & Longmore, 2013). Moreover, CMZ clouds are strongly affected by their motion on eccentric orbits in a strong gravitational potential, such as through tidal compression (Kruijssen et al., 2015).

1.4.2.2 Extragalactic methods

Due to the inherent constraints of resolution and sensitivity that are a part of extragalactic observations, measurements of the lifetimes of molecular clouds have heretofore only been undertaken in a small number of nearby galaxies. A few methods have been applied extragalactically. I divide the

methods that I cover here into three broad categories: those that involve taking a population census of molecular clouds and age-dated young stellar regions, those that rely on general dynamical arguments and those that rely on the spiral arm travel time. I also introduce the "uncertainty principle of star formation", a statistical method that is applied to determine molecular cloud lifecyles in this thesis.

1.4.2.3 Population censuses

The most extensively applied method has been that of taking some from of "population census" of the association of molecular clouds and young stellar regions. This method relies upon matching molecular cloud observations to another evolutionarily related population that can be age-dated (such as stellar clusters). By identifying members of each population and classifying them as associated or unassociated with a member of the other population, one can then infer a lifetime of the molecular clouds by statistical arguments.

Observations linking molecular gas and young stars to a timescale were undertaken by Bash et al. (1977), who searched for molecular gas associated with a sample of 63 open clusters in the Milky Way. They found that clusters aged more than 30 Myr had no associated CO emission. Leisawitz et al. (1989) also undertook a survey in CO of age-dated clusters. They found that clusters with ages $\lesssim 5$ Myr were associated with molecular clouds, whilst those with ages $\gtrsim 10$ Myr were not. This suggests that the timescale for stellar clusters to clear their environment of gas or to move away from their natal clouds of $\sim 5-10$ ten Myr, in general.

Within the Milky Way such surveys are constrained to taking observations of one population based on a pre-selected sample of another population, such as Leisawitz et al. (1989) who searched for CO (as a tracer of molecular clouds) based on a sample of stellar clusters. However, in an extragalactic context one avoid such biases by measuring the co-spatiality of molecular clouds with young stellar regions with imaging across a galaxy without reference to a target population. Such an analysis was first applied to the large Magellenic Cloud (LMC) (Fukui et al., 1999; Yamaguchi et al., 2001; Kawamura et al., 2009). An illustration of this method is shown in Figure 1.10. For this method an evolutionary timeline is assumed such that molecular clouds start out with no co-spatial stellar regions (Type I in Figure 1.10). After some time stars will form and HII regions will form within the molecular clouds (Type II in Figure 1.10). Later still young stellar clusters will become visible at the same location of the cloud (Type III in Figure 1.10). Finally, the molecular cloud will be dispersed leaving only the young stellar clusters. One can then measure the relative lifetimes of the phases by identifying molecular clouds, classifying them in one of these stages and then calculating the fractions of clouds in each phase. By comparing to the ages of stellar clusters one can then calculate an absolute lifetime of the molecular cloud. For example, Kawamura et al. (2009) found that ~ 66 per cent of the clusters aged less than 10 **Myr** in the LMC were associated with a giant molecular cloud (GMC). They thus argue that molecular clouds survive for ~ 66 per cent of this 10 **Myr** cluster lifetime and accordingly estimate the timescale for Type III clouds as 7 **Myr**. By then using the relative numbers of GMC assigned to each type they estimate lifetimes for Type I and Type II as 6 Myr and 13 Myr, respectively, giving an overall estimate of the molecular cloud lifetime of 20-30 **Myr**.

Application of the same method to M33 with a partial CO(3-2) survey found a similar 20-40 **Myr** lifetime (Miura et al., 2012). More recently, (Corbelli et al., 2017) used young stellar cluster candidates in combination with a more complete CO(2-1) survey of molecular gas in M33 to estimate a 14.2 **Myr** cloud lifetime. This method has also been utilised in an extragalactic context to determine the timescale over which molecular clouds cease to be associated with their molecular clouds. Grasha et al. (2018) find the timescale during which stellar clusters are associated with their natal GMCs is $2-3$ Myr in NGC7793 whereas Grasha et al. (2019) find a longer $4-6$ Myr

timescale for M51. Overall, cloud lifetimes estimated with this method are in general in the low tens of Myr. These estimates are indicative of some variation in the lifecycles of molecular clouds between galaxies. The scheme adopted for classifying regions is, however, a source of uncertainty for these studies as a range of different approaches may be taken.

1.4.2.4 Dynamical arguments

An alternative way of calibrating the evolutionary timeline of molecular clouds is to use the timescale associated to some dynamical process. Within the Milky Way early studies by Bash & Peters (1976) and Bash et al. (1977) concluded that molecular clouds in the Milky Way have ages of $\sim 20-30$ Myr by comparison of velocities of molecular clouds with a dynamical model for stars perturbed by the potential of the Milky Way.

Dynamical arguments have also been applied in an extragalactic context. Engargiola et al. (2003) examined HI and CO emission in M33. They concluded that GMCs in M33 form from HI filaments and found a close association between GMCs (traced by CO) and HI filaments. By comparing the velocity offsets between the two populations and the average size of the HI filaments they conclude that a GMC lifetime longer than 10 - 20 Myr would allow the clouds to travel away from the HI filaments, which would break the association they observe. As this method requires HI observations that resolve HI filaments, it is currently constrained to the nearest galaxies by the inferior resolution of 21 cm HI transitions observations in comparison to observations of CO at millimetre wavelengths. This is due to the fact that the angular resolution, θ, of a telescope of diameter, D, is proportional to the wavelength of the observations ($\theta \approx \lambda/D$).

1.4.2.5 Spiral arm travel time arguments

The observation of molecular clouds in the interarm regions of the Milky Way, was used by Scoville et al. (1979) to conclude that the lifetimes of molecular clouds must exceed ~ 100 Myr. Koda et al. (2009) similarly concluded that molecular clouds in M51 must have lifetimes of ~ 100 Myr (or approximately the timescale for clouds to cross the region between two arms), due to the detection of massive clouds in these interarm regions.

More recently, Meidt et al. (2015) leveraged the spiral arm crossing time in combination with cloud counting to measure a 20-30 Myr cloud lifetime in M51. Their method combines a dynamical reference time with population statistics for molecular clouds. This method relies on the travel time for clouds between spiral arms ($t_{\rm travel}$) to derive a cloud lifetime and is thus restricted to galaxies where spiral arms can be identified. Figure 1.11 illustrates the method. In the scheme adopted by Meidt et al. (2015), clouds proceed from one spiral arm to the other along roughly circular orbits. This interarm region is divided into two zones defined by the midpoint between the two arms: zone I, the region closer to the arm that clouds leave and zone II, the region closer to the arm the clouds are travelling towards. During this motion, some clouds are destroyed and new clouds may also form. Under the assumption that no new clouds are formed, the number of clouds in each region can be translated into a lifetime for the clouds. As a shorter average cloud lifetime would result in a greater fraction of clouds being destroyed in their motion from zone I to zone II, the cloud lifetime can be calculated as

$$t_{\rm cloud} = \frac{t_{\rm travel}}{2}\frac{1}{F_{\rm lost}}, \tag{1.21}$$

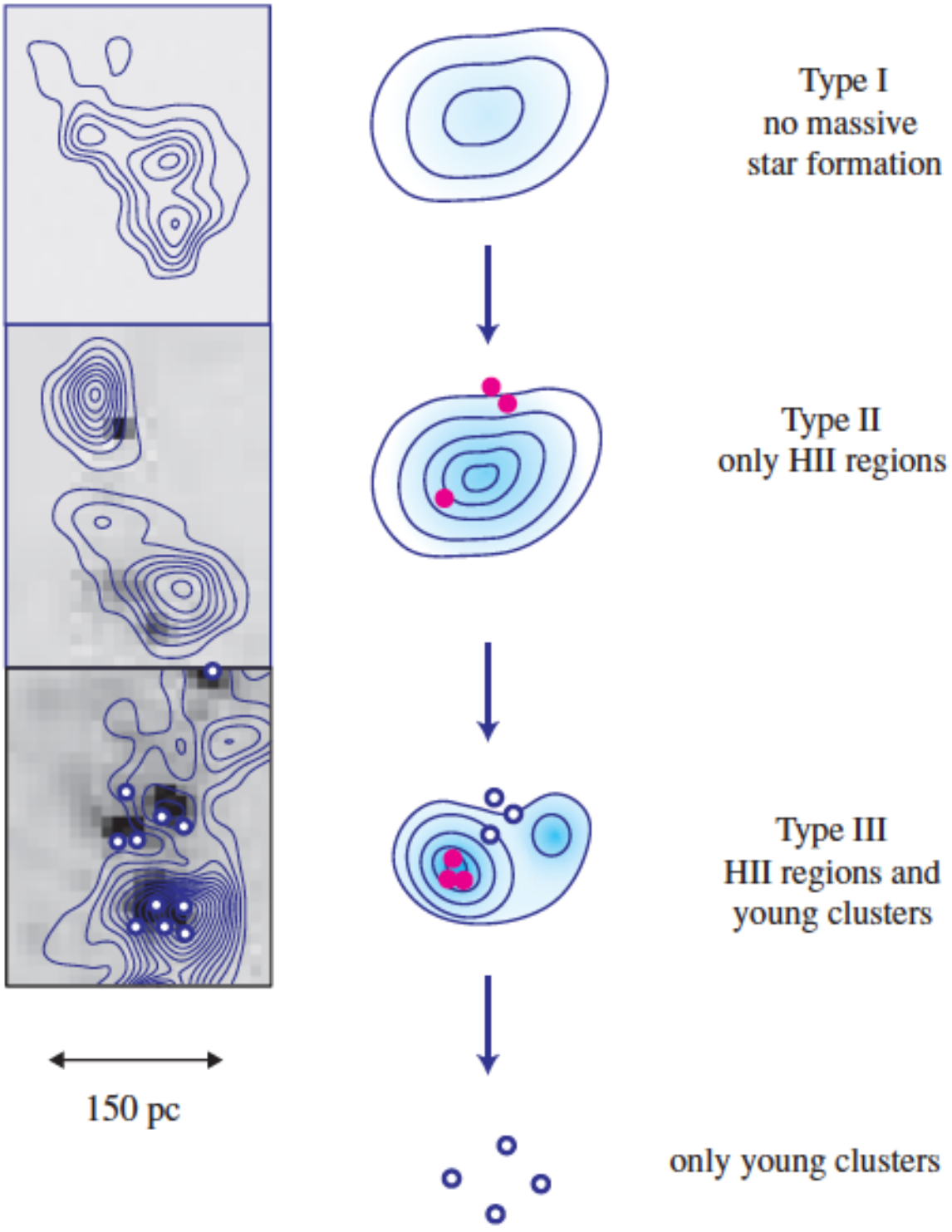

Figure 1.10: An illustration of the method of determining molecular cloud lifetimes by classifying them through their stellar content. Regions are classified based on their molecular cloud and young stellar content, as indicated on the figure. Figure taken from Kawamura et al. (2009).

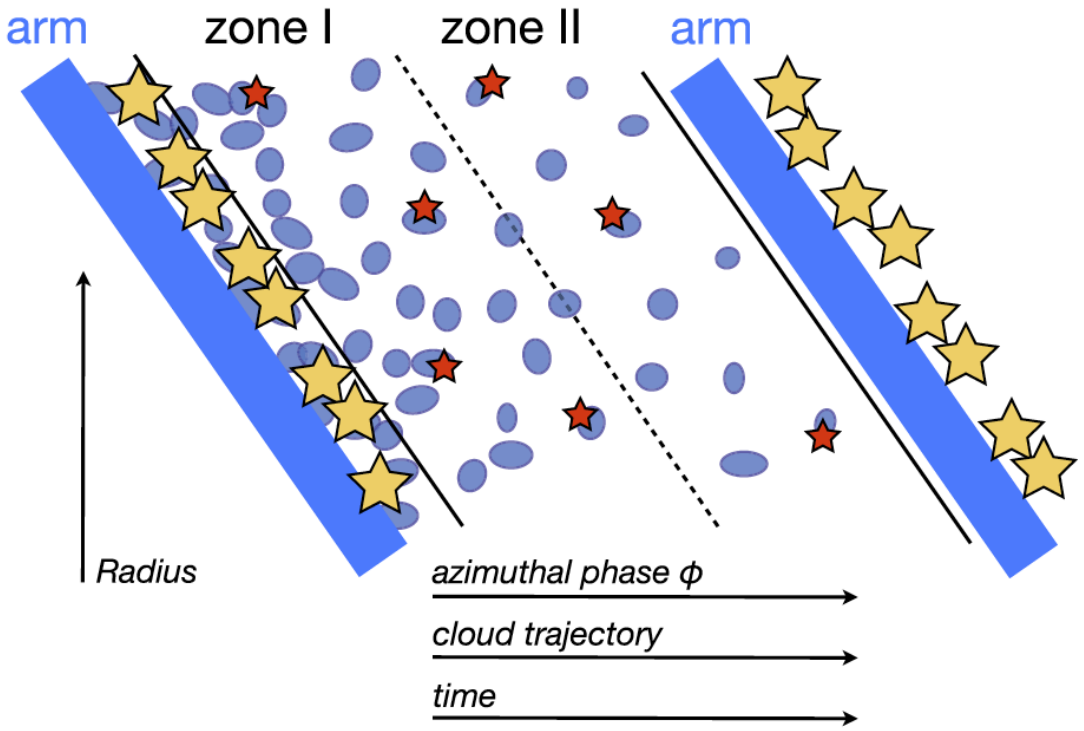

Figure 1.11: Figure taken from Meidt et al. (2015) illustrating their method for measuring cloud lifetimes. Two spiral arms (blue rectangles) and their intervening inter-arm region are shown in polar co-ordinates. Clouds identified between the two spiral arms are indicated as blue ellipses. The interarm region is divided into two halves, zone I and zone II, with clouds moving from zone I to zone II. In this formalism, clouds move from one arm to the next and are destroyed during this motion, leading to a decrease in the number of clouds in zone II in comparison to zone I.

where the fraction of clouds lost between zone I and zone II, $F_{\rm lost}$ is defined as

$$F_{\rm lost} = \frac{N_{\rm I}}{N_{\rm I} - N_{\rm II}}, \tag{1.22}$$

where $N_{\rm I}$ and $N_{\rm II}$ are the number of clouds in zones I and II, respectively (Meidt et al., 2015).

1.4.2.6 The uncertainty principle for star formation

The work presented in this thesis utilises the "uncertainty principle for star formation" - a statistical method for constraining the lifecycles of phases of the star formation process. The principle of the method was presented by Kruijssen & Longmore (2014) and implemented for application to data as the HEISENBERG code by Kruijssen et al. (2018). Here I give a quick summary of this method. The method is able to characterise the relative lifetimes of any two phases in a Lagrangian evolutionary sequence. However, for simplicity I will discuss how the method can be used to measure the evolutionary timeline of "star-forming regions" from molecular clouds ("gas") into young stars ("stars"). This process takes place in three stages, which are illustrated in Figure 1.12. First a molecular cloud forms, which initially contains no young stars. This cloud lives for a time, $t_{\rm gas}$, before it is dispersed or destroyed. At some point during the lifetime of the cloud, stars form within it; these stars are visible in some tracer for a time, $t_{\rm star}$. At the time of their formation these stars

are co-spatial with their natal gas cloud and co-exist with the cloud for a time, $t_{\rm over}$, before the cloud is dispersed or destroyed.

The HEISENBERG code works by fitting a statistical model to measurements taken on observations of the gas and stellar phases. Therefore, in order to apply the method one requires two images, one to trace molecular clouds (such as CO) and one to trace young stars (such as Hα). Figure 1.13 phenomenologically illustrates the application of the HEISENBERG code. First, peaks in the stellar and gas emission distributions are identified, which correspond to sites of recent star formation and molecular clouds, respectively. Apertures, ranging in size down from the size of the galaxy to a few times the size of the star-forming regions are centred on these peaks. At each size of aperture, measurements are taken of the gas-to-stellar flux ratio. This process is illustrated in Figure 1.14. With large aperture sizes the galactic average gas-to-stellar flux ratio is recovered regardless of whether apertures are focussed on peaks in the gas or stellar distribution, as the small-scale structure of the galaxy is blurred out. However, measurements of the gas-to-stellar flux ratio in small apertures deviate from the galactic average and depend on whether measurements are taken at the location of gas or stellar peaks, as the small-scale structure of the galaxy driven by the evolution of individual star-forming regions is resolved.

For measurements with these small apertures an increase in the gas-to-stellar flux ratio compared to the galactic average is observed when focussing on gas peaks. In contrast, a decrease in the gas-to-stellar flux ratio compared to the galactic average is observed when focussing on stellar peaks. This gives rise to two "branches" of measurements: one focussed on gas peaks and the other on stellar peaks. Datapoints at different size-scales along these two branches are measured by placing a set of non-overlapping apertures that covers the set of peaks in the corresponding tracer. As not every peak will have an aperture placed on it in such a scenario, each measurement is averaged over a large number of Monte Carlo samples of peak placement. The statistical model of the HEISENBERG code is then fitted to the measurements of both of these branches together. This model is defined by three fundamental parameters: $t_{\rm gas}$, $t_{\rm over}$ and the mean region separation length, λ. The impact of these parameters on the statistical model is illustrated in Figure 1.15. I now proceed to detail each parameter.

First, λ is determined by the size scale at which measurements focussed on stellar peaks and those focussed on gas peaks diverge. Cases where star-forming regions are more closely packed together (lower λ) start to exhibit this divergence at smaller size scales than those where the star-forming regions are more distantly separated from one another (higher λ). This is due to the fact that larger apertures are needed for larger λ to cover a sufficient portion of the star forming regions such that variations in the gas-to-stellar flux ratio, due to different star forming regions being at different evolutionary stages, are blurred out.

The asymmetry of the size of the deviation away from the galactic average between the two branches is set by the ratio of the visibility timescales for the two tracers i.e. $t_{\rm gas}/t_{\rm star}$. In the example shown in Figure 1.13, $t_{\rm gas}$ is longer than $t_{\rm star}$. In this case, stellar regions are rarer than gas regions (due to their shorter visibility lifetime). Thus at small aperture sizes, fewer apertures are required to cover the rarer stellar peaks than the more common gas peaks. This smaller set of apertures focussed on stellar peaks therefore captures a small fraction of the gas flux. This results in a large change in the measured gas-to-stellar ratio in comparison to the galactic average value. For the larger set of apertures that cover the more common gas peaks, a larger fraction of the flux from the stellar peaks is recovered and thus the value of the gas-to-stellar flux ratio measured from this aperture set is closer to the galactic average.

The second timescale, $t_{\rm over}$, has the effect of saturating the amount to which the gas-to-stellar flux ratio changes with respect to the galactic average. This is because when a star forming region is in a phase where both gas and stars overlap, the contribution of the region to the total gas and

stellar fluxes is captured by both sets of peaks. The higher the fraction of regions in this phase, due to the longer t_{over}, the greater the fraction of the flux in each map is always captured by both sets of peaks. This effect leads to a smaller the change in the gas-to-stellar flux ratio at small aperture sizes.

As with the other, previously detailed methods, a known reference timescale is required with which to calibrate the cloud evolutionary timeline. The HEISENBERG code itself measures the ratios of t_{gas}, t_{star}, and t_{over} in relation to each other and thus any of these could be used for this purpose. Haydon et al. (2018) presented a prescription for t_{star} (excluding t_{over}) as a function of metallicity for the commonly used SFR tracers Hα and UV. These prescriptions were developed using hydrodynamical galaxy simulations. From these simulations, synthetic Hα and UV emission maps were produced along with maps of the mass surface density of star particles within the simulations of a given age range. The age range of these stellar particle maps provides then a known timescale with which to measure a characteristic timescale, within the HEISENBERG framework, for Hα and UV. This characteristic timescale is measured by applying the HEISENBERG code on combinations of the synthetic emission maps and the age-dated stellar particle maps.

1.5 Outline of this thesis

In this introduction, I have summarised a number of key results regarding the physics of star formation. I have also highlighted a number of key questions surrounding the star formation process such as "what sets the lifetimes of molecular clouds?" and "how quickly are they destroyed or dispersed by feedback?" Answering these questions requires reliable observational methods to constrain the lifecycles of molecular clouds.

The work that I present in this thesis utilises the HEISENBERG code, which makes such measurements. However, the statistical method employed in the HEISENBERG code models the flux coming from star-forming regions and thus contaminant diffuse emission can bias results from the method. As many common tracers are known to have diffuse emission components (see Section 1.2.1.2, for example) this represents a challenge for the application of the method. In Chapter 2, I present a method for separating the diffuse and compact emission components of tracer images that allows the HEISENBERG code to be applied without the biasing impact of diffuse emission. In Chapter 3, I apply the HEISENBERG code including this diffuse filtering solution to the nearby galaxy M33. Then, in Chapter 4 I use this diffuse filtering method to measure the significance of the diffuse emission in nine nearby galaxies and correlate it to a number of physical parameters describing the galaxies including those constrained by the HEISENBERG code.

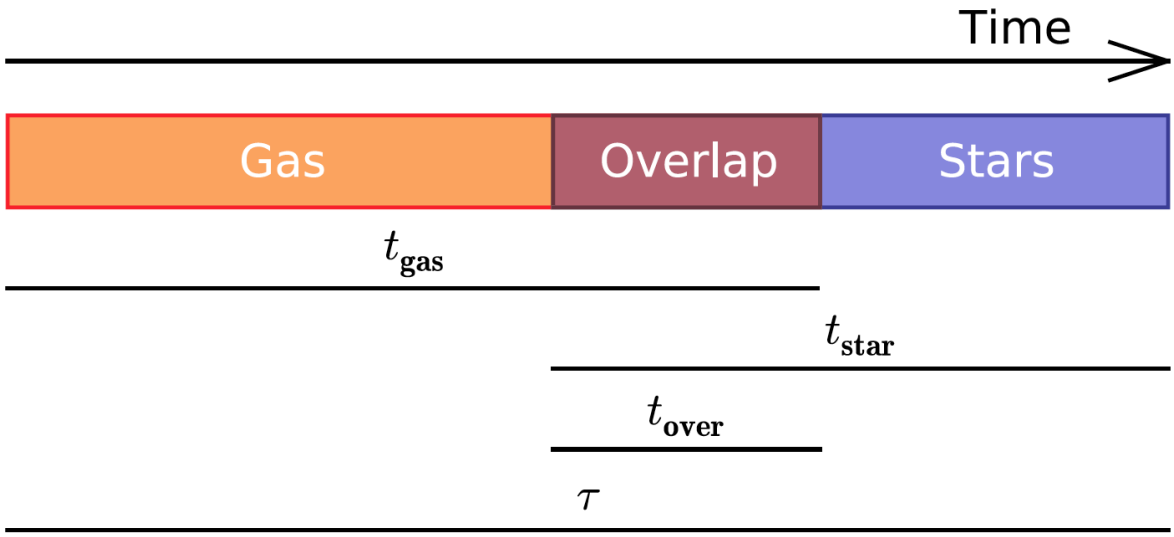

Figure 1.12: A simple three-stage timeline of star formation. First, molecular gas clouds form and become visible. These gas clouds live for a time, t_{gas}, at some point during which stars form. These stars are visible in a tracer for a time, t_{star}. After these stars have formed they begin to disperse their natal gas cloud via the impact of stellar feedback. The time taken for the stars to disperse their cloud is the time that they overlap with their natal gas cloud, t_{over}. This scenario has a total timeline duration of $\tau = t_{\mathrm{gas}} + t_{\mathrm{star}} - t_{\mathrm{over}}$. Figure taken from Kruijssen et al. (2018).

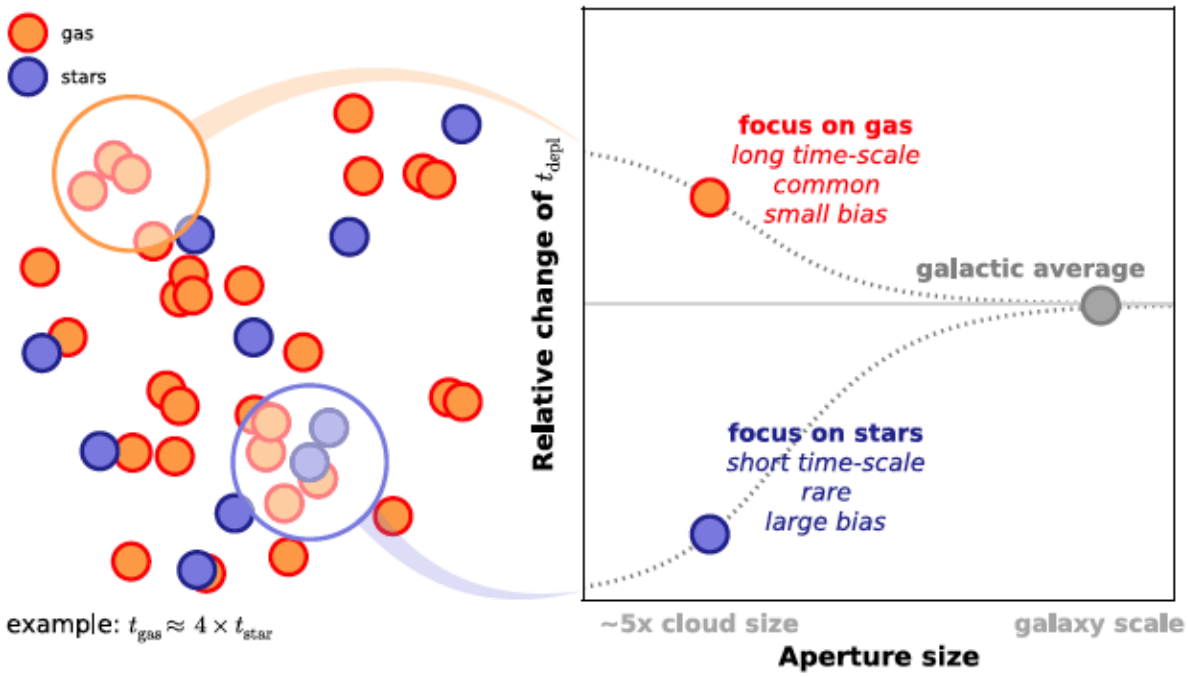

Figure 1.13: An illustration of the "uncertainty principle for star formation". A cartoon of a galaxy consisting of gas regions (in orange) and stellar regions (in blue) is shown on the left of the figure. The plot on the right side of the figure shows the relative change of $t_{\rm depl}$ (which is calculated from the gas-to-stellar flux ratio) with respect to the galactic average. Measurements in large galaxy-scale apertures recover the galactic average regardless of whether they are focussed on stellar or gas regions. However, as the size of the apertures is decreased towards the cloud-scale, the measured $t_{\rm depl}$ deviates away from the galactic average. In this example $t_{\rm gas}$ is longer than $t_{\rm star}$ and thus a larger bias away from the galactic average is measured when focussing apertures on stellar peaks. This behaviour is described by a statistical model (indicated by the grey, dashed line), which can be fitted to the measurements to recover the underlying timescales. Figure taken from Kruijssen et al. (2018).

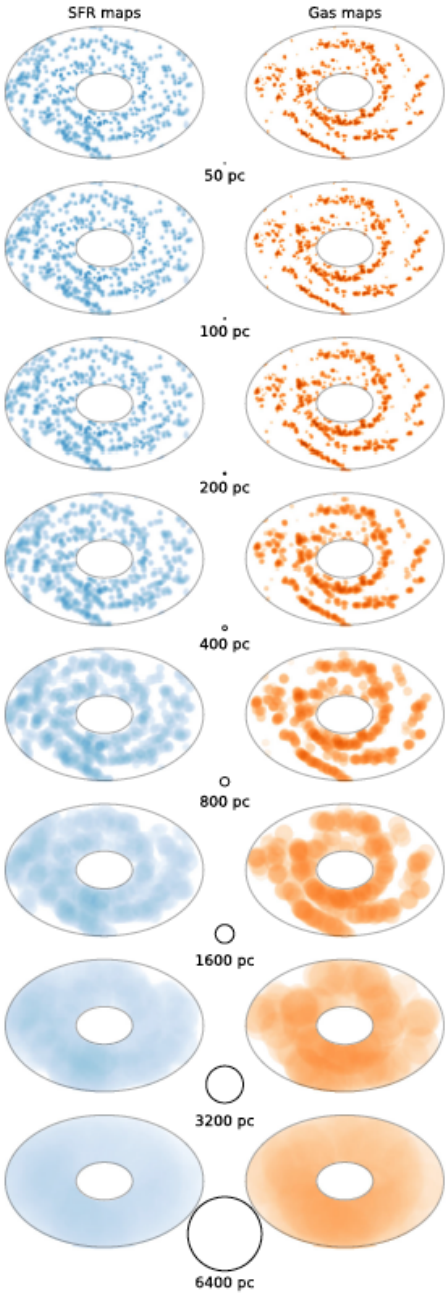

Figure 1.14: An illustration of the measurement of the gas-to-stellar flux ratio at different size scales. The left and right columns of images show a star formation rate tracer and gas mass tracer convolved to different aperture size-scales, the sizes of which are indicated by the white circles in between the two columns. As larger and larger apertures are used, the small scale structure in the tracer images is blurred out. Figure taken from Kruijssen et al. (2018).

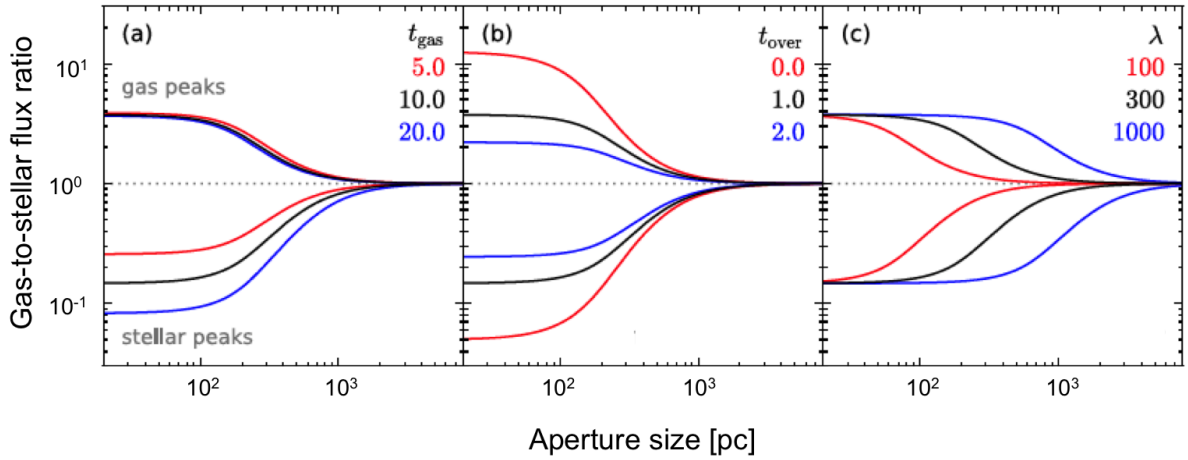

Figure 1.15: Figure adapted from Kruijssen et al. (2018) illustrating how the statistical model of the HEISENBERG code changes as a function of the three fundamental fitting parameters t_{gas}, t_{over} and λ. The left panel shows the impact of t_{gas}. Increasing t_{gas} relative to t_{star} increases the rarity of the stellar phase in comparison to the gas phase. Selecting peaks in a relatively rarer phase leads to a greater asymmetry between the two branches of measurements. The middle panel shows the impact of t_{over}. Increasing the fraction of their lifetimes that regions are visible in both phases decreases the amount of bias away from the galactic average gas-to-stellar flux ratio at small aperture sizes. Last, the right panel shows the impact of λ which sets the physical size scale at which decorrelation between the two branches is observed. If regions are more closely packed together (smaller λ) decorrelation is first observed at much smaller size scales than if the regions are separated more widely from each other (larger λ).

2 On the nature and filtering of diffuse emission

Abstract

Diffuse emission is observed in galaxies in many tracers across the electromagnetic spectrum, including tracers of star formation, such as Hα and ultraviolet (UV), and tracers of gas mass, such as carbon monoxide (CO) transition lines and the 21-cm line of atomic hydrogen (HI). Its treatment is key to extracting meaningful information from observations such as cloud-scale star formation rates. Finally, studying diffuse emission can reveal information about the physical processes taking place in the ISM, such as chemical transitions and the nature of stellar feedback (through the photon escape fraction). We present a physically-motivated method for decomposing astronomical images containing both diffuse emission and compact regions of interest, such as HII regions or molecular clouds, into diffuse and compact component images through filtering in Fourier space. We have previously presented a statistical method for constraining the evolutionary timeline of star formation and mean separation length between compact star forming regions with galaxy-scale observations. We demonstrate how these measurements are biased by the presence of diffuse emission in tracer maps and that by using the mean separation length as a critical length scale to separate diffuse emission from compact emission, we are able to remove its biasing effect. Furthermore, this method provides, without the need for interferometry or ancillary spectral data, a measurement of the diffuse emission fraction in input tracer maps and decomposed diffuse and compact emission maps for further analysis.

2.1 Introduction

One of the key challenges in observational astronomy is separating populations of interest from other contaminant populations present in data, due to the fact that observations do not take place in controlled laboratory settings. It has been known for a number of decades that there is a significant diffuse component in Hα observations of ionised gas (known as diffuse ionised gas or DIG) in our own Galaxy (see e.g. Reynolds et al. 1973). Detection of diffuse Hα emission in the discs (Monnet, 1971) of external galaxies and their haloes (Rand et al. 1990; Dettmar 1990) confirmed the phenomenon is not restricted to the Milky Way and, as technology has advanced, its ubiquity and significance in other galaxies has been confirmed (e.g. Lacerda et al. 2018). The physical origin of the diffuse Hα emission is still debated, but it has been shown that photoionization of the warm neutral medium (WNM) by Lyman continuum leaking out of bright HII regions (e.g. Mathis, 1986; Sembach et al., 2000; Wood et al., 2010), ionisation from post-asymptotic giant branch stars (Binette et al., 1994; Sarzi et al., 2010; Flores-Fajardo et al., 2011; Yan & Blanton, 2012) or dust scattering (Seon & Witt, 2012) can provide an important contribution to this diffuse component. In addition, shocks may also contribute secondarily (Pety & Falgarone, 2000; Collins & Rand, 2001). The diffuse Hα emission contaminates samples of compact HII regions, where star formation takes place (e.g. Liu et al. 2011), but also carries unique astrophysical information. A physically-motivated separation between these components is challenging, but necessary.

Studies of the Warm Ionised Medium with Hα indicate significant variation in the Hα diffuse fraction (see e.g. Thilker et al. 2002; Oey et al. 2007; Lacerda et al. 2018) between different galaxies. For example, Oey et al. (2007) find diffuse Hα fractions of between 12 per cent and 100 per cent, by comparing the total Hα flux of a sample of 109 galaxies to the flux of their HII regions as identified by the automated HII region photometry package HIIPHOT (Thilker et al., 2000). In addition, Lacerda et al. (2018) measure distributions of the Hα diffuse fraction that shift with Hubble type, observing that the contribution of the DIG is generally smaller in later-type galaxies. Within galaxies, the diffuse Hα fraction is observed to vary between different environments. For example, Blanc et al. (2009) observe higher Hα diffuse fractions in fainter HII regions in M51 and Kreckel et al. (2016) find higher Hα diffuse fractions in spiral-arm HII regions than in inter-arm HII regions.

Due to the high optical depth of the Earth's atmosphere in the ultraviolet (UV) part of the spectrum, it was not until the advent of space telescopes that studies of diffuse UV could be made. Studies of the UV diffuse fraction indicate variation, as with Hα. For example, Hoopes et al. (2001) find that the diffuse emission not associated to Hα-selected HII regions contributes 72 - 91 per cent of the total FUV flux of 10 spiral galaxies. This could reflect the difference in the lifetimes of the Hα and UV-bright phases of young stellar populations, with the UV-bright phase lifetime being roughly a factor of 5 longer (Haydon et al., 2018). Moreover, comparisons indicate that there are differences between diffuse fractions in different phases and within galaxies themselves. For example, Thilker et al. (2005) find that the ratio of FUV diffuse fraction to Hα diffuse fraction changes radially. Consequently, the question arises as to whether these variations can be linked to galaxy properties or the physical processes driving the star formation process.

Furthermore, diffuse emission has also been found across a wide range of tracers used as direct probes of star formation rate or in composite star formation prescriptions, including infrared (see for e.g. in 8 μm Crocker et al. 2013 and 24 μm (cirrus) Leroy et al. 2012); diffuse X-ray in starbursts (Fabbiano et al., 1990) and normal galaxies (Bregman & Pildis, 1994) (see also Strickland et al. 2004 for a larger sample of galaxies with diffuse X-ray emission); and [C II] (Kapala et al., 2015), which is also used as a tracer of molecular gas mass.

Taking account of the presence of diffuse emission is important for comparisons between inte-

grated galaxy-scale measurements and small scale measurements of star formation rate and for properly interpreting the source of observed ionising radiation (see e.g Blanc et al. 2009 and Leroy et al. 2012). Diffuse emission also impacts other measurements such as line-ratios and therefore the interpretation of diagnostic diagrams (such as the BPT diagram, see Baldwin et al. 1981) and measurements of metallicity (Zhang et al., 2017). Thus correctly dealing with diffuse emission is key to proper interpretations of observations.

Gas tracers may also include diffuse emission. Comparison of the ^{12}CO to ^{13}CO ratio using single dish and interferometric observations of regions in M33 by Wilson & Walker (1994) indicated that diffuse molecular clouds contribute up to 60 per cent of the ^{12}CO emission. More recently, comparisons between interferometric and single-dish CO line observations across the discs of galaxies have revealed that observed molecular gas consists of both a compact clumpy component (molecular clouds) and a component spread-out over large scales (diffuse emission) (Caldú-Primo et al. 2013; Caldú-Primo et al. 2015). Furthermore, this diffuse component can be a significant fraction of the emission, with for example ∼50 per cent of observed CO(1-0) emission in M51 originating from scales in excess of 1.3 kpc (Pety et al., 2013). The nature of diffuse CO emission is unknown. It may consist of unresolved, low-mass clouds, or be truly diffuse in nature.

A number of different approaches have been taken to separate diffuse emission from compact emission. Examples of definitions are: the flux lost in an interferometric map compared to the flux from a single dish measurement (e.g. Pety et al. 2013), the flux of identified regions of interest versus the total flux in an image (e.g. application of automated HII region photometry package HIIPHOT Thilker et al. 2000, by Thilker et al. 2002), the use of additional spectral information available with integral field unit (IFU) datacubes to divide pixels into diffuse and non-diffuse pixels (e.g an Hα equivalent width criterion employed by Lacerda et al. 2018), the use of a critical value for a single quantity (e.g. the Hα surface brightness criterion of Zhang et al. 2017), and the use of diagnostic line ratios to separate the contribution of diffuse emission (e.g. [SII]/Hα ratio to separate DIG from HII region emission by Blanc et al. 2009 and Kreckel et al. 2016). Very few of these methods are physically motivated and they all depend on properties of the observations. Furthermore, methods of identifying diffuse emission are sometimes based on assumptions about the origin of the diffuse emission that do not always apply and affect their applicability in the case of mixed origins of the diffuse emission. To take one particular example, Lacerda et al. (2018) show that an Hα surface brightness criterion can be invalid in certain cases as it may misidentify diffuse gas ionised by hot low-mass evolved stars (see e.g. Flores-Fajardo et al. 2011) as star-forming regions and may misidentify faint star-forming regions as diffuse.

These factors, in part, explain why current measurements in the literature exhibit significant differences and that the role of this diffuse emission for the star formation process remains unclear. A general, physically motivated approach to separate diffuse emission from compact emission is therefore desirable in order to make progress on better understanding the nature and origin of diffuse emission.

Finally, we have recently developed a statistical method for constraining the evolutionary timeline of star formation and mean separation length between compact star-forming regions with galaxy-wide, cloud-scale observations of (molecular) gas and young stellar emission (Kruijssen & Longmore, 2014; Kruijssen et al., 2018). This method ('an uncertainty principle for star formation', hereafter KL14 principle) has been prepared for observational applications in the form of the IDL code HEISENBERG (Kruijssen et al., 2018). The method fundamentally assumes that all emission contained in the gas and young stellar maps belongs to individual regions evolving on an underlying evolutionary timeline. However, in practice, the maps generally contain both the regions of interest (e.g. molecular clouds or HII regions) and diffuse emission that does not emanate from these regions. This requires the diffuse component of each map to be isolated and separated out. Because

the HEISENBERG code is suitable for applications across a wide range of tracers, including HI, CO, Hα and UV, we require an objective method that is not restricted to a particular instrumental setup and can be applied uniformly to different tracers.

This paper presents a method for the separation of diffuse emission from tracer maps through filtering in Fourier space implemented into the HEISENBERG code. This method uses the HEISENBERG code to identify the units within galaxies undergoing evolutionary cycling and then filters out emission on larger spatial scales, which is assumed to be unrelated to the identified units. This method makes no assumptions regarding the physical origin or flux level of the diffuse emission and is independent of instrumental setup. It can therefore be applied across a wide wavelength range. The structure of the paper is as follows. We outline the KL14 principle in Section 2.2. We then describe our new method of diffuse emission filtering in Section 2.3 and its implementation into the HEISENBERG code in Section 2.4. Following this, we detail the steps taken to generate simulated data, on which we test the method in Section 2.5. We show the results of this testing in Section 2.6, focusing on how the compact regions of interest can be affected by the filtering of large-scale emission, and in Section 2.7, focusing on how the quantities measured by HEISENBERG are improved by our filtering method and how well it retrieves the fraction of emission within an image that is diffuse. Finally, we present a summary of our results and conclusions in Section 2.8.

2.2 Uncertainty principle for star formation

This section provides a brief summary of the 'uncertainty principle' for star formation within which the method in this paper is implemented. For a full description, the reader is referred to Kruijssen & Longmore (2014) for the theoretical basis, Kruijssen et al. (2018) for the complete method and its realisation in the form of the HEISENBERG code, and Haydon et al. (2018) for the calibration of the obtained evolutionary timelines through the use of characteristic 'reference' time-scales of star formation rate tracers such as Hα or UV emission.

In short, the KL14 principle describes how variations in the spatially resolved flux ratio between two tracers of successive phases of a given evolutionary sequence are controlled by the relative lifetimes of emission peaks in these tracers, together with the mean separation length between these regions. The HEISENBERG code applies the KL14 principle such that it can measure the evolutionary timeline describing different phases of the star formation process from observed emission maps tracing these phases. It places circular apertures of different sizes on emission peaks in both maps, calculates the enclosed flux ratio difference relative to the average across the entire field of view, and fits a statistical model to this relative flux ratio difference as a function of the aperture size to measure the peak lifetimes and separation length (see Figure 2.1 for an illustration of this process).

In order to apply the HEISENBERG code, one requires tracer maps of two phases of a Lagrangian evolutionary timeline, in which intensity peaks evolve from being bright in one tracer to being bright in the other. An example of such a timeline is as follows: CO-traced gas clouds live for $t_{\rm gas}$ and evolve into young stars which are visible in Hα for $t_{\rm star}$ and both co-exist for $t_{\rm over}$, giving a total evolutionary timeline duration of $\tau = t_{\rm star} + t_{\rm gas} - t_{\rm over}$. When placing an aperture with a size such that it spans the whole galaxy, the same galactic average value of the gas-to-stellar flux ratio is measured regardless of whether that aperture is centred on a gas tracer peak or a stellar tracer peak. At small aperture sizes, the measured gas-to-stellar flux ratio deviates from the galactic average value, with the direction of the deviation away from the galactic average value depending on whether the aperture is focussed on a gas or a stellar peak. On average, apertures centred on gas peaks will measure an enhanced gas-to-stellar flux ratio in comparison to the galactic average value, while apertures centred on stellar peaks will measure a depleted gas-to-stellar flux ratio compared to the galactic average value. Thus we observe a bifurcation of the measurement into

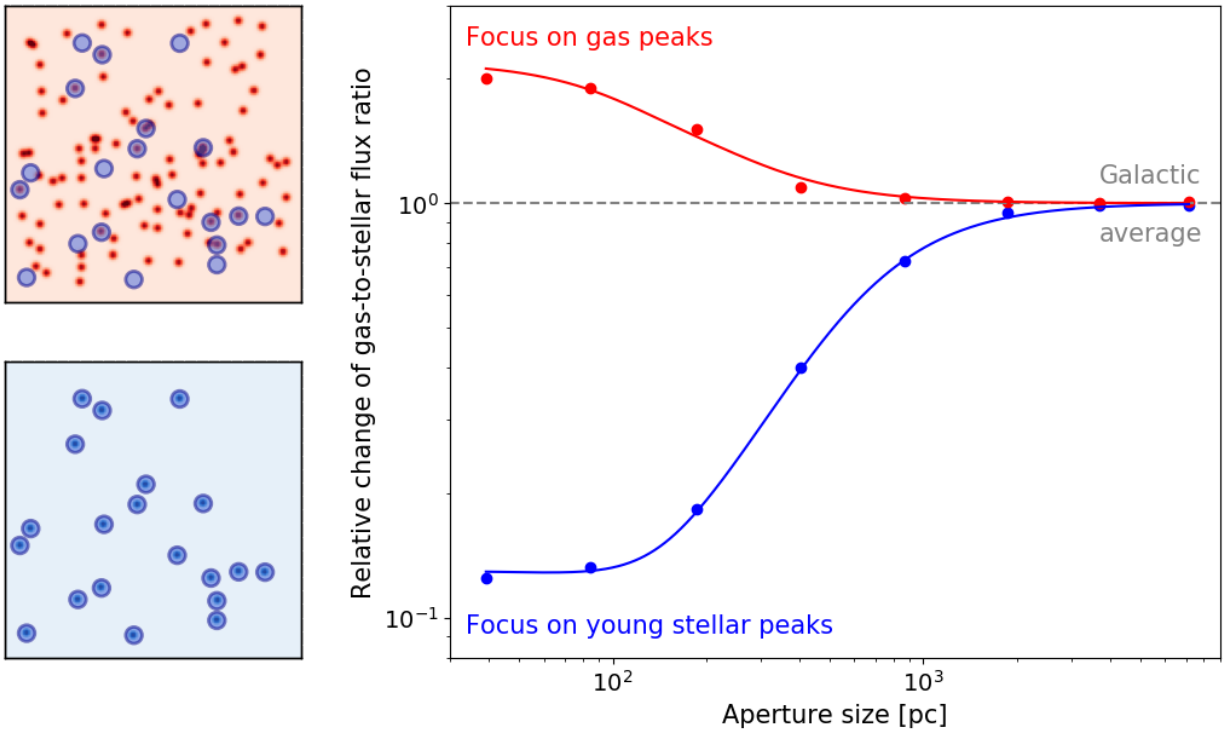

Figure 2.1: Illustration of the application of the HEISENBERG code to a dataset. In this example the gas cloud visibility lifetime is five times longer than the visibility lifetime of the young stars. This translates is to a five-times greater abundance of gas peaks in the gas tracer map (top left) than the young stellar tracer map (bottom left). The HEISENBERG code works by placing apertures of varying sizes on emission peaks and measuring the ensemble average of the gas-to-stellar flux ratio in these apertures. An example set of small apertures focussed on the stellar peaks is shown on both tracer maps as blue circles. This measurement is repeated at a number of different size-scales focussing on emission peaks in the young stellar and gas maps. The right panel shows measurements, for the example, of the relative change of the gas-to-stellar flux ratio from the galactic average as a function of the aperture size. Measurements in the bottom branch (blue circles), focussing on stellar peaks, show a large relative decrease of the gas-to-stellar flux ratio at small aperture size. This is due to the fact that the apertures, as a result of their selection, incorporate the full set of (rare) young stellar emission peaks and their flux, while missing a large amount of flux coming from the (common) gas peaks. In contrast, measurements in the top branch (red circles), focussing on the gas peaks, show a relatively small increase from the galactic average. This is due to the fact that the larger number of apertures incorporating the full set of common gas peaks will capture a large fraction of the flux from the (rare) stellar peaks. By fitting the statistical model of the HEISENBERG code (indicated for the example as the red and blue lines on the right panel) the evolutionary timeline of regions in the dataset and their mean separation is measured.

two branches depending on whether apertures of a particular size are centred on gas or stellar peaks. The magnitude of the deviation from the galactic average value in each branch is set by the underlying evolutionary timeline.

Indeed, the magnitude of the deviation from the galactic average value of each branch is set by the relative duration of the visibility of a phase in a tracer, which translates directly into the abundance of emission peaks in a map of that tracer. That is, the number of emission peaks of a short-lived phase will be small compared to the number of peaks of the long-lived one.

As a result, the number of apertures required to cover all the (rare) emission peaks of a short-lived phase is relatively small. At small aperture sizes, this sparse sampling of the galaxy will capture only a relatively small portion of the flux that traces a long-lived evolutionary phase, leading to a large deviation of the gas-to-stellar flux ratio from the galactic average. In contrast, incorporating the full set of emission peaks in a long-lived evolutionary phase necessitates a large number of apertures that cover a larger fraction of the galaxy. Even for small aperture sizes, these apertures will capture a relatively large fraction of the flux from the short-lived phase, leading to a smaller deviation of the gas-to-stellar flux ratio from the galactic average. For instance, if $t_{\rm star}$ is shorter than $t_{\rm gas}$, the amplitude of the branch obtained by focusing apertures on young stellar peaks will be larger than that of the branch focusing apertures on gas peaks.

The duration of the overlap phase, $t_{\rm over}$, sets the value of the gas-to-stellar flux ratio at which the gas and stellar branches saturate at small aperture sizes. In the case of non-zero overlap duration some fraction of regions in one phase will always be co-spatial with a region in the other phase, thus leading to a saturation in the ensemble average of the gas-to-stellar flux ratio for apertures below a certain size. Thus, by applying the HEISENBERG code, we directly measure two lifetime ratios: $t_{\rm gas}/t_{\rm star}$ and $t_{\rm over}/t_{\rm star}$. Given a priori knowledge of $t_{\rm star}$, based on the results of stellar population synthesis modelling from Haydon et al. (2018) for Hα and UV emission, we can convert these relative lifetimes to the absolute timescales $t_{\rm gas}$ and $t_{\rm over}$.

Lastly, the size-scale at which the two branches diverge is set by the mean region separation length, λ. A population of regions more widely separated (i.e. a large value of λ) will exhibit divergence away from the galactic average gas-to-stellar flux ratio at larger aperture sizes than a population of regions more closely packed together (i.e. small λ). Thus, in order to observe this divergence and so apply the method successfully to a dataset, it must resolve λ. Detailed testing of the method shows that $\geqslant 1.5$ resolution elements are required for accurate measurement of λ (see figure 23 of Kruijssen et al., 2018). In nearby galaxies, where $\lambda = 100{-}300$ pc (Kruijssen et al., 2019; Hygate et al., 2019; Ward et al., 2020; Chevance et al., 2019), this translates to a required resolution of $70{-}200$ pc or better.

Extensive testing of the method in Kruijssen et al. (2018) shows that a number of criteria, in addition to the resolution requirement, should be satisfied by tracer images used such that accurate measurements are obtained from application of the HEISENBERG code. A minimum of 35 peaks per tracer map is required to obtain precision better than 50 per cent, with a greater number of peaks resulting in better precision. The blending between these peaks (i.e. the ratio of the region size to their mean separation length, λ) should be low enough to allow adjacent peaks to be identified and to minimise flux contamination between peaks. Significant cross-peak flux contamination will lead to an overestimate of the overlap timescale, $t_{\rm over}$. Furthermore, more accurate results are obtained for lower values of $|\log_{10}(t_{\rm star}/t_{\rm gas})|$, i.e. the more equal the values of the gas and stellar lifetimes are, with a difference of less than or equal to an order of magnitude necessary to avoid systematic bias. In addition, regions should be visible in both tracers at some point in their lifetimes, though not necessarily at the point that the tracer image is taken. The star formation rate should also not vary significantly over the evolutionary timeline length τ. For a full description of these criteria, see section 4.4 of Kruijssen et al. (2018). We will generate simulated datasets satisfying these

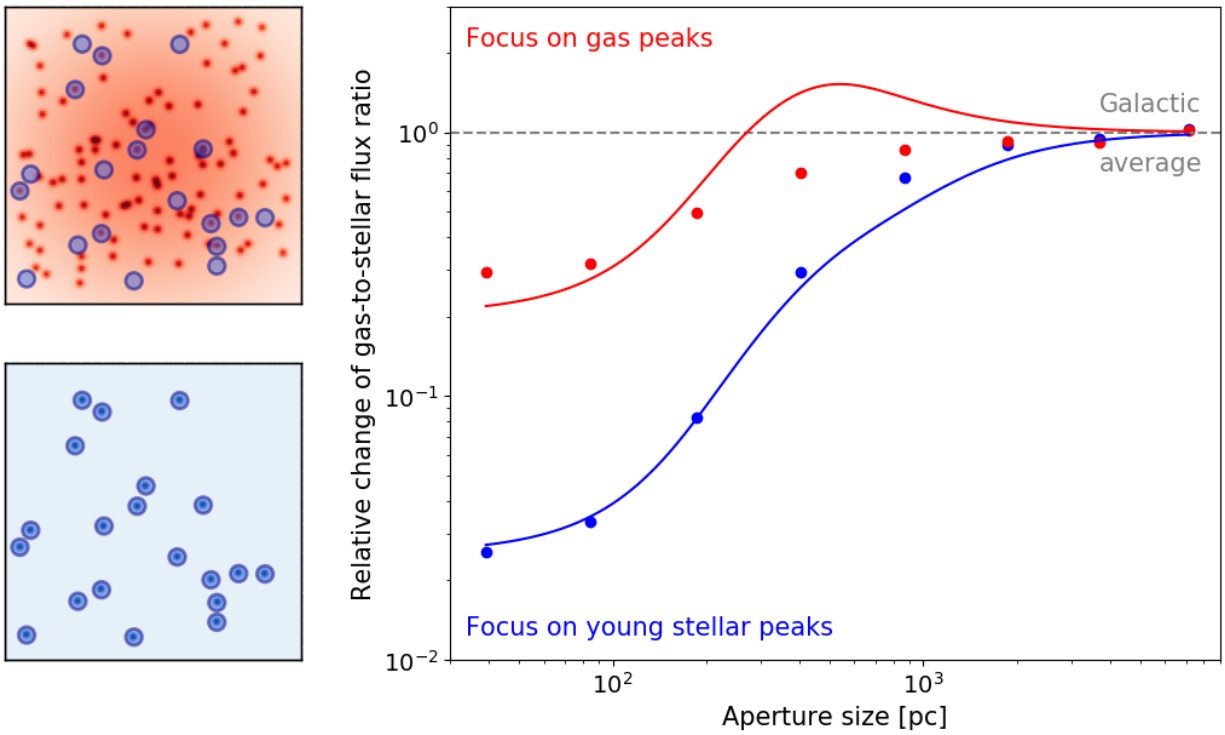

Figure 2.2: Illustration of the application of the HEISENBERG code to a dataset containing a significant fraction of diffuse emission. The application of the HEISENBERG code is shown, as described in Figure 2.1. However, the gas tracer map (top left) contains an additional significant diffuse emission reservoir, while the young stellar tracer map (bottom left) contains no diffuse emission. In this case, measurements in the top (red) branch, focussing on gas peaks, show a decrease of the gas-to-stellar flux ratio relative to the galactic average at small apertures – the opposite of the behaviour when there is no diffuse emission. Under these circumstances the statistical model employed in the HEISENBERG code is not able to fit the data. This is seen most readily by the poor fit of the statistical model (top, red line) to the gas peak-focussed measurements (top, red circles). As a result the HEISENBERG code does not accurately recover the underlying evolutionary timeline or mean separation of the emission peaks in the dataset, due to the presence of significant diffuse emission.

requirements in order to test the method presented in this paper in Sections 2.6 and 2.7.

A final requirement that is critical in the context of this paper, is that focusing an aperture on a peak in a tracer map should not lead to a deficit of the flux from that tracer relative to the galactic average. For example, focussing on a gas peak should lead to an enhanced or equal gas-to-stellar flux ratio compared to the galactic average value and not a reduced value. This criterion can be violated due to the presence of a diffuse background component. For instance, substantial diffuse emission in the gas tracer could cause a galaxy to have a larger global gas-to-stellar flux ratio than in the vicinity of gas emission peaks (see Figure 2.2 for an illustration of this effect).

In this paper, we will investigate how the three key parameters measured by the HEISENBERG code, λ, $t_{\rm gas}$ and $t_{\rm over}$ are impacted by the presence of additional flux from diffuse emission present in tracer maps and present a modification of the HEISENBERG code that removes the diffuse emission with Fourier filtering. By using (a multiple of) the region separation length, λ, as the critical wavelength for defining the separation between diffuse and compact emission, this method presents a physically-motivated way of decomposing the tracer maps into diffuse and compact emission images, thus allowing the fractions of diffuse and compact emission in these images to be measured.

Furthermore, this method extends the application of the Heisenberg code to observational data containing diffuse emission, without bias to the measurements from this diffuse emission. It is applied to observational data in a series of published or upcoming papers: including NGC300 (Kruijssen et al., 2019), M33 (Hygate et al., 2019), the LMC (Ward et al., 2020), and an initial sample of nearby galaxies (Chevance et al., 2019).

2.3 Method for decomposing emission maps into diffuse and compact components

We exploit the differing spatial distribution between regions of interest (for example molecular clouds), which are relatively small and concentrated, and the diffuse emission, which spans large scales. While these two emission components are co-spatial in a map, in 'real space', they are more easily distinguished in Fourier space where their emission is primarily located in different Fourier frequency regions. We therefore use filtering in Fourier space to separate these two types of emission.

For a given two-dimensional astronomical image $f(m,n)$ of size $N_{\mathrm{pix},x} \times N_{\mathrm{pix},y}$, we transform the image into Fourier space using a discrete Fourier transform:

$$F(u,v) = \frac{1}{N_{\mathrm{pix},x} N_{\mathrm{pix},y}} \sum_{m,n} f(m,n) e^{-i2\pi(um+vm)}, \tag{2.1}$$

where $N_{\mathrm{pix},x}$ and $N_{\mathrm{pix},y}$ are the number of pixels in the x and y dimensions, respectively. The Fourier frequencies (u,v) are defined as:

$$u = \frac{p - \left\lfloor \frac{N_{\mathrm{pix},x}-1}{2} \right\rfloor}{N_{\mathrm{pix},x}} \tag{2.2}$$

$$v = \frac{q - \left\lfloor \frac{N_{\mathrm{pix},y}-1}{2} \right\rfloor}{N_{\mathrm{pix},y}} \tag{2.3}$$

with $p \in \mathbb{N} \mid 0 \leqslant p \leqslant N_{\mathrm{pix},x} - 1$ and $q \in \mathbb{N} \mid 0 \leqslant q \leqslant N_{\mathrm{pix},y} - 1$. We note that $\lfloor x \rfloor$ represents the floor function of x, i.e. the value obtained when rounding x down to nearest integer. These Fourier frequencies define the frequency axes of the Fourier space into which we transform the image. For these frequencies, all values are such that $-0.5 < u,v \leqslant 0.5$. Each frequency axis also has a value at zero, with the $u = 0$, $v = 0$ component, known as the 'DC' component, representing the mean flux of the image. Within Fourier space, the emission characterised by long-wavelength Fourier modes, i.e. that from extended large-scale emission, is concentrated in the low frequency part of space, whereas the emission characterised by short-wavelength Fourier modes, i.e. that from compact regions in real space, is concentrated in the high frequency part of space.

The transformed image $F(u,v)$ is then multiplied with a mask, $\Psi(u,v)$, with values between 0 and 1 (corresponding to 0 per cent and 100 per cent transmission respectively), defined by one of the filters defined in Section 2.3.1 and transformed back into the image domain with an inverse

Fourier transform:

$$f'(m,n) = \Omega(m,n) \sum_{u,v} \Psi(u,v) F(u,v) e^{i2\pi(um+vm)}, \tag{2.4}$$

where $\Omega(m,n)$ is a post-processing mask applied to the result of the inverse Fourier transform (see Section 2.3.2) and $f'(m,n)$ is the filtered image with diffuse emission removed or reduced. An illustration of this process can be seen in Figure 2.3.

2.3.1 Filters

As a basis for describing frequency-based filters, we define two key quantities. Firstly, we define a distance for each component of the Fourier spectrum, in two-dimensional frequency space, from the zero-frequency $(u = 0, v = 0)$ 'DC' component:

$$D(u,v) = \sqrt{u^2 + v^2}. \tag{2.5}$$

Secondly, we define a critical distance in frequency space:

$$D_{\text{crit}} = \frac{l_{\text{pix}}}{n_\lambda \lambda}, \tag{2.6}$$

where λ is a physical size scale such that Fourier modes with wavelengths above this value are considered to be diffuse. We use the region separation length, λ, as measured by the HEISENBERG code to define this distance. The filtering-to-region separation length scale ratio, n_λ, is a multiplicative factor of λ that softens the cut, reducing the value of D_{crit} and thus reducing the amount of attenuation from the filter. An illustration of its impact on the shape of a filter can be seen in Figure 2.4. Finally, l_{pix} is the length of one pixel in the same physical units as λ, where the pixels must be square.

We require a filter that removes diffuse emission while leaving the emission from the populations of interest (e.g. gas clouds and regions of star formation) intact. As these populations are compact, the Fourier transform of their emission will be concentrated in the low wavelength/high spatial-frequency part of Fourier space. Conversely, large scale diffuse emission, such as that from a sheet of gas or a galaxy scale Gaussian, will be primarily located in the high wavelength/low spatial-frequency part of Fourier space. For this reason, we only consider highpass filters, which allow high spatial frequencies to pass through the filter. We consider three different highpass filters:

1. Ideal highpass filter

$$\Psi(u,v) = \begin{cases} 0 & D(u,v) \leq D_{\text{crit}} \\ 1 & D(u,v) > D_{\text{crit}} \end{cases} \tag{2.7}$$

2. Gaussian highpass filter

$$\Psi(u,v) = 1 - \exp\left(-\frac{(D(u,v))^2}{2{D_{\text{crit}}}^2} \right) \tag{2.8}$$

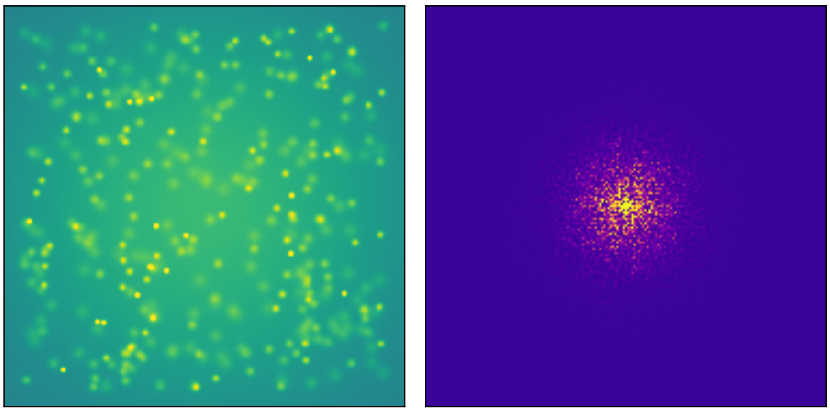

(a) original image **(b)** power spectrum

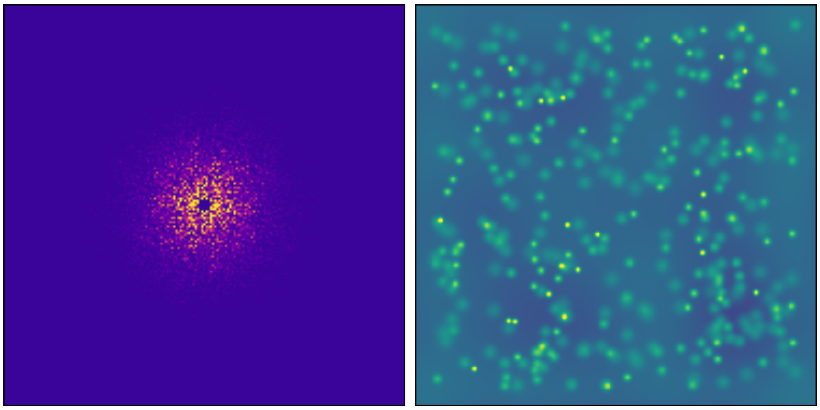

(c) filtered power spectrum **(d)** filtered image

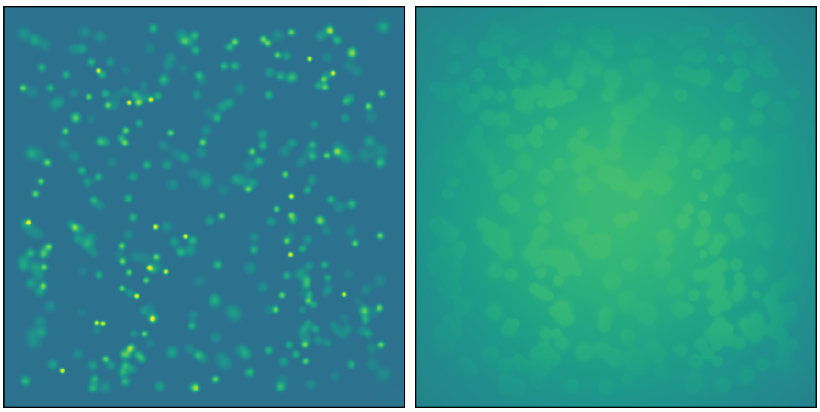

(e) positive filtered image **(f)** diffuse image

Figure 2.3: An illustration of the process of filtering diffuse emission in Fourier space. a) $f(m,n)$ the original unfiltered image, which is a combination of compact regions and a diffuse background model. b) $|F(u,v)|^2$, the Fourier power spectrum of the original image. c) The Fourier power spectrum of the image with an Ideal filter applied, $|\Psi(u,v)F(u,v)|^2$, masking a portion of the low frequency, large-spatial wavelength region of Fourier space. d) The image after the application of the highpass Ideal filter in the Fourier domain and transformation back to the image domain. This has removed the large-scale diffuse emission from the image. As the 'DC' component of the Fourier spectrum has been set to zero the image has zero mean flux and thus parts of the image are negative, seen in the image as the dark blue patches. e) The final filtered image, $f'(m,n)$ after the application of a mask to all negative pixels (see equation 2.4). f) An image of the diffuse emission in the original image, obtained by subtracting the filtered image from the original image $(f(m,n) - f'(m,n))$.

3. Butterworth highpass filter

$$\Psi(u,v) = \frac{1}{1+\left(\frac{D_{\text{crit}}}{D(u,v)}\right)^{2n_b}} \tag{2.9}$$

with the Butterworth order $n_b \in \mathbb{N} \mid n_b \geqslant 1$.

A visual comparison of the Ideal, Gaussian, and Butterworth filters can be seen in Figure 2.5. For a given value of D_{crit}, the Ideal filter is the sharpest filter, fully attenuating frequencies lower than D_{crit} (the diffuse component) and allowing frequencies higher than D_{crit} (the compact component) to pass with no attenuation. On the other hand the Gaussian filter has a smoother roll-off and thus attenuates the compact part of frequency-space while not fully removing the diffuse part of frequency space. The Butterworth filter has a tunable sharpness that approaches a fully sharp Ideal filter as $n_b \to \infty$. However, the advantage, of smoother roll-off is that application of a smoother filter will create less 'ringing' or distortion in the resultant filtered image than a sharp filter does. We assess the suitability of these filters for use in filtering diffuse emission from input images for the HEISENBERG code in Section 2.7.

2.3.2 Image post-processing

Due to the mathematical definition of the three highpass filters that we consider, the zero-frequency ($u=0, v=0$) 'DC' component, which represents the mean flux of the image, is always set to zero (i.e. $\Psi(0,0)=0$). This necessarily results in a filtered image with zero mean flux and thus roughly zero total flux. As flux remains in the filtered image corresponding to the parts of frequency space that were unattenuated or partially attenuated by the filter, this leads to negative pixels in the filtered image. As we do not expect negative emission from a tracer map, this problem may be solved simply by applying a binary mask that sets all pixels to zero wherever the reverse Fourier transform is negative:

$$\Omega(m,n) = \begin{cases} 0 & \sum_{u,v} \Psi(u,v)F(u,v)e^{i2\pi(um+vm)} < 0 \\ 1 & \sum_{u,v} \Psi(u,v)F(u,v)e^{i2\pi(um+vm)} > 0 \end{cases}. \tag{2.10}$$

This results in a filtered image $f'(m,n)$ with a positive total flux. This is done in order to avoid an image with approximately zero flux after the removal of the 'DC' component. In the case where an image contains noise, this has the effect of biasing the image with positive noise flux. We investigate this effect in more detail in Appendix 2.9.2.

2.3.3 Diffuse fraction measurement

The method that we employ to filter diffuse emission has the added benefit of decomposing an input tracer map into a map of compact emission and a map of diffuse emission. This allows us to quantify the fraction of emission within the map that is diffuse. The fraction of the flux in an image that is compact is simply the ratio of the total flux in the filtered (compact emission) image $f'(m,n)$ to the total flux in the original unfiltered image $f(m,n)$:

$$f_{\text{compact}} = \frac{\sum_{m,n} f'(m,n)}{\sum_{m,n} f(m,n)}. \tag{2.11}$$

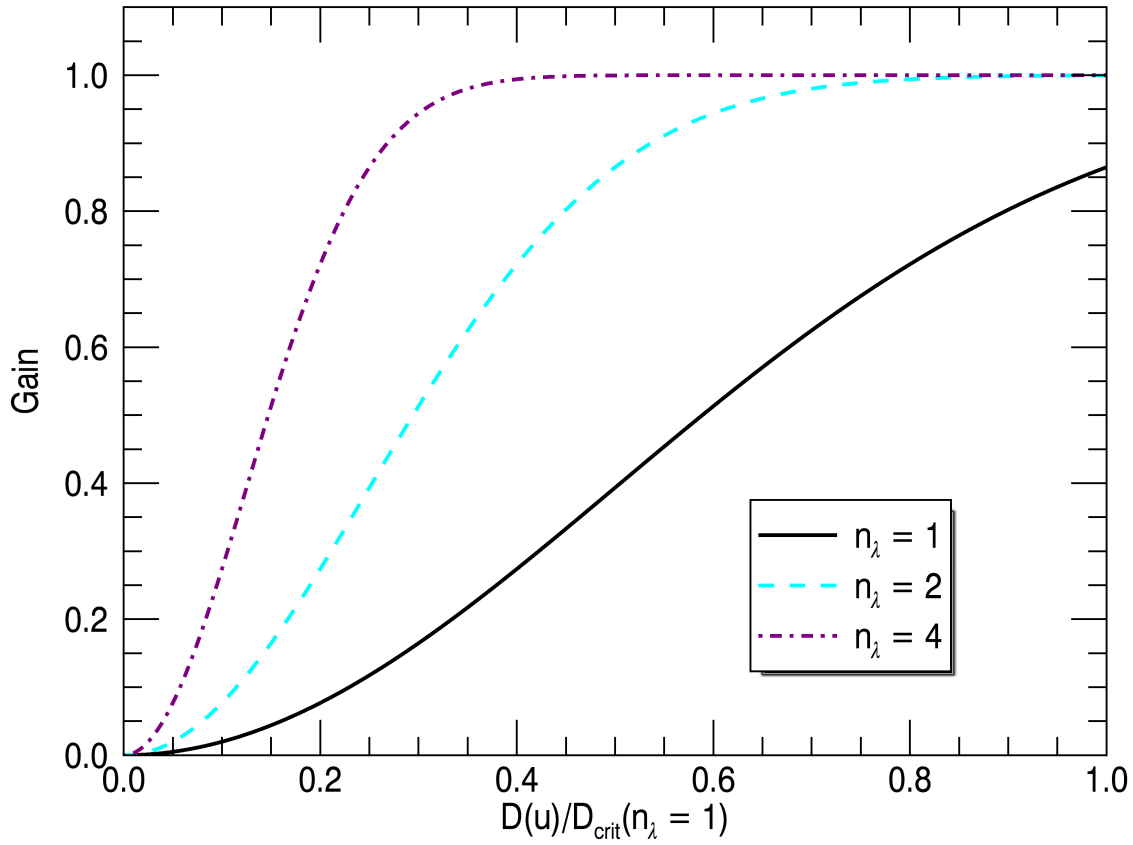

Figure 2.4: An illustration of the impact of choosing different values of the filtering-to-region separation length scale ratio, n_λ. The frequency response (gain) of three 1D Gaussian filters are shown are shown against the 1D frequency distance $D(u)$ normalised to the critical frequency, as calculated with $n_\lambda = 1$: $D_{\text{crit}}(n_\lambda = 1)$. It can be seen that higher values of n_λ have the effect of lowering the critical frequency and reducing the amount of attenuation from the filter.

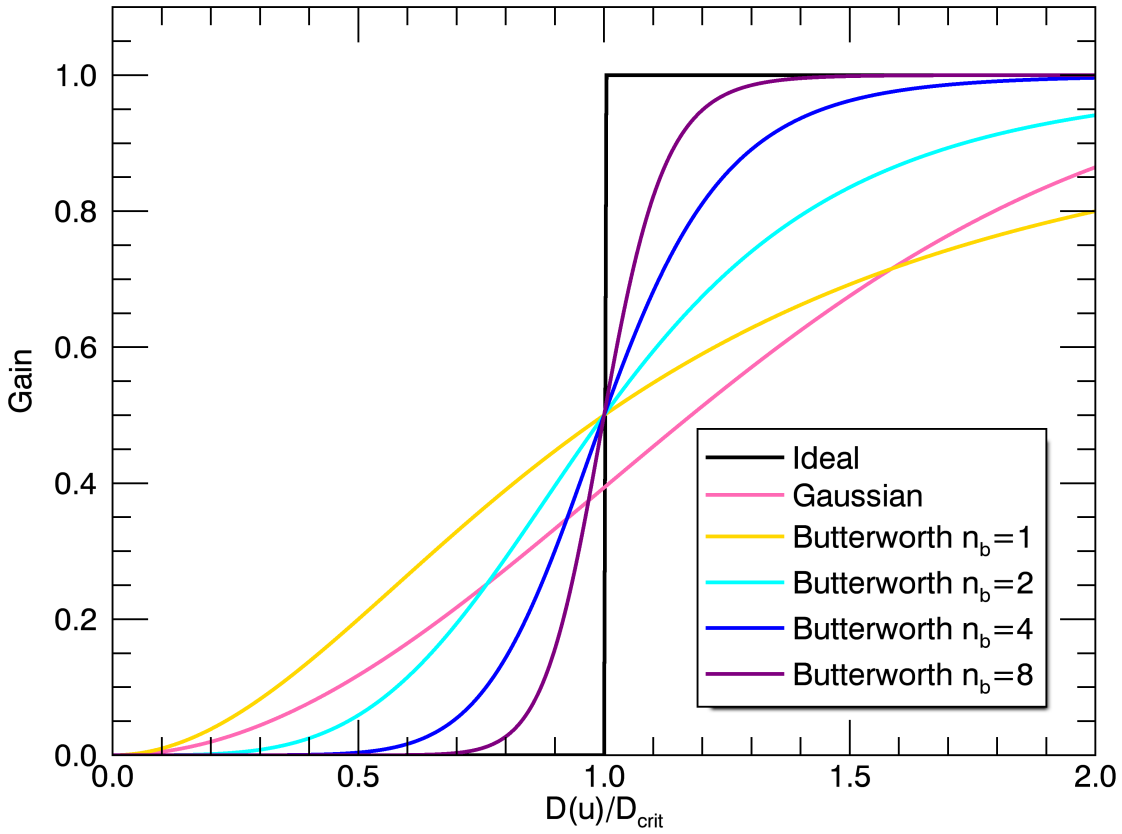

Figure 2.5: A comparison of the attenuation of the 1D counterparts of the filters described in Section 2.3.1. The frequency response (gain) of each of the filters is shown against the 1D frequency distance $D(u)$ normalised to the critical frequency D_{crit}.

The relationship of $f'(m,n)$ to $f(m,n)$ is described by equations 2.1 and 2.4. The diffuse fraction is then simply $f_{\text{diffuse}} = 1 - f_{\text{compact}}$, as all flux must be either diffuse or compact. This gives us a physically motivated measure of the relative contribution of the diffuse and compact emission components in the tracer map. We use the cloud-separation length, λ, as the dividing line between diffuse and compact emission , with emission at spatial wavelengths greater than $n_\lambda \lambda$ being diffuse emission and that at spatial wavelengths less than $n_\lambda \lambda$ being compact emission. For example, in the case where $f(m,n)$ is a tracer map of the molecular gas phase in a galaxy, the compact emission fraction represents the fraction of emission that comes from compact structures such as molecular clouds, whereas the diffuse fraction represents the fraction of the emission coming from large scale diffuse emission such as a reservoir of diffuse molecular gas or unresolved, low-mass molecular clouds.

2.4 Implementation within the HEISENBERG code

We present a method, using iterative filtering in Fourier space, to remove diffuse emission present in tracer maps to be used with the HEISENBERG code (Kruijssen et al., 2018). As with the HEISENBERG code, we have implemented this method in the Interactive Data Language (IDL)[10], in part using routines from the IDL Astronomy User's Library[11] and the IDL COYOTE Library.[12]

A flowchart summarising the steps taken in the method can be seen in Figure 2.6. A user has two options of how to start the filtering process: they can either supply the original images alone, in which case HEISENBERG is called to obtain a value λ for the initial calculation of $D_{\rm crit}$; or, if the user has calculated a value of λ externally, this value may also be supplied to the code for the initial calculation of $D_{\rm crit}$, in which case the images are pre-filtered, before the first call to HEISENBERG is made. After that, the HEISENBERG code is fitted to the filtered maps, and a new value of λ and thus $D_{\rm crit}$ is calculated. The code then checks for convergence and either repeats the process of fitting HEISENBERG in the case of no convergence or terminates and outputs the final values of all output parameters.

2.4.1 Input parameters

In order to run the presented method, a user has to specify a number of input flags, shown in Table 2.1, and input parameters, shown in Table 2.2, in addition to those flags and parameters described in Tables 1 and 2 of Kruijssen et al. (2018).

Both the flags and input parameters are divided into two groups separated by white space. The first of these comprises flags and parameters added to HEISENBERG itself and the second comprises flags and parameters that control the iterative diffuse filtering process. We consider most of these to be well described by reference to Tables 2.1 and 2.2. We provide some further explanation for some of the flags and parameters:

1. If the flag `peak_find_tui` is set, the user is presented with a text-user-interface allowing them to adjust peak selection (see section 3.2.7 of Kruijssen et al. 2018 for details). The user is also presented with a DS9 window[13], showing the input images with their identified peaks overlaid. The user may then adjust the parameters controlling peak selection through the text-user-interface and repeat the peak-finding process until they are satisfied with the identified peaks. This feature is of particular use during the iterative Fourier filtering process, as it allows the user to alter their peak selection parameters to adjust peak-finding after the removal of the diffuse background.

2. Together, the parameters $q_{\rm crit}$, a fractional tolerance between the measured value of λ in the current iteration and previous iteration and $r_{\rm crit}$, the number of iterations over which the criterion should be satisfied, specify the iteration's stopping condition:

$$q_{\rm crit} < \left| \frac{\lambda_{i-r} - \lambda_i}{\lambda_i} \right|, \tag{2.12}$$

[10] http://www.harrisgeospatial.com/SoftwareTechnology/IDL.aspx
[11] https://idlastro.gsfc.nasa.gov/
[12] http://www.idlcoyote.com/
[13] This optional feature requires the user to have the DS9 software package, which can be obtained from: http://ds9.si.edu

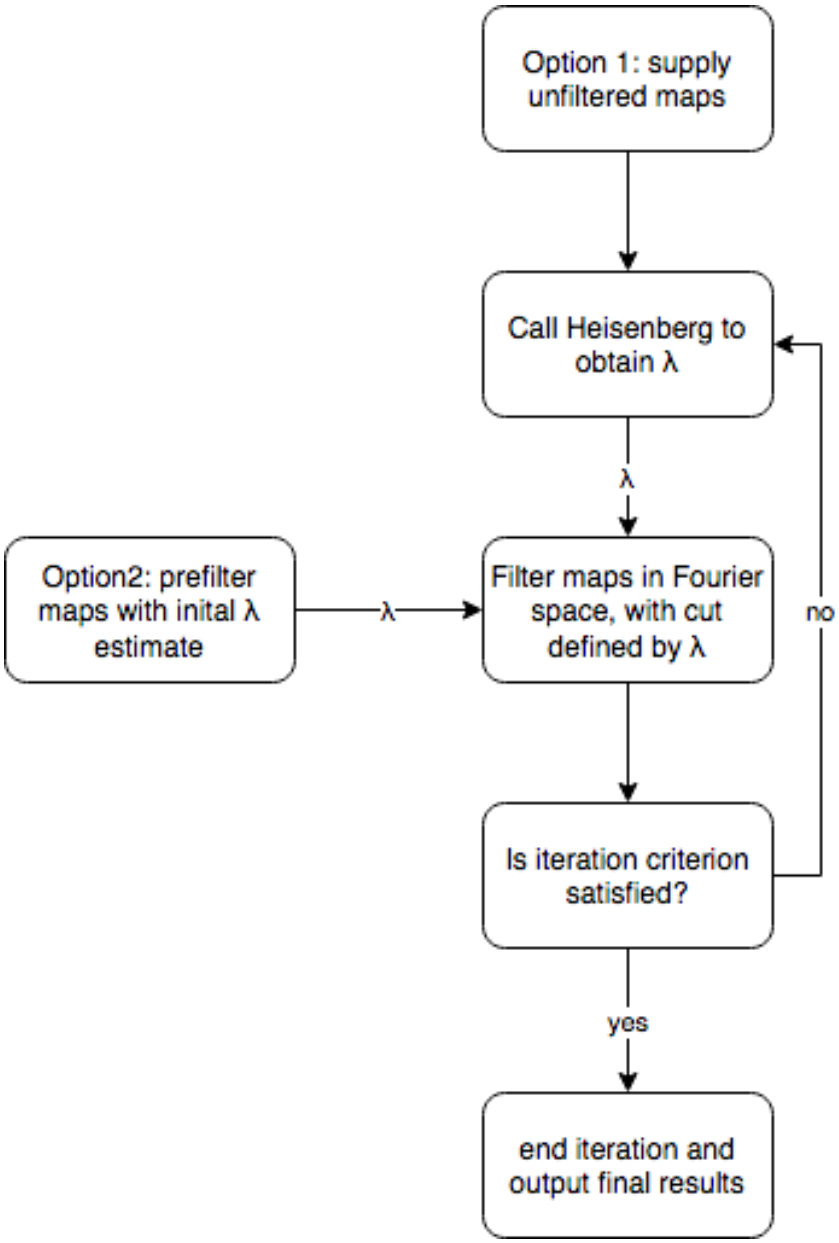

Figure 2.6: Flowchart summarising the iterative diffuse filtering method.

Table 2.1: Flags to be set for the presented analysis additional to those described in table 1 of Kruijssen et al. (2018)

Flag	Values (**default**)	Description
`diffuse_frac`	0/**1**	Calculate diffuse fraction in images (off/**on**)
`peak_find_tui`	**0**/1	Use interactive peak identification interface to refine initial peak selection (**off**/on)
`f_filter_type`	0	Use an Ideal filter for the determination of diffuse fractions (see equation 2.7)
	1	Use a Gaussian filter for the determination of diffuse fractions (see equation 2.8)
	2	Use a Butterworth filter for the determination of diffuse fractions (see equation 2.9)
`use_sds`	0	Automatically calculate map sensitivity limits as described in section 3.2.6 of Kruijssen et al. (2018)
	1	Pass in externally calculated values of map sensitivity limits to the code
`use_guess`	**0**	Calculate $D_{\rm crit}$ for the first filtering step by fitting HEISENBERG to the unfiltered maps (option 1 in Figure 2.6)
	1	Use an initial estimated value of λ to determine $D_{\rm crit}$ for the first filtering step (option 2 in Figure 2.6)

for $r \in \mathbb{N} \mid 1 \leqslant r \leqslant r_{\rm crit}$. i.e. if the relative difference between value of λ calculated in the current iteration step and all values of λ calculated in the $r_{\rm crit}$ previous steps is less than $q_{\rm crit}$, the iteration is considered to have converged and is terminated.

3. In addition, $r_{\rm max}$ sets the maximum number of iterative steps that will be taken ($r_{\rm max} + 1$) before the code will terminate even if convergence has not been reached.

2.4.2 Code output

Each iterative step applies the HEISENBERG code and the quantities described by Kruijssen et al. (2018) in their table 4 are measured and returned, in addition to the image compact emission fractions, as described in Table 2.3. The quantities are tracked and figures are made for the user showing how they change with each iterative step. Figure 2.7 shows examples of these figures for the fundamental physical quantities, λ, $t_{\rm gas}$ and $t_{\rm over}$, which are measured by HEISENBERG. This allows the user to quickly visually inspect that convergence in the value of λ, on which the method's iteration condition is based, has also resulted in satisfactory convergence of the other quantities. In addition, the filtered map (of compact emission) and the diffuse emission map produced in each step are saved to disk. This makes these maps available for further analysis on the two components and allows the user to visually inspect the filtered map for distortions. An example of these maps can be seen in panels e and f of Figure 2.3.

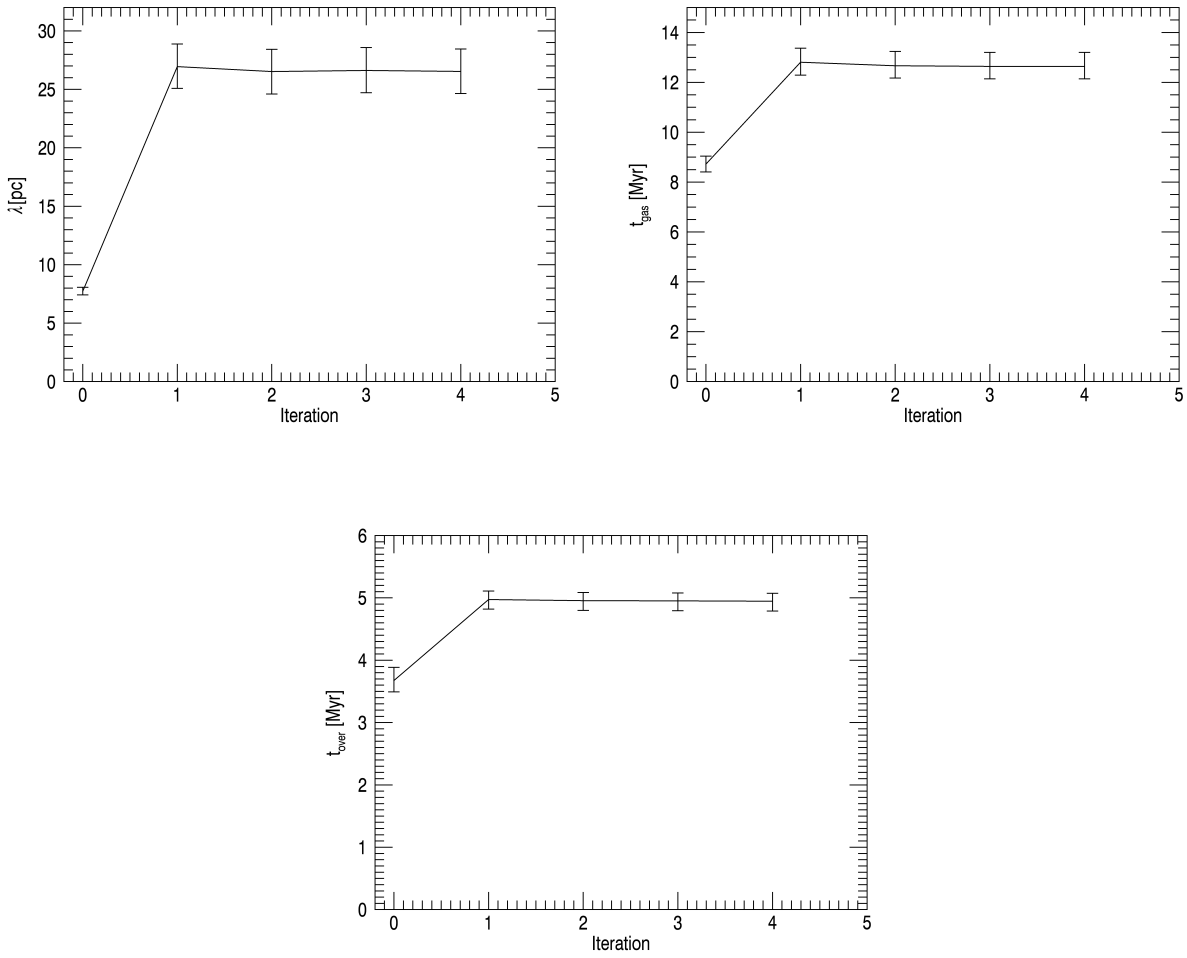

Figure 2.7: Example output from a successful run, in which convergence has been reached, showing how the quantities λ, $t_{\rm gas}$ and $t_{\rm over}$ vary with iteration number. A change in the values of all three quantities can be seen from the leftmost data-point in each plot, where no Fourier filtering has been applied, and all subsequent points after the application of Fourier filtering.

Table 2.2: Input parameters to be set for the presented analysis additional to those described in table 2 of Kruijssen et al. (2018)

Parameter	Default	Description
$n_{b,\mathrm{diffuse}}$	2	The order of the Butterworth filter used to calculate map diffuse fractions (only used if `f_filter_type` = 0)
$n_{\lambda,\mathrm{diffuse}}$	1.0	Multiplicative factor used in calculating map diffuse fractions for calculating D_{crit} that reduces filter attenuation for a given value of λ (see equation 2.6)
$\sigma_{\mathrm{sens,star}}$	-	The measured sensitivity limit of the star formation tracer map in units of the map
$\sigma_{\mathrm{sens,gas}}$	-	The measured sensitivity limit of the gas tracer map in units of the map
$\lambda_{\mathrm{initial}}$	-	Length in pc of the initial estimate of lambda (only used if `use_guess` = 1)
q_{crit}	0.05	Maximum fractional difference between λ and previous λ value(s) that triggers the iteration process to terminate
r_{crit}	2	Number of steps over which the iteration criterion, q_{crit}, must be true for iteration to terminate
r_{max}	10	Maximum number of steps in the iterative diffuse filtering process, before the iteration is terminated
$n_{b,\mathrm{iter}}$	2	The order of the Butterworth filter used in the iterative diffuse filtering process (only relevant if `f_filter_type` = 0)
$n_{\lambda,\mathrm{iter}}$	1.0	Multiplicative factor used in the iterative diffuse filtering process for calculating D_{crit} that reduces filter attenuation for a given value of λ (see equation 2.6)

Table 2.3: Quantities constrained by HEISENBERG additional to those described in table 4 of Kruijssen et al. (2018)

Quantity	Equation	Description
f_{cl}	2.11	The fraction of emission in the stellar tracer map that is not diffuse
f_{GMC}	2.11	The fraction of emission in the gas tracer map that is not diffuse
$q_{\mathrm{con,star}}$	2.31	The relative flux loss from compact stellar regions due to filtering in Fourier space (see Section 2.6)
$q_{\mathrm{con,gas}}$	2.31	The relative flux loss from compact gas regions due to filtering in Fourier space (see Section 2.6)
η_{stars}	2.33	The evolutionary phase lifetime adjusted star formation filling factor (see Section 2.6)
η_{gas}	2.34	The evolutionary phase lifetime adjusted gas filling factor (see Section 2.6)
$q_{\eta,\mathrm{star}}$	2.35	The relative flux loss from stellar regions due to overlap between regions in the stellar map (see Section 2.6)
$q_{\eta,\mathrm{gas}}$	2.35	The relative flux loss from gas regions due to overlap between regions in the gas map (see Section 2.6)

2.5 Generation of test images

In order to test and validate the presented iterative diffuse filtering method we generate test input datasets. Each test dataset consists of a pair of test images, of size $N_{\mathrm{pix},x} \times N_{\mathrm{pix},x}$, such that both images in the pair are square and of the same size. We note that these choices are made for simplicity and are not restrictions of the method. Each image $f(m,n)$ is made up of two components: a compact component $s(m,n)$ and a background component $b(m,n)$:

$$f(m,n) = s(m,n) + b(m,n). \tag{2.13}$$

An example image generated in this manner is shown in Figure 2.8.

2.5.1 The signal component

For the HEISENBERG code to be applied we require two maps: one representing a progenitor phase and one representing a descendent phase in an evolutionary sequence. In order to create the compact component for these maps, we generate three compact populations: a population that is visible only in the progenitor map, one that is visible only in the descendant map and an 'overlap' population that is visible in both maps. Hereafter, we will assume that our progenitor population is made up of gas clouds and that our descendent population is made up of young stellar regions (HII regions) and thus refer to them as 'gas' and 'stars'. In this scenario, our overlap population represents the phase of star formation where young stars have been formed and are still co-spatial with their natal cloud. This is the phase during which feedback operates to eventually cause the cloud to cease be visible in the gas tracer map (for example through photodissociation or physical transportation of the gas away from the young stars). We note, however, that the HEISENBERG code may be applied more generally, to any scenario characterised by an evolution from a population visible in one tracer map to a descendent population visible in another tracer map. Likewise, the presented method of removing diffuse emission from a tracer map may be used in other situations, in which one wishes to remove an extended diffuse component from a tracer map containing both this diffuse component and a population of compact regions.

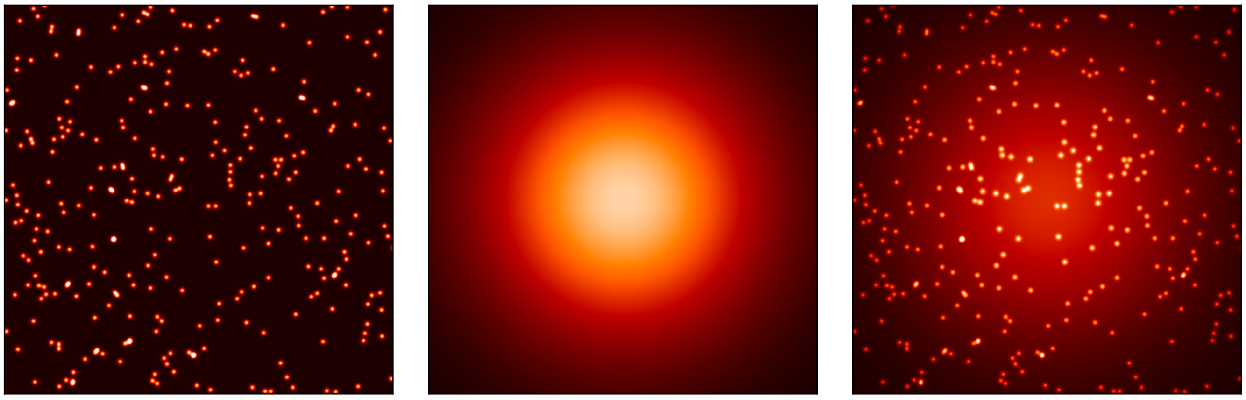

Figure 2.8: Example generated image and its components. Left panel: the compact component. Note that the placement of Gaussians is entirely random such that they may overlap partially or entirely with other Gaussians, leading to pixels brighter than the peak brightness of a single Gaussian. Middle panel: the background component, here a single large 'galaxy scale' Gaussian function. Right panel: the final generated image with both components summed together.

To simulate the gas, stellar and overlap populations, we generate Gaussian functions and position them randomly within our maps. We determine the position $(m_{\mathrm{gc,i}}, n_{\mathrm{gc,i}})$ of the central pixel of the i^{th} Gaussian function by drawing random numbers from a uniform distribution:

$$\left\{m_{\mathrm{gc,i}} \in \mathbb{N} \mid 0 \leqslant m_{\mathrm{gc,i}} \leqslant N_{\mathrm{pix,x}} - 1\right\} \tag{2.14}$$

$$\left\{n_{\mathrm{gc,i}} \in \mathbb{N} \mid 0 \leqslant n_{\mathrm{gc,i}} \leqslant N_{\mathrm{pix,y}} - 1\right\}. \tag{2.15}$$

We set the characteristics of the compact component with the following parameters: $N_{\mathrm{peak,gas,input}}$, the number of Gaussian functions appearing in the gas map only; $N_{\mathrm{peak,star,input}}$, the number of Gaussian functions appearing in the stellar map only; $N_{\mathrm{peak,over,input}}$, the number of peaks appearing in both the gas and stellar maps; and $G_{\mathrm{FWHM,star}}$ and $G_{\mathrm{FWHM,gas}}$, the full width at half maximum (FWHM) of the Gaussian functions seeded into the stellar and gas maps, respectively. We consider a number of different models for the FWHMs of the regions:

1. Uniform FWHM model:
   In this model, all the Gaussian regions in each pair (stellar and gas) of images have the same FWHM:

   $$G_{\mathrm{FWHM,star,i}} = G_{\mathrm{FWHM,gas,i}} = \phi \tag{2.16}$$

   where ϕ is a uniform random number chosen for each experiment such that $\phi \in \mathbb{R} \mid \phi_{\mathrm{min}} < \phi < \phi_{\mathrm{max}}$. In this model, the total flux of each region is equal to that of each other region.

2. Asymmetric uniform FWHM model:
   In this model, we set a common FWHM value for all Gaussian regions in the stellar map, and another one for all the Gaussian regions in the gas map:

   $$G_{\mathrm{FWHM,star,i}} = \phi_{\mathrm{star}} \tag{2.17}$$

   $$G_{\mathrm{FWHM,gas,i}} = \phi_{\mathrm{gas}}, \tag{2.18}$$

   where ϕ_{star} and ϕ_{gas} are individually chosen uniform random numbers chosen for each experiment such that $\phi_{\mathrm{star}} \in \mathbb{R} \mid \phi_{\mathrm{min}} < \phi_{\mathrm{star}} < \phi_{\mathrm{max}}$ and $\phi_{\mathrm{gas}} \in \mathbb{R} \mid \phi_{\mathrm{min}} < \phi_{\mathrm{gas}} < \phi_{\mathrm{max}}$.As with the previous model, the flux of each region is equal to that of each other region.

3. FWHM spread model:
   In this model, each individual Gaussian region in the stellar and gas maps has a randomly selected FWHM, selected within the same range of values for both maps

   $$G_{\mathrm{FWHM,star,i}} \in \mathbb{R} \mid \phi_{\mathrm{min}} < G_{\mathrm{FWHM,star,i}} < \phi_{\mathrm{max}} \tag{2.19}$$

   $$G_{\mathrm{FWHM,gas,i}} \in \mathbb{R} \mid \phi_{\mathrm{min}} < G_{\mathrm{FWHM,gas,i}} < \phi_{\mathrm{max}}. \tag{2.20}$$

As with the previous models, the flux of each region is equal to that of the other regions, irrespective of the randomly selected FWHM of a region.

4. FWHM flux spread model:
   The FWHM of regions in this model is selected in the same way as the 'FWHM spread model' (i.e. according to equations 2.19 and 2.20). However, in this model the flux of regions are not equal to that of each other region, instead the flux of a region is proportional to its size, i.e. $\mathcal{F}_i \propto G_{\mathrm{FWHM}i}$.

For each of these models, regions in the overlap phase are selected from the same size distribution as the gas and stellar regions. For the asymmetric uniform FWHM model, an overlap region has size ϕ_{star} in the stellar map and size ϕ_{gas} in the gas map.

In order to test the effectiveness of the method, we compare measured values of the three key quantities measured by the HEISENBERG code (the gas cloud lifetime, t_{gas}, the overlap phase lifetime, t_{over}, and the mean separation length between regions, λ; recall that the young stellar lifetime t_{star} is assumed to be known a priori) to values known from the generation of the test datasets. The relative visibility lifetimes of each population are linked to the relative number of regions in each population. Therefore, for t_{gas} and t_{over} in relation to t_{star} we have:

$$t_{\mathrm{gas}} = t_{\mathrm{star}} \frac{N_{\mathrm{peak,gas,input}} + N_{\mathrm{peak,over,input}}}{N_{\mathrm{peak,star,input}} + N_{\mathrm{peak,over,input}}} \tag{2.21}$$

and

$$t_{\mathrm{over}} = t_{\mathrm{star}} \frac{N_{\mathrm{peak,over,input}}}{N_{\mathrm{peak,star,input}} + N_{\mathrm{peak,over,input}}}, \tag{2.22}$$

where t_{star} is used as the reference time-scale. As we are not directly simulating a particular tracer, the actual value of the reference time-scale is not relevant. We choose $t_{\mathrm{star}} = 10\,\mathrm{Myr}$, which is close to typical values found for visibility lifetimes of star formation tracers by Haydon et al. (2018).

For each image, we select a value of the filling factor, ζ, the region size-to-mean separation ratio. Given our selected value of G_{FWHM} and ζ, we calculate a value of the mean separation length between regions, λ, following the definition of ζ in equations 136 and 137 in Kruijssen et al. (2018), which we reproduce here:

$$\zeta_{\mathrm{star}} = \frac{G_{\mathrm{FWHM,star}}/\sqrt{2\ln 2}}{\lambda} \tag{2.23}$$

$$\zeta_{\mathrm{gas}} = \frac{G_{\mathrm{FWHM,gas}}/\sqrt{2\ln 2}}{\lambda} \tag{2.24}$$

where $G_{\mathrm{FWHM}}/2\sqrt{2\ln 2} = r_{\mathrm{peak}}$ from the original definition in Kruijssen et al. (2018). This filing factor represents the amount of blending between peaks and is a key quantity in determining the applicability of the HEISENBERG code. Testing performed by Kruijssen et al. (2018) shows that the quality of measurements obtained declines as ζ increases above 0.5. We will therefore assess the quality of the presented diffuse filtering method at different filling factors based on that criterion.

Lastly, we determine the number of pixels, $N_{\mathrm{pix},x}$, of the image to be generated, by using the total number of peaks in the image set, the mean separation length, λ, and the pixel length scale, l_{pix}:

$$N_{\mathrm{pix},x} = \sqrt{\frac{\pi N_{\mathrm{peak,total,input}}}{{l_{\mathrm{pix}}}^2}\left(\frac{\lambda}{2}\right)^2}, \tag{2.25}$$

where $N_{\mathrm{peak,total,input}} = N_{\mathrm{peak,gas,input}} + N_{\mathrm{peak,star,input}} + N_{\mathrm{peak,over,input}}$. As $N_{\mathrm{pix},x}$ must be an integer number, this calculation introduces a small rounding error. We therefore recalculate the effective value of λ from the definition of the geometric mean separation length for the total number of regions in the total area of a map (appendix A2 of Kruijssen & Longmore, 2014), which in practice is an inversion of equation (2.25).

2.5.2 The background component

We consider a number of different models of the diffuse background, with increasing levels of complexity:

1. Constant background:
   The simplest model that we consider is that of a spatially uniform constant diffuse background:

   $$b(m,n) = \beta_{\mathrm{const}}, \tag{2.26}$$

   with $\beta_{\mathrm{const}} \in \mathbb{R} \mid \beta_{\mathrm{const}} > 0$ selected such that the fraction of the diffuse background may vary in significance relative to the compact component.

2. Extended Gaussian and constant background:
   This background model consists of both a constant background and a large 'galaxy-scale' Gaussian function.

   $$b(m,n) = \beta_{\mathrm{const}} + \beta_{\mathrm{Gauss}} \exp\left(\frac{x^2+y^2}{\beta_{\mathrm{FWHM}}/2\sqrt{2\ln 2}}\right), \tag{2.27}$$

   with the normalisation factors, $\beta_{\mathrm{const}} \in \mathbb{R} \mid \beta_{\mathrm{const}} > 0$ and $\beta_{\mathrm{Gauss}} \in \mathbb{R} \mid \beta_{\mathrm{Gauss}} > 0$ varying such that the two components may vary in significance in relation to each other and that the significance of the background component may vary relative to the compact component. The FWHM of the 'galaxy-scale' Gaussian, β_{FWHM}, is chosen such that $\beta_{\mathrm{FWHM}} \lesssim N_{\mathrm{pix,x}}$ so as to represent a large galactic background that decreases smoothly with radius.

3. Envelopes, Extended Gaussian and constant background:
   In addition to the constant and galaxy scale Gaussian background, this background model includes Gaussian envelopes with centres co-spatial to the compact Gaussian regions seeded into the maps. The FWHM of the envelopes is set to be a multiple of the region separation length, λ, where we consider $\mathrm{FWHM}_{\mathrm{envelope}} = 0.5\lambda, 1.0\lambda, 2.0\lambda$. As with the previous models, the normalisation of each of the components is randomly chosen for each experiment such that the significance of each component varies and the significance of the total background varies in relation to the compact component.

The true value of the compact emission fraction ($f_{\text{compact,true}}$) in an image $f(m,n)$ is calculated as the total flux in the compact component divided by the total flux in the image (including the background component):

$$f_{\text{compact,true}} = \frac{\sum_{m,n} s(m,n)}{\sum_{m,n} \left(s(m,n) + b(m,n)\right)}. \tag{2.28}$$

Overlap between regions causes flux loss from compact regions after the application of Fourier filtering. In Section 2.6, we use the method presented here to generate simulated datasets to investigate this effect. In Section 2.7, we again use the method to generate datasets to evaluate the performance of the method at removing diffuse emission. A summary of the parameter spaces used for each section is presented in Table 2.2.

2.6 The impact of filtering on compact regions

The value of f_{compact} given by equation 2.11 assumes that filtering removes none of the flux of the compact regions. However, the flux from a Gaussian region is spread out in Fourier space, such that the application of a filter in Fourier space removes some of the flux from compact regions. This flux loss should be quantified, so that it can be corrected for.

We identify two such sources of flux loss when filtering an image in Fourier space: the flux lost from a single isolated Gaussian function after the application of a filter and the additional flux lost due to overlap between regions in an image containing multiple regions. We define the fraction of flux remaining in an image containing a single Gaussian function, $f_{\text{single}}(m,n)$, after filtering as:

$$q_{\text{con}} = \frac{\sum_{m,n} f'_{\text{single}}(m,n)}{\sum_{m,n} f_{\text{single}}(m,n)}, \tag{2.29}$$

where $f'_{\text{single}}(m,n)$ is the resultant filtered image, as defined by Equation 2.4.

We next define a corrective factor q_η that quantifies the additional fractional flux loss, in an image with multiple Gaussian regions as compared an image with a single regions, due to overlapping regions causing more flux from compact regions to appear at high-spatial wavelengths. We define q_η such that $q_{\text{con}} q_\eta$ is the fraction of flux remaining in an image containing multiple Gaussian regions, after filtering:

$$q_\eta = \frac{\sum_{m,n} f'(m,n)}{\sum_{m,n} f(m,n)} \Big/ \frac{\sum_{m,n} f'_{\text{single}}(m,n)}{\sum_{m,n} f_{\text{single}}(m,n)} = \frac{1}{q_{\text{con}}} \frac{\sum_{m,n} f'(m,n)}{\sum_{m,n} f(m,n)}. \tag{2.30}$$

2.6.1 Flux loss for a single Gaussian region

We first investigate the flux remaining in an image containing a single Gaussian region after the application of Fourier filtering, q_{con}. Figure 2.9 shows q_{con} after the application of Gaussian filters, where D_{crit} is set with variable values of $n_\lambda \lambda$. For the smallest, $G_{\text{FWHM}} = 1$ pixel region, which we do not show, we do not see a smooth function between the flux fraction and critical filter length-scale, as the function is insufficiently resolved.

In the right-hand panel of Figure 2.9, we see that q_{con} can be well fitted by a simple analytical function of the relative width of the Gaussian filter over the width of the compact regions, $n_\lambda \lambda / G_{\text{FWHM}}$, for all the Gaussian functions with $G_{\text{FWHM}} \geqslant 2$ pixels.

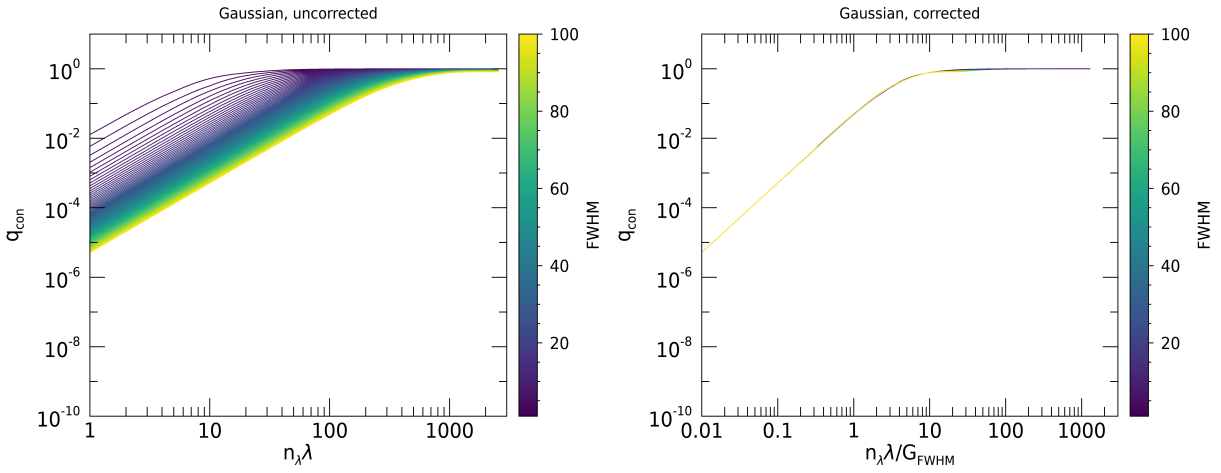

Figure 2.9: The fraction of flux remaining in an image containing a single Gaussian function of varying FWHM (as indicated by the colour bar) after the application of a Gaussian filter. Left panel: the remaining flux fraction as a function of $n_\lambda\lambda$. Right panel: the remaining flux as a function of $n_\lambda\lambda/G_{\mathrm{FWHM}}$, i.e. where the x-axis has been normalised by the FWHM of the Gaussian function. After application of this correction we recover a simple analytic relationship for all the images where $G_{\mathrm{FWHM}} \geqslant 2$.

By again plotting q_{con} against $n_\lambda\lambda/G_{\mathrm{FWHM}}$ for the other considered filters, the Ideal filter and Butterworth filters, we obtain relationships of varying quality, which are shown in Figure 2.10. We again find the smallest ($G_{\mathrm{FWHM}} = 1$ pixel) Gaussian functions to be insufficiently resolved and thus we impose the condition that the FWHM of the Gaussian regions in the image $G_{\mathrm{FWHM}} \geqslant 2$ pixels for the successful application of the method. While the remaining flux fraction is strictly less than or equal to unity after the application of the Gaussian filter, it is above one (even up to ~ 5) in some cases after the application of the Ideal filter, due to the significant distortions introduced into the image. For this reason, we discard the Ideal filter from further consideration. The Butterworth filter is tunable, where at low values of n_b the filter is smooth, akin to the Gaussian filter, but becomes sharper, approaching an Ideal filter as $n_b \to \infty$. For the 1$^{\mathrm{st}}$ order Butterworth filter, we again obtain a simple analytical function, where $q_{\mathrm{con}} \leqslant 1$. For $n_b \geq 2$, however, we see that q_{con} is greater than 1 in some instances, with the magnitude of the effect greater as n_b increases.

We fit a sigmoidal function for q_{con}, as a function of $n_\lambda\lambda/G_{\mathrm{FWHM}}$:

$$q_{\mathrm{con}} = q_{\mathrm{con},\infty} + \frac{(a - q_{\mathrm{con},\infty})}{\left(1 + \left(\frac{n_\lambda\lambda}{G_{\mathrm{FWHM}}}/c\right)^b\right)}, \tag{2.31}$$

where we set $q_{\mathrm{con},\infty} = 1$ for all filters, so that as $n_\lambda\lambda/G_{\mathrm{FWHM}} \to \infty$, $q_{\mathrm{con}} \to 1$, as this represents 0 per cent flux loss from the Gaussian region in the image. The value of a sets the zero point of the function, such that $q_{\mathrm{con}} = a$ for $n_\lambda\lambda/G_{\mathrm{FWHM}} = 0$. The value of b sets the steepness of the transition between $q_{\mathrm{con}} = q_{\mathrm{con},\infty}$ and $q_{\mathrm{con}} = a$, with higher values of b representing a steeper transition. The value of c is the value of $n_\lambda\lambda/G_{\mathrm{FWHM}}$ at which $q_{\mathrm{con}} = a + ((a-1)/2)$. The best fitting values of these parameters are shown in Table 2.4 and a comparison of the fitted functions is shown in Figure 2.11.

We first compare the Gaussian and 1st order Butterworth filters, which both have the property that the flux remaining after their application in the single Gaussian region is strictly less than

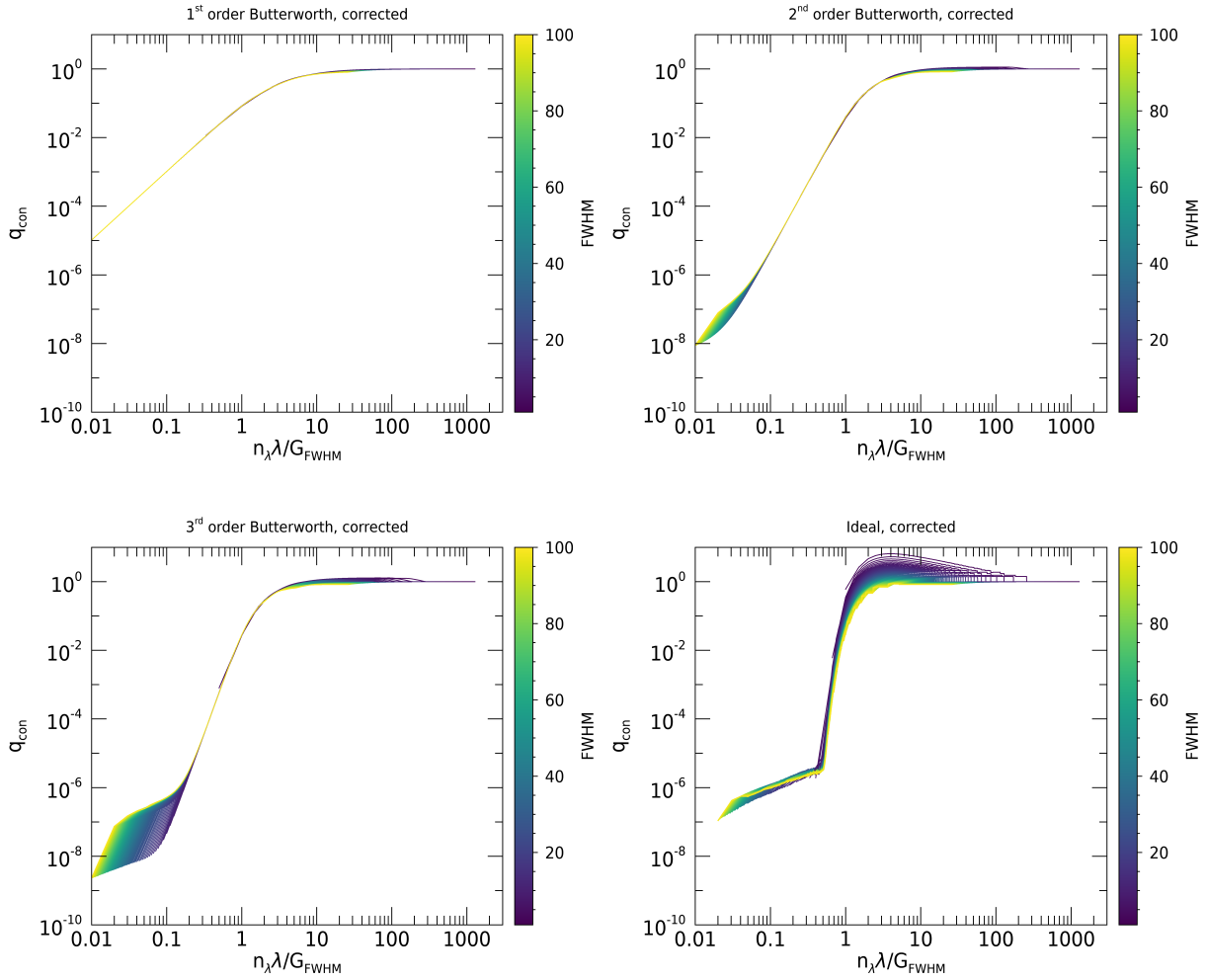

Figure 2.10: The fraction of flux remaining in an image containing a single Gaussian function of varying FWHM (as indicated by the colour bar) as a function of $n_\lambda \lambda / G_{\mathrm{FWHM}}$ after the application of a 1$^{\mathrm{st}}$ order Butterworth filter (top left), a 2$^{\mathrm{nd}}$ order Butterworth filter (top right), a 3$^{\mathrm{rd}}$ order Butterworth filter (bottom left) and an Ideal filter (bottom right). As with the Gaussian filter, the remaining flux fraction for the 1$^{\mathrm{st}}$ order Butterworth filter is strictly less than or equal to unity and well fitted with a simple analytic function. By contrast, the remaining flux after the application of an Ideal filter significantly exceeds unity in some cases, due to the significant distortions introduced into the image. Butterworth filters with order greater than one also lead to remaining flux fractions greater than unity with the magnitude of the excess increasing with order.

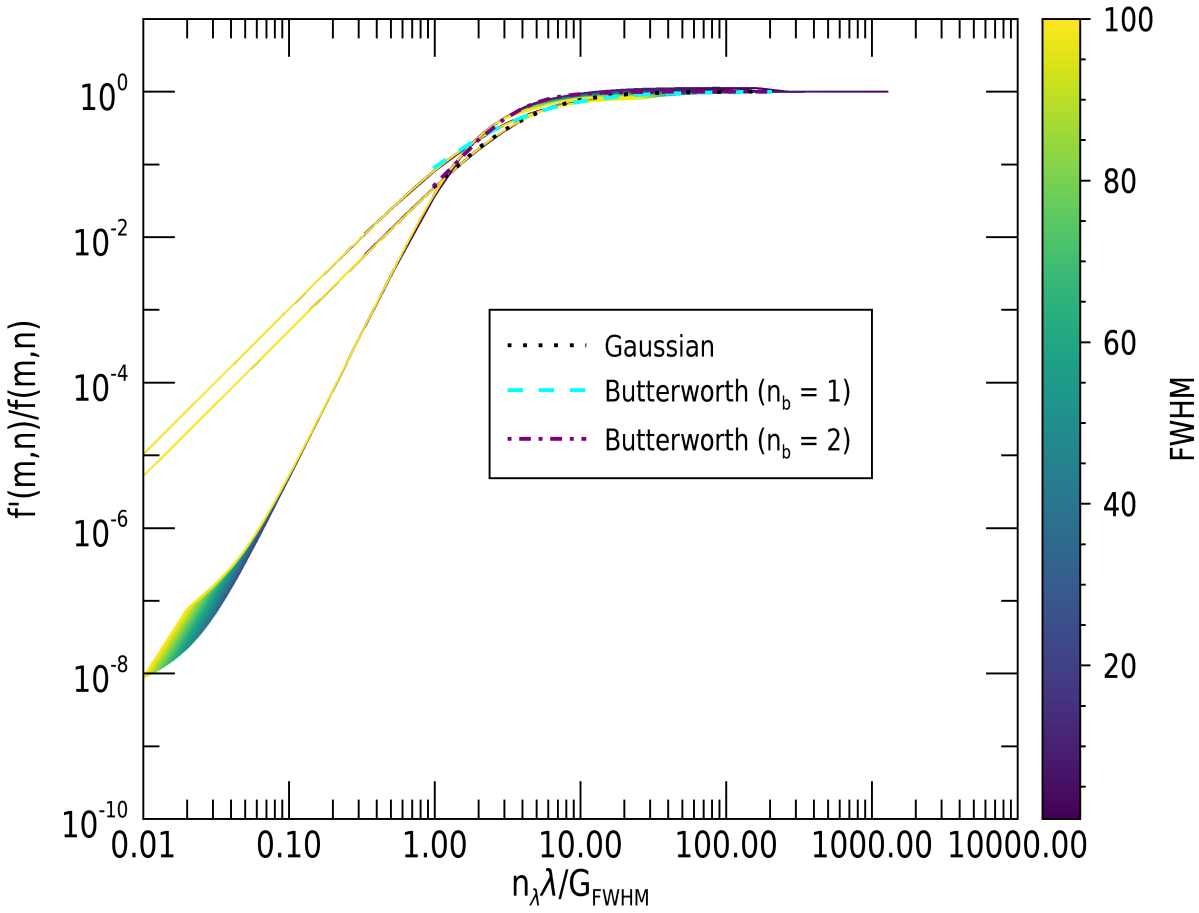

Figure 2.11: A comparison of the fitted remaining flux fraction, $q_{\text{con}} = f'(m,n)/f(m,n)$, after the application of a Gaussian filter and a 1st and 2nd order Butterworth filter as a function of the ratio between the cut length, $n_\lambda \lambda$, over the region size, G_{FWHM}, from experimental datasets (solid coloured lines) and from fits to this data with a functional form shown in Equation 2.31 (dotted and dashed lines). It can be seen that the 2nd order Butterworth filter offers the steepest response curve of those considered, followed by the Gaussian and 1st order Butterworth respectively.

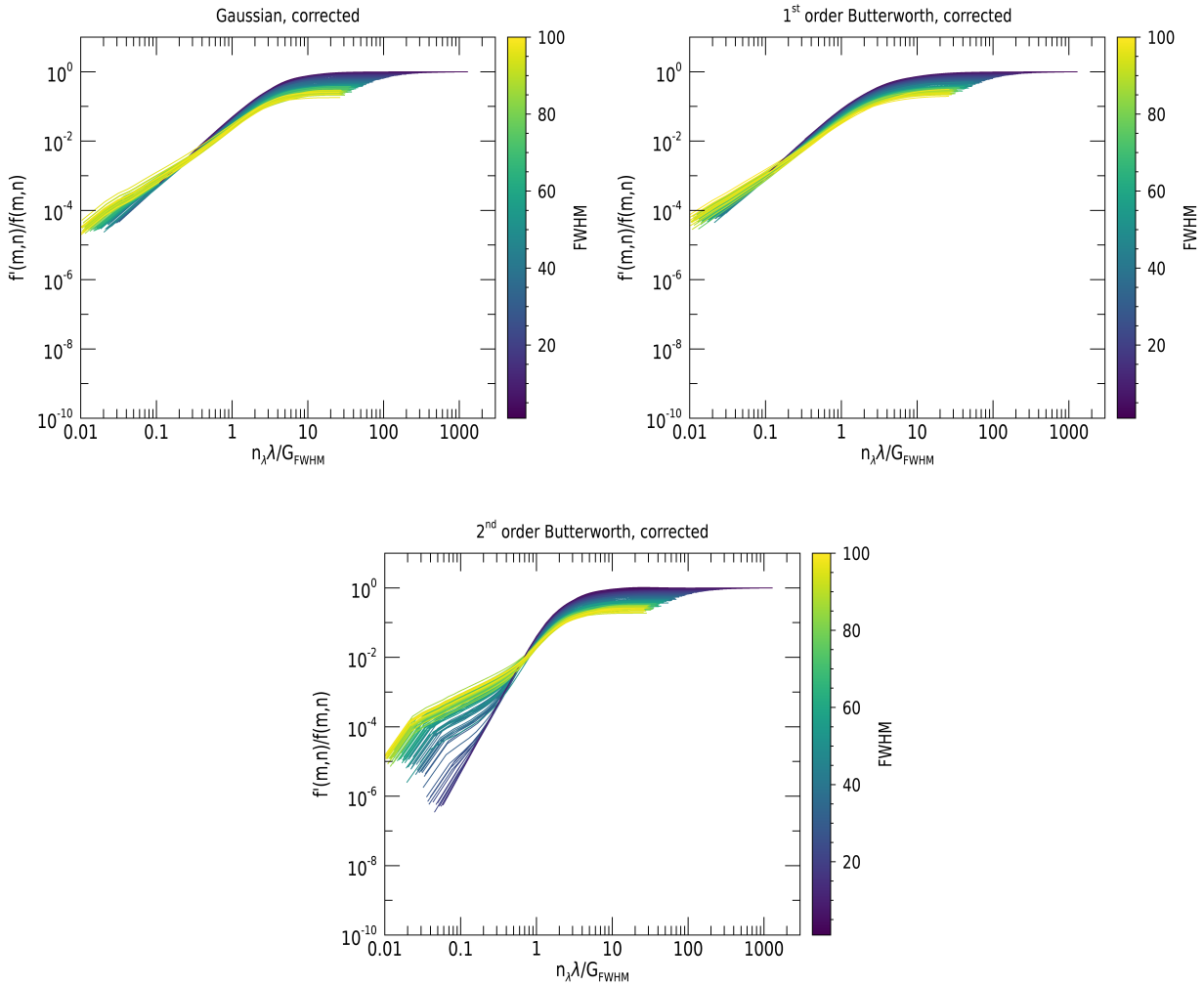

Figure 2.12: The fraction of flux remaining in an image containing multiple Gaussian functions of uniform FWHM after the application of a Gaussian filter (top left), a 1st order Butterworth filter (top right) a 2nd order Butterworth filter (bottom) against $n_\lambda \lambda / G_{\mathrm{FWHM}}$. In contrast to the case with only a single Gaussian region, shown in Figures 2.9 and 2.10, where tight relationships are obtained, there is still a significant trend of the remaining flux with FWHM, due to the increasing amount of overlap between regions with increasing region size.

Table 2.4: The best fitting parameters for the sigmoidal function the flux loss from a single Gaussian region due to application of a filter in Fourier space, $q_{\rm con}$ (see equation 2.31), fitted to the response curves of the Gaussian and 1st and 2nd order Butterworth filters (shown in Figures 2.9 and 2.10).

Parameter	Gaussian	1st order BW	2nd order BW
a	-0.016	-0.038	0.0019
b	1.69	1.30	2.38
c	4.86	4.45	3.43

BW = Butterworth

or equal to 100 per cent of the original flux. Between the two, the Gaussian filter offers a steeper response curve that removes less flux from the compact regions than the 1st order Butterworth filter. Butterworth filters of 2nd order and greater offer a significantly steeper response curve than the Gaussian filter and thus remove less flux from the compact regions than the Gaussian filter. However, due to introduced distortions, application of the filter does not necessarily result in an image that has $\leqslant 100$ per cent of the flux of the original image. As the Gaussian filter shows few distortions we chose to focus on this filter for the remainder of our analysis.

We can now correct the measured value of $f_{\rm compact}$ for the lost emission from a single Gaussian region as follows:

$$f_{\rm compact} = \frac{1}{q_{\rm con}} \frac{\sum_{m,n} f'(m,n)}{\sum_{m,n} f(m,n)}. \tag{2.32}$$

2.6.2 Flux loss for a set of overlapping Gaussian regions

Astronomical images do not consist of only single isolated Gaussian functions. Instead, there are a number of overlapping regions distributed within each image. As Figure 2.12 demonstrates, in the case of an image made up of a field of multiple Gaussian functions, we no longer recover a simple analytical relationship between the remaining flux fraction, $q_{\rm con}$, and $n_\lambda \lambda / G_{\rm FWHM}$. We can characterise the effect of overlap between regions in terms of in terms of the evolutionary phase lifetime adjusted filling factor, η, which we define as:

$$\eta_{\rm stars} = \sqrt{\frac{t_{\rm star}}{\tau}} \zeta_{\rm star} = \sqrt{\frac{t_{\rm star}}{\tau}} \frac{G_{\rm FWHM,star}/\sqrt{2\ln 2}}{\lambda}, \tag{2.33}$$

for the stellar map, and

$$\eta_{\rm gas} = \sqrt{\frac{t_{\rm gas}}{\tau}} \zeta_{\rm gas} = \sqrt{\frac{t_{\rm gas}}{\tau}} \frac{G_{\rm FWHM,gas}/\sqrt{2\ln 2}}{\lambda}, \tag{2.34}$$

for the gas map, where $\tau = t_{\rm star} + t_{\rm gas} - t_{\rm over}$ is the total duration of evolutionary timeline. Thus, η is given by the global filling factor, ζ,[14] multiplied by $\sqrt{t_{\rm star}/\tau}$ and $\sqrt{t_{\rm gas}/\tau}$ for the stellar and gas maps, respectively, in order to weight the global filling factor by the number of regions in each of the two tracer maps, as expected from the evolutionary timeline.

[14] For the definition of this filling factor, see Equations 2.23 and 2.24.

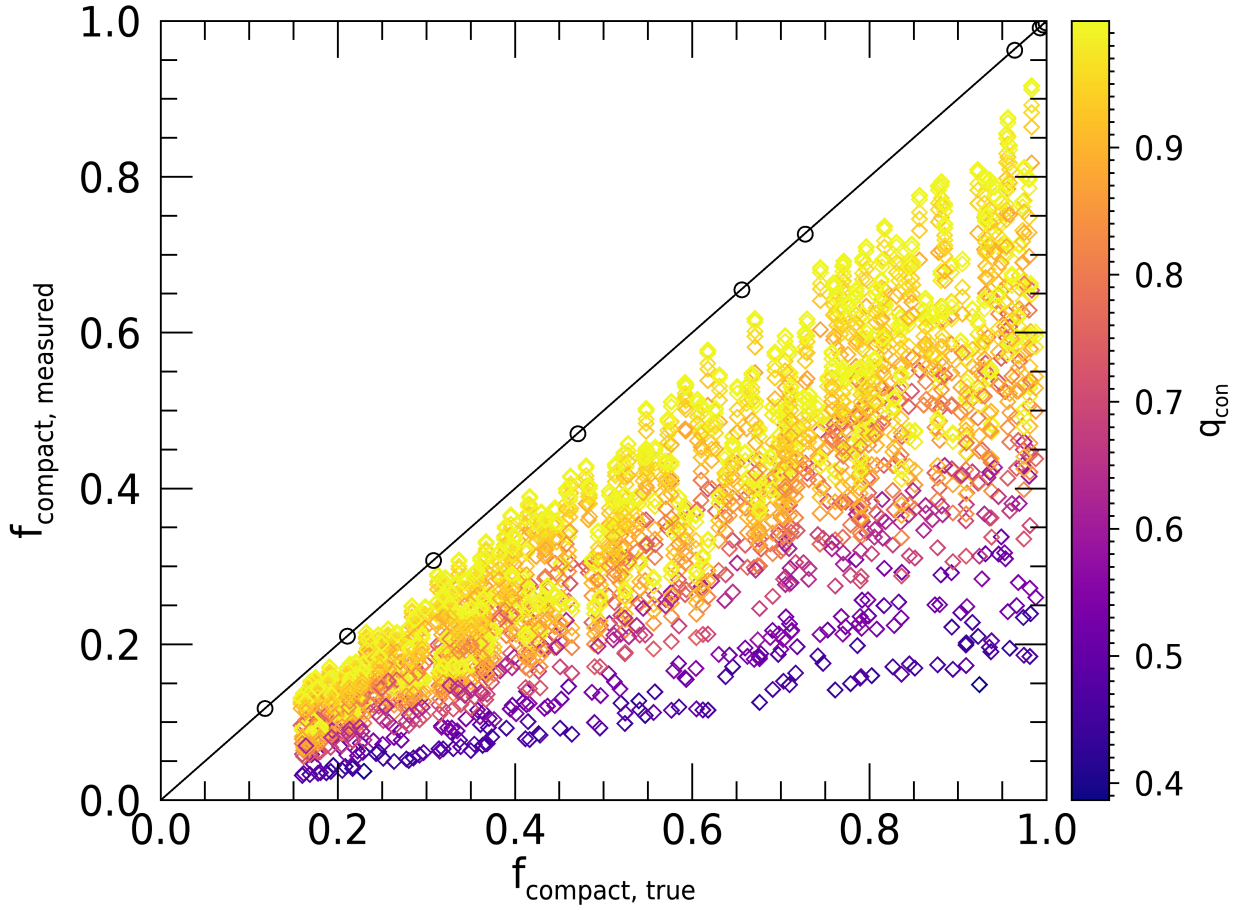

Figure 2.13: The value of the fraction of emission in an image that is compact, f_{compact}, measured with the application of a Gaussian filter, against the true value for a number of images. The solid black line shows the 1:1 relationship between these two quantities. The black circles show the results from generated map sets where compact regions are simulated with single-pixel points. In this case, there is no effect on $f_{\text{compact,measured}}$ from increasing amounts of the wings of compact regions overlapping with increasing η or of flux loss from spatially extended regions and we recover $f_{\text{compact,true}}$ without needing to apply any corrections to the measured result. The coloured diamonds show results from generated map sets where compact regions are simulated with Gaussian Functions. The diamonds are coloured by the calculated value of q_{con}, as calculated from equation 2.31 with the appropriate values of $n_\lambda \lambda$ and G_{FWHM}.

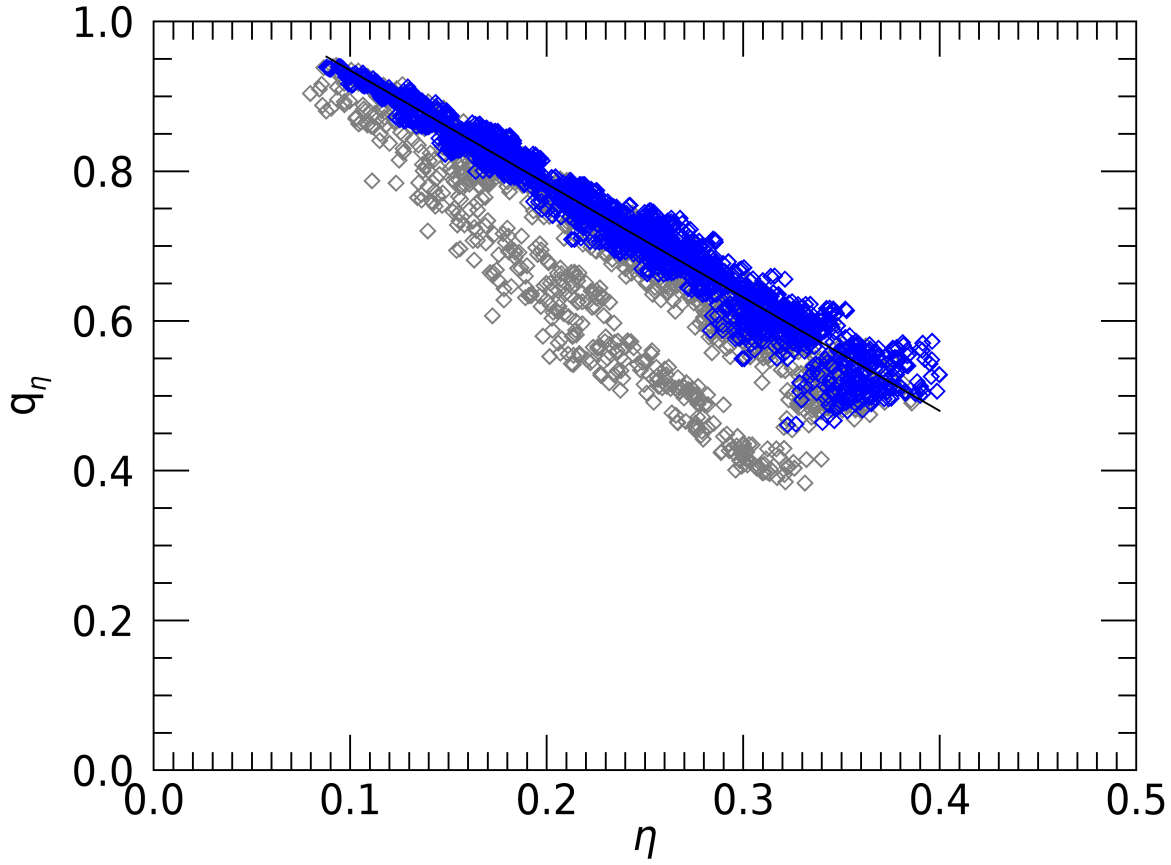

Figure 2.14: The ratio of $f_{\text{compact,measured}}$ to $f_{\text{compact,true}}$ for the same set of experiments as in Figure 2.13 after the application of the correction factor, q_{con}, against the tracer map filling factor, η. Blue diamonds correspond to experiments that satisfy the criterion $q_{\text{con}} \geqslant 0.9$, whereas grey points do not. The solid black line shows the best-fitting line to the blue points, which is used to calibrate the correction factor q_η.

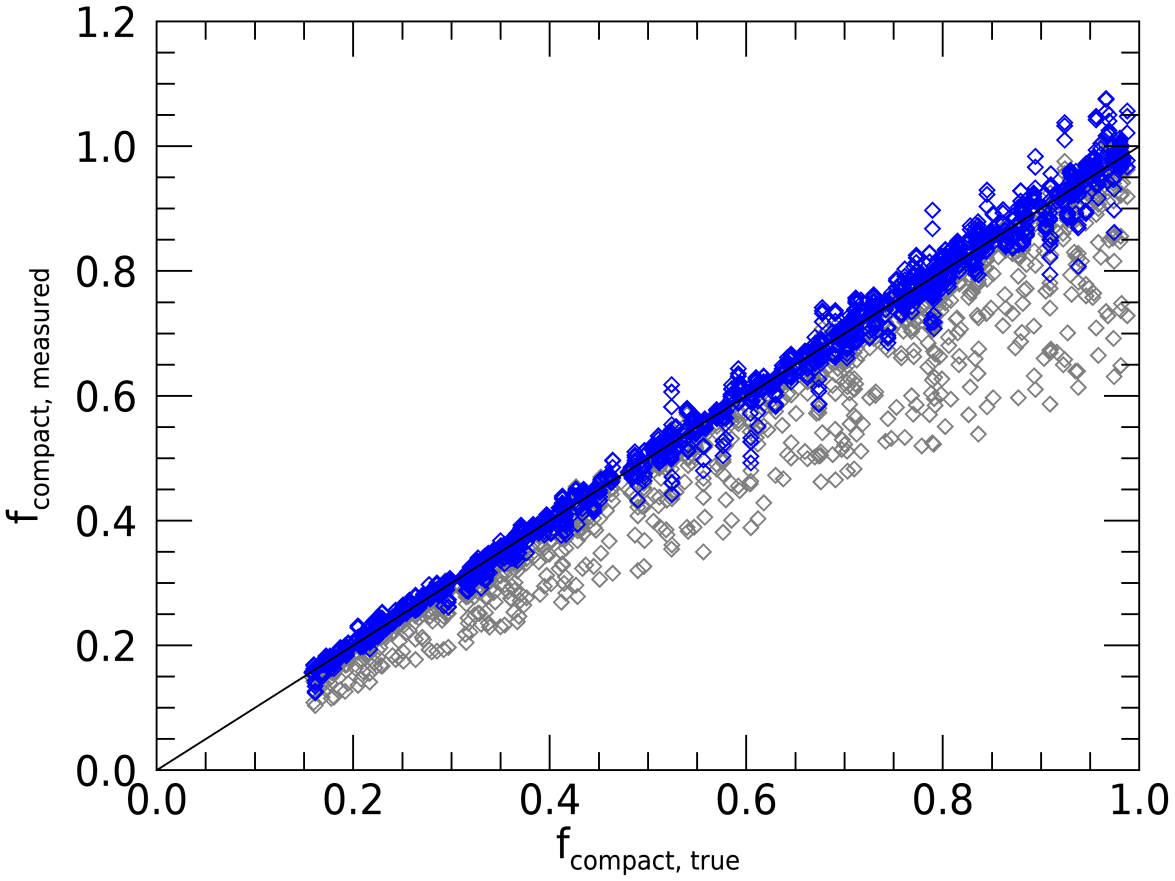

Figure 2.15: The measured compact emission fraction, f_{compact}, for the same set of experiments as in Figure 2.13 after the application of the correction factors q_{con} and q_{η} against the true value of f_{compact}. Blue diamonds correspond to experiments that satisfy the criterion $q_{\text{con}} \geqslant 0.9$, whereas grey points do not. The solid black line indicates the 1:1 relationship between $f_{\text{compact,measured}}$ and $f_{\text{compact,true}}$. It can be seen that $f_{\text{compact,measured}}$ is well-correlated with $f_{\text{compact,true}}$ after correction by q_{con} and q_{η}, with the correlation somewhat worse for experiments where $q_{\text{con}} < 0.9$ (grey diamonds).

Table 2.5: A summary of the properties of the experiment sets used in Section 2.6 (q_η points and q_η Gaussians) and in Section 2.7 (Main set 1 and Main set 2). For a full explanation of these properties see Section 2.5

	Value range				
Parameter	q_η points	q_η Gaussians	Main set 1	Main set 2	Origin
ζ	N/A[a]	$0.2-0.5$	$0.2-0.7$	$0.2-0.7$	input
G_{FWHM}	N/A[a]	$63-135$ pc[b]	$45-99$ pc[b]	$45-99$ pc[b]	input
$N_{\mathrm{peak,star,input}}$	250	$100-400$	200	$0-120$	input
$N_{\mathrm{peak,gas,input}}$	250	$100-1000$	$100-1200$	$540-1200$	input
$N_{\mathrm{peak,over,input}}$	100	$100-200$	$0-400$	$120-N_{\mathrm{peak,star,input}}$	input
f_{compact}	$12-100\%$	$15-100\%$	$10-100\%$	$10-100\%$	input
t_{star}	10 Myr	10 Myr	10 Myr	10 Myr	Equation 2.21
t_{gas}	10 Myr	$10-50$ Myr	$5-60$ Myr	$45-100$ Myr	Equation 2.21
t_{over}	2.9 Myr	$2.9-5$ Myr	$0-10$ Myr	$0-10$ Myr	Equation 2.22
λ	177 pc[b,c]	$107-573$ pc[b]	$55-420$ pc[b]	$55-420$ pc[b]	Equation 2.23

[a] The definitions of ζ and G_{FWHM} do not apply to single pixel regions
[b] For all quantities in units of pc we have applied a pixel length scale of $l_{\mathrm{pix}} = 9$pc
[c] For images containing point sources, we calculate lambda with equation 2.25 by specifying the image size $N_{\mathrm{pix},x}$

We generate a set of simulated datasets with single pixel compact regions and a constant background to serve as a control dataset ('q_η points'). As point sources are not extended in space, we expect no flux loss from the compact regions after the application of a filter in Fourier space (i.e. $q_\eta = 1$ and $q_{\mathrm{con}} = 1$). For Gaussian compact regions ('q_η Gaussians'), we do expect flux loss due to overlapping regions. For all of these datasets, we set $t_{\mathrm{star}} = 10$Myr. The value of f_{compact} is randomly selected to be between 15 per cent and 100 per cent of the total flux in each image.

We generate these datasets such that they satisfy the criteria for accurate application of the Heisenberg code summarised in Section 2.2. In particular, we generate our datasets such that there is a minimum of 200 peaks in each image. As we will use this dataset to fit for an empirical relationship between q_η and η, we ensure good performance of the Heisenberg code by considering a restricted range of t_{gas}, i.e. 10-50 Myr. Detailed testing of the Heisenberg code by Kruijssen et al. (2018) shows that the condition $\zeta < 0.5$ should be satisfied to minimise the impact of blending between compact regions for accurate measurements to be obtained from the code. We therefore ensure that blending between compact regions is a small effect by choosing values up to the maximum recommended filling factor $\zeta < 0.5$ (i.e. $\zeta = 0.2, 0.3, 0.4, 0.5$). A summary of the parameters used to generate these datasets is given in Table 2.5. For a full description of the method used to generate these images see Section 2.5.

Figure 2.13 shows the measured value of the image compact emission fraction against the true compact emission fraction, measured according to equation 2.11 with the application of Gaussian filters with varying values of $n_\lambda \lambda$. This figure illustrates how, for images where the compact regions are single pixels, the true value of the compact emission fraction is recovered with equation 2.11. However, for those images where the compact regions are extended Gaussians, the true value is not accurately recovered.

We correct these measurements for the flux loss from a single Gaussian, q_{con}. The resulting measurements of f_{compact} (according to Equation 2.32) are shown in Figure 2.14 as a function of η. It can be seen that, while the spread in measured values has been greatly reduced, we do not yet

Table 2.6: The best fitting parameters for the fitting function for flux-loss in compact regions due to overlap between regions for the Gaussian filter, q_η (see equation 2.35)

Parameter	Gaussian
A	-1.52
B	1.09

recover the true values of f_{compact} and that $f_{\text{compact,measured}}/f_{\text{compact,true}}$ decreases with increasing η.

We then calibrate an empirical relationship between η and the ratio of the measured flux fraction to the true flux fraction, after the flux fraction has been corrected for the flux lost from a single Gaussian region. We adopt a critical value of $q_{\text{con}} = 0.9$, because, as can be seen in the right hand panel of Figure 2.9, a small uncertainty in the measurement of $n_\lambda \lambda / G_{\text{FWHM}}$ leads to a small uncertainty in the measured value of q_{con} above this threshold. By contrast, a small measurement uncertainty in $n_\lambda \lambda / G_{\text{FWHM}}$ below this threshold leads to a large uncertainty in q_{con}, making this correction unreliable. Indeed, the experiments with $q_{\text{con}} > 0.9$ display a clear relation with η in Figure 2.14, because they represent cases for which a small fraction of the compact emission is filtered out. We fit a linear relationship between the flux loss due to overlap, q_η, and the evolutionary timeline normalised filling factor, η, truncated such that q_η may never be greater than unity:

$$q_\eta = \min(A\eta + B, 1). \tag{2.35}$$

The best-fitting slope and intercept for the Gaussian filter are listed in Table 2.6 and is plotted in Figure 2.14.

Thus applying this empirical correction in addition to the correction for the flux lost from a single Gaussian region, the final measurement of the compact emission fraction, f_{compact}, in an image, $f(m,n)$ is:

$$f_{\text{compact}} = \frac{1}{q_{\text{con}} q_\eta} \frac{\sum_{m,n} f'(m,n)}{\sum_{m,n} f(m,n)}. \tag{2.36}$$

The original measurements shown in Figure 2.13 are shown with these corrections applied in Figure 2.15. The true value of f_{compact} is then recovered, with some scatter for those cases where $q_{\text{con}} \geq 0.9$. For cases where $q_{\text{con}} \leq 0.9$, the scatter on the measured value of f_{compact} increases. In addition, due to the impact of a tight Fourier filter on the compact regions, the measured value of G_{FWHM} is decreased after filtering, leading to a systematic underestimate of the corrective factor that should be applied. This leads to a systematic bias in the measurement of f_{compact} for $q_{\text{con}} \leq 0.9$. For this reason we recommend the choice of the filtering-to-region separation length scale ratio, n_λ, such that $q_{\text{con}} \geq 0.9$. q_{con} depends on G_{FWHM}, which corresponds to the region size if the region is resolved or to the image PSF size if they are barely resolved or unresolved. Lower image resolution that smooths out the regions will therefore permit less tight filtering. We can quantify this recommendation for n_λ in terms of the region filling factor, ζ, by substituting equations 2.23 and 2.24 into equation 2.31 for q_{con} and rearranging for n_λ:

$$n_\lambda = \sqrt{2 \ln 2}\ \zeta_{\text{max}}\ c \left(\frac{q_{\text{con}} - a}{q_{\text{con},\infty} - q_{\text{con}}} \right)^{\frac{1}{b}}, \tag{2.37}$$

where $\zeta_{\rm max} = \max(\zeta_{\rm star}, \zeta_{\rm gas})$ is the maximal filling factor for the pair of gas and stellar maps. For the Gaussian filter (recall that values of the fitting parameters, a, b and c are shown in Table 2.4) at the maximally recommended value of the filling factor ($\zeta = 0.5$, from testing by Kruijssen et al. 2018) and given our recommendation that $q_{\rm con} \geq 0.9$ we would therefore recommend $n_\lambda \geqslant 15$. For a lower value of the filling factor ($\zeta = 0.2$) this equation implies a recommendation of $n_\lambda \geqslant 6$, allowing much tighter filtering. In the case that one wishes to filter out wavelengths shorter than allowed given these recommendations, a sharper filter, such as a second order Butterworth filter may be considered.

We note that we have modelled the compact regions as Gaussian (see Section 2.5), while it is well-known that star-forming regions (such as molecular clouds in CO and HII regions in Hα observations) exhibit complex and structured shapes when observed at high resolution. This is justified, due to the intent to apply the method to extragalactic observations at spatial resolutions (observational or convolved) of tens of parsecs, where complex structure in star forming regions is blurred out by the beam, resulting in maps containing approximately Gaussian regions (see e.g. Pety et al., 2013; Druard et al., 2014, for state-of-the-art CO observations of M51 and M33 at such resolutions, respectively). At higher spatial resolution (less than a few parsecs), the assumption of Gaussianity for the regions will no longer hold. However, the resolved structure of star forming regions encodes information about the internal evolution of the regions that is not necessary for the application of the HEISENBERG code. Indeed, in order to measure the lifecycle of the regions themselves rather than their internal substructure, the method is ideally applied at resolutions where this substructure is not resolved.

2.7 Testing and validation

We now test the performance of the method at separating diffuse and compact emission in the generated images. We test this performance with regards to the recovered values of the three key fitting parameters of the HEISENBERG code: the gas cloud lifetime, $t_{\rm gas}$, the region overlap timescale, $t_{\rm over}$, and the mean separation length λ, and the image compact emission fraction, $f_{\rm compact}$.

We test the method on two test datasets, 'Main set 1', for short to intermediate values of $t_{\rm gas}$ and 'Main set 2', for intermediate to long values of $t_{\rm gas}$. We make this division for computational reasons. In our simulated datasets, increasing the value of $t_{\rm gas}$ leads to an increase in the size of the maps in the datasets (see Equation 2.25). In order to run datasets with large values of $t_{\rm gas}$ in a reasonable time, we reduce the number of Gaussian regions seeded into our reference stellar map (see Table 2.2) and thus the required number of Gaussian regions in the gas maps, leading to a reduction in the overall size of the maps. For these datasets, we set the reference timescale to 10 Myr. (i.e. $t_{\rm star} = 10$Myr). We consider a range of $t_{\rm gas}$ between 5 Myr and 100 Myr (i.e. $0.5 - 10\ t_{\rm star}$). For $t_{\rm over}$, the range of possible values for a dataset is between 0 Myr and the minimum of $t_{\rm gas}$ and $t_{\rm star}$ (i.e. $0\,{\rm Myr} - \min(t_{\rm gas}, 10\,{\rm Myr})$). Initial applications of HEISENBERG to nearby galaxies that are currently being undertaken (Kruijssen et al., 2019; Hygate et al., 2019; Chevance et al., 2019; Ward et al., 2020) have measured values of ζ between ~ 0.2 and ~ 0.6. We will thus consider values of ζ over a suitable range (i.e. $\zeta = 0.2, 0.3, 0.4, 0.5, 0.6$ and 0.7). We note, however, that detailed testing of the HEISENBERG code by Kruijssen et al. (2018) shows that the condition $\zeta < 0.5$ should be satisfied for good performance of the HEISENBERG code. For this reason, we focus our analysis on those experiments with $\zeta \leqslant 0.5$, keeping experiments with $\zeta = 0.5$ as borderline cases. We otherwise ensure that the generated datasets conform to the criteria for accurate application of the HEISENBERG code summarised in Section 2.2.

Together, the selected evolutionary timelines and values of ζ translate to a range of λ between 55 pc for datasets with the highest value of the filling factor ($\zeta = 0.7$), and 420 pc for datasets with the

Table 2.7: The plotting symbols used in Figures 2.16 and 2.17 for each combination of compact and diffuse models.

	Diffuse Model			
Compact Model	none	constant	large Gaussian	envelopes
Uniform FWHM	◇	◇	◇	◇
Asymmetric FWHM	○	○	○	○
Spread FWHM	□	□	□	□
Flux spread FWHM	△	△	△	△

Experiments with unsatisfactory filling factor ($\zeta > 0.5$) are displayed as grey hexagons (⬡) regardless of the combination of diffuse and compact model

lowest value of the filling factor ($\zeta = 0.2$). For all images, the compact emission fraction, f_{compact}, can vary between 10 per cent and 100 per cent. For each combination of compact region model (detailed in Section 2.5.1) and diffuse model (detailed in Section 2.5.2) and each considered value of the filling factor, ζ, we generate 100 experiment datasets (50 each for main dataset 1 and main dataset 2).[15] For main dataset 1 and main dataset 2, we generate 50 gas and stellar map pairs, for each combination of compact region model and each considered value of the filling factor, ζ.

This equates to a total of 100 experiments for each combination ζ.[16] For each map pair, we select a randomised evolutionary timeline, where t_{gas} may vary between 5 **Myr** and 100 **Myr** (i.e. $0.5-10\ t_{\text{star}}$) and t_{over} may vary between 0 **Myr** and the minimum of t_{gas} and t_{star} (i.e. $0\,\text{Myr} - \min(t_{\text{gas}}, 10\,\text{Myr})$). The value of f_{compact} is randomly selected to be between 10 per cent and 100 per cent of the total flux of the image. For full details on the generation of experiment datasets see Section 2.5 and for the full set of parameters used in this generation see Table 2.5.

A summary of the measured quantities for these experiments, both before and after filtering, is shown in Figure 2.16 for t_{gas}, t_{over} and λ and in Figure 2.17, for f_{compact}. Experiments with unsatisfactory values of the filing factor ($\zeta = 0.6, 0.7$) are shown as grey hexagons and those with satisfactory filling factor ($\zeta \leqslant 0.5$) are shown as coloured symbols. A key to the plotting symbols used for each combination of compact and diffuse model is shown in Table 2.7. A summary of the measured quantities for these experiments, both before and after filtering, is shown in Figure 2.16 for t_{gas}, t_{over} and λ and in Figure 2.17, for f_{compact}.

For experiments with no added diffuse reservoir, we recover values of these quantities close to the correct values both before and after Fourier filtering. For f_{compact} this is unity, due to there being no diffuse reservoir in the images. This indicates that the distortions introduced into the images do not significantly affect the total flux of the image or the correct identification of peaks (i.e. only few spurious peaks are introduced into the image by filtering) and thus in turn the measurement of these quantities. However, the addition of diffuse reservoirs does significantly affect the measured values of the quantities in the unfiltered images. After Fourier filtering, and the removal of the diffuse reservoir, we again measure values of these quantities that are close to the true values. The distribution of the recovered quantities is also not significantly different between experiments with added diffuse emission and without, with the exception of the measured compact emission fraction, which is ~ 1 for all the experiments without an added diffuse background. Indeed, for measurements of t_{gas}, t_{over} and λ from simulated datasets that differ only in their randomly added diffuse background or lack thereof, we find that after filtering we often measure values that are not only close to the true value, but also close to the value measured with the HEISENBERG code on

[15] For f_{compact}, this equates to 200 measurements per combination as we make a measurement of the compact fraction in the stellar map and the gas map of each experiment dataset.

[16] For f_{compact}, this equates to 200 measurements per combination as we make a measurement of the compact fraction in the stellar map and the gas map of each experiment map pair.

the dataset without added diffuse emission. This can be seen as overlapping, differently-coloured points in Figure 2.16.

We do find a number of other elements that can bias the measurements. For instance, the measurement of $t_{\rm gas}$ is less accurate for more dissimilar $t_{\rm star}$ and $t_{\rm gas}$, as described in Kruijssen et al. (2018). For $t_{\rm over}$, we note that the overdensity of points in the middle left panel in Figure 2.16 (at $t_{\rm over,measured} = 10\,{\rm Myr}$) is due to the fact that in all cases $t_{\rm over} \leq \min(t_{\rm star}, t_{\rm gas})$, because it is physically impossible for regions to coexist with other regions for a time longer than their own lifetime (and $t_{\rm star} = 10$ Myr for all of our experiments).[17] Following the guideline that $t_{\rm over}$ should be greater than 5 per cent of the total evolutionary timeline duration, τ, (Kruijssen et al., 2018), we do not display measurements of $t_{\rm over}$ before or after filtering from datasets that do not fulfil this criterion after filtering. We note that applying this cut to measurements of $t_{\rm over}$ obtained before filtering would remove some datasets where $t_{\rm over}$ is underestimated, but would not alter our conclusion that the presence of a diffuse reservoir introduces a large scatter in the measurement of $t_{\rm over}$ before filtering that is strongly reduced after filtering.

For λ, we note that our prediction, as given in equation 2.25, systematically overestimates the values measured in our experiments, by ~ 10 per cent (see the bottom right panel of Figure 2.16). As there is no significant offset between the values of λ measured for experiments without added diffuse emission both before and after filtering we conclude that this is not an offset introduced by Fourier filtering. Instead this discrepancy is due to the geometric mean separation between regions that we calculate being an overestimate of the actual local mean separation of the regions. After all, the scatter introduced by the random positioning of the peaks causes them more often than not to be positioned closer to their near neighbours than the geometric mean separation length. This slight overestimation of λ propagates into a corresponding, minor underestimation of the compact emission fraction in Figure 2.17.

For those datasets with unsatisfactory values of the filling factor (i.e. $\zeta = 0.6, 0.7$), indicated as grey hexagons in Figures 2.16 and 2.17, the accuracy of the measurements decreases for larger values of $t_{\rm gas}$. As the amount of blending in an individual tracer map ($\eta_{\rm stars}$ and $\eta_{\rm gas}$, see Equations 2.33 and 2.34) scales with the lifetime of that particular tracer in units of the total duration of the timeline, the effect of blending in both maps is roughly equal when $t_{\rm gas} \sim t_{\rm star}$. However, as $t_{\rm gas}$ increases, $\eta_{\rm gas}$ increases too (while $\eta_{\rm stars}$ decreases due to the increase of the total duration of the timeline), leading to more severe blending in the gas map and more inaccurate results overall.

In summary, we see that the filtering method performs well regardless of the compact region model used, with no significant difference between the scatter of measured values between the different models after filtering. With respect to the diffuse background models, successful filtering of the constant diffuse model and the Gaussian diffuse model is relatively insensitive to the value of the filtering-to-region separation length scale ratio, n_λ, chosen, due to the fact that a constant sheet of diffuse gas and a galaxy-scale Gaussian correspond to infinite and very large spatial wavelengths, respectively, whereas λ is typically much smaller than a galactic radius. Galaxies with radii ~ 10 kpc have a typical region separation length $\lambda \sim 100$ pc (as measured from initial applications of the method: Kruijssen et al. 2019; Hygate et al. 2019; Chevance et al. 2019; and Ward et al. 2020), giving a factor of ~ 100 in size between the two. Thus the value of n_λ selected is relatively unimportant with regards to the filtering of galactic-scale components of diffuse emission. By contrast, the envelope diffuse model requires filtering with lower values of n_λ, because the modelled envelopes are much closer in size to λ. Figure 2.18 shows how the performance of the method at removing each of these diffuse models varies with the chosen value of n_λ. This summarises the above discussion, i.e. the value of n_λ does not affect the filtering of galactic-scale emission, but in order to accurately filter diffuse envelopes of regions, we require $n_\lambda < 30\,{\rm FWHM_{envelope}}/\lambda$. The

[17] In a minority of experiments, $t_{\rm gas}$ is shorter than $t_{\rm star}$. In this case, $t_{\rm gas}$ sets the upper limit for $t_{\rm over}$

criterion is easily satisfied, as in practice one would expect $\mathrm{FWHM}_{\mathrm{envelope}} \sim \lambda$ and the resulting $n_\lambda < 30$ is a very generous condition.

Overall, we are able to accurately constrain the cloud lifecycle (t_{gas} and t_{over}), the cloud separation length (λ) and the diffuse and compact emission fractions after filtering the diffuse emission in Fourier space, regardless of the significance of the added diffuse emission. We are able to do this for all of the compact region models and diffuse emission region models that we consider.

Finally, we note that the results presented in this section are based upon idealised datasets that contain no noise and are perfectly aligned in astrometry. In reality tracer maps will contain observational noise and two different tracer maps may be astrometrically offset from each other. We detail the impact that these two observational limitations have on the method in Appendix 2.9. In Appendix 2.9.1, we show that astronometric uncertainty less than one third compact region FWHM (i.e $\leqslant G_{\mathrm{FWHM}}/3$) must be achieved for meaningful constraints of t_{over} and in Appendix 2.9.2 we show that the use of low or intermediate signal to noise data will lead to biased results, unless a method to reduce the noise is used.

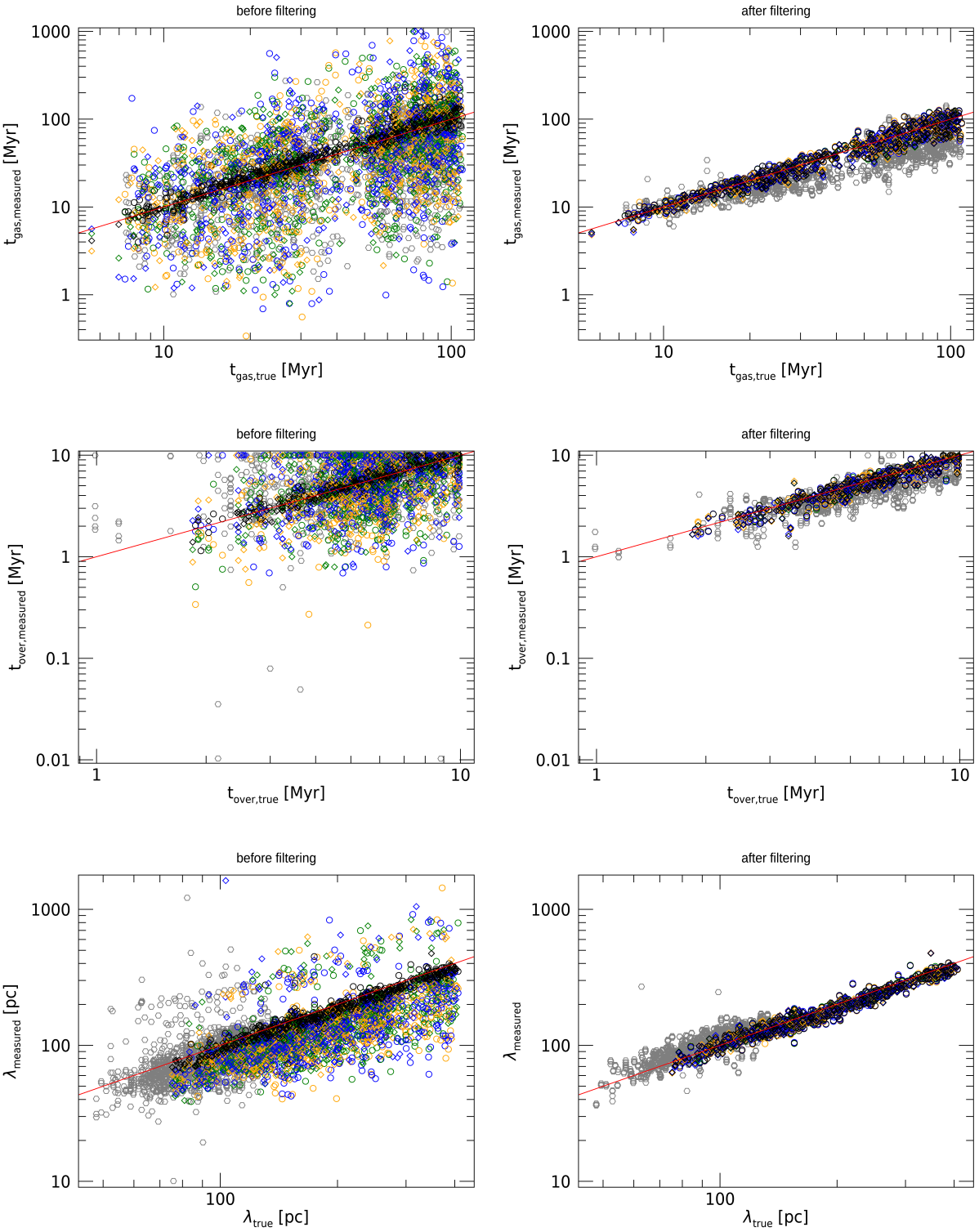

Figure 2.16: The measured values of t_{gas} (top row), t_{over} (middle row) and λ (bottom row) against the true value before filtering diffuse emission in Fourier space (left column) and after filtering (right column). The red line shows the 1:1 relation between the true and measured values for each of the quantities. Each combination of compact model and diffuse model is shown with a different symbol/colour combination, which we summarise in Table 2.7. Experiments not meeting the filling factor criterion for the HEISENBERG code (i.e $\zeta > 0.5$) are shown as grey hexagons. This figure shows that a diffuse emission reservoir can significantly affect the measured values of these quantities and that the application of the presented Fourier filtering results in a much more accurate measurement.

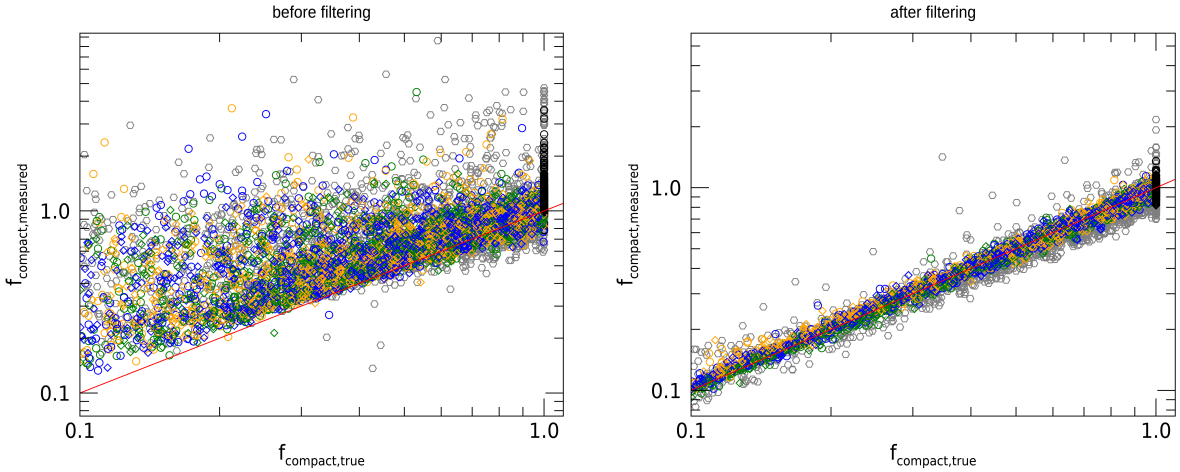

Figure 2.17: The measured compact emission fraction, $f_{\mathrm{compact,measured}}$, against the true compact emission fraction, $f_{\mathrm{compact,true}}$. Each combination of compact model and diffuse model is shown with a different symbol/colour combination, which we summarise in Table 2.7. Experiments not meeting the filling factor criterion for the HEISENBERG code (i.e $\zeta > 0.5$) are shown as grey hexagons. Left panel: values of $f_{\mathrm{compact,measured}}$ calculated on the basis of the value of λ measured on the unfiltered map (i.e. at the end of the first iteration). Right panel: values of $f_{\mathrm{compact,measured}}$ calculated at the end of the iterative filtering process after the measured value of λ has converged. After convergence, we recover values of $f_{\mathrm{compact,measured}}$ that are tightly correlated around the 1:1 line with $f_{\mathrm{compact,true}}$.

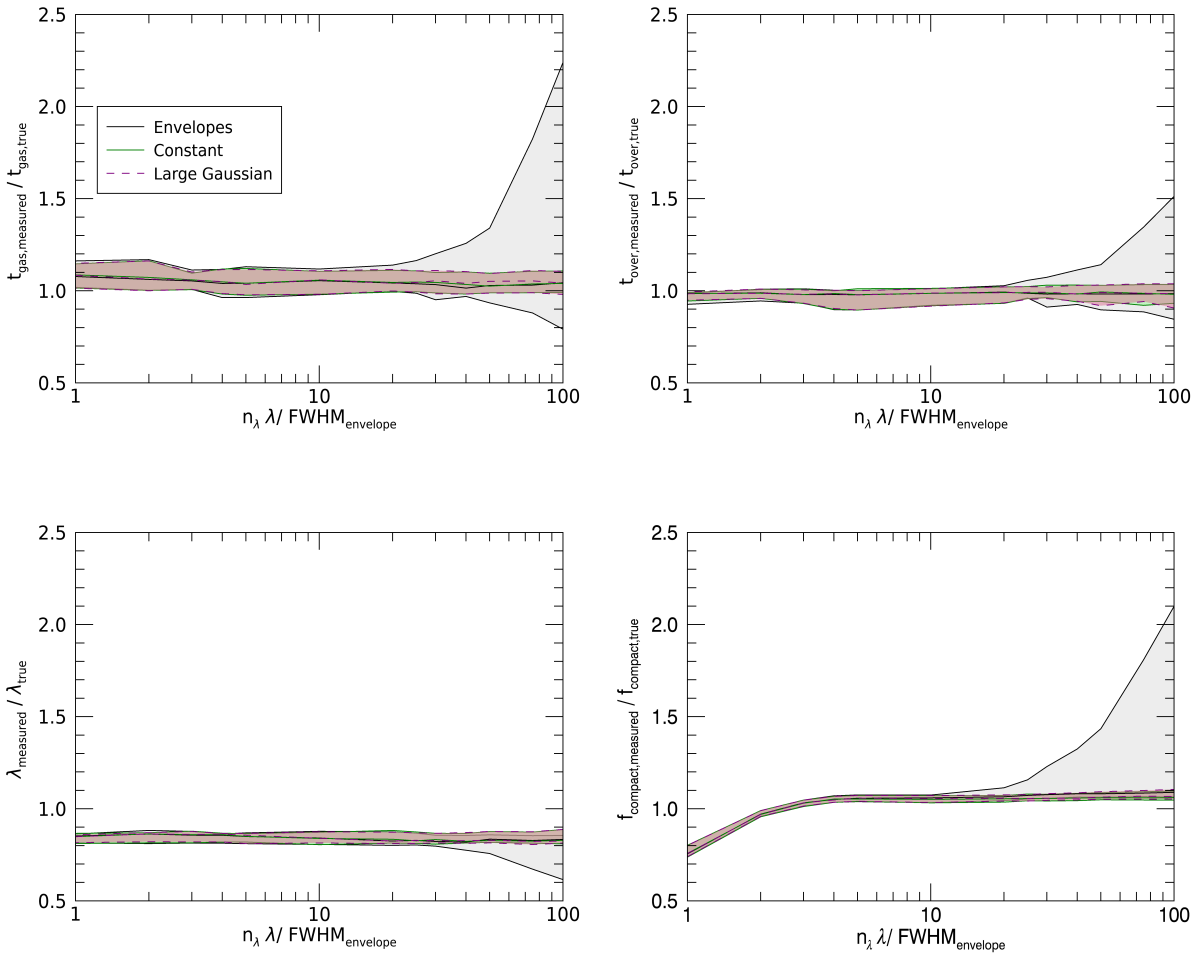

Figure 2.18: Measured values in units of the true value of $t_{\rm gas}$ (top left), $t_{\rm over}$ (top right), λ (bottom left), and $f_{\rm compact}$ (bottom right) against the ratio of the critical length scale of the applied highpass filter normalised by the FWHM of the diffuse envelope, $n_\lambda \lambda / \mathrm{FWHM}_{\rm envelope}$. Shaded regions show the 1σ region of measurements around the median for an example set of 10 image pairs with constant diffuse background (green), large-scale Gaussian background (purple) and envelope only (i.e. containing envelopes around the compact regions, but no constant or large-scale Gaussian background) background (grey). Both the constant and large-scale Gaussian backgrounds are well-removed across the entire considered range of the filtering-to-region separation length scale ratio, n_λ. By contrast, the measurement scatter for the envelope-only model increases significantly at $n_\lambda > 30\,\mathrm{FWHM}_{\rm envelope}/\lambda$, where the applied filter has not sufficiently removed the diffuse background. At $n_\lambda < 3\,\mathrm{FWHM}_{\rm envelope}/\lambda$, the measured value of $f_{\rm compact}$ is affected by the introduction of distortions to the image and the large amount of flux being removed from the compact regions. Due to the tight Fourier filters applied in this regime, the recommendation that $q_{\rm con} < 0.9$ has been violated and $G_{\rm FWHM}$ is systematically underestimated, leading to a systematic underestimate of $f_{\rm compact}$ (see Section 2.6)

2.8 Conclusions

We have presented a physically motivated method for the filtering and measurement of diffuse emission (such as the diffuse Warm Ionised Medium that is observed in Hα along with compact HII regions) in images by filtering in Fourier space. We have validated our method's performance within the HEISENBERG code (Kruijssen et al., 2018) by testing for the accurate recovery of the three key fitting-parameters measured by the HEISENBERG code ($t_{\rm gas}$, $t_{\rm over}$ and λ). These tests are based on a range of models of compact regions and diffuse backgrounds, as detailed in Section 2.5. We demonstrate that the presence of diffuse emission can have a significant impact on the measurement of the measured cloud-scale quantities, but also demonstrate that our filtering method accurately alleviates this problem. A summary of these tests can be seen in Figure 2.16. We have also validated its performance for measuring the fractions of diffuse and compact emission within tracer maps, which is summarised in Figure 2.17. Finally, we report a number of criteria that need to be satisfied for the reliable application of the method, which we summarise here:

- The observed compact regions need to be sufficiently resolved ($G_{\rm FWHM} \geqslant 2$ pixels) or to be point sources.
- The value of the filtering-to-region separation length scale ratio, n_λ, should be chosen such that the flux-loss from compact regions due to the application of the Fourier filter is minimised, i.e. $q_{\rm con} \geqslant 0.9$. The resolution of the map will restrict the available choice of n_λ. Equation 2.37 quantifies the minimal recommended value of n_λ in terms of the region filling factor, ζ. By reference to Figure 2.18, it is possible to determine whether this value of n_λ is sufficient to remove the diffuse emission.
- For meaningful constraints on the value of $t_{\rm over}$, the astrometric uncertainty between images should be less than one third the FWHM of the regions of interest (i.e $\leqslant G_{\rm FWHM}/3$), see Appendix 2.9.1.
- In the case of low or intermediate signal to noise, the presence of noise will lead to biased results unless a noise-reduction method is employed such as lowpass Fourier filtering (See Appendix 2.9.2).

We also note that common reduction techniques for astronomical data may reduce the amount of diffuse emission present in a tracer map. For example, the practice of filtering molecular gas tracer maps to exclude emission that is not associated in velocity space with HI emission (see Gratier et al. 2010a) may remove some fraction of the diffuse emission from the final tracer map, depending on the filtering parameters chosen for this reduction process. The presented method will only measure the fraction of diffuse emission remaining in the map presented to it after any prior reduction process is complete.

In conclusion, we have demonstrated how, by filtering in Fourier space using the mean region separation length, λ, we can remove diffuse emission from tracer images. This allows the HEISENBERG code to be applied to observationally constrain cloud scale ISM physics, such as cloud lifecycles, without the biasing impact of diffuse emission. In addition, by separating the diffuse and the compact emission within the images, we are able to measure their relative contribution to the total emission within the images. The method also produces maps of the compact and diffuse emission within each input tracer map that may be used for further analysis such as investigating spatial variations in the diffuse emission fraction within galaxies. This approach will provide critical astrophysical constraints on e.g. the unresolved population of low-mass GMCs, and the ionised photon escape fraction.

2.9 Observational Considerations

For the main body of the paper, we have tested diffuse emission filtering in Fourier space on idealised simulated datasets. In this appendix, we consider the impact of two features of astronomical observations on the validity of the method. We firstly consider the impact of astrometric offsets between two input images and then we consider the impact of noise in images.

2.9.1 Systematic astrometric offsets

One issue that impacts the accuracy of parameters measured by the HEISENBERG code is that of systematic astrometric offsets between the two tracer images used (i.e. the gas image and the stellar image). In order to test the impact of astrometric offsets, we generate test datasets, as described in Section 2.5, and then apply the presented method to them with a range of introduced offsets. Figure 2.19 shows the measured values of the gas cloud lifetime, $t_{\rm gas}$, the overlap phase lifetime, $t_{\rm over}$, the mean separation length between regions, λ and the compact emission fraction, $f_{\rm compact}$, relative to their true values against introduced astrometric offset for these simulated datasets. In addition to the standard dataset, we also generate control datasets containing no regions in the overlap phase (i.e. $t_{\rm over} = 0$). For the control datasets, there is no impact with increasing astrometric offset for these parameters up to astrometric offsets of a few times the FWHM of the compact regions. However, for the datasets containing overlap regions, the astrometric disassociation of the overlap regions affects the measured quantities. The most susceptible of the measured quantities to the effects of astrometric offset is the overlap time-scale, $t_{\rm over}$. The gas and stellar 'coexistence time-scale', $t_{\rm over}$, is determined through the statistical spatial correlation between regions from one tracer with regions in the other tracer map. As the size of the astrometric offset increases with respect to the region size, these overlapping regions increasingly decorrelate with their counterparts in the other tracer map and cease to be co-spatial. For this reason, the measured value of $t_{\rm over}$ drops sharply with increasing offset, reaching 0 per cent of the true value at offsets of $\simeq 75$ per cent the FWHM of the compact regions.

In Kruijssen et al. (2018), it was left undecided over what length scale feedback ejecta need to be displaced for the gas and stars to become decorrelated. Either the region separation length or region radius can be used in conjunction with the overlap time-scale to calculate quantities related to the feedback outflow (see e.g. their equations 138 and 139). Figure 2.19 demonstrates that the coexistence of regions becomes undetectable for a displacement of the order the region radius, hence the region radius should be used when calculating the feedback outflow-related quantities.

In order to provide meaningful constraints on the value of $t_{\rm over}$, high astrometric precision is required. As a minimum, for a good estimate of $t_{\rm over}$ (i.e. $t_{\rm over,measured} \geqslant 75\%\ t_{\rm over,true}$) one requires an astrometric offset that is less than 1/3 times the FWHM of the compact regions within the maps (such as molecular gas clouds or HII regions). Uncertainty in the astrometry of a dataset introduces a systematic upwards uncertainty on $t_{\rm over}$ of the magnitude indicated by Figure 2.19.

For λ, the decorrelation between overlapping regions leads to the measurement of smaller separation lengths, with the minimum value of λ measured at offsets of $\sim 0.7\,\mathbf{FWHM}$ corresponding to the point at which $t_{\rm over} = 0$. After this point, the value of λ increases, returning back to the true value at offsets of $\gtrsim 1.5\,\mathbf{FWHM}$. This is due to the fact that initially the regions become separated in both tracer maps, appearing to be nearby regions not in the overlap phase, thus decreasing λ. At larger offsets they become separated enough that they no longer decrease the value of λ. The impact in the measured value of λ is greater the more significant a fraction of the total evolutionary timeline $t_{\rm over}$ is.

The measured compact emission fraction, $f_{\rm compact}$, increases due to the decreasing value of λ, with again larger values of $t_{\rm over}/\tau$ leading to a greater impact. As each image is filtered in Fourier

space individually, a systematic offset between the astrometry of the two images has no impact on the filtering process directly. Instead it impacts the proper alignment of the compact regions during the application of the HEISENBERG code and the proper measurement of λ, which sets the size of the filter. The reduced values of λ cause an overestimate of the compact emission fraction in the images, due to an overcorrection for the presence of overlapping emission peaks (q_η, see Section 2.6).

The measured gas cloud lifetime, $t_{\rm gas}$, can also increase as a result of the decreased value of λ. However, this is dependent on a negative covariance between the two quantities in the affected datasets. Those datasets that have greater measured negative covariance coefficients at zero offsets also have, in general, greater measured negative correlation coefficients and a larger increase in the measured value of $t_{\rm gas}$ at offsets of $\sim 0.7\,\mathbf{FWHM}$, where the effect on λ is greatest. Thus observational datasets with uncertain astrometry and a larger covariance between λ and $t_{\rm gas}$ are most likely to be affected.

Overall, precision astrometry is important for the measurement of the region separation length, λ, crucial for measurement of the overlap time-scale, $t_{\rm over}$, and can have a small impact on measurements of the gas cloud lifetime, $t_{\rm gas}$, and compact emission fraction, $f_{\rm compact}$. The recommended maximum astrometric uncertainty required for accurate measurements of λ and $t_{\rm over}$ is 1/3 the FWHM of the regions of interest, such as molecular gas clouds or HII regions. This corresponds to the physical region size if they are resolved, or to the PSF size if they are barely resolved (or not resolved at all).

2.9.2 Noise

For the main results of the paper, we have so far not considered the impact of noise on our results. However, as noise is typically evenly distributed around zero in a well-prepared astronomical image (i.e. there is equal negative flux from noise as there is positive noise), the masking of all negative flux in an image as is done in the method (see Section 2.3.2 for details) will remove the negative noise flux and leave behind the positive noise flux. This may bias measurements made with the HEISENBERG code, depending on the significance of the noise. As a method for mitigating this effect, we utilise lowpass filtering in Fourier space, predicated on the basis that flux from the noise is concentrated in the very low spatial wavelength (very high frequency)[18] part of Fourier space, whereas the flux from the compact regions and the diffuse emission is concentrated in intermediate to large wavelength portions of Fourier space. For this purpose we define a lowpass Gaussian filter to remove noise from the images:

$$\Psi(u,v) = \exp\left(-\frac{(D(u,v))^2}{2{D_{\rm crit,low}}^2}\right). \tag{2.38}$$

The lowpass critical frequency, $D_{\rm crit,low}$, is defined as:

$$D_{\rm crit,low} = \frac{l_{\rm pix}}{l_{\rm pix} n_{\rm pix}} = \frac{1}{n_{\rm pix}}, \tag{2.39}$$

where $n_{\rm pix}$ is the number of pixels taken as the critical length scale over which to filter and $l_{\rm pix}$ is the pixel length scale.

[18] We note that this assumption does not hold for interferometric images where each baseline, including those baselines that encode flux from large scale, contributes to the noise.

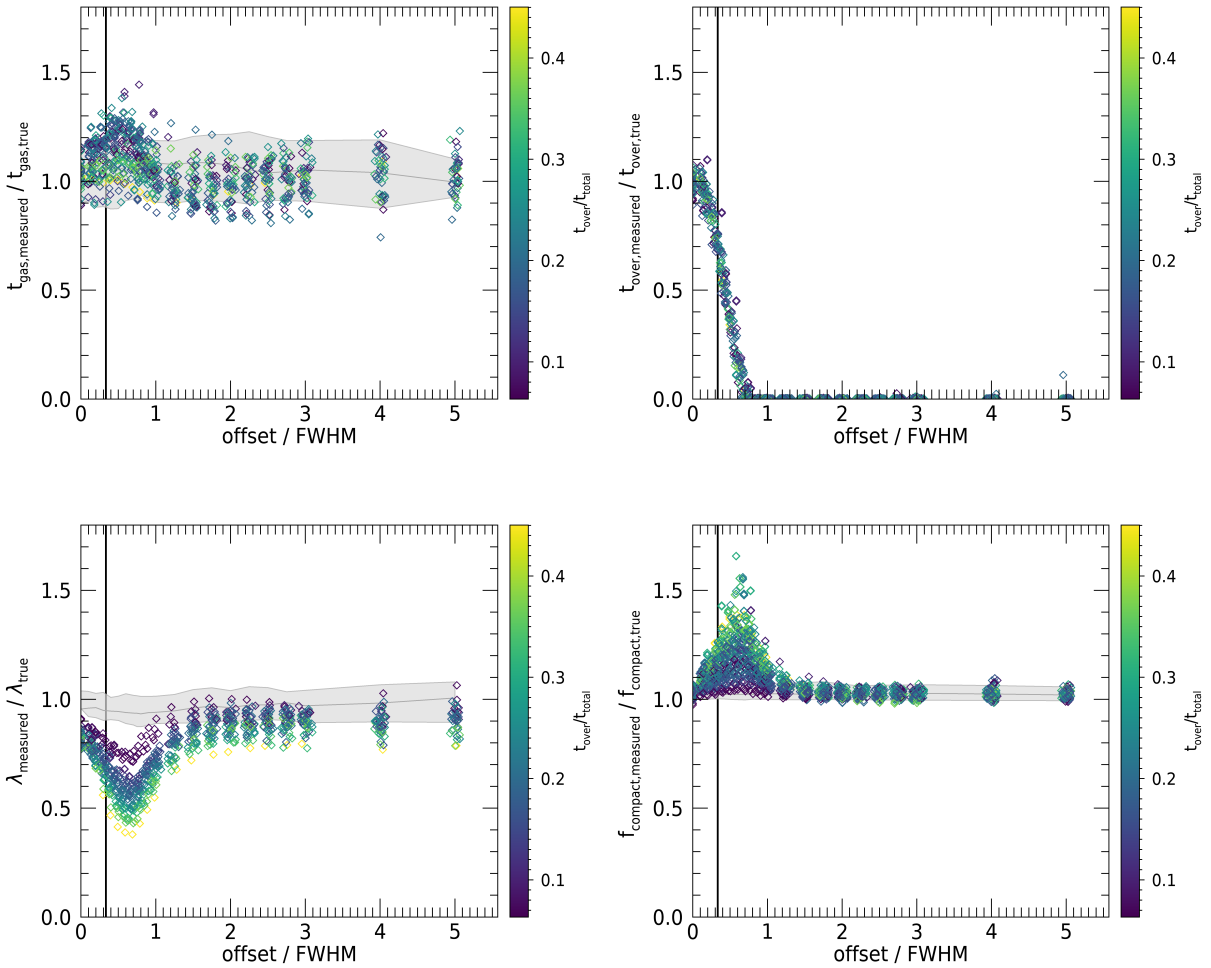

Figure 2.19: Measured values in units of the true value of $t_{\rm gas}$ (top left), $t_{\rm over}$ (top right), λ (bottom left), and $f_{\rm compact}$ (bottom right) against the astrometric offset introduced between the two input images in each experiment. The points are coloured to show the lifetime of the overlap phase relative to the total duration of evolutionary timeline ($t_{\rm over}/\tau$). For each panel except the top right (showing $t_{\rm over}$), a grey shaded area shows the 1σ region of measurements from experiments performed on control datasets with no regions in the overlap phase (i.e. $t_{\rm over} = 0$). The three dark grey lines show the 86th percentile, median and 14th percentile values from top to bottom. In each panel, the vertical line indicates an astrometric offset of FWHM/3, below which the impact of the offset on the measured values is small. Measurements from the control datasets are not significantly affected by offsets of a few times the FWHM for any of the quantities, while in the datasets with a time overlap all the quantities are affected. Most notably, for $t_{\rm over}$, measured values are scattered around the true value at zero offset. However, as the offset is increased, the measured value decreases sharply until reaching zero at offsets $\simeq 70$ per cent of the FWHM of the compact regions. This in turn has an impact on the measured values of the other quantities.

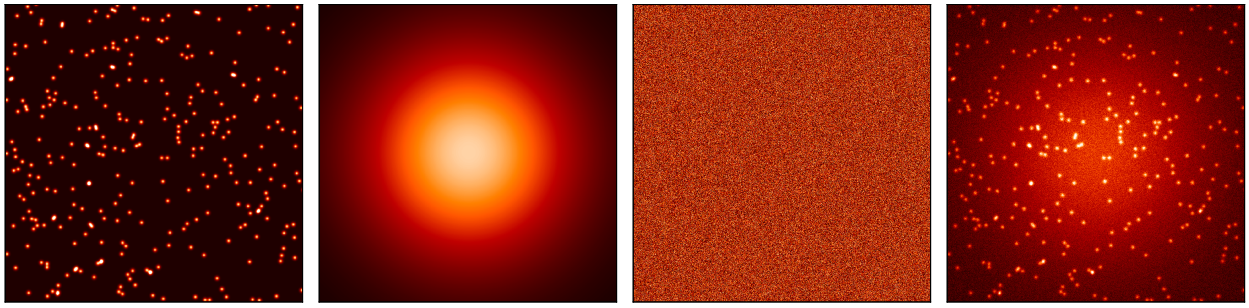

Figure 2.20: Example generated image and its components. Left panel: the compact component. Note that the placement of Gaussians is entirely random such that they may overlap partially or entirely with other Gaussians, leading to pixels brighter than the peak brightness of a single Gaussian. Middle left panel: the background component, here a single large 'galaxy scale' Gaussian function. Middle right panel: the noise component. Right panel: the final generated image with all three components summed together.

In order to test the resilience of the method to the presence of noise, we generate test images as described in Section 2.5. However, in addition to the basic model of a compact region component $s(m,n)$ and background component $b(m,n)$ (see equation 2.13), we add an additional noise component $k(m,n)$:

$$f(m,n) = s(m,n) + b(m,n) + k(m,n). \tag{2.40}$$

We consider two different models for the noise. Firstly uniform random noise:

$$k(m,n) = \kappa_{\text{uniform}}(m,n) \tag{2.41}$$

where the noise at position (m,n) is a uniform random number κ_{uniform} such that $\{\nu_{\text{uniform}} \in \mathbb{R} \mid -\nu_{\text{magnitude}} \leqslant \nu_{\text{uniform}} \leqslant \nu_{\text{magnitude}}\}$ and $\nu_{\text{magnitude}}$ is a constant that sets the magnitude of the noise, which is determined in relation to the resultant signal to noise ratio (S/N) of the generated image.

The second model we consider is Gaussian noise:

$$k(m,n) = \kappa_{\text{Gauss}}(m,n), \tag{2.42}$$

where the noise at position (m,n) is a Gaussian random number such that $\{\nu_{\text{Gauss}} \in \mathbb{R}\}$ selected from a distribution with standard deviation $\sigma(k)$.

For both models, we define the S/N as the ratio of the peak brightness of the mean Gaussian function in the compact component, s_{peak}, to the standard deviation of the noise component, $\sigma(k)$:

$$S/N = \frac{s_{\text{peak}}}{\sigma(k)} \tag{2.43}$$

An example image generated in this fashion is displayed in Figure 2.20.

We create simulated datasets where we add noise to the stellar map only, for simplicity of interpretation. We simulate ten different levels of noise spaced equally in logarithmic space in the

range $\log_{10} S/N = 0.230$–2.544. Before we apply the diffuse filtering method presented in this paper, we apply lowpass filters with a critical length scale from 0−4 times the FWHM of the Gaussian regions in the image, with a critical length scale of zero resulting in no filtering. The results of these experiments are summarised in Figure 2.21, for the uniform noise model and Figure 2.22, for the Gaussian noise model. In the regime of high signal-to-noise ($S/N \geqslant 20$), there is very little impact on the measured parameters without any lowpass filtering. However, as the noise in the datasets increases in significance, the added noise causes two main effects. Firstly, spurious noise peaks may be identified as star formation peaks. Secondly, as negative pixels are masked, as described in Section 2.3.2, the remaining positive noise in the map results in a similar effect as when a diffuse emission reservoir is present in the map. This excess flux mainly affects galactic scales, over which the mean flux density is lower than in emission peaks.

These effects lead to systematically incorrect measurements of $t_{\rm gas}$ and $t_{\rm over}$ at intermediate and low signal to noise. The measured value of the compact emission fraction in the stellar maps, $f_{\rm cl}$, is also increased due to the positive noise flux remaining in the map, even after filtering the diffuse emission, because the noise resides at high frequencies in Fourier space. This makes the compact component appear more significant than in actuality. As we have not introduced noise into the gas maps, the only effect on the measured compact gas fraction is as a result of an incorrectly measured λ, and we therefore do not display these measurements. The measured value of λ, is primarily affected by the introduction of spurious noise peaks. This effect is mitigated at intermediate signal to noise by the fact that the HEISENBERG code selects only peaks above some threshold of the noise level, allowing for the accurate recovery of λ. For lower signal to noise, where it is more likely that a noise peak could be of comparable brightness to the compact regions themselves and thus pass through this peak filtering process, the measured value of λ systematically decreases.

Lowpass filtering reduces the significance of the noise in the images and thus reduces the impact on the measured parameters. We see in Figures 2.21 and 2.22 that a lowpass filter with critical length scale twice that of the FWHM of the compact regions[19] allows accurate measurements of $t_{\rm gas}$, $t_{\rm over}$ and $f_{\rm compact}$ in the intermediate-to-high noise regime. We thus recommend that applications of the method to noisy data employ a lowpass filter prior to the application of the diffuse filtering method, in order to mitigate the impact of noise emission. However, we note that application of a lowpass filter will introduce bias into the measurements of $t_{\rm gas}$, $t_{\rm over}$, λ and $f_{\rm compact}$. With a critical length scale of twice the FWHM of the signal regions or less this effect is small (< 10 per cent for all quantities) increasing to a ~ 10 per cent systematic uncertainty at four times the FWHM (< 40 per cent for all quantities). Alternatively, another approach may be considered if the noise flux is evenly distributed in negative and positive flux, such as applying a signal-to-noise threshold after highpass filtering.

[19] We note that applying a lowpass filter to the images suppresses the high-frequency information in the compact regions to a certain extent. This has the effect of 'blurring' the map, leading the signal regions to appear larger, with a ~ 10 per cent increase in the measured value of $G_{\rm FWHM}$ in comparison to the true value for a filter with a critical length scale twice that of the FWHM of the signal regions

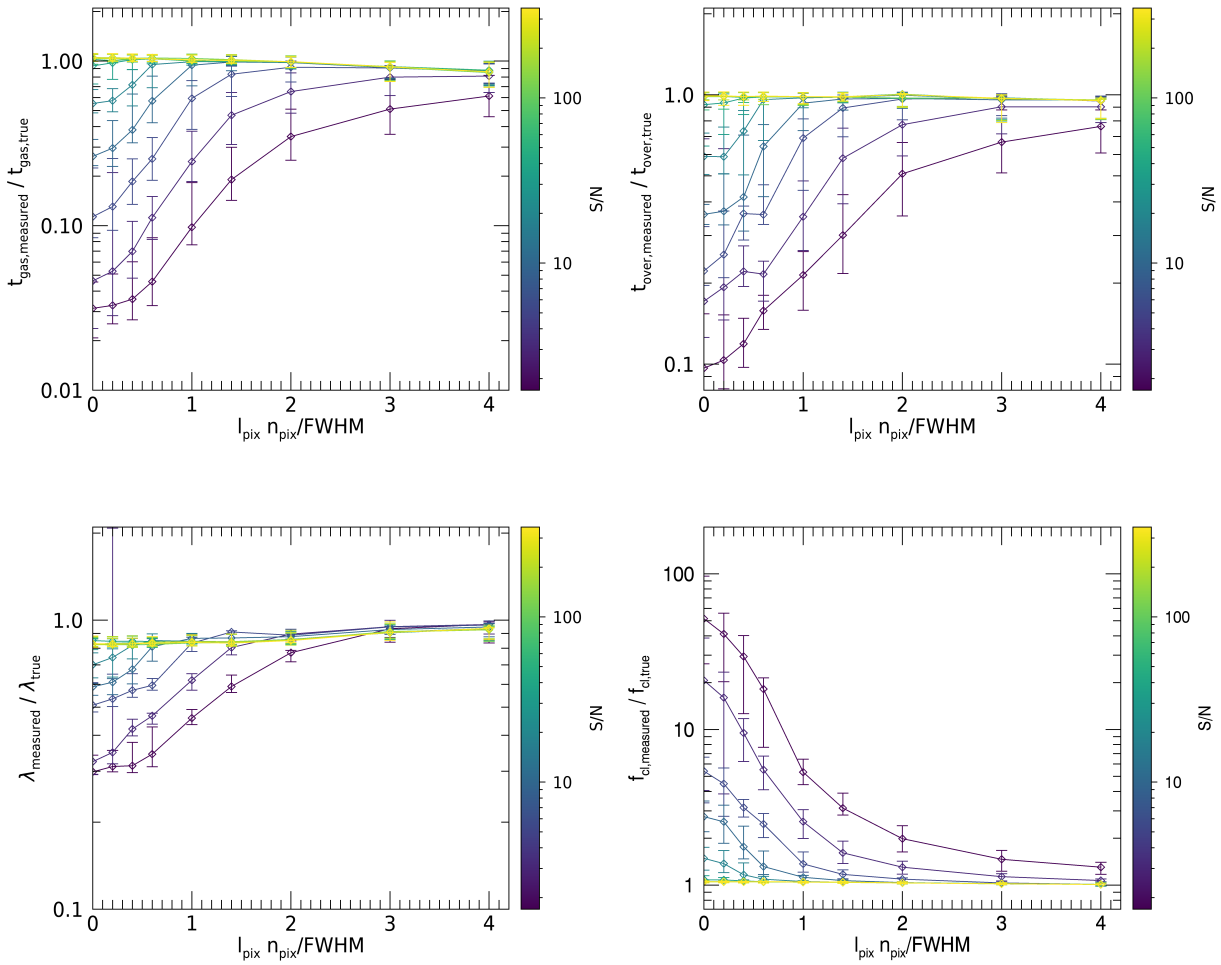

Figure 2.21: Measured values in units of the true value of $t_{\rm gas}$ (top left), $t_{\rm over}$ (top right), λ (bottom left), and $f_{\rm compact}$ (bottom right) for datasets with added uniform noise as a function of the critical length scale, $l_{\rm pix}n_{\rm pix}$, of the applied lowpass filter in units of the compact region FWHM. The line colours indicate the S/N of the map, with 10 lines placed equally in logarithmic space in the range $\log_{10} S/N = 0.230$–2.544. For each measured quantity, the presence of noise in the stellar map biases the result, with the magnitude of this effect decreasing with the application of lowpass filters with larger critical length scales. However, at larger critical length scales ($l_{\rm pix}n_{\rm pix}/\mathrm{FWHM} > 3$), the lowpass filtering introduces a small bias into the measured quantities.

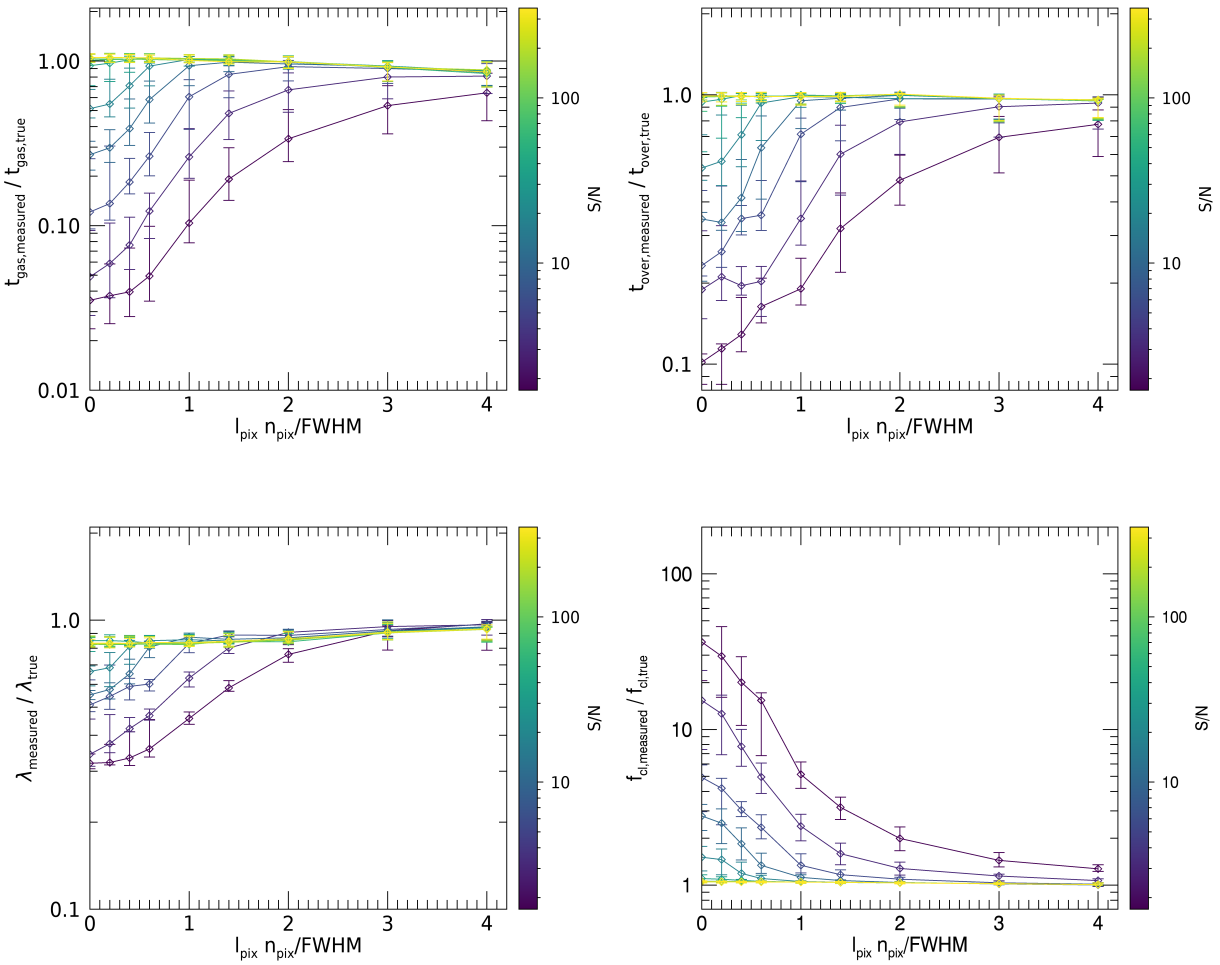

Figure 2.22: Measured values in units of the true value of $t_{\rm gas}$ (top left), $t_{\rm over}$ (top right), λ (bottom left), and $f_{\rm compact}$ (bottom right) for datasets with added Gaussian noise as a function of the critical length scale, $l_{\rm pix}n_{\rm pix}$, of the applied lowpass filter in units of the compact region FWHM. The line colours indicate the S/N of the map, with 10 lines placed equally in logarithmic space in the range $\log_{10} S/N = 0.230$–2.544. For each measured quantity, the presence of noise in the stellar map biases the result, with the magnitude of this effect decreasing with the application of lowpass filters with larger critical length scales. However, at larger critical length scales ($l_{\rm pix}n_{\rm pix}/\mathrm{FWHM} > 3$), the lowpass filtering introduces a small bias into the measured quantities.

3 The molecular cloud lifecycle in M33

Abstract

The observational characterisation of the cloud-scale physics that drive the process of star formation and feedback is crucial for the understanding of galaxy evolution. We report results from an analysis of these physics in M33. We use three star formation rate (SFR) tracers (Hα, FUV and NUV), which establish a reference time-scale, to constrain the lifetimes of molecular clouds and their destruction by feedback. We find broad agreement between measurements obtained with these tracers. We measure a molecular cloud lifetime of $19.5^{+3.0}_{-3.2}$ Myr averaged across the three tracers, in general agreement with previous estimates from different methods. Considering this cloud lifetime and our measurement of the star formation efficiency per star formation event of $3.6^{+0.6}_{-0.6}$ per cent, we conclude that star formation events in M33 are inefficient at transforming molecular clouds into stars and take place relatively quickly. We measure a time-scale for the destruction or dispersal of molecular clouds by feedback of $5.2^{+0.9}_{-1.3}$ Myr from Hα, but find shorter time-scales using the two UV tracers. We ascribe this difference to the greater effect of dust extinction at UV wavelengths. We find a mean separation length between star-forming regions of ~ 170 pc. From decomposition of the images in Fourier space, we find the compact emission fraction (i.e. that emerging from regions that undergo the characterised evolutionary lifecycles) to be 52^{+2}_{-3}, 37^{+1}_{-1} and 33^{+1}_{-1} per cent in Hα, FUV and NUV, respectively. These results characterise the molecular cloud lifecycle and the structure of the ISM in M33.

3.1 Introduction

An important driver of the evolution of galaxies is the conversion of gas into stars that takes place within molecular clouds. These stars are then observed to interact with the interstellar medium via feedback (see e.g. Lopez et al., 2014; McLeod et al., 2019). This feedback injects energy, momentum and metals into the surrounding interstellar medium and ultimately causes disruption of the molecular cloud from which the stars formed (see reviews by Dobbs et al., 2014; Krumholz et al., 2014; Dale, 2015). Furthermore, these feedback processes may be the cause of galactic-scale winds, which impact large-scale galaxy structure (see review by Veilleux et al., 2005). Understanding the physics that drives star formation and feedback is therefore crucial to understanding galaxy evolution.

A fundamental uncertainty regarding molecular clouds is that of their lifecycle, namely for how long do they live once formed and how quickly are they destroyed by feedback? The answers to these questions allow us to discriminate between different physical mechanisms that are driving the evolution of these clouds. Estimates for the molecular cloud lifetime disagree as to whether clouds have short (~ 10Myr) lifetimes (Bash & Peters, 1976; Bash et al., 1977; Blitz & Shu, 1980; Engargiola et al., 2003; Kawamura et al., 2009; Murray, 2011; Miura et al., 2012; Meidt et al., 2015; Corbelli et al., 2017), approximately the duration of a cloud freefall time or long ~ 100Myr lifetimes (Scoville et al., 1979; Scoville & Hersh, 1979; Scoville & Wilson, 2004; Koda et al., 2009), on the order of the time-scale of galactic rotation, which require the clouds to be supported against gravitational collapse. The time-scale of destruction of molecular clouds tells us whether these clouds are able to survive quick-acting feedback mechanisms until the onset of the first supernovae (~ 3Myr Leitherer et al. 2014) or, as observed in NGC300 (Kruijssen et al., 2019), are destroyed rapidly by fast-acting stellar feedback mechanisms such as photoionization and stellar winds, before the onset of the first supernovae.

Galaxy simulations have for some time been able to well-reproduce star formation on galactic scales, for example reproducing the Schmidt-Kennicutt relation between the surface densities of gas mass and SFR (see e.g. Governato et al., 2007; Gnedin et al., 2009; Agertz et al., 2011). Moreover, simulations using a number of different cloud-scale star formation prescriptions can produce similar integrated galaxy-scale star-formation rates that are consistent with the Schmidt-Kennicutt relation. However, the spatial distribution of molecular gas within these simulated galaxies are strongly affected by the chosen star formation prescription (Hopkins et al., 2013). The effect of differing feedback prescriptions too has a significant impact on the small-scale distribution of gas in galaxies (Haas et al., 2013; Scannapieco et al., 2012). However, it is known from observations that the scaling between gas mass and star formation rate breaks down on small scales (see e.g. Bigiel et al. 2008; Leroy et al. 2013, in a sample of galaxies; and Schruba et al. 2010 and Onodera et al. 2010 for M33 specifically). This small-scale breakdown is driven by the evolution of star-forming regions and therefore allows us to characterise the cloud-scale evolution of these star-forming regions and thus to discriminate between different evolutionary scenarios (Kruijssen & Longmore, 2014).

M33 is a nearby (0.84 Mpc; Gieren et al. 2013) moderately inclined ($i = 55°$; Koch et al. 2018) flocculent disc galaxy. It is well covered by high-resolution imaging of molecular gas in addition to multiple tracers of star formation. It is therefore a perfect target, in which to characterise the lifecycle of molecular clouds. Indeed, a number of other methods have been employed to estimate the molecular cloud lifetime in M33, leading to a variety of values. Engargiola et al. (2003) noted that GMCs in M33 are closely associated with HI filaments. They estimated an upper limit of 10-20 Myr for the molecular cloud lifetime by comparing the offsets in velocity between these two populations with the typical sizes of the HI filaments, noting that a significantly longer cloud lifetime would allow clouds to move away from the HI filaments, breaking the observed spatial

association. By classifying 71 molecular clouds identified in CO(3-2) based on co-spatiality or not of the molecular cloud with HII regions and age-dated young stellar groups, Miura et al. (2012) used an evolutionary sequence model (developed and previously employed by Fukui et al. 1999; Yamaguchi et al. 2001; Kawamura et al. 2009) to estimate a lifetime of 20-40 **Myr** for molecular clouds more massive than 10^5 $M_\odot$. More recently, Corbelli et al. (2017) estimated a 14.2 **Myr** molecular cloud lifetime, using a method similarly predicated on classifying the evolutionary stage of molecular clouds in relation to observed stellar clusters and HII regions, making use of a much larger catalogue of 566 molecular clouds, identified in CO(2-1), and 630 young stellar young stellar cluster candidates. Given these multiple experiment designs, it has been unclear up to now if the variety of molecular cloud lifetimes measured in M33 (between 10 and 40 **Myr**) highlight physical differences between different objects, or simply linked to the specific method used.

These analyses were performed at a variety of fixed scales. In the analysis of the recent star formation process the diffuse emission is a contaminant that affects the analysis of star formation process at levels of significance depending on the size-scale considered. Comparing measurements taken at different size-scales in galaxies requires correct handling of diffuse emission, as large-scale diffuse emission captured in galaxy-scale apertures may not be captured in apertures targeted on populations of interest, such as HII regions (see e.g Blanc et al. 2009, Leroy et al. 2012 and Hygate et al. 2019). Moreover, diffuse emission can be a significant contaminant. Previous estimates in M33 have found significant diffuse emission in commonly-used star formation tracers. Thilker et al. (2005) find that $\sim$ 65 per cent of the FUV emission is diffuse across most of the galactic disc with higher values in the galaxy centre and at very large galactocentric radii, and that ~ 40 per cent of the Hα emission is diffuse across most of M33, but increasing to 60 per cent in the galaxy's centre and decreasing precipitously at large galacocentric radii. Other studies of M33 report a similar fraction of the total Hα emission from M33 is diffuse: 43 ± 3 per cent (Greenawalt, 1998), 38 ± 3 per cent (Hoopes et al., 2001) and 44 per cent (Schruba et al., 2010).

Thilker et al. (2005) find that the ratio of the fraction of diffuse emission in Hα to the fraction of diffuse emission in FUV exhibits radial variation in M33, which may be caused by variation in ISM structure, due to the different physical origins of diffuse emission in the two tracers. Studies in the Milky-way show that dust-scattered stellar light accounts for the majority of the UV background (Sasseen et al., 1995; Schiminovich et al., 2001; Murthy et al., 2010; Hamden et al., 2013). In contrast, a number of different physical mechanisms are considered to be possible sources for diffuse Hα emission, including ionisation of the warm neutral medium by Lyman continuum emission that leaks from HII regions (e.g. Mathis, 1986; Sembach et al., 2000; Wood et al., 2010) and post-asymptotic giant branch stars (Binette et al., 1994; Sarzi et al., 2010; Flores-Fajardo et al., 2011; Yan & Blanton, 2012), dust scattering (Seon & Witt, 2012) and shocks (Pety & Falgarone, 2000; Collins & Rand, 2001).

A number of studies have also quantified the diffuse molecular gas emission in M33. Wilson & Walker (1994) found an upper limit of ~ 60 per cent of the CO emission is diffuse by comparing the flux recovered by single dish and interferometric observations. They also found that a lower limit of 30 ± 30 per cent of the ^{12}CO emission observed in M33 may come from a population of diffuse molecular clouds by comparing the variation of the line ratio of ^{12}CO and ^{13}CO between single dish and interferometric observations. A more recent study by Rosolowsky et al. (2007) found that ~ 20 per cent of single dish CO(1-0) emission was recovered with interferometric observations suggesting a large fraction of non-compact emission. Another study by Tosaki et al. (2011) found no smoothly distributed diffuse molecular gas component in ^{12}CO(1-0) above their sensitivity.

We have developed a statistical method to characterise cloud-scale physical properties related to the process of star formation in galaxies, including the duration of the successive phases of the evolutionary cycle between molecular clouds and star formation as well as the ISM fragmentation

length. Kruijssen & Longmore (2014, hereafter KL14) presented the theoretical basis of the method. We then presented the HEISENBERG code implementation of the method in Kruijssen et al. (2018). In Haydon et al. (2018), we presented a determination of the characteristic time-scales associated with Hα and UV star formation tracers within the HEISENBERG framework, which allows for their use as reference time-scales and thus the determination of absolute visibility time-scales for other tracers. Lastly, in Hygate et al. (2019) we presented a method for filtering diffuse emission from tracer images in Fourier space. This Fourier filtering method allows the application of the HEISENBERG code to tracer maps containing diffuse emission in addition to emission emanating from the populations of interest as well as measurement of the fraction of emission that is diffuse in these tracer maps. This statistical method has been successfully applied to the flocculent galaxy NGC300 (Kruijssen et al., 2019) and a sample of nearby spiral galaxies (Chevance et al., 2019) to measure the duration of the molecular cloud lifetime in these galaxies. We use these targets as a reference for the results we derive for M33.

In this paper, we present the measurements of cloud-scale physical properties obtained from the application of the HEISENBERG code to M33. Details of the data used in this analysis and their preparation are presented in Section 3.2. Section 3.3 gives a brief summary of the HEISENBERG method along with some of the specifics of its application to M33. We present our results on the timeline of cloud evolution, star formation and feedback and the fraction of (non-)diffuse emission in the CO(2-1), FUV, NUV and Hα images used in the analysis, in Section 3.4. Lastly we summarise our conclusions in Section 3.5.

3.2 Data

In order to measure the molecular cloud lifecycle, we require a tracer of the molecular gas, for which we use CO(2-1), and reference tracers with an associated time-scale that trace another part of the star formation evolutionary sequence. In this case we use Hα, FUV and NUV to trace young stars formed from molecular clouds. In addition, we require these tracer images to have cloud-scale resolution and to cover the whole star-forming disk.

3.2.1 Molecular gas observations

We use the IRAM 30m telescope CO(2-1) dataset presented in Gratier et al. (2010b) and Druard et al. (2014) to trace the molecular gas mass in M33.[20] To create an integrated intensity (moment-zero) map of high significance, we start from the HI windowed data cube presented by Druard et al. (2014) and apply a signal masking method in order to reduce the amount of noise in the moment-zero map and thus reduce the impact of this noise on the measurements we make with the HEISENBERG code.[21] We firstly create a noise cube with the CPROPS (Rosolowsky & Leroy, 2006) routine ERRMAP_SR. We then determine two masks: for the first mask, any pixel in any channel with significance below 5σ is blanked; and for the second mask, any pixel in any channel with significance below 2σ is blanked. We then grow the first mask such that any contiguous region of pixels with signal-to-noise greater than or equal to 2σ that is connected spatially or in velocity space to at least one pixel of signal-to-noise greater than or equal to 5σ is included in the new mask. We present the resulting moment-zero map in Figure 3.1. This masking process results in a number of lines of sight being blanked, but has only a small impact on the flux of the brightest pixels in the moment-zero map. This reduction method may well reduce the amount of diffuse emission remaining in the map and thus impact our measurement of the CO diffuse fraction. We

[20] Available from: http://www.iram.fr/ILPA/LP006/

[21] See appendix A2 of Hygate et al. (2019) for a discussion of the impact of noise on the HEISENBERG code.

therefore probe only the diffuse emission remaining in our reduced map. We measure a total CO luminosity $L'_{CO1-0} = 1.7 \times 10^7$ K km s^{-1} pc^{-2}. We apply a CO to molecular gas mas conversion factor $\alpha_{CO} = 8.6$, double the Milky Way value to account for the approximately half-solar metallicity of M33 (Bresolin, 2011). This results in a total measured gas mass of 1.4×10^8 M$_\odot$.

Adopting a twice-Milky Way α_{CO} is not uncommon for M33 (see e.g. Druard et al., 2014), though other studies have applied different values (see e.g. Rosolowsky et al., 2007; Onodera et al., 2010; Tosaki et al., 2011). However, we note that applying a different value of α_{CO} would have no impact on the measured fitting parameters of the HEISENBERG code or the diffuse emission fractions in the maps, as multiplying a tracer map by a constant does not impact these measurements (for a detailed explanation see Kruijssen et al., 2018). It would, however, impact the derived star formation efficiency, ϵ_{sf}, and the mass loading factor, η_{fb}, due to their definition in terms of the measured depletion time, which depends on the measured gas mass.

3.2.2 Star formation rate tracer observations

We use three separate data sets to trace the SFR in M33. We use the KPNO 0.6m Hα image first presented in Greenawalt (1998) (further information about the data reduction procedure for the image can be found in Hoopes & Walterbos 2000). In addition, we use FUV and NUV images from the Galaxy Evolution Explorer space telescope (Martin et al., 2005, GALEX), first presented by Thilker et al. (2005).

From the GALEX images, we subtract a sky background of 5.16×10^{-4} and 3.87×10^{-3} counts from the FUV and NUV images, respectively, as calculated for M33 by Gil de Paz et al. (2007). We identify and mask the foreground stars which represent significant contamination of the NUV image. To do this, we identify and mask point-spread-function-like objects that have a peak NUV-to-FUV intensity ratio above 15 (following the NUV-to-FUV threshold given by Leroy et al. 2008).

For all three data sets we correct for the effect of reddening due to Galactic dust extinction. We apply a correction according to the prescription of Fitzpatrick & Massa (2007). For an R_V of 3.1 and a value of $E(B-V) = 0.0413$, obtained from the reference pixel at M33's centre in the dust maps of Schlegel et al. (1998)[22], this translates to corrective factors of: $A_{H\alpha} = 0.10$ mag, $A_{FUV} = 0.35$ mag and $A_{NUV} = 0.37$ mag.

After accounting for Galactic extinction, we calculate the SFR using the prescriptions given by Kennicutt & Evans (2012). The SFR in units of M$_\odot yr^{-1}$ for a given tracer 'x' is

$$\mathrm{SFR}_x = C_x L_x, \tag{3.1}$$

where L_x is the luminosity of the tracer in units of ergs s^{-1} and C_x is a conversion constant. For the three SFR tracers we use, the values of this conversion constant are $C_{FUV} = 4.47 \times 10^{-44}$, $C_{NUV} = 6.76 \times 10^{-44}$ and $C_{H\alpha} = 5.37 \times 10^{-42}$. We calculate a total SFR for M33 of 0.18 M$_\odot$yr^{-1} for Hα and FUV, but 0.27 M$_\odot$yr^{-1} for NUV. We note that adopting different SFR conversion constants does not impact measured values of t_{CO}, t_{fb} and λ, due to the fact that a constant scaling factor applied to a tracer map does not affect the measured values of these parameters (Kruijssen et al., 2018). We note that these measurements are lower than previous literature values as we neglect internal attenuation (see e.g. SFRs derived using a number of different prescriptions, which range from 0.17 to 0.45; M$_\odot$yr^{-1} Verley et al. 2009; Williams et al. 2018; Elson et al. 2019). However, for the calculation of the global depletion time (used for the calculation of ϵ_{sf} and η_{fb}, only)we use a

[22]We obtain this value of E(B-V) from the NASA/IPAC Infrared Science Archive Galactic Dust Reddening and Extinction Service at https://irsa.ipac.caltech.edu/applications/DUST/

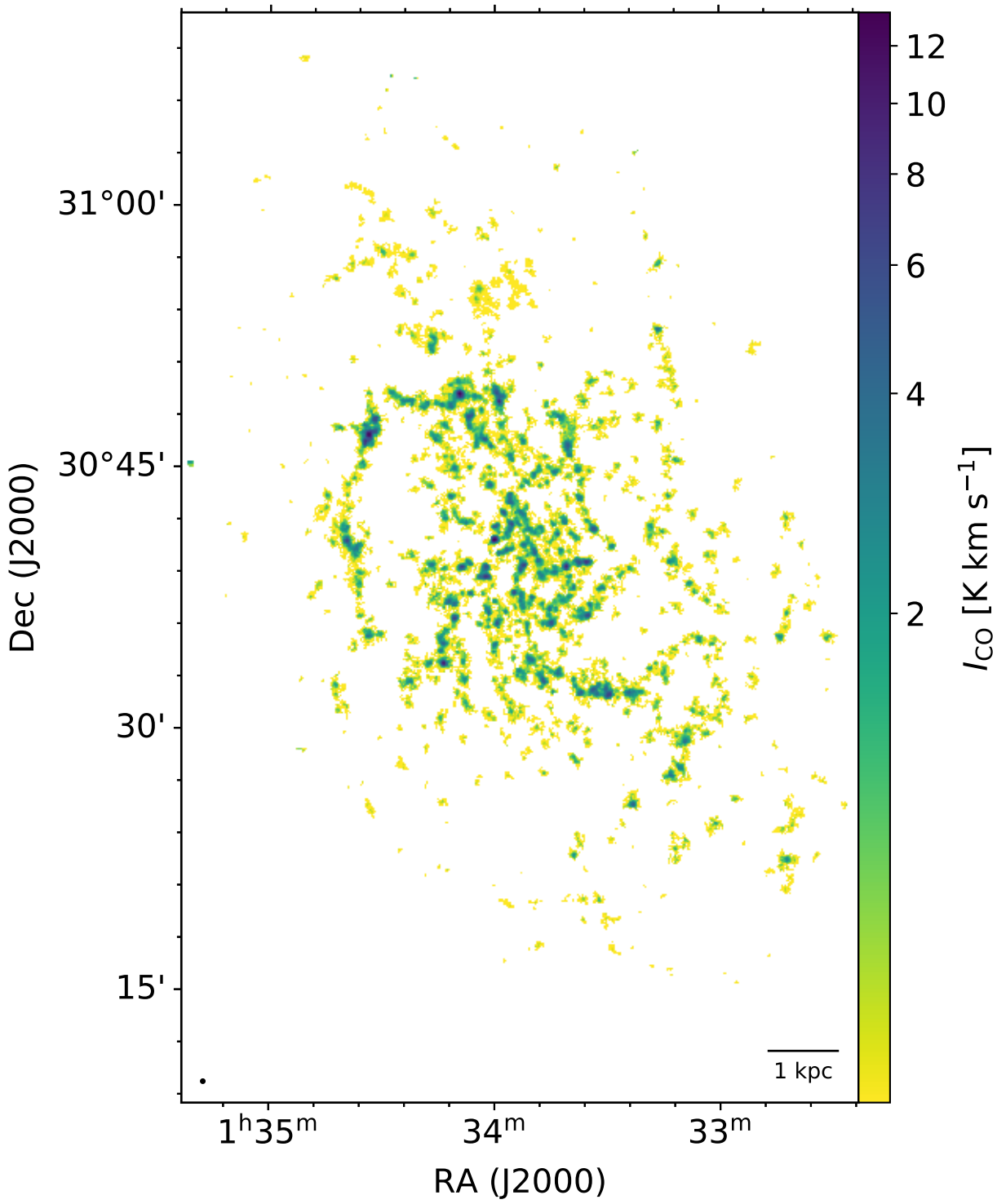

Figure 3.1: CO(2-1) integrated intensity map in units of K km s^{-1}. The map was created from the dataset presented in Gratier et al. (2010b) and Druard et al. (2014) with additional reduction as described in Section 3.2.1. The reduction process results in some lines of sight being entirely blanked, these are shown as white in the figure. The beam is shown as the black circle in the bottom left corner and the black bar in the bottom right corner represents an unprojected distance of 1 kpc.

combination of GALEX FUV and WISE W4 to trace embedded and unembedded star formation (see Section 3.4.2).

3.2.3 Convolution to common resolution

The IRAM CO map is the dataset with the coarsest resolution ($12''$ = 49pc at a distance of 0.84 Mpc). This sets the minimum resolution of our analysis and thus the smallest aperture size used in our application of the HEISENBERG code. We therefore convolve the Hα, FUV and NUV star formation tracer maps to a matching symmetrical $12''$ Gaussian beam.

3.2.4 Tracer map astrometric offsets

We apply the "uncertainty principle for star formation" (which we present in Section 3.3.1), in order to constrain the durations of phases of the star formation evolutionary cycle. This method investigates the spatial (de-)correlation between the molecular gas and star formation rate tracer maps. As a result, an astrometric offset between the molecular gas and young stellar maps artificially separates regions that are in reality in a phase of spatial co-existence in both tracer maps. This would lead to an underestimation of the duration of the co-existence phase between the tracers. Tests on simulated datasets (Hygate et al., 2019) show that, to achieve reliable measurements of this coexistence time-scale between molecular gas clouds and young stars (the time-scale for feedback to disperse or destroy the clouds, $t_{\rm fb}$), we require astrometric offsets between our star formation and gas mass tracer maps of less than one third of the full-width at half-maximum (FWHM) of the compact regions of interest in the tracer maps (e.g. HII regions imaged in Hα and molecular clouds imaged in CO).

We compare the positions of field stars identified in the GALEX NUV image to their positions as listed in the GAIA DR2 catalogue (GaiaCollaboration et al., 2018). We find an offset in astrometry between the NUV image and the GAIA DR2 astrometric solution of less than $0.3''$, which is less than a fifth of the $1.5''$pixel size. We then cross compare the positions of field stars identified in both the Hα and NUV images. From this comparison we find that offsets in position between the images are at most on the pixel scale. For the GALEX FUV image, there are only a few visible field stars. Offsets between these field stars and between regions identified in M33's disc are again small, comparable to the pixel scale. As these $\sim 1.5''$ offsets are significantly (~ 8 times) less than the $12''$angular resolution of the CO dataset, the dataset with the poorest resolution, we conclude that they are not significant and will not bias our measurements.

Assuring a common astrometric solution between the star formation tracer images and the molecular gas tracer (CO) image is more challenging as no point sources are visible in both maps. We compare the positions of giant molecular clouds (GMCs) between the IRAM CO(2-1) image used in this study and a CO(1-0) image taken with the Nobeyama Radio Observatory (NRO) 45m telescope (Tosaki et al., 2011). As GMCs are by their nature not point sources, having instead complex shapes, and as we compare two different CO transitions, we can only assess whether the two maps broadly agree in position. Moreover, Greve et al. (1996) state an rms pointing accuracy for the IRAM 30m telescope of $3.5''$, whereas the NRO dataset has a pointing accuracy of $7.5''$ (Tosaki et al., 2011). We perform a cross correlation analysis for the two images using the SCIKIT-IMAGE (van der Walt et al., 2014) task REGISTER_TRANSLATION.[23] We find an offset between the images of $2.4''$, smaller than the images' pixel scales and the pointing uncertainties of the telescopes. From the application of the HEISENBERG code to the data, the smallest measured characteristic region FWHM of our three SFR tracers is $15''$. The pointing uncertainty of the IRAM telescope is thus

[23]The function REGISTER_TRANSLATION implements an algorithm for determining subpixel image offsets presented by Guizar-Sicairos et al. (2008)

the most significant source of astrometric uncertainty. This 3.5″pointing accuracy is 0.23 times the region size, better than the one third region size accuracy required for measurements of $t_{\rm fb}$.

3.2.5 Auxiliary data

In addition to the tracer maps of molecular gas and star formation that constitute our main dataset, we describe below some of the properties of M33 used in our analysis.

1. We adopt a distance to M33 of 0.84 Mpc, as determined from photometry of long-period Cepheids by Gieren et al. (2013).

2. The central position of M33's disc is at a right ascension of $\alpha = 23.4607°$ and declination of $\delta = 30.6583°$. We also adopt an inclination of 55.08° and position angle of 201.12°, for the disc. These disc parameters are measured from an atomic hydrogen (HI) emission map created from combining observations from the Karl G. Jansky Very Large Array (VLA) and short-spacing information from the Green Bank Telescope (GBT) (Koch et al., 2018).

3. For the metallicity in M33, we adopt a value for the galaxy's centre of $12 + \log {\rm O/H} = 8.48 \pm 0.04$ with a gradient of -0.042 ± 0.010 kpc^{-1}, as measured by Bresolin (2011).

3.3 Method

3.3.1 The Uncertainty Principle for Star Formation

In this paper we employ the "uncertainty principle for star formation" to measure the the successive phases of the cycle of cloud evolution, star formation and feedback in M33. The basic theory of the method is presented in KL14. The full implementation of the method for application to observational data in the form of the HEISENBERG code is presented in Kruijssen et al. (2018).

3.3.1.1 Concept of the analysis method

In applying the method to M33, we consider a three stage model for the evolution of the star formation process. This starts with molecular clouds, visible in CO, which at some stage form stars. These young stars are visible in tracers of star formation (Hα, FUV and NUV, in this paper). As these stars form within molecular gas clouds, they spatially coexist with their natal gas cloud at first. This phase ends after the cloud is destroyed or dispersed by stellar feedback. The total lifetime of the molecular cloud, $t_{\rm CO}$, is the time-scale from which the cloud becomes visible in CO until it becomes no longer visible due to the effects of feedback. The time-scale of the co-visibility of young stars with their natal gas cloud represents the time-scale for feedback to disperse or destroy the cloud, $t_{\rm fb}$. The final time-scale, $t_{\rm star}$, is the amount of time young stars are visible in the star formation tracer map.

We illustrate the method in Figure 3.2 and provide a brief summary here (see Kruijssen et al. 2018 for a full explanation). To apply the method, two images are required that each trace a sequential phase of an evolutionary process. In this paper these two phases are molecular clouds traced by CO ("CO") and the young stars traced by Halpha, FUV or NUV ("stars") that form from the molecular clouds.

We measure values of the gas-to-stellar flux ratio in apertures of varying sizes placed around peaks of a gas tracer map and peaks of a star formation rate tracer map across M33. At small enough aperture sizes, the measured gas-to-stellar flux ratio deviates from the galactic average and the measured value depends on whether apertures are focussed on gas or stellar emission peaks

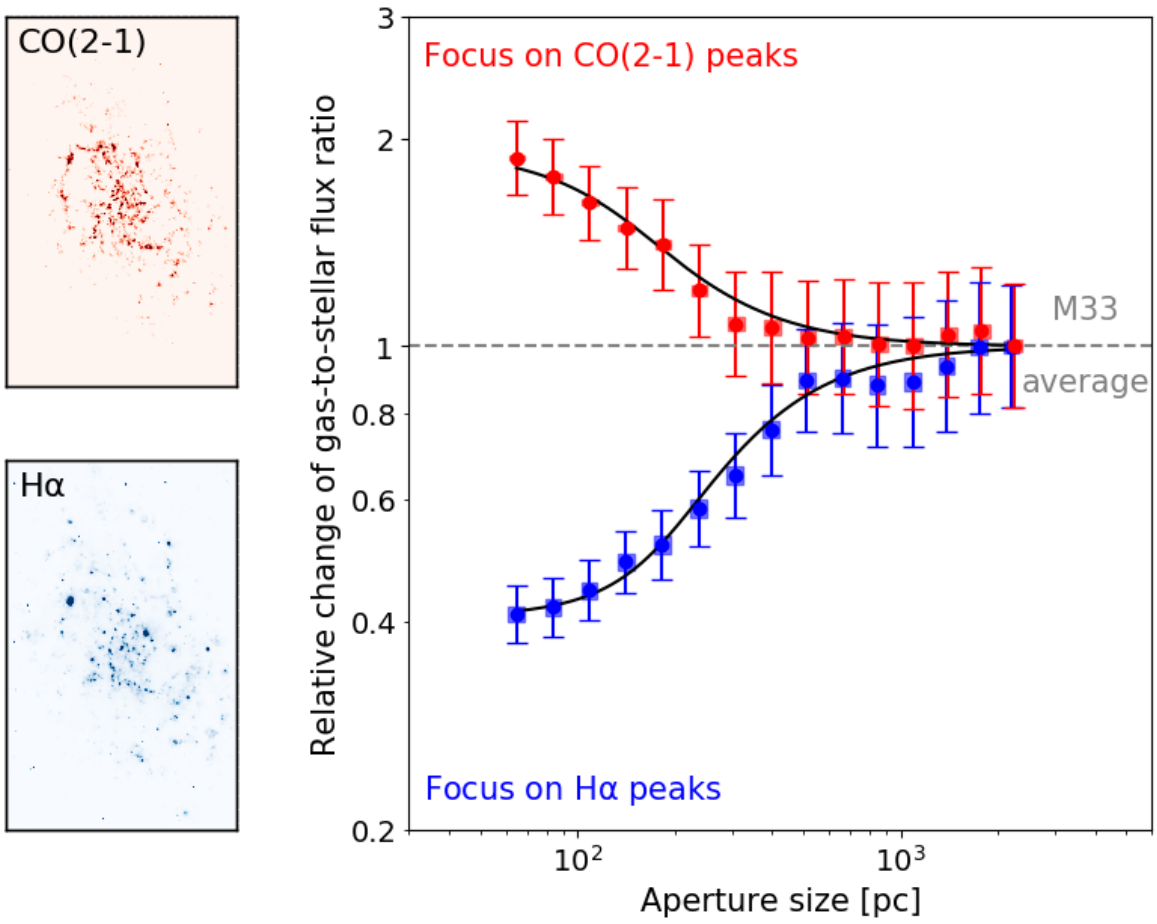

Figure 3.2: A depiction of the application of the HEISENBERG code. [Top left panel] The CO(2-1) and [Bottom left panel] Hα images of M33. [Right-hand panel] The relative change of the ensemble average of the gas-to-stellar flux ratio compared to the galactic average is measured in apertures of varying sizes that are centred on peaks in the CO(2-1) (the red dots) or Hα (the blue dots) distributions. For each measurement the 1σ error range is indicated by the error bars and the 1σ error range taking into account covariance between data points is indicated by the shaded rectangles. At large aperture sizes the galactic average value is recovered for M33 regardless of whether apertures are centred on CO(2-1) or Hα peaks. As the aperture size is decreased, focussing on peaks in one tracer or the other leads to significantly different measurements of the gas-to-stellar flux ratio compared to the galactic average, with measurements of the gas-to-stellar flux ratio focussing on Hα peaks decreasing with smaller apertures, whilst those focussed on CO(2-1) peaks increase at small aperture sizes. This behaviour is observed as a result of the fact that a set of apertures that is selected to cover the emission peaks in one tracer will, at small aperture sizes, miss flux from non-overlapping peaks in the other tracer. Furthermore the rarity of emission peaks in a tracer, determines the magnitude of this effect. A set of peaks focussed on rare emission peaks will not include relatively more of the emission from more common peaks. Thus focussing on rarer peaks will produce a larger bias away from the galactic average. If a population of objects are undergoing an evolutionary sequence, for example molecular clouds (as traced by CO(2-1)) evolving into young stars (as traced by Hα), then their relative frequency in a tracer is linked to their visibility lifetime in that tracer. Thus, by fitting the HEISENBERG model to the observed measurements, we are able to measure the relative visibility lifetimes of molecular clouds and young stars.

(Schruba et al., 2010). Thus we find two branches of measurements, one branch with an enhanced gas-to-stellar flux ratio relative to the galactic average, when focussing on gas peaks and one with a reduced gas-to-stellar flux ratio relative to the galactic average, when focussing on stellar peaks. We fit a statistical model to this deviation of the measured gas-to-stellar flux ratio from the galactic average, when focussing on gas peaks or stellar peaks, as a function of decreasing aperture size using the HEISENBERG code. This model depends on three free parameters: λ, $t_{\rm CO}$ and $t_{\rm fb}$, which we explain in turn below. As the model is fitted to the relative change of the gas-to-stellar-flux ratio from the galactic average, multiplying the tracer maps by a constant factor (as is done to convert our raw data into physical units in Sections 3.2.1 and 3.2.2) does not impact measurements of these free parameters.

The first, and most conceptually straight-forward parameter is λ, the mean separation between independent star-forming regions. The size-scale at which measurements in the two branches diverge away from the galactic average value sets λ. Star-forming regions that are on average more distant from each other will exhibit this divergence at larger aperture sizes than more tightly-packed regions.

The direction of this deviation is determined by the tracer on which apertures are focussed, with the ensemble average of the gas-to-stellar flux ratio increasing for apertures focussed on gas peaks and decreasing for apertures focussed on stellar peaks. The magnitude of the deviation away from the galactic average of both branches is determined by the relative visibility time-scales of the evolutionary phases being traced (i.e. $t_{\rm CO}$ and $t_{\rm star}$). This can be understood as follows. Schematically, the number of emission peaks in a tracer is linked to the relative duration of the visibility of emission peaks in that tracer, with a tracer of a shorter-lived phase of evolution having, on average, fewer emission peaks than one that traces a longer-lived phase of evolution. Accordingly, fewer apertures are needed to encompass all the emission peaks in a short-lived phase than are needed to encompass all peaks in a longer-lived phase. Thus, at small aperture sizes, the (less numerous) set of peaks covering the shorter-lived evolutionary phase captures a small portion of the flux of the longer-lived phase and lead to a large deviation of the gas-to-stellar flux ratio at small aperture sizes. Conversely the (more numerous) set of peaks covering the longer-lived evolutionary phase captures a large fraction of the flux emanating from the shorter-lived phase, due to the fact that they cover a greater fraction of the galaxy's surface area, and thus lead to smaller deviations of the gas-to-stellar flux ratio. Thus, from the relative magnitude of the deviations of the measured gas-to-stellar flux ratio in each branch, the HEISENBERG code enables us to measure the ratio of the lifetimes of the two phases ($t_{\rm CO}/t_{\rm star}$).

When young stars do not destroy their clouds instantly after becoming visible (i.e. $t_{\rm fb} > 0$), some fraction of peaks in each tracer spatially co-exist with peaks in the other tracer. This results in the gas-to-stellar flux ratio of each branch saturating at small aperture sizes. The higher the fraction of their visibility lifetime that stars spend co-existing with gas, the closer to the galactic average value of the gas-to-stellar ratio at which measurements in the stellar branch will saturate. By fitting this saturation, the HEISENBERG code enables us to measure the ratio of this co-existence (feedback) time-scale to the stellar visibility time-scale ($t_{\rm fb}/t_{\rm star}$).

The full lists of flags and input parameters required for the Heisenberg code are available from tables 1 and 2 of Kruijssen et al. (2018). In the following sections, we describe some of the input parameters adapted for M33. The remaining parameters have been set to their default values.

3.3.1.2 Reference time-scales

As explained above, this method fundamentally only allows us to measure the ratios of the duration of each of the phases relative to the other phases. In order to convert the measured time-scale ratios ($t_{\rm CO}/t_{\rm star}$ and $t_{\rm fb}/t_{\rm star}$) into absolute time-scales ($t_{\rm CO}$, $t_{\rm fb}$ and $t_{\rm star}$), we require a priori knowledge of one of these time-scales. For this purpose we use the prescription for $t_{\rm star}$ as a function of metallicity

derived from stellar population synthesis modelling, as presented in Haydon et al. (2018). We calculate reference time-scales for our SFR tracers, namely Hα, FUV and NUV. We therefore use three different values of $t_{\rm star}$ in our analysis, corresponding to our three star formation tracer images: $t_{\rm H\alpha}$, $t_{\rm FUV}$ and $t_{\rm NUV}$. We specifically use equations 11 and 13 from Haydon et al. (2018) to calculate the Hα and UV time-scales, respectively. To calculate these time-scales we use the metallicity at a radius of 2.5 kpc (the mean radius of unmasked region we consider), $12 + \log {\rm O/H} = 8.38$ (see Section 3.2.5). For this purpose, we adopt a solar oxygen abundance of $12 + \log {\rm O/H} = 8.69$ from solar photosphere measurements (Asplund et al., 2009). In addition, we find that, for the characteristic star-forming region masses probed by our analysis in M33, there is no effect from incomplete sampling of the stellar initial mass function (IMF) on the reference time-scales we calculate (see section 6 of Haydon et al. 2018). We summarise the calculated reference time-scales that are used in this analysis in Table 3.1.

3.3.1.3 Diffuse emission

Another step that must be taken to properly apply the Heisenberg code is to account for diffuse emission in the tracer images, as the presence of large-scale diffuse emission can significantly bias measurements from the Heisenberg code (Hygate et al., 2019). This is due to the assumption inherent within the method that emission in the tracer maps comes from individual regions at some stage in the evolutionary timeline (for example HII regions in Hα) and not from contaminant large-scale emission. Diffuse emission therefore alters measurements of the gas-to-stellar flux ratio and can lead to biased measurements from fitting the statistical model. We use the iterative Fourier filtering method presented in Hygate et al. (2019) to separate out the diffuse emission present in our tracer images and remove this biasing effect. This method isolates the emission emanating from compact regions participating in the evolutionary star formation sequence (such as molecular clouds and HII regions) from large scale diffuse emission. In practice this is done by applying a filter in Fourier space to attenuate emission at high spatial wavelengths. We apply a Gaussian filter in Fourier space, defined in terms of the attenuation $\Psi(u,v)$ at spatial frequencies u,v, which can vary between 1 (no attenuation) and 0 (complete attenuation), as

$$\Psi(u,v) = 1 - \exp\left(-\frac{(D(u,v))^2}{2\left(\frac{l_{\rm pix}}{n_\lambda \lambda}\right)^2}\right), \tag{3.2}$$

where $l_{\rm pix}$ is the pixel length scale, $D(u,v)$ is the distance in Fourier space from the zero-frequency "DC component" and n_λ is a softening factor that is applied to the filter.

The spatial wavelengths attenuated by the filter are defined on the basis of the mean region separation length, λ. This therefore necessitates an iterative process, as the initial measurement of λ is also biased by the presence of diffuse emission. We consider this iterative process to converge when there is a change of less than 5 per cent in the measured value of λ over three iterative steps. Because we use a Gaussian filter, emission on all spatial wavelengths will in principle be affected by the filtering, including to some level the emission from the compact regions of interest. To compensate for this effect, we use a correction factor, $q_{\rm con}$, to retrieve the total emission from the compact regions after filtering (see below). However, this correction becomes more uncertain when the flux filtered from the compact regions increases. Hygate et al. (2019) recommend that a minimum of 90 per cent of the compact emission should be preserved during the filtering process. As a result, we chose a softening factor $n_\lambda = 11$ as a compromise between this requirement and

Table 3.1: Reference time-scales used in this analysis, calculated for the observed metallicity of M33, according to the prescriptions given by Haydon et al. (2018).

Tracer	Reference lifetime (Myr)
Hα	$4.6^{+0.2}_{-0.2}$
FUV	$19.2^{+0.5}_{-0.5}$
NUV	$23.2^{+0.5}_{-0.5}$

the necessity to filter a maximum of the diffuse emission. We further investigate the impact of the choice of the parameter n_λ on our results in Appendix 3.6. In summary, we find that the choice of n_λ, for values above $n_\lambda = 11$, does not have a strong impact on the measured value of λ. However, increasing the value of n_λ causes our measured value of $t_{\rm CO}$ to decrease (up to a factor of ~ 2 at $n_\lambda = 500$). This effect is due to the fact that large-scale diffuse emission is not adequately removed. After applying this filter in Fourier space, we apply a threshold at twice the noise level in the tracer map, as calculated from the standard deviation of a region of the tracer map chosen to avoid emission from M33 and field stars.

As a result of decomposing the input images into diffuse and compact components, we are able to calculate the fraction of emission in the images that is in compact structures (and likewise the fraction that is diffuse). In order to do this, we apply corrective factors for emission that is lost from compact regions due to application of the filter in Fourier space. This is due to the fact that a Gaussian filter has a smooth roll-off from the totally attenuated part of Fourier space to the unattenuated part of Fourier space, avoiding the introduction of distortions into the maps. Therefore some of the flux from the compact regions of interest is attenuated by the filter. We apply two corrections. The first correction, $q_{\rm con}$, accounts for the flux that would be lost from a single region due to the extended nature of the region and the filter in Fourier space. $q_{\rm con}$ has been calibrated in Hygate et al. (2019) and is calculated as

$$q_{\rm con} = 1 + \frac{-1.016}{\left(1 + \left(\frac{n_\lambda \lambda}{G_{\rm FWHM}}/4.86\right)^{1.69}\right)}, \tag{3.3}$$

where $G_{\rm FWHM}$ is the compact region FWHM and $n_\lambda \lambda$ is the characteristic size of the filter.

The second correction, $q_{\rm overlap}$, accounts for the additional flux that is lost due to overlapping regions as a result of overlapping regions causing a greater fraction of the flux from compact regions to appear in the longer spatial wavelength part of Fourier space and thus causing more attenuation of this flux from the applied filter. This correction is based on the distribution of nearest neighbour distances between identified emission peaks in the image. We calculate $q_{\rm overlap}$ using Equation 3.6. This correction factor differs from q_η presented in Hygate et al. (2019), and is calibrated in Appendix 3.7. For the compact emission fractions reported in this paper, this prescription produces results that broadly agree with those obtained applying the method of Hygate et al. (2019) (see Table 3.7)

3.3.2 Peak identification and masking

We use CLUMPFIND[24] (Williams et al., 1994) to identify peaks in each of our tracer maps. In all maps we impose a minimum number of pixels ($N_{\rm pix,min} = 10$) and a threshold above the map flux

[24] http://www.ifa.hawaii.edu/users/jpw/clumpfind.shtml

Table 3.2: The logarithmic depth below the maximum flux in a tracer map, $\Delta \log_{10} \mathcal{F}$, and the logarithmic interval between flux contour levels, $\delta \log_{10} \mathcal{F}$, used to determine peak locations in the tracer maps utilised for the presented analysis.

Tracer	$\Delta \log_{10} \mathcal{F}$	$\delta \log_{10} \mathcal{F}$
CO	1.1	0.4
Hα	2.0	0.5
FUV	2.5	0.5
NUV	2.5	0.5

sensitivity limit, σ, ($N_\sigma = 5.0$) for a peak to be valid. For each tracer map we define a logarithmic range below the tracer map flux maximum, $\Delta \log_{10} \mathcal{F}$, and a logarithmic interval between flux contour levels, $\delta \log_{10} \mathcal{F}$, for the peak finding process. The values for each tracer map are summarised in Table 3.2. We select these values such that peaks in the three SFR tracer maps that are co-spatial regions, visible in all maps are identified in all maps and that highly significant regions that can be identified by eye are also identified by the algorithm. The impact of the peak finding parameters on the parameters measured in the analysis is discussed in Appendix 3.8. We find that the value of $\Delta \log_{10} \mathcal{F}$ used to identify peaks in the stellar maps has little impact on our results after the brightest peaks have been identified at $\Delta \log_{10} \mathcal{F} = 2.0$. Further explanation of the parameters used for peak identification are given in section 3.2.1 of Kruijssen et al. (2018). The resultant identified peaks for each of the tracer maps that we use in the presented analysis are displayed in Figure 3.3.

We also apply a mask to our data that is displayed in Figure 3.3 and we only select peaks that are located in a position that is not masked. We mask a number of regions in the stellar images using the masking routine in the HEISENBERG code, for this purpose we set the keywords MASK_IMAGES = 1 and MSTAR_INT = 1 . We mask the tracer images outwith an ellipse of 5kpc radius centred on M33's centre and adjusted for inclination to ensure good coverage with our tracer images. We mask foreground stars, the identification of which we describe in Section 3.2.2. For identifying emission peaks we apply only these masks. However, when running our analysis we also mask the brightest HII region in M33, NGC604, as it may have formed as a result of tidal interaction between M33 and M31 (Tachihara et al., 2018) and thus may not represent the normal mode of star formation in the rest of M33. We examine the impact of this masking choice on our results in Appendix 3.9. Overall, we find that including NGC604 does not significantly affect our analysis, leading most notably to an increase in the value of $t_{\rm CO}$ measured with FUV.

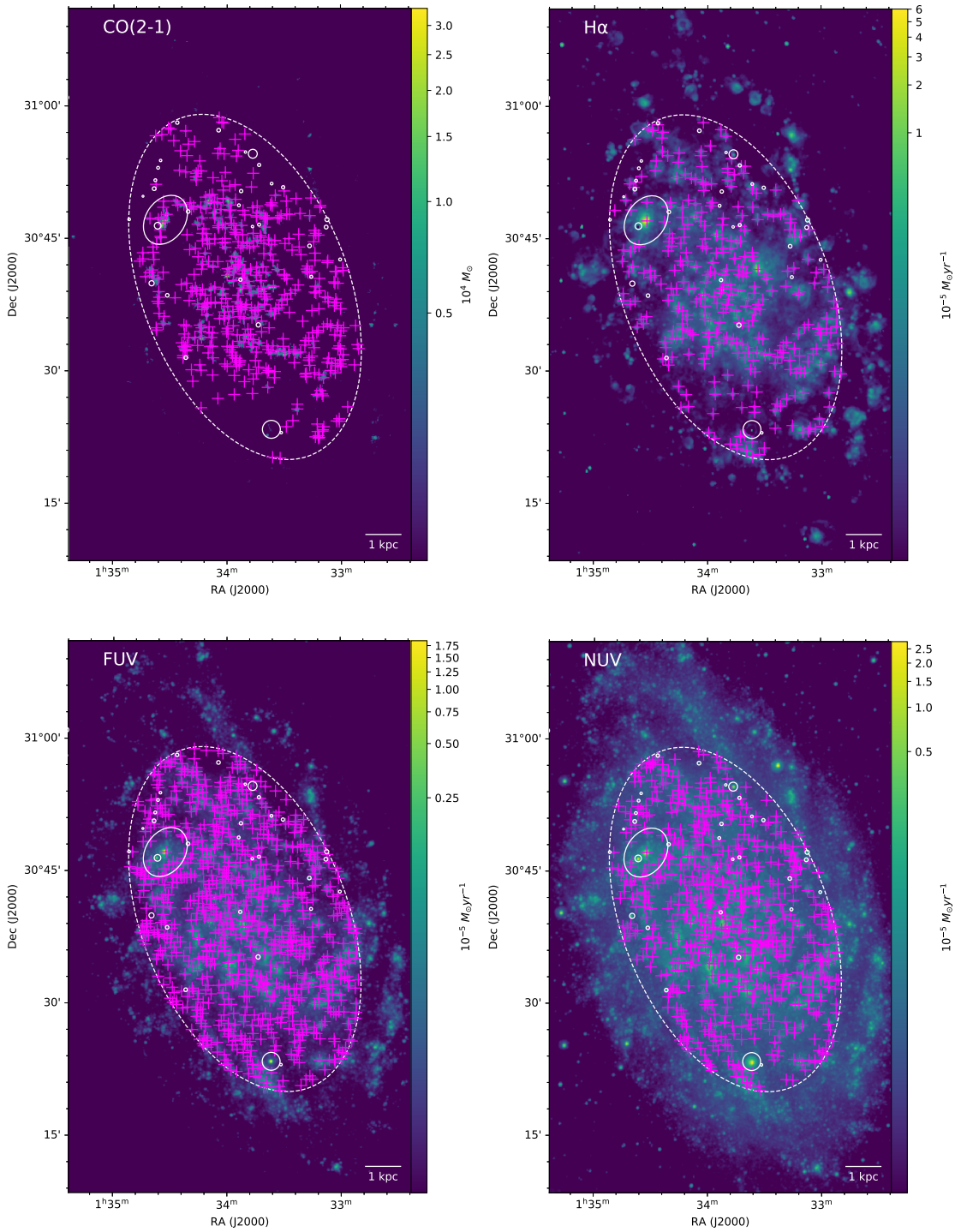

Figure 3.3: Identified peaks on which apertures are centred during the application of the HEISENBERG code (magenta crosses), and masked regions white ellipses in [Top left panel] CO(2-1), [Top right panel] Hα, [Bottom left panel] FUV and [Bottom right panel] NUV. We note that we are displaying peaks that have been identified on the filtered maps presented in Figures 3.5-3.8. The solid white circles are stars masked due to their UV colour (see Section 3.2.2). The large solid ellipse in the north-east (top left) is the mask applied to the largest HII region in M33, NGC604. Lastly the dashed ellipse indicates the 5 kpc region to which the analysis is restricted.

3.4 Results and discussion

We present the results of the application of the HEISENBERG code to the nearby flocculent spiral galaxy M33. As already stated, we use CO(2-1) to trace the molecular gas and three separate tracers of the SFR (Hα, FUV and NUV). For all the tracers, we consider only the range $0-5$ kpc in galactocentric radius and apply a mask that we describe in Section 3.3.2. We display measurements of the gas-to-stellar flux ratio in apertures ranging in size from the resolution of the dataset (49 pc, uncorrected for inclination) to kpc-scales where a galactic average value is recovered (~ 2.2 kpc), for each SFR tracer in combination with CO, along with the best-fitting model in Figure 3.4. The key quantities constrained from these analyses ($t_{\rm CO}$, $t_{\rm fb}$, λ, $\epsilon_{\rm sf}$, $\eta_{\rm fb}$ and $v_{\rm fb}$) along with the goodness of fit statistic, $\chi^2_{\rm red}$, for each experiment are summarised in Table 3.3. Our main conclusion from these measurements is that star formation in M33 proceeds quickly in about one to two cloud freefall times ($t_{\rm CO} = 19.5^{+3.0}_{-3.2}$ Myr, compared to $t_{ff} \sim 15$Myr; Schruba et al. 2019) and that star formation events are inefficient at converting gas into stars, with $\epsilon_{\rm sf} = 3.6^{+0.6}_{-0.6}$ per cent in each star-forming cycle.

We first present the fundamental fitting parameters that we obtain from the HEISENBERG code: λ, $t_{\rm CO}$ and $t_{\rm fb}$. We then discuss the secondary quantities that can be obtained from these parameters.

3.4.1 The evolutionary cycle of cloud and star formation in M33

We find good agreement between measurements of the mean region separation length between our best-fitting HEISENBERG models for our three different star formation tracers, with $\lambda_{\rm H\alpha} = 185^{+49}_{-35}$ pc, $\lambda_{\rm FUV} = 159^{+19}_{-17}$ pc and $\lambda_{\rm NUV} = 169^{+19}_{-18}$ pc. The values are all well within the 1σ error bounds of the other measurements.

For the measured values of the molecular cloud lifetime, we find that the measurements are in reasonable agreement with each other. We measure $19.7^{+3.1}_{-3.6}$ Myr with Hα, $16.5^{+2.1}_{-1.8}$ Myr with FUV and $20.4^{+2.5}_{-2.1}$ Myr with NUV. The agreement we find between the cloud lifetimes measured from the three different tracers presents observational evidence for the validity of the prescriptions presented by Haydon et al. (2018) for the visibility lifetimes of these tracers, which are used in our analysis to calibrate our measured star formation time-lines. We calculate an average gas cloud lifetime of $19.5^{+3.0}_{-3.2}$ Myr by combining the full probability density functions (PDFs) from each measurement using a weighting scheme described in Appendix 3.10. These cloud lifetimes are short, being approximately one to two times the ~ 15 Myr cloud freefall time-scale in M33 (Schruba et al., 2019). Therefore star formation in M33 proceeds rapidly from the formation of molecular clouds.

A number of previous studies (Discussed in Section 3.1) have estimated the cloud lifetime in M33. Most recently, Corbelli et al. (2017) estimated a 14.2 Myr GMC lifetime by classifying GMCs by the presence of young stellar clusters and HII regions. We measure cloud lifetimes that broadly agree with this estimate within $1-2\sigma$. We find that our measured values of the molecular cloud lifetime all lie within (or just above) the 10-20 Myr cloud lifetime estimate of Engargiola et al. (2003), which is predicated on dynamical arguments. Miura et al. (2012) estimate a cloud lifetime of 20-40 Myr, by age dating GMCs in relation to stellar objects. Our measurements agree with the lower range of their estimate, with most of their range being somewhat in excess of our measurements. However, their estimate is based on a smaller catalogue of 71 GMCs with masses in excess of 10^5 $M_\odot$ and therefore may be measuring the lifetimes of only the most massive GMCs, which we expect to have longer lifetimes. Indeed, at the low molecular gas surface density across the majority of M33's disc (see e.g. Druard et al. 2014), we expect the cloud lifetime to be mainly set by internal dynamical processes (such as the cloud free fall time or the cloud crossing time; Chevance et al. 2019). Furthermore Miura et al. (2012) have only partial, discontinuous observational coverage of M33 and they target the galactic centre and spiral arm regions of M33. These factors may bias

their cloud lifetime estimate. Indeed, Kruijssen et al. (2019) find that the molecular cloud lifetime increases towards the centre of NGC300, a nearby flocculent spiral with about half the mass of M33. Overall, we find that our measurements are broadly consistent with previous estimates of the cloud lifetime in M33.

With regards to the feedback time-scale, our measurements are consistent with the clouds surviving until the earliest onset of supernovae at ~ 3 Myr (Leitherer et al., 2014). For our individual tracers, we find a small discrepancy between the measured values of the feedback time-scale, $t_{\rm fb}$. The values measured using the two UV tracers ($2.1^{+0.9}_{-0.9}$ Myr and $2.3^{+1.0}_{-1.1}$ Myr for FUV and NUV, respectively) agree well with each other, with the 1σ errors including the central values of the other measurement. The Hα-based measurement, $5.2^{+0.9}_{-1.3}$ Myr, is somewhat larger. We attribute this difference to the differing impact of extinction on the SFR tracers. As the duration of the derived evolutionary cycle is calibrated using the duration of the isolated SFR tracers (once the gas has been cleared), the total duration of a cycle is unaffected by potential extinction. However, the measured duration of the feedback time-scale can be affected by extinction if the earliest, embedded phase of star formation becomes totally obscured in the considered tracer. This would reduce the visibility time of a star formation tracer and lead to a shorter duration of the co-existence phase between CO and the given SFR tracer (i.e. $t_{\rm fb}$). The UV tracers, at short wavelengths, are presumably more affected by extinction, leading to a shorter $t_{\rm fb}$. However, we do not expect a large impact from the extinction we observe in M33 on the overall evolutionary timeline that we measure. Indeed, Kruijssen et al. (2019) find that the Hα emission traces most of the massive star formation (~ 97 per cent) in NGC300 (a flocculent spiral at half-solar metallicity), by comparing Hα emission to 24μm emission (which traces embedded star formation), showing that the impact of extinction on the cloud-scale is not necessarily significant for Hα in a similar galaxy. In addition, Haydon et al. (2019) demonstrate that for the mean extinction on the galaxy scale to have a significant impact on measurements of the overall evolutionary timeline with the Heisenberg code, the mean galactic extinction needs to exceed $A_{\rm V} \sim 0.5$ mag for GALEX FUV and NUV and $A_{\rm V} \sim 1.0$ mag for Hα. The mean galactic extinction across M33's disk in the V-band, $A_{\rm V} \sim 0.3$ mag (Verley et al., 2009; Williams et al., 2019), is significantly below these thresholds. Therefore we do not expect a significant impact on our measured timescales from the galaxy averaged extinction.

3.4.2 Derived physical properties

A number of additional physical parameters can be derived from the fundamental parameters we present in Section 3.4.1. Similarly to our measurements of $t_{\rm fb}$, we find different feedback velocities for our UV and Hα tracers. We find that the feedback velocities, $v_{\rm fb}$, measured using a UV tracer of the young-stellar phase ($16.9^{+12.4}_{-4.9}$ km s^{-1} from FUV and $15.6^{+12.8}_{-4.5}$ km s^{-1} from NUV) are faster than the value measured from Hα ($6.7^{+1.9}_{-0.8}$ km s^{-1}). We again attribute this to the impact of extinction on the tracers due to the fact that we calculate $v_{\rm fb}$ as the ratio of the molecular gas region radius to the feedback time-scale $r_{\rm CO}/t_{\rm fb}$, where $r_{\rm CO}$ is the characteristic size of a CO region, as measured with the Heisenberg code. Thus an underestimate of $t_{\rm fb}$ leads to an overestimate of $v_{\rm fb}$. This feedback velocity in molecular gas is consistent to within a factor of ~ 2 with measured velocities of expanding holes in atomic gas. Deul & den Hartog (1990) find that small HI holes in M33 with a diameter less than 200 pc, which is approximately the mean separation between star-forming regions (λ), are well correlated with OB associations and somewhat less well correlated with HII regions. They measure expansion velocities of 4-28 km s^{-1} for the HI holes, with the majority having expansion velocities of ~ 15 km s^{-1}. This is also consistent with typical expansion velocities of HII regions measured in the Milky Way and nearby galaxies (e.g Bertoldi & McKee, 1990; Murray & Rahman, 2010; Kruijssen et al., 2019; McLeod et al., 2019).

We calculate the star formation efficiency per star formation event, $\epsilon_{\rm sf}$, as

$$\epsilon_{\rm sf} = \frac{t_{\rm CO}}{t_{\rm depl}}, \tag{3.4}$$

where we calculate the depletion time, $t_{\rm depl}$, as the ratio of the gas mass located in compact molecular clouds to the total SFR. In order to account for unextincted and extincted star formation when calculating $t_{\rm depl}$, we measure the SFR from a combination of the GALEX FUV and WISE W4 tracers, as presented in Leroy et al. (2019). We also calculate the gas mass using the mass remaining after Fourier filtering.[25] For both the gas mass and SFR we calculate values only within the unmasked areas of the galaxy. We measure low star formation efficiency from our experiments with all three star formation tracers, with $\epsilon_{\rm sf,H\alpha} = 3.6^{+2.6}_{-0.7}$ per cent, $\epsilon_{\rm sf,FUV} = 3.1^{+0.4}_{-0.3}$ per cent and $\epsilon_{\rm sf,NUV} = 3.8^{+0.4}_{-0.3}$ per cent. We calculate an averaged value, $3.6^{+0.6}_{-0.6}$ per cent, by weighting the PDFs for each measurement using the procedure detailed in Appendix 3.10.

We also report the mass loading factor, $\eta_{\rm fb}$, which is the time-averaged outflow rate of mass from star-forming regions in units of the SFR, calculated from $\epsilon_{\rm sf}$ as

$$\eta_{\rm fb} = \frac{1-\epsilon_{\rm sf}}{\epsilon_{\rm sf}}. \tag{3.5}$$

For the three different star formation tracers the values we measure are: $\eta_{\rm fb,H\alpha} = 27^{+6}_{-4}$, $\eta_{\rm fb,FUV} = 30^{+3.8}_{-3.6}$ and $\eta_{\rm fb,NUV} = 27^{+6}_{-4}$. We calculate an averaged value of 26^{+5}_{-4}, again by weighting the PDFs for each measurement using the procedure detailed in Appendix 3.10.

3.4.3 Comparison with the flocculent galaxy NGC300

M33 and NGC300 are in many respects similar galaxies, with both having a total mass of $\sim 10^{10}$M$_\odot$ (see Kam et al. 2017 for an analysis of the mass of M33 and Westmeier et al. 2011 for NGC300). M33 is approximately two to three times as active in star formation and as massive (overall and in terms of stellar and molecular gas mass), than NGC300, though NGC300 has a greater atomic mass reservoir (see Schruba et al. 2019). Despite many similarities in the physical properties of M33 and NGC300, there are, however, a number of differences between the two galaxies. The differing environment of the two galaxies may play a role. M33 is on a close orbit ($\sim$ 200kpc current separation) around the massive spiral galaxy M31 (Brunthaler et al., 2005). In contrast, NGC300 is relatively isolated - with the most significant galaxy in close proximity (seperated by $\sim$ 0.5 Mpc) being NGC55 (Karachentsev et al., 2003), a galaxy of similar mass to NGC300 (Westmeier et al., 2013). There is, furthermore, evidence that M33's gas disc has been tidally disrupted 1-3 Gyrs ago (Putman et al., 2009). In addition the star formation histories of NGC300 and M33 are observed to be different, with NGC300 having formed many more of its stars at earlier times than M33 (Gogarten et al., 2010; Kang et al., 2017), with the mean age in the centres of the galaxies being 6.37 Gyr and 7.70 Gyr for M33 and NGC 300, respectively.

The HEISENBERG code has also been applied to the nearby flocculent galaxy NGC300 using CO(1-0) and Hα as tracers of the molecular gas and SFR, respectively (Kruijssen et al., 2019). We find, similarly to NGC300, that star formation in M33 is fast and inefficient with relatively short $t_{\rm CO}$ and small $\epsilon_{\rm sf}$. For NGC300, Kruijssen et al. (2019) measure a CO-visible molecular cloud lifetime of $10.8^{+2.1}_{-1.7}$ Myr and a star formation efficiency of $2.5^{+1.9}_{-1.1}$ per cent. We measure a significantly longer

[25] We note, however, that as the compact fraction in the CO map is close to 100 per cent, this choice makes little difference to the measured value of $\epsilon_{\rm sf}$.

cloud lifetime in M33 (an averaged value of $t_{\rm CO} = 19.5^{+3.0}_{-3.2}$ Myr), but our measured star formation efficiency is comparable with that in NGC300. Interestingly, the measured feedback time-scale in NGC300 ($t_{\rm fb} = 1.5^{+0.2}_{-0.2}$ Myr), is significantly shorter than the value we measure in M33 ($t_{\rm fb} = 5.2^{+0.9}_{-1.3}$ Myr with Hα). Schruba et al. (2019) find that the molecular gas surface density of GMCs in M33 and NGC300 are approximately the same, but the radius of clouds in M33 are approximately twice those of NGC300 and M33's clouds are roughly 2.5 times as massive as those in NGC300. This combination of mass and radius would lead to twice as long a time-scale for dispersal of clouds by photoionization in M33. Additionally, the lower cloud volume density in M33, may also mean that feedback couples less well to the cloud and thus allowing a greater fraction of emission to escape during earlier evolutionary states in M33. Thus, slower destruction of clouds as a result of feedback in M33 may contribute to the longer observed cloud lifetime. In addition, cloud time-scales derived from internal dynamics are longer in M33 than NGC300. Schruba et al. (2019) calculate a freefall time of 15.0 Myr in M33 and 8.8 Myr in NGC300. Similarly, they measure the crossing time at 10.6 Myr in Myr and 6.3 Myr in NGC300. The structure of the ISM may well also play a role in the lifetime of molecular clouds and we find that the star-forming region separation length is somewhat shorter in NGC300 ($\lambda = 104^{+22}_{-18}$ pc), compared to our measurement in M33 ($\lambda = 185^{+49}_{-35}$ pc using Hα).

With only two galaxies, it is not possible to draw definitive conclusions from the differences that are observed. A proper understanding of the factors that drive differences in cloud lifecycles and other cloud-scale physical properties between different galaxies necessitates measurements of these quantities in a larger sample of galaxies. Such an application to the PHANGS pilot sample of nine galaxies is presented in Chevance et al. (2019). These galaxies have stellar masses that are an order of magnitude larger than that of M33. Similarly to the findings of Kruijssen et al. (2019) and this paper, Chevance et al. (2019) find short ($\sim 10 - 30$ Myr) cloud lifetimes. They find that the cloud lifetime correlates with the time-scales of galactic dynamical processes at high (azimuthally-averaged) molecular gas surface densities, $\Sigma_{\rm H_2} \geqslant 8$ M$_\odot$ pc^{-2}, whereas at low (azimuthally-averaged) molecular gas surface densities, $\Sigma_{\rm H_2} \leqslant 8$ M$_\odot$ pc^{-2}, it correlates with the cloud's internal dynamical time-scales (the freefall and crossing times). Whilst NGC300's molecular surface density profile remains below ~ 3 M$_\odot$ pc^{-2} (Kruijssen et al., 2019), M33's molecular gas surface density profile ranges between ~ 10 M$_\odot$ pc^{-2} at the galactic centre and ~ 1 M$_\odot$ pc^{-2} at 5 kpc (see Druard et al. 2014), which is the edge of the region we cover. The higher gas surface densities reached in M33 may further explain the differences observed in comparison with NGC300. Indeed, in M33's inner region, we therefore expect galactic dynamics to play a role in setting the molecular cloud lifetime, while at the low-surface densities of NGC300, clouds are decoupled from galactic dynamics and their lifetime is expected to be set by internal processes.

3.4.4 Diffuse and compact emission decomposition

We apply the Fourier filtering method presented in Hygate et al. (2019), as updated in Appendix 3.7, to decompose our tracer maps into diffuse and compact emission images. These maps are presented for the three star formation tracer maps we utilise: Hα, FUV and NUV in Figures 3.5, 3.6 and 3.7, respectively. We note that for CO, we have three separate decompositions corresponding to each experiment with each star formation tracer. However, as there is very little variation between our measurements of λ and thus of the decompositions of the CO tracer map, we display only the decomposition from the experiment using Hα as the star formation tracer in Figure 3.8.

From these decomposed maps we are able to measure the fraction of diffuse and compact emission. We list the compact fraction in each tracer along with the corrective factors $q_{\rm con}$ and $q_{\rm overlap}$ in Table 3.4. For the three star formation tracers we measure: $f_{\rm compact,H\alpha} = 52^{+2}_{-3}$ per cent,

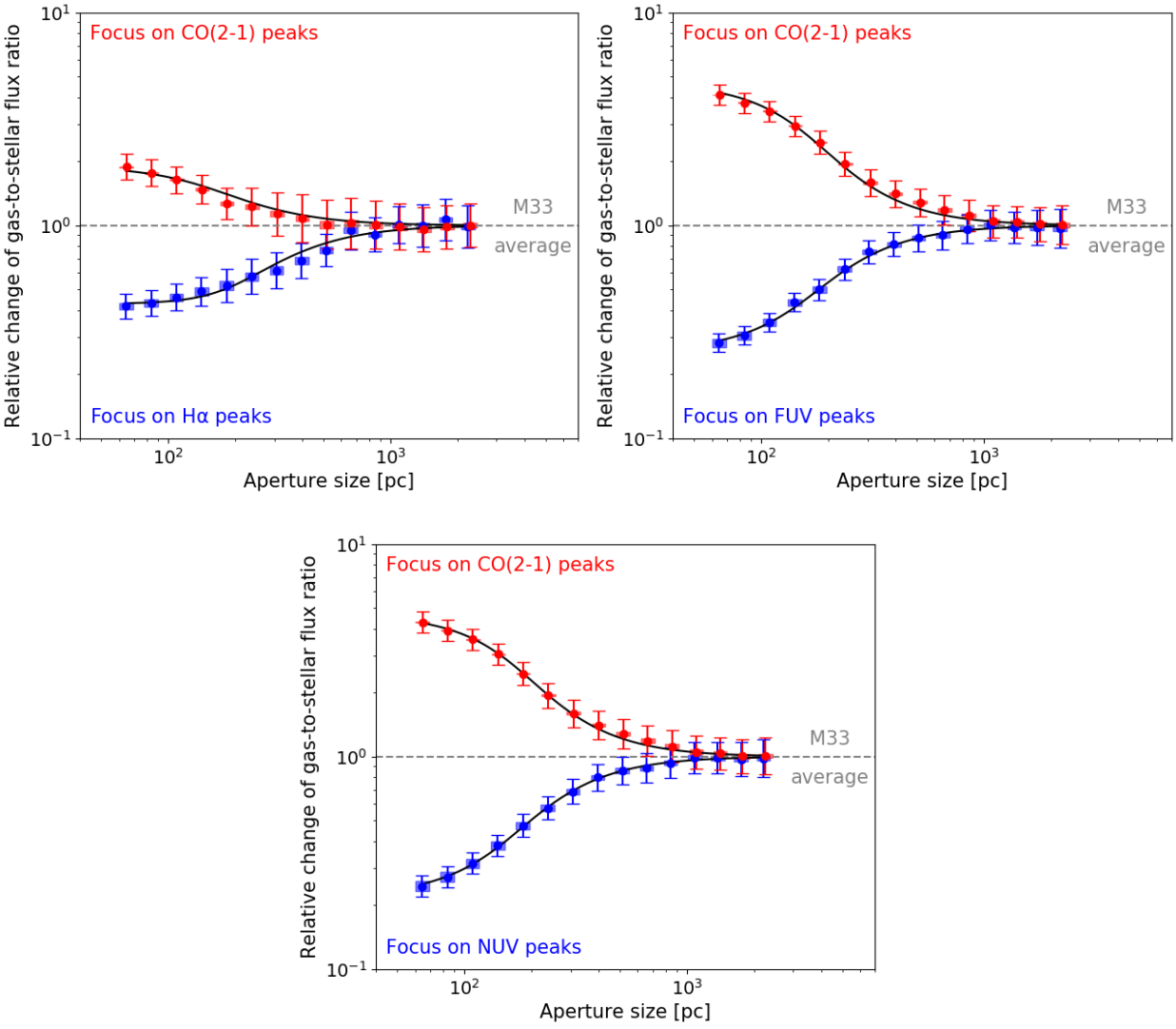

Figure 3.4: The best-fitting HEISENBERG models with CO(2-1) as the gas tracer and [Left panel] Hα, [Middle panel] FUV and [right panel] NUV as the young-stellar tracer. The diagrams show the measured ratio of the depletion time in an ensemble of apertures centred on peaks in the gas or young-stellar distributions, normalised to the galactic average depletion time, against the size of the apertures in which the measurement is calculated, $l_{\rm ap}$. An explanation of these diagrams is given in Figure 3.2. Measurements from apertures focussed on peaks in the gas distribution are shown as filled red circles and those from apertures focussed on peaks in the stellar distribution are shown as blue filled circles. The 1σ uncertainties are indicated by the error bars and the shaded rectangles indicate the 1σ uncertainties, calculated accounting for the covariance between data points. The best-fitting model is shown as the solid green lines. The black arrow indicates the value of the mean region separation length, λ, measured from the model.

Table 3.3: The best fitting values of the parameters constrained by our analysis for Hα, FUV and NUV in combination with CO(2-1). We also present results combined using the method presented in Appendix 3.10. We list the values, with their 1σ uncertainties, of the molecular cloud lifetime ($t_{\rm CO}$), the feedback time-scale ($t_{\rm fb}$), the mean separation length between regions (λ), the star formation efficiency per star formation event ($\epsilon_{\rm sf}$), the mass loading factor ($\eta_{\rm fb}$), the feedback velocity ($v_{\rm fb}$) and the reduced χ^2 statistic for the HEISENBERG code fit ($\chi^2_{\rm red}$). The first three parameters are directly derived from the fit of the model (see Section 3.3.1) while the other quantities are derived from these parameters as described in Kruijssen et al. (2018).

SFR tracer	$t_{\rm CO}$ [Myr]	$t_{\rm fb}$ [Myr]	λ [pc]	$\epsilon_{\rm sf}$ [%]	$\eta_{\rm fb}$ [-]	$v_{\rm fb}$ [kms^{-1}]	$\chi^2_{\rm red}$ [-]
Hα	$19.7^{+3.1}_{-3.6}$	$5.2^{+0.9}_{-1.3}$	185^{+49}_{-35}	$3.6^{+2.6}_{-0.7}$	27^{+6}_{-4}	$6.7^{+1.9}_{-0.8}$	0.55
FUV	$16.5^{+2.1}_{-1.8}$	$2.1^{+0.9}_{-0.9}$	159^{+19}_{-17}	$3.1^{+0.4}_{-0.3}$	$30^{+3.8}_{-3.6}$	$16.9^{+12.4}_{-4.9}$	0.42
NUV	$20.4^{+2.5}_{-2.1}$	$2.3^{+1.0}_{-1.1}$	169^{+19}_{-18}	$3.8^{+0.4}_{-0.3}$	27^{+6}_{-4}	$15.6^{+12.8}_{-4.5}$	0.14
Combined	$19.5^{+3.0}_{-3.2}$	-	-	$3.6^{+0.6}_{-0.6}$	26^{+5}_{-4}	-	-

Table 3.4: Measurements of the compact emission fractions, $f_{\rm compact}$ and corrective factors, $q_{\rm con}$ and $q_{\rm overlap}$ (see Section 3.3.1.3 for an explanation of these terms) for our analyses with each of our SFR tracers (Hα, FUV and NUV) in combination with CO(2-1). We also present a combined CO diffuse fraction using the method described in Appendix 3.10

SFR tracer	$f_{\rm compact,SFR}$ [%]	$q_{\rm con,SFR}$ [-]	$q_{\rm overlap,SFR}$ [-]	$f_{\rm compact,CO}$ [%]	$q_{\rm con,CO}$ [-]	$q_{\rm overlap,CO}$ [-]
Hα	52^{+2}_{-3}	0.93	0.82	95^{+3}_{-3}	0.94	0.69
FUV	37^{+1}_{-1}	0.92	0.74	92^{+4}_{-3}	0.92	0.70
NUV	33^{+1}_{-1}	0.93	0.75	93^{+3}_{-3}	0.92	0.70
Combined	-	-	-	94^{+3}_{-4}	0.93	0.70

$f_{\rm compact,FUV} = 37^{+1}_{-1}$ per cent and $f_{\rm compact,NUV} = 33^{+1}_{-1}$ per cent.

Firstly, we note that we find a very similar fraction of diffuse emission in the FUV and NUV tracers. Such similarity is not unexpected, as observations of diffuse UV emission in the Milky Way show strong correlation between the diffuse NUV and FUV backgrounds (Murthy et al., 2010; Murthy, 2014).

A number of previous determinations of the Hα diffuse fraction have been made in M33 to which we can compare our measurement. As, in the method of Hygate et al. (2019), the total flux in the image is simply the sum of the compact and diffuse emission, we measure $f_{\rm diffuse,H\alpha} = 48^{+3}_{-2}$ per cent. This is sightly larger than previous measurements of the diffuse fraction in Hα. Greenawalt (1998) measure a diffuse fraction of 43 ± 3 per cent and Hoopes et al. (2001) report a diffuse fraction of 38 ± 3 per cent, Other estimates are ~ 40 per cent (Thilker et al., 2005) and 44 per cent (Schruba et al., 2010).

In comparison to our method, Greenawalt (1998), Hoopes et al. (2001) and Thilker et al. (2005) use an image created with a smoothed median filter to remove diffuse emission. The different studies create this image at different size-scales: 900 pc (Greenawalt, 1998), 1 kpc (Hoopes et al., 2001) and 1.5 kpc (Thilker et al., 2005). The definition of the diffuse emission of these studies differs to the Gaussian Fourier filter employed in this study, which attenuates flux over size-scales differently to a median filter. Broadly, however, these studies and this paper agree that the majority of the diffuse Hα emission in M33 is on large scales ($\gtrsim 1$ kpc) much greater than the size scale of the separation between star formation regions ($\lambda \sim 170$pc).

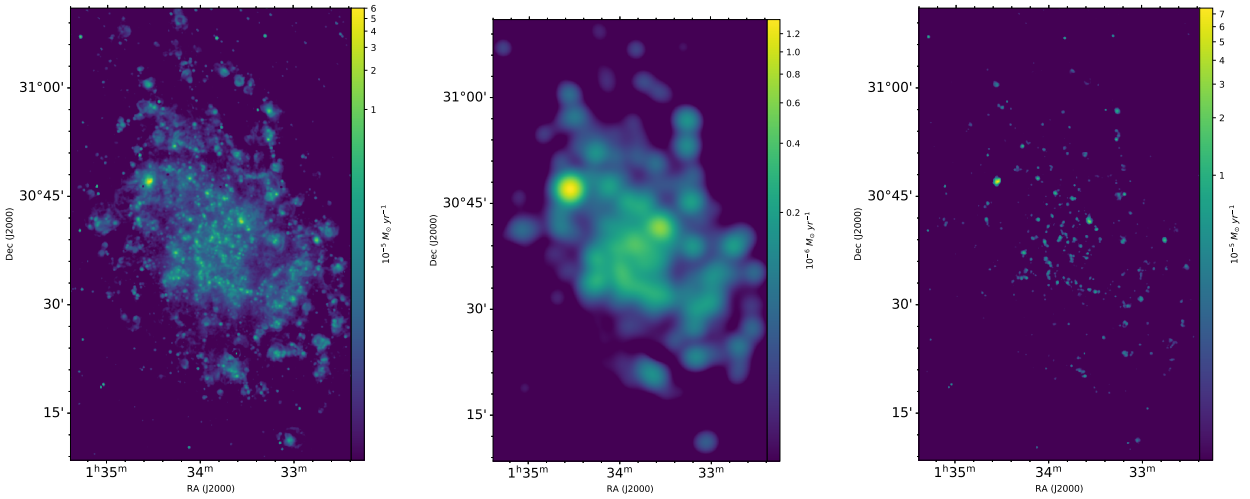

Figure 3.5: Decomposition of the Hα tracer map [Left Panel] into diffuse [Middle Panel] and compact [Right Panel] components. Note the different intensity scales for each of the panels.

The diffuse UV fraction of M33 has been studied far less extensively. However, Thilker et al. (2005) report an FUV diffuse emission fraction of ~ 65 per cent in M33, in reasonable agreement with our measurement of $f_{\mathrm{diffuse,FUV}} = 63^{+1}_{-1}$ per cent. However, it should again be noted that our definition of the diffuse emission differs to that of Thilker et al. (2005), who use a 1.5 kpc circular median filter to construct their diffuse component map, in contrast to the Fourier analysis applied here.

For the CO compact emission fraction we make three measurements, one for each of the experiments with a different star formation tracer: $f_{\mathrm{compact,CO\,(H}\alpha)} = 95^{+3}_{-3}$ per cent, $f_{\mathrm{compact,CO\,(FUV)}} = 92^{+4}_{-3}$ per cent and $f_{\mathrm{compact,CO\,(NUV)}} = 93^{+3}_{-3}$ per cent. We calculate an average value, 94^{+3}_{-4} per cent, using the method presented in Appendix 3.10. The weights that minimise the variance in the final derived emission fraction are $\alpha_{\mathrm{H}\alpha} = 0.47$, $\alpha_{\mathrm{NUV}} = 0.18$, and $\alpha_{\mathrm{FUV}} = 0.35$. We find that the measurements for each of the experiments agree well with each other. Comparing our finding of a small fraction of diffuse emission in CO(2-1) to previous measurements requires careful consideration of the methods used. In agreement with our measurement, Tosaki et al. (2011) report no smooth diffuse component above their sensitivity limit. The interferometric imaging reported by Rosolowsky et al. (2007) only recovered the brightest molecular gas peaks in the galaxy, which resulted in a recovery of 20 per cent of the total flux obtained by single dish measurements. However, differences in method, definition, field of view and sensitivity between these studies may explain these different measurements.

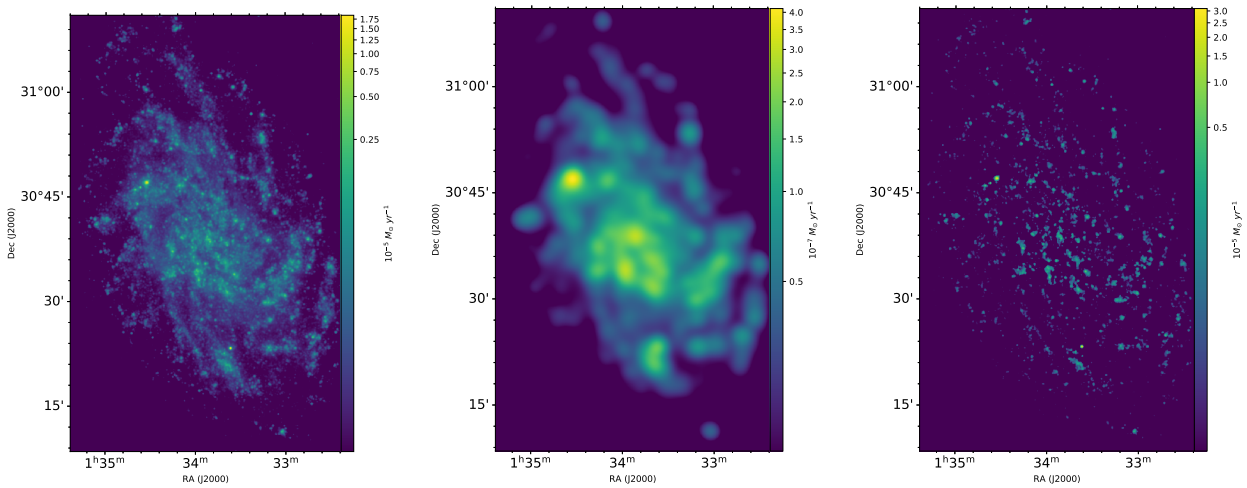

Figure 3.6: The decomposition of the FUV tracer map [Left Panel] into its diffuse [Middle Panel] and compact [Right Panel] components. Note the different intensity scales for each of the panels.

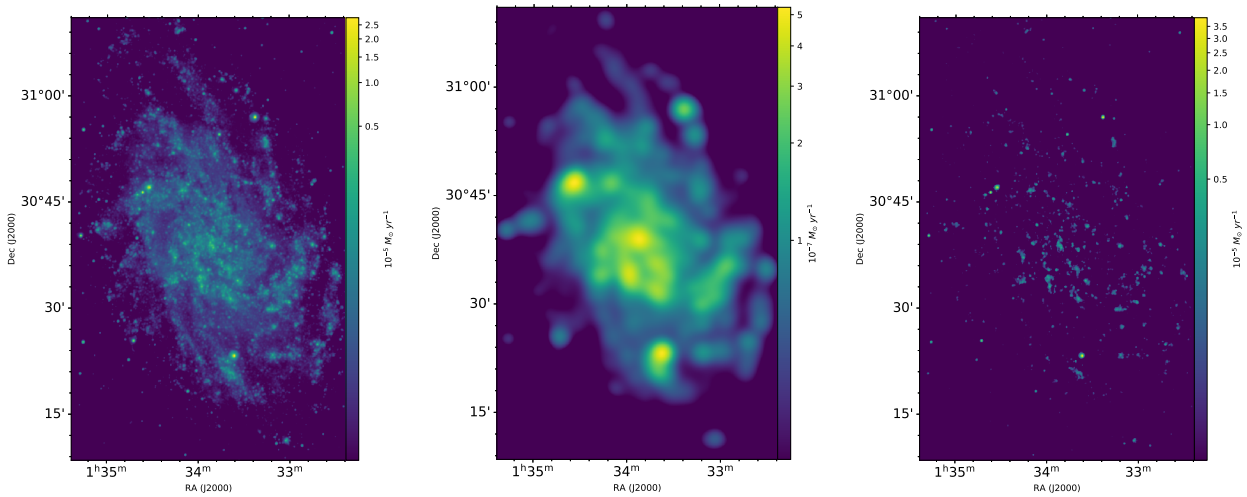

Figure 3.7: The decomposition of the NUV tracer map [Left Panel] into its diffuse [Middle Panel] and compact [Right Panel] components. Note the different intensity scales for each of the panels.

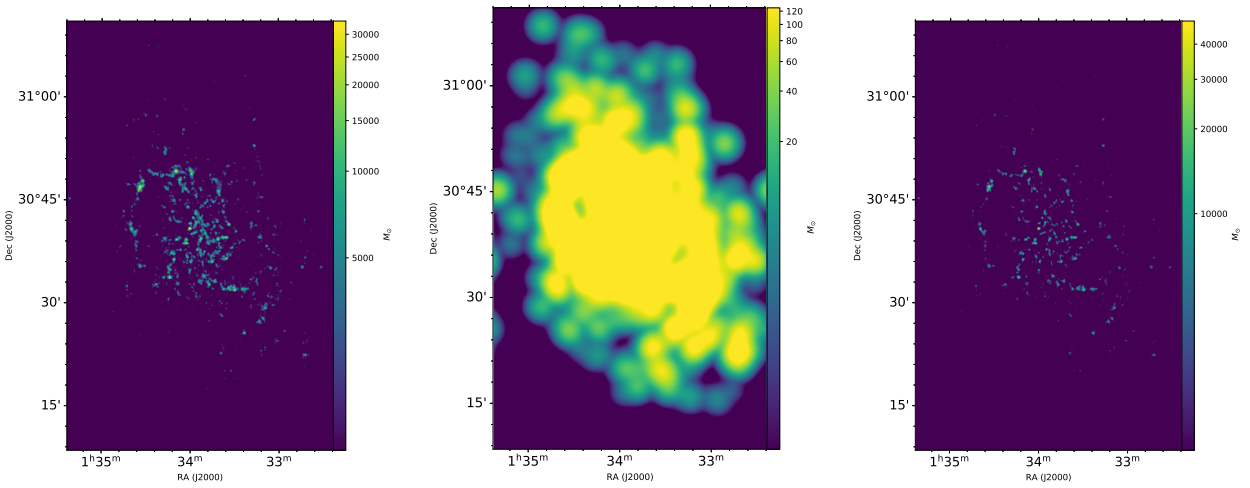

Figure 3.8: The decomposition, from the experiment with Hα as the tracer of star formation, of the CO tracer map [Left Panel] into its diffuse [Middle Panel] and compact [Right Panel] components. Note the different intensity scales for each of the panels.

3.5 Conclusions

We use a statistical analysis method, the HEISENBERG code (Kruijssen et al., 2018), to constrain cloud-scale quantities describing the ISM and star formation process in the Local Group flocculent spiral galaxy M33, including the molecular cloud lifetime, the duration of the feedback phase and the mean separation between star-forming regions. We have also applied the Fourier filtering method developed by Hygate et al. (2019) to decompose our tracer maps into diffuse and compact components and measure the fraction of diffuse emission in the images. Our major conclusions are as follows:

1. We measure a CO-visible molecular cloud lifetime, averaged from measurements with three different SFR tracers, of $t_{\rm CO} = 19.5^{+3.0}_{-3.2}$ Myr. We find broad agreement between measurements with our three SFR tracers. This agreement offers observational evidence for the validity of the visibility lifetimes of these tracers derived from simulations by Haydon et al. (2018), which we use as reference time-scales.

2. We measure a time-scale for the destruction of molecular clouds, $t_{\rm fb}$, of $5.2^{+0.9}_{-1.3}$ Myr from Hα, but shorter time-scales from our UV tracers ($t_{\rm fb,FUV} = 2.1^{+0.9}_{-0.9}$ Myr and $t_{\rm fb,NUV} = 2.3^{+1.0}_{-1.1}$ Myr). We ascribe this to the higher impact of extinction on the UV part of the spectrum than Hα. Caution should therefore be used when interpreting feedback related quantities measured with the HEISENBERG code when using a tracer heavily impacted by interstellar dust extinction such as GALEX FUV and NUV, as used in this analysis. An analysis that quantifies the impact of extinction on measurements made with the HEISENBERG code using synthetic observations is presented by Haydon et al. 2019.

3. We find that the mean separation length between star formation regions is ~ 170 pc. We also find good agreement between the values obtained when tracing recent star formation in FUV, NUV, or Hα.

4. We measure low star formation efficiency per star formation event in M33, as also found in other star-forming environments (including the Milky Way), with an averaged value of

$\epsilon_{sf} = 3.6^{+0.6}_{-0.6}$ per cent, with good agreement between our three SFR tracers.

5. We derive a mass loading factor, η_{fb}, with an averaged value of 26^{+5}_{-4}. Values of η_{fb} in excess of unity imply that only a small part of the cloud needs to be converted to stars release sufficient feedback to disperse the cloud.

6. We measure a significant fraction of diffuse emission in our SFR tracers. We find that 48^{+3}_{-2} per cent of emission in Hα is diffuse - in reasonably good agreement with other measurements from the literature (Greenawalt, 1998; Hoopes et al., 2001; Thilker et al., 2005; Schruba et al., 2010). We find that 63^{+1}_{-1} per cent of emission in FUV is diffuse, in reasonable agreement with a previous measurement by Thilker et al. (2005). We find that 67^{+1}_{-1} per cent of emission in NUV is diffuse, which closely matches our measurement of diffuse emission in FUV.

7. We find that very little of the CO(2-1) emission in our signal masked map is diffuse, with almost 100 per cent of the emission contained in compact regions.

8. We also present an update to the diffuse fraction measurement method of Hygate et al. (2019) in Appendix 3.7. This update more appropriately treats the flux loss due to overlap between regions in observational images and should be used in future applications of the method to observations.

In summary, we find that star formation in M33 is fast and inefficient. Star formation in M33 proceeds quickly, with clouds living for approximately one to two dynamical times. Clouds are able to survive the effects of feedback until the earliest onset time for supernovae, but are dispersed not long thereafter. Furthermore, each star formation event in M33 is inefficient with only a few per cent of the mass of molecular mass of clouds being converted into stars before the cloud is destroyed by feedback.

3.6 Impact of n_λ on our results

In the definition of the filter used in Fourier space to remove diffuse emission, we include a softening factor, n_λ, that reduces attenuation from the filter on compact regions (see Equation 3.2). We select the value of n_λ such that q_{con}, the flux remaining in individual compact regions in the tracer maps after the application of the filter is greater than 90 per cent, a threshold prescribed by testing of the method on simulations by Hygate et al. (2019). In this appendix we investigate how the parameter n_λ affects our results. For this purpose we re-run our experiments with all input parameters unchanged, including the identified peaks, except for the value of n_λ. Figure 3.9 shows the variation of the HEISENBERG code fitting parameters t_{CO}, t_{fb} and λ and the compact fractions of the stellar (f_{cl}) and CO (f_{GMC}) tracer maps with n_λ.

As the value of n_λ increases, less flux from larger spatial wavelengths is filtered from the maps leading to larger measured values of f_{cl} and f_{GMC} and increasing the biasing impact of diffuse emission on our measured parameters. For λ, we find that the measured value does not depend strongly on n_λ as long as the condition that $q_{con} > 0.9$ is satisfied. The large scale diffuse emission that is not filtered out at large values of n_λ does impact the values of t_{CO} and t_{fb}. The value of t_{CO} decreases gradually from ~ 20Myr at $n_\lambda = 11$ to ~ 10Myr at $n_\lambda = 200$, as less of the large scale diffuse emission is filtered out. For t_{fb}, we find a discrepancy between t_{fb} measured with Hα (longer t_{fb}) and t_{fb} measured with the two UV tracers (shorter t_{fb}) at low values of n_λ, however, at higher values of n_λ we measure similar values from all tracers.

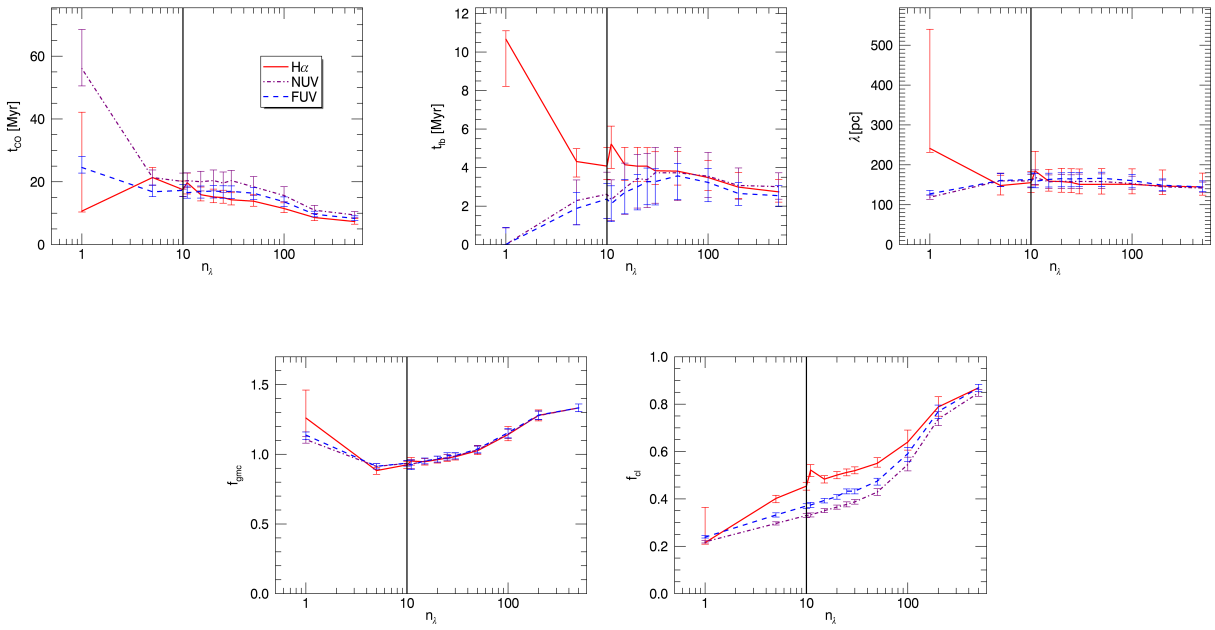

Figure 3.9: The variation of the measured values of [Top left panel] $t_{\rm CO}$, [Top middle panel] $t_{\rm fb}$, [Top right panel] λ, [Bottom left panel] the CO compact emission fraction, $f_{\rm GMC}$, and [Bottom right panel] the stellar tracer diffuse fraction, $f_{\rm cl}$, against n_λ, a softening factor in the Gaussian filter applied in Fourier space to remove diffuse emission (see Equation 3.2). The vertical black line indicates the point at which $q_{\rm con} = 0.9$ (testing of the method on simulations by Hygate et al. (2019) shows that $q_{\rm con} > 0.9$ for good application of the method). To the left of this line (i.e. $q_{\rm con} < 0.9$), a large fraction of flux (> 10 per cent) is removed from the compact regions and this has an adverse affect on the measured values. As n_λ increases to the right of this line (i.e. $q_{\rm con} > 0.9$), there is a gradual change in the measured parameters as flux from larger size-scales become included in the compact emission map.

3.7 Measuring compact emission fractions in observational images

In Hygate et al. (2019), we presented a method for measuring the fraction of diffuse and compact emission in astronomical images by separating the diffuse and compact emission in Fourier space based on the mean separation distance between independent regions, λ. For spatially extended compact regions, applying a filter in Fourier space can result in a fraction of flux from these compact regions also being removed by the filter. We identified two sources of this flux loss from compact regions: the flux loss from a single region when a filter is applied; and the additional flux loss, due to close regions overlapping and pushing more flux into the longer spatial wavelength part of Fourier space than would be expected for a single region. We developed and presented corrections for these sources of flux loss based upon simulated datasets in sections 6.1 and 6.2 of Hygate et al. (2019), respectively. In applying the prescription developed by Hygate et al. (2019) we find that the method does not work as intended on observational data. The simulated datasets on which this method was calibrated are generated with totally random placement of regions. However, observational images contain substructure, which causes peak separation to deviate from the totally random case. Thus, in this appendix we develop a new correction for the flux lost due to overlap on the basis of the observed distribution of identified peaks in the image.

These simulated datasets are generated with the method described in section 5 of Hygate et al.

(2019), which we summarise here. We generate images by randomly seeding Gaussian functions (which represent compact regions of interest such as molecular clouds) within a square area. A large-scale background may be added to the image to simulate diffuse emission. Each simulated dataset consists of a pair of images, representing two evolutionary phases in an evolutionary sequence. Gaussian functions are seeded into three populations: one appearing only in the first image, one appearing in only the second image and a third 'overlap' phase that appears in both images. These images may be used to represent any two phases in such a sequence, however, for consistency with the analysis presented in this paper we shall refer to first phase as "CO" and the second as "stars". The properties of the image are controlled with a number of input parameters. First, the number of Gaussian regions seeded into each population ($N_{\mathrm{peak,star,input}}$, $N_{\mathrm{peak,CO,input}}$, $N_{\mathrm{peak,over,input}}$) determines the relative lifetimes of the phases. G_{FWHM} sets the size of the Gaussian regions. The map filling factor, ζ,[26] sets how widely separated, on average, all the Gaussian regions are from one another. A tracer map of phase 'a' will have regions more closely spaced than that of phase 'b' when $N_{\mathrm{peak,a,input}} > N_{\mathrm{peak,b,input}}$, for a given value of ζ. Last, the fraction of the image that is in the compact phase is set by f_{compact}.

The separation between emission peaks in an image determines the extent to which flux is lost from these peaks due to overlap between them. Figure 3.10 shows the flux remaining in an image containing two or four Gaussians after filtering in Fourier space and correcting for the flux expected to be lost from single isolated Gaussians, q_{con}, against their separation in terms of the size of the peaks. The amount of additional flux lost due to overlap increases to a peak at around 2.5 FWHMs before decreasing again. Similar behaviour is seen for four Gaussian regions arranged in a cross, however, the amount of additional flux loss increases, as does the separation at which maximum flux loss occurs.

Therefore, to assess the appropriateness of the corrective method developed in Hygate et al. (2019), we investigate the distribution of the separations between the peaks themselves in the observational images used in this analysis and in simulated datasets. Figure 3.11 shows histograms of the distances between emission peaks in the simulated datasets, coloured according to η, a map filling factor that is the basis for the overlap flux loss correction in Hygate et al. (2019).[27] For these simulated images the value of η is a reasonable predictor of the separation profile of the images. Overplotted are histograms for the observed images of M33 used in this paper along with the values of η calculated for these images. The figure shows that the histograms of the distance between pairs of peaks for the M33 images are similar to the histograms for simulated images, however, with significantly lower η than that measured. We thus conclude that the prescription we developed in Hygate et al. (2019) does not accurately reflect the distribution of emission peaks in our observational images.

Thus, we accordingly proceed to develop a new correction for the flux lost due to overlap on the basis of the observed distribution of identified peaks in the image. To calibrate this correction, we generate simulated datasets using the method described in section 5 of Hygate et al. (2019) and summarised above. We list the parameters used to generate these datasets in Table 3.5. We chose a range of parameters that covers a large range of potential images and are optimised for accurate measurements. Testing of the HEISENBERG code gives a number of criteria that need to be satisfied for accurate measurements to be obtained (see section 4.4 of Kruijssen et al. 2018 for a full description of these criteria). In particular, we restrict the value of $\zeta < 0.5$ to minimize blending

[26] The filling factor ζ is defined for a particular tracer as $\zeta_{\mathrm{tracer}} = \frac{G_{\mathrm{FWHM,tracer}}/\sqrt{2\ln 2}}{\lambda}$

[27] The exact correction is $f_{\mathrm{compact,corrected}} = f_{\mathrm{compact,measured}}/q_\eta$, where $q_\eta = \min(1.09 - 1.52\eta, 1)$. η itself is defined as $\eta = \sqrt{\frac{t_{\mathrm{tracer}}}{\tau}}\ \frac{G_{\mathrm{FWHM,tracer}}/\sqrt{2\ln 2}}{\lambda}$, where t_{tracer}, is the lifetime associated to the tracer being corrected, τ is the duration of the total evolutionary timeline, $G_{\mathrm{FWHM,tracer}}$ is the FWHM of the regions in the tracer image and λ is the mean region separation length.

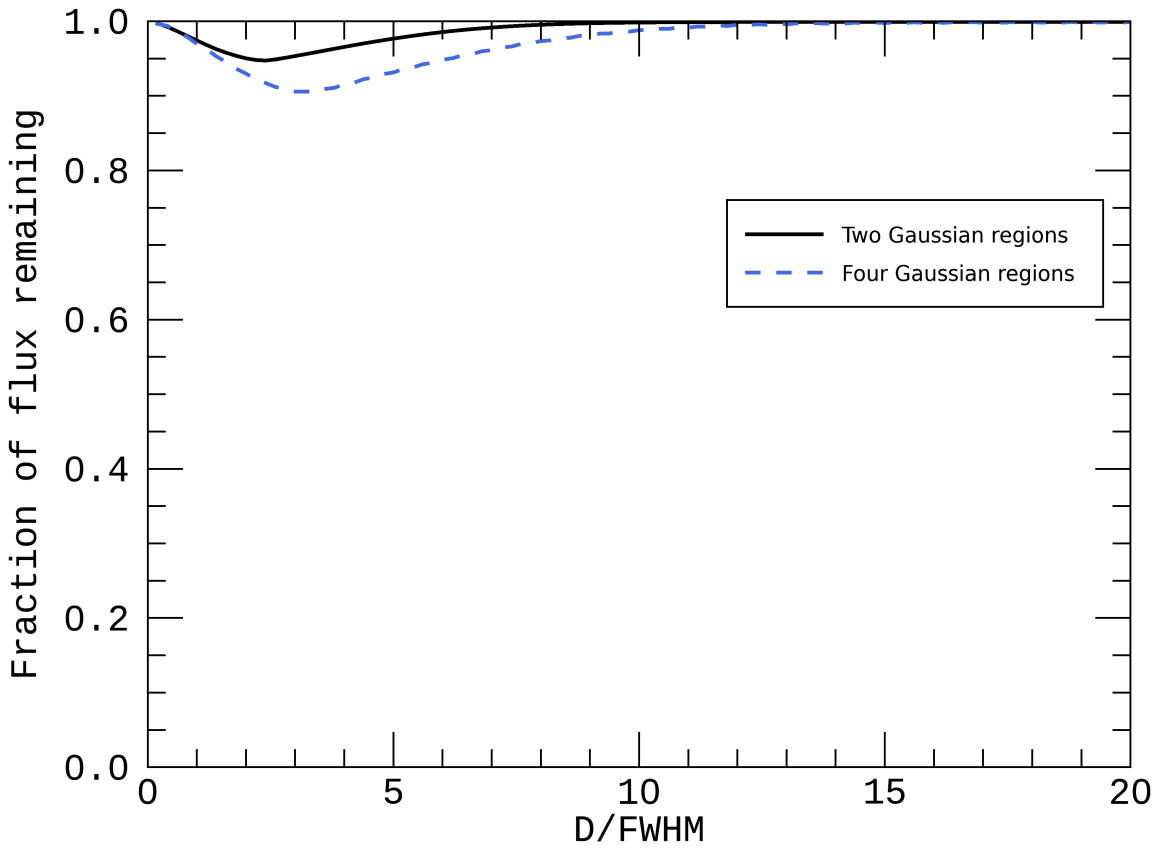

Figure 3.10: The fraction of flux remaining in an image containing two or four Gaussian regions after the application of a filter in Fourier space and correcting for the flux lost from single Gaussian regions against the separation distance between the regions normalised by the full-width at half-maximum of the regions. At large enough separations, the regions do not significantly overlap and there is no additional flux loss. At zero separations, also, there is no additional flux loss as the regions simply appear as one brighter region of the same size. However, as the regions are moved apart the amount of flux loss increases to a maximum before reducing as they move further apart. Moreover, this maximum increases and occurs at larger distances as the number of Gaussian regions increases.

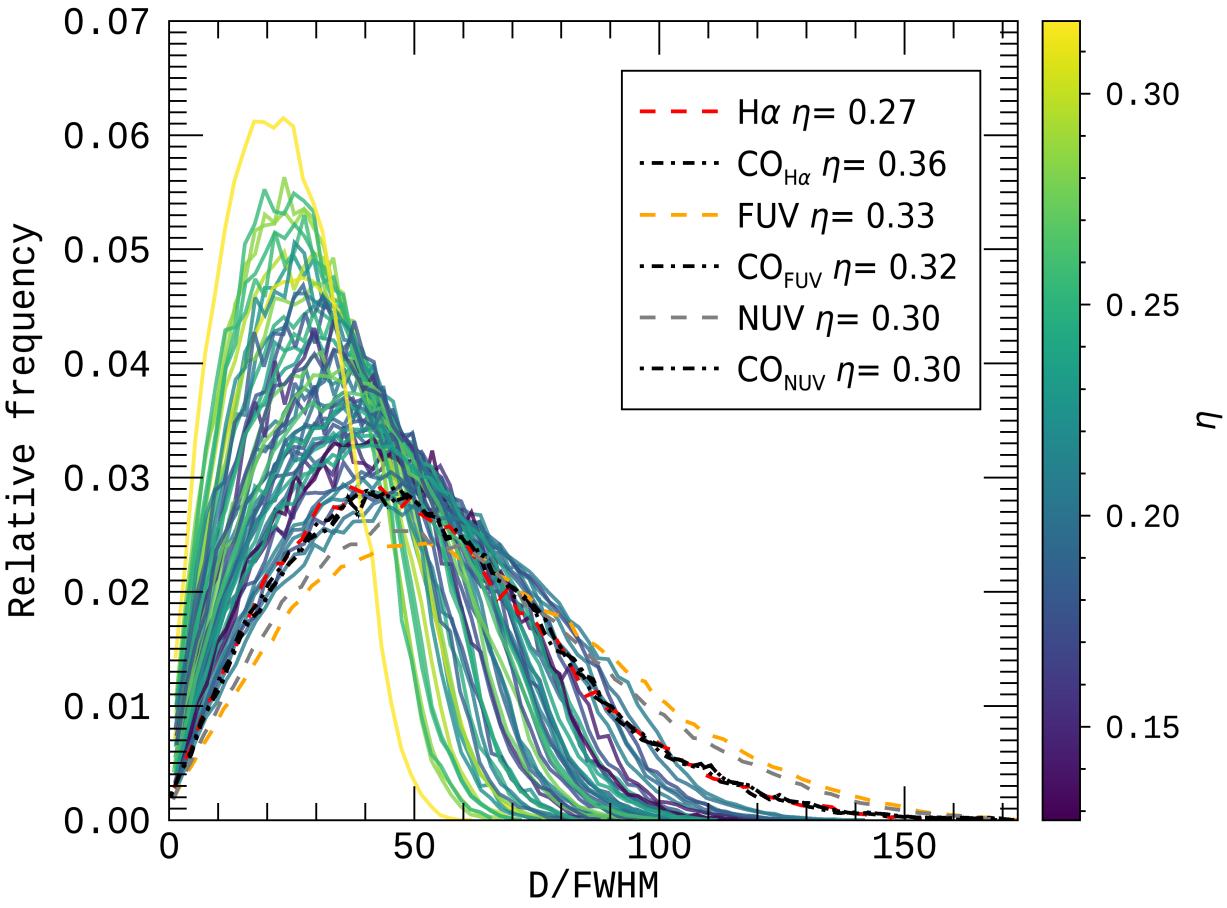

Figure 3.11: A relative frequency histogram showing the distribution of distances (D) between pairs of peaks in an image, normalised by the mean FWHM of the peaks in the image. All histograms have bins of width twice the FWHM. The solid lines show distributions for simulated datasets from Hygate et al. (2019) coloured according to the value of η, a statistic defined in Hygate et al. (2019) as a basis for a correction of flux loss due to overlap between regions. Simulated datasets with peaks spaced more closely together have, in general, higher values of η. The dashed lines show the distributions for the three star formation tracer maps of M33 used in this analysis. The dotted-dashed lines show the distribution for the CO map of M33 used in this analysis, as calculated from experiments with each of the three star formation tracers. As the same peaks are identified in the CO map regardless of star formation tracer used, the three CO histograms produced from these experiments are the same. For all tracer maps of M33, the value of η that we measure, shown in the legend, is higher than the value of η for simulated datasets with similar distributions of peak separations. As a higher measured value of η results in a higher correction for flux loss, this leads to an overcorrection for the flux lost due to overlap. Additionally, a different value of η is measured for the CO map depending on the star-formation tracer used in the analysis, in spite of the fact that the distribution of peaks, and thus the amount of flux loss due to overlap is unchanged. These two points show that a correction based on η is unsuitable for observational data.

Table 3.5: Parameters used in the method presented in section 5 of Hygate et al. (2019) to generate the simulated datasets for Appendix 3.7.

Parameter	Value	Origin
ζ	$0.1-0.5$	input
G_{FWHM}	$45-99$ pc[b]	input
$N_{\mathrm{peak,star,input}}$	$100-400$	input
$N_{\mathrm{peak,CO,input}}$	$100-1500$	input
$N_{\mathrm{peak,over,input}}$	$100-200$	input
f_{compact}	100%	input
t_{star}	10 Myr	input
t_{CO}	$10-95$ Myr	equation 21[a]
t_{fb}	$2.5-10$ Myr	equation 22[a]
λ	$76-840$ pc[b]	equation 23[a]

[a] These refer to equations in (Hygate et al., 2019)
[b] We have applied a conversion factor of $l_{\mathrm{pix}} = 9\mathrm{pc}$ to quantities displayed in units of pc

of compact regions in the maps. We also set a minimum of 200 regions in each map to ensure our results are not adversely affected by scatter introduced from a small number of regions. For these experiments we do not add any diffuse background, as we are only interested in the flux lost from the signal regions.

Figure 3.12 shows the flux remaining in the images after filtering and applying the correction for flux loss from a single Gaussian, q_{con},[28] against, $\tilde{D}_{\mathrm{nearest}}$[29], the median distance from peaks in the image to their nearest neighbouring peak, normalised by the mean FWHM of the peaks in the image. We calculate this median nearest neighbour distance using the locations and sizes of emission peaks that are identified during the application of the HEISENBERG code with CLUMPFIND (Williams et al., 1994).[30]

We fit a sigmoidal function for q_{overlap} as a function of the median nearest neighbour distance for emission peaks in an image, $\tilde{D}_{\mathrm{nearest}}$, normalised by the mean FWHM of the peaks in the image

$$q_{\mathrm{overlap}} = d + \frac{(a-d)}{\left(1+\left(\frac{\tilde{D}_{\mathrm{nearest/FWHM}}}{c}\right)^{b}\right)}, \tag{3.6}$$

where d is the value that q_{overlap} tends to as $\tilde{D}_{\mathrm{nearest}}$ tends to infinity. The fitting parameters a, b and c determine the shape of the function. The value of the function when $\tilde{D}_{\mathrm{nearest}} = 0$ is determined by a. The parameter b determines how quickly the value of the function moves from a to $q_{\mathrm{overlap},\infty}$, with faster changes corresponding to a higher value of b. Lastly, at $\tilde{D}_{\mathrm{nearest}} = a + ((a-1)/2)$, the value of the function is c. We present the best-fitting values of the parameters a, b, c and d in Table 3.6. This function for the corrective factor can be applied to values of $\tilde{D}_{\mathrm{nearest}}/\mathrm{FWHM}$ greater than those over which it was constrained without significant impact on the measured values of f_{compact}, as at the largest possible values of $\tilde{D}_{\mathrm{nearest}}/\mathrm{FWHM}$ the true value of q_{overlap} is 1, while the function will return 0.98. However, the correction should not be applied at values of $\tilde{D}_{\mathrm{nearest}}/\mathrm{FWHM} \lesssim 1.6$, as

[28] The value of q_{con} is given by equation 31 in Hygate et al. (2019).
[29] We note that $\tilde{D}$ denotes the median of D.
[30] http://www.ifa.hawaii.edu/users/jpw/clumpfind.shtml

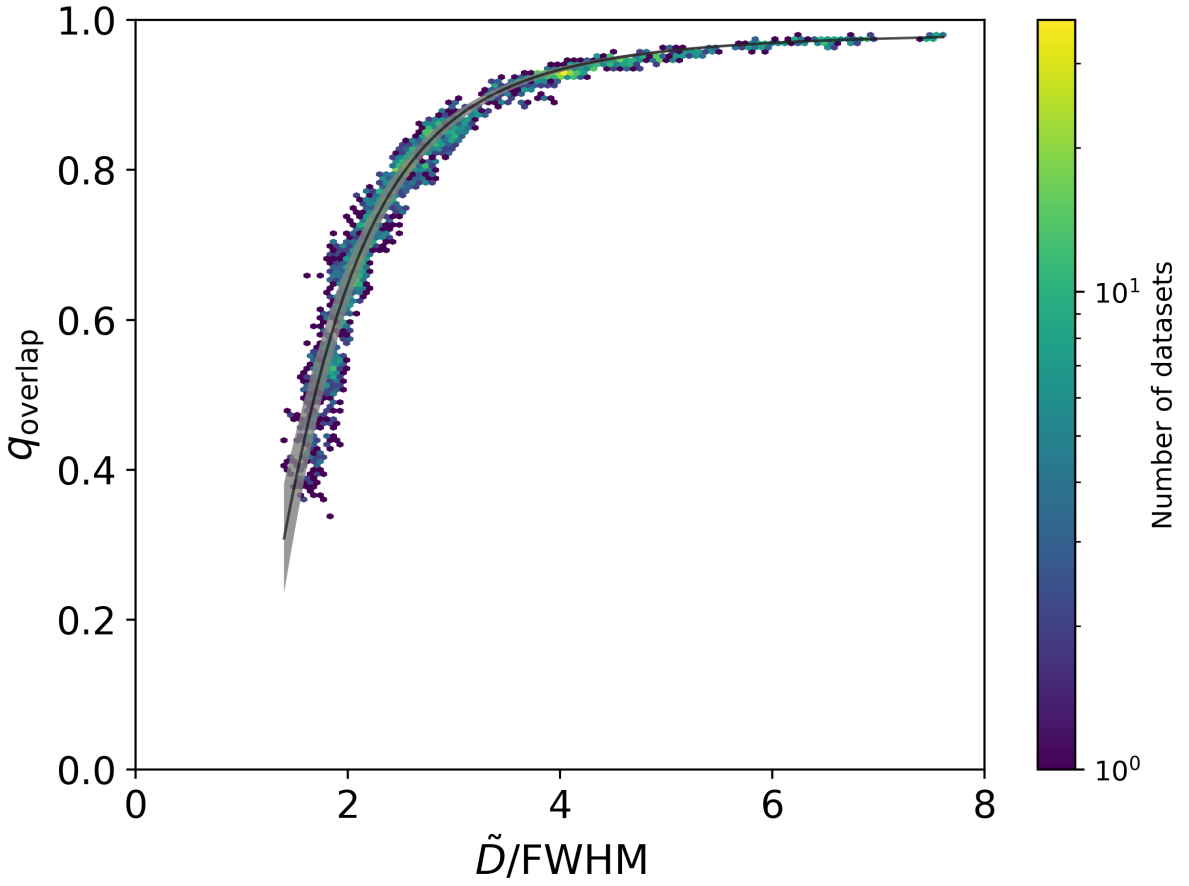

Figure 3.12: Flux remaining in an image after application of a Fourier filter and correction for the flux lost from single isolated regions,q_{overlap}, against the median nearest neighbour distance, $\tilde{D}_{\mathrm{nearest}}$, between peaks in an image, for a number of simulated datasets normalised by the mean FWHM of the Gaussian regions in the image. Measurements from simulated datasets are shown as hexbins, with the number of datasets in each hexbin indicated by the colour. The best-fitting relation, as described by Equation 3.6, is shown as the solid black line. The grey shaded region shows the 1σ uncertainty on the fitted model.

there this could lead to a significant mis-correction.

We report the values of the measured compact emission fractions for each image and the associated corrective factors in Table 3.7. With the new method presented here, we recover values of the CO compact emission fraction that agree between each of the three experiments (Hα, FUV and NUV) and are not unphysical (i.e. they are not significantly above 100 per cent). Finally, we note that this change in the method used to calculate the corrective factor has no impact on the iterative filtering process or the measured values of other fundamental parameters of the method, only the reported values of the compact and diffuse fractions for the tracer images.

Table 3.6: The best-fitting parameters for the sigmoidal function fitted for the flux loss due to overlapping regions in Equation 3.6.

Parameter	Value
a	-0.35
b	3.10
c	1.41
d	0.98

Table 3.7: Measurements of compact emission fractions, f_{compact} and corrective factors, q_{overlap}, using the method presented in Hygate et al. (2019) and the method presented in this appendix.

Parameter	Hygate et al. 2019	This paper
$f_{\text{compact,H}\alpha}$	58^{+1}_{-1} %	52^{+2}_{-3} %
$f_{\text{compact,FUV}}$	42^{+1}_{-1} %	37^{+1}_{-1} %
$f_{\text{compact,NUV}}$	36^{+1}_{-1} %	33^{+1}_{-1} %
$f_{\text{compact,CO}\,(\text{H}\alpha)}$	103^{+12}_{-8} %	95^{+3}_{-3} %
$f_{\text{compact,CO}\,(\text{FUV})}$	95^{+3}_{-3}	92^{+4}_{-3} %
$f_{\text{compact,CO}\,(\text{NUV})}$	94^{+3}_{-2} %	93^{+3}_{-3} %
$q_{\text{overlap,H}\alpha}$	0.73	0.82
$q_{\text{overlap,FUV}}$	0.66	0.74
$q_{\text{overlap,FUV}}$	0.69	0.75
$q_{\text{overlap,CO}\,(\text{H}\alpha)}$ [a]	0.63	0.69
$q_{\text{overlap,CO}\,(\text{FUV})}$ [a]	0.68	0.70
$q_{\text{overlap,CO}\,(\text{NUV})}$ [a]	0.70	0.70

[a] CO (X) is a measurement for CO from an analysis using tracer X (Hα, FUV or NUV) as the star formation tracer

3.8 Impact of peak identification on our results

A crucial step in the process of applying the HEISENBERG code is the identification of emission peaks within the tracer maps. We discuss the process we employ for this purpose in Section 3.3.2 and, in this appendix, we investigate the impact of different peak identification choices on the parameters constrained by the HEISENBERG code in this analysis.

The depth to which peaks are identified in the tracer map is set by $\Delta \log_{10} \mathcal{F}$, with higher values equating to greater depth and thus more identified peaks. Figure 3.13 shows the variation of measured parameters against the chosen value of $\Delta \log_{10} \mathcal{F}$ for the stellar tracer map. We consider values of $\Delta \log_{10} \mathcal{F}$ between 1.0 and 3.5 in increments of 0.5 All other peak identification parameters, including the value of $\Delta \log_{10} \mathcal{F}$ in the CO image, are kept unchanged (see Section 3.3.2). In comparison to SFR tracers, which have dynamic ranges between their pixels in excess of 10^9, the CO map has a much lower dynamic range of $\sim 10^2$. This combined with the signal-masking of the map makes identifying peaks in the CO map more obvious. As with the main analysis, we identify these peaks first on maps with NGC604 included and then apply a mask that excludes the area around this HII region when running our analysis. At small values of $\Delta \log_{10} \mathcal{F}$, we do not identify a number of regions of interest (such as HII regions in the Hα map) in the stellar maps that are significant enough in luminosity to be obviously identified by eye. This leads to overestimates of

the separation between independent star-forming regions, λ, and the gas cloud lifetime, $t_{\rm CO}$. As the value of $\Delta\log_{10}\mathcal{F}$ is increased, the number of peaks increases, due to the fact that we identify peaks at lower brightness levels.

Almost all the peaks in the Hα and NUV images are identified at $\Delta\log_{10}\mathcal{F} \geqslant 2.0$, whereas a significant number of peaks continue to be identified in the FUV map with increasing $\Delta\log_{10}\mathcal{F}$, including up to the maximum value of $\Delta\log_{10}\mathcal{F}$ that we consider. Nevertheless, we find that for all three tracer maps there is no significant change to the measured values of the HEISENBERG code fitting parameters $t_{\rm CO}$, $t_{\rm fb}$ and λ. Indeed, the number of additional identified peaks and the resulting impact on the values decreases with increasing $\Delta\log_{10}\mathcal{F}$, with only a small change between $\Delta\log_{10}\mathcal{F} = 2.5$ and $\Delta\log_{10}\mathcal{F} = 3.0$. This is due to the fact that the additional identified peaks have a decreasing luminosity, and thus a decreasing effect on our luminosity-weighted analysis. For the compact emission fraction in the gas map, $f_{\rm GMC}$, we find little dependence on the depth to which peaks are identified in the stellar map. However, for the compact emission fraction in the stellar map, $f_{\rm cl}$ we find a $\lesssim 15$ per cent increase from $\Delta\log_{10}\mathcal{F} = 1.0$ to $\Delta\log_{10}\mathcal{F} = 2.5$. This is due to underestimation of the amount of flux lost from blending between compact regions, resulting from an overestimate of the distance between compact regions as a result of their under-identification (see Appendix 3.7 for details of the correction applied to the compact emission fraction due to blending between peaks.). In summary, we find that the depth down to which peaks are found, $\Delta\log_{10}\mathcal{F}$, has little impact after all obvious peaks are identified.

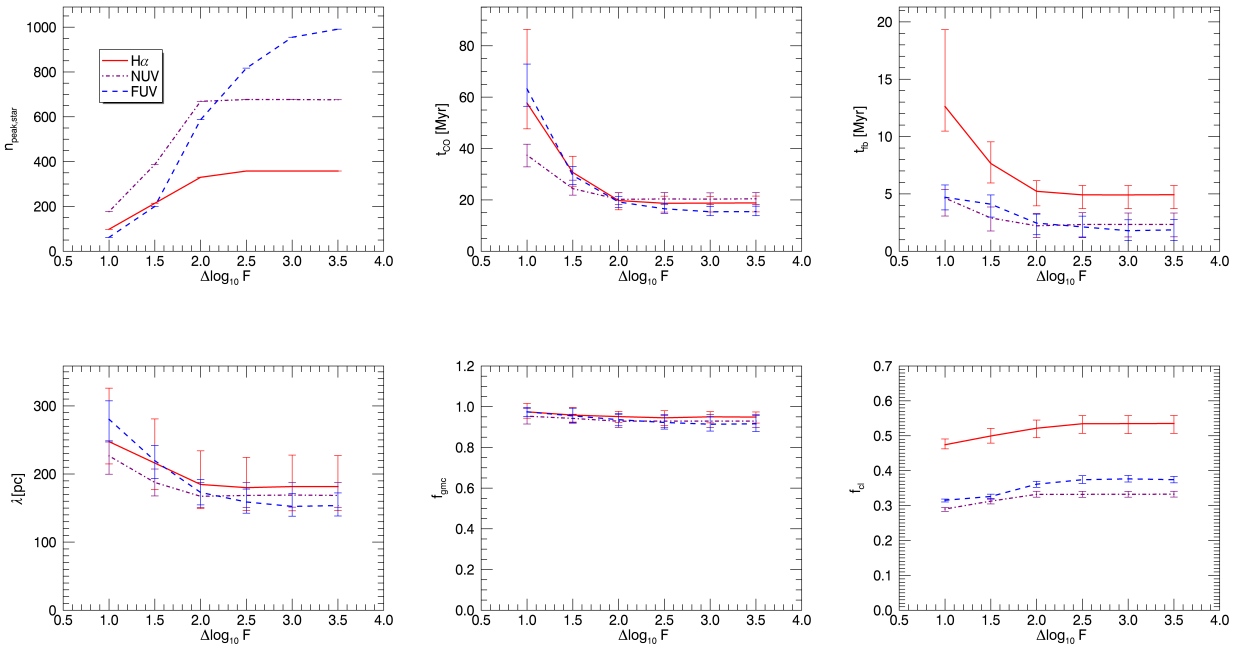

Figure 3.13: The variation of the measured values of [Top left panel] the number of identified peaks in the stellar map, $n_{\mathrm{peak,star}}$, [Top middle panel] t_{CO}, [Top right panel] t_{fb}, [Bottom left panel] λ, [Bottom middle panel] the CO compact emission fraction, f_{GMC}, and [Bottom right panel] the stellar tracer diffuse fraction, f_{cl}, against the logarithmic range below the tracer map flux maximum, $\Delta \log_{10} \mathcal{F}$, down to which peaks are identified in the maps. Experiments with Hα are shown with a solid red line, those with FUV as a dashed blue line and those with NUV as a dotted-dashed purple line. The impact of the selected value of $\Delta \log_{10} \mathcal{F}$ depends on the luminosity function of the emission peaks in the images. The Hα image has a much flatter distribution of luminosity in comparison to the two UV tracers. Therefore all Hα peaks are identified at low values of $\Delta \log_{10} \mathcal{F}$ (from $\Delta \log_{10} \mathcal{F} = 1.5$), whilst increasing the value of $\Delta \log_{10} \mathcal{F}$ continues to increase the number of peaks identified and thus alter the measured values of t_{CO} and λ in the UV maps up to much larger values (from $\Delta \log_{10} \mathcal{F} \sim 2.5$).

3.9 The effect of masking NGC604

For the main analysis of the paper we mask M33's brightest HII region, NGC604 (see Section 3.3.2). In this appendix we consider the impact on our results of not masking it. We therefore redo our analysis without masking NGC604, but otherwise keeping the method and input parameters unchanged. We present the results of this analysis in Table 3.8. Overall we find that the impact on our results is small, with a general increase of the measured values of t_{CO} from our tracers, the most significant of which being an increase in the value of t_{CO} measured with FUV from $16.5^{+2.1}_{-1.8}$ Myr to $19.0^{+2.9}_{-2.5}$ Myr, bringing it into closer agreement with the values measured with the other SFR tracers. Following the method presented in Apendix 3.10, we combine these measurements of t_{CO} into an averaged measurement of $22.3^{+3.6}_{-4.1}$ Myr. This agrees to within 1σ with the average measurement we derive from experiments with NGC604 masked ($19.5^{+3.0}_{-3.2}$ Myr). The weights that minimise the variance in the final derived time-scale are $\alpha_{\mathrm{H}\alpha} = 0.24$, $\alpha_{\mathrm{NUV}} = 0.53$, and $\alpha_{\mathrm{FUV}} = 0.21$. Applying this same weighting we calculate average values of $\epsilon_{\mathrm{sf}} = 23^{+5}_{-3}$ per cent for the star formation efficiency and $\eta_{\mathrm{fb}} = 4.1^{+0.7}_{-0.7}$ for the mass loading factor. These values also agree to within 1σ with measurements from experiments with NGC604 masked.

Table 3.8: The best fitting values of the parameters constrained by our analysis for Hα, FUV and NUV in combination with CO(2-1) including the region of NGC604. We also present results combined using the method presented in Appendix 3.10. We list the values, with their 1σ uncertainties, of the molecular cloud lifetime (t_{CO}), the feedback time-scale (t_{fb}), the mean separation length between regions (λ), the star formation efficiency per star formation event (ϵ_{sf}), the mass loading factor (η_{fb}), the feedback velocity (v_{fb}) and the reduced χ^2 statistic for the HEISENBERG code fit (χ^2_{red}).

SFR tracer	t_{CO} [Myr]	t_{fb} [Myr]	λ [pc]	ϵ_{sf} [%]	η_{fb} [-]	v_{fb} [kms^{-1}]	χ^2_{red} [-]
Hα	$20.1^{+3.0}_{-3.8}$	$5.3^{+0.9}_{-1.3}$	185^{+49}_{-35}	$3.7^{+0.6}_{-0.7}$	26^{+6}_{-4}	$6.7^{+1.9}_{-0.8}$	0.55
FUV	$19.0^{+2.9}_{-2.5}$	$2.1^{+1.1}_{-1.0}$	164^{+21}_{-18}	$3.6^{+0.5}_{-0.5}$	27^{+4}_{-4}	$17.2^{+15.1}_{-5.5}$	0.28
NUV	$22.4^{+3.6}_{-2.3}$	$2.4^{+1.2}_{-1.2}$	173^{+22}_{-18}	$4.2^{+0.7}_{-0.4}$	23^{+3}_{-3}	$17.2^{+15.1}_{-5.5}$	0.16
Combined	$22.3^{+3.6}_{-4.1}$	-	-	$4.1^{+0.7}_{-0.7}$	23^{+5}_{-3}	-	-

3.10 Combining time-scales

Due to the underlying correlations between non-independent estimates of physical quantities, the practice of combining experimental estimates through an average weighted only by the uncertainties in the derived time-scale is often unreliable. Following the method outlined in Lyons et al. (1988), we combine the derived PDFs for t_{CO} using a set of weights α such that for a given value of the PDF $y(x)$:

$$y(x) = \sum_i \alpha_i y(x)_i \tag{3.7}$$

The optimum values of α are defined such that the variation, σ, is minimised, where σ is defined by the summation over the products of the weight values α with the Error matrix **E**:

$$\sigma^2 = \sum_i \sum_j E_{ij}\alpha_i\alpha_j \tag{3.8}$$

E is defined such that:

$$E_{ij} = r_{ij}\sigma_i\sigma_j \tag{3.9}$$

where r is a correlation coefficient between two measurements and σ_i and σ_j are the variations in the ith and jth measurements. In the case of combining the three time-scales derived in this work, E is defined as:

$$\mathbf{E} = \begin{pmatrix} \sigma_1^2 & r_{12}\sigma_1,\sigma_2 & r_{13}\sigma_1\sigma_3 \\ r_{21}\sigma_2,\sigma_1 & \sigma_2^2 & r_{23}\sigma_2,\sigma_3 \\ r_{31}\sigma_3,\sigma_1 & r_{32}\sigma_3,\sigma_2 & \sigma_3^2 \end{pmatrix} \tag{3.10}$$

where the subscripts 1, 2, and 3 correspond to the experiments using the three different star formation tracers.

While the degree to which the derived time-scale estimates are correlated is wholly dependent on

the reference map, the reference time-scale used, and the peak selection in the reference map, it is not possible to determine the r coefficients in an analytical fashion. This is because any underlying biases between reference maps that are not already taken into account by the reference time-scale calculated by Haydon et al. (2018) are unknown.

Therefore we determine the degree to which two estimates are correlated in a post hoc fashion, using the knowledge that, as the reference maps and time-scales are the only significant factors that change, any deviation from a perfect correlation between PDFs must be indicative from a similar deviation from a correlation between the methods used to derive the time-scale. We therefore define the correlation coefficient between two estimates, r_{ij}, as the median of the deviation of the measured differential between two PDFs from the expected differential across the range of possible values of $t_{\rm CO}$:

$$r_{i,j} = \mathrm{med}\left(\frac{dPj}{dPi}_{\rm meas} - \frac{dPj}{dPi}_{\rm exp}\right) \tag{3.11}$$

where $\frac{dPj}{dPi}$ is the derivative between the probabilities for the two PDFs j and i for a given time-scale. The uncertainties in the time-scales derived with the Heisenberg code are asymmetric, meaning that selecting an appropriate value of σ for each PDF is a non-trivial problem. As we only use this value to determine the weighting of each PDF and not to directly determine the uncertainties in the final combined value of $t_{\rm CO}$, we elect to use a simple geometric average between the upper and lower uncertainties for each value, as in Lyons et al. (1988).

The weights that minimise the variance in the final derived time-scale are $\alpha_{\rm H\alpha} = 0.26$, $\alpha_{\rm NUV} = 0.42$, and $\alpha_{\rm FUV} = 0.29$. Once these weights are established, the final PDF is constructed according to equation 3.7. In order to take account for the asymmetric nature of the PDF, the final PDF is then fitted with two Gaussian profiles that overlap by 20 pixels around the maximum value of the distribution. We show this PDF and the fitted model in Figure 3.14. The most likely time-scale is then determined to be the mean centroid of the two Gaussian profiles with the positive and negative uncertainties taken as the standard deviations of the positive upper and lower fits, respectively. The resulting time-scale for CO emission in M33 is $19.5^{+3.0}_{-3.2}$ Myr. Applying the same weighting to the PDFs for the star formation efficiency we calculate $\epsilon_{\rm sf} = 3.6^{+0.6}_{-0.6}$ per cent and for the mass loading factor we calculate $\eta_{\rm fb} = 26^{+5}_{-4}$.

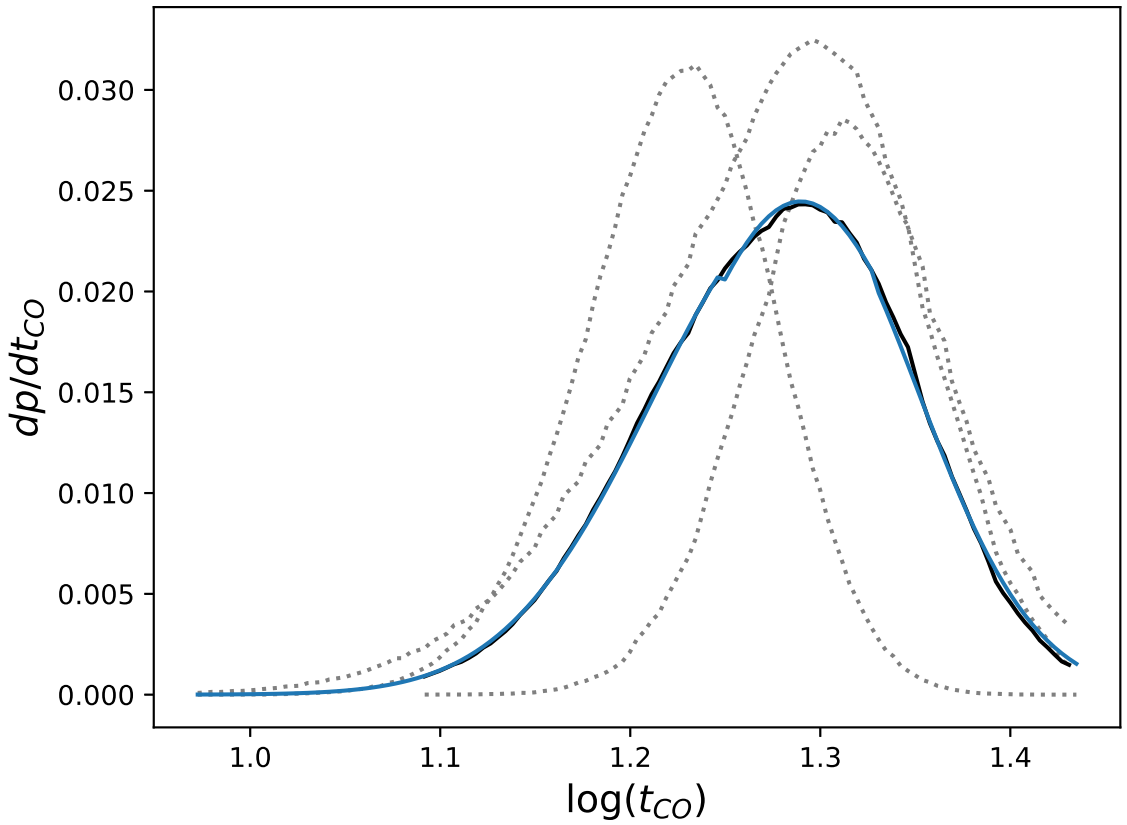

Figure 3.14: Combination of t_{CO} PDFs. The PDFs from our three experiments are shown as grey dotted lines. The PDF constructed according to Equation 3.7 is shown as the solid black line and the model fitted to this PDF as the solid blue line.

4 Diffuse molecular and ionised gas in nearby galaxies

Abstract

We present measurements of the fraction of emission emanating from compact structures (as opposed to emission from extended, diffuse structure) in the molecular (CO-traced) and ionised (Hα-traced) gas in a sample of nine nearby star-forming galaxies, observed as part of the PHANGS-ALMA Survey. These measurements are made by decomposing images of the galaxies in Fourier space, using the mean separation between star-forming regions as a physical size-scale with which to separate compact and diffuse emission. We perform a correlation analysis between these compact fractions and a number of quantities describing the structure and evolution of galaxies. First, we find no statistical correlation between the compact emission fractions in the two phases, though both phases are anti-correlated with the surface density of molecular gas, stars and SFR. The compact molecular gas fraction correlates with parameters related to the structure of the interstellar medium and more weakly to parameters characterising stellar feedback. These correlations suggest that feedback and other processes regulating the structure of the ISM may play a role in setting the compact molecular gas fraction. The compact ionised gas fraction, on the other hand, is found to be higher in galaxies with later morphological types and also higher at further radial distances from the centres of galaxies. We also observe anti-correlation with the Toomre Q parameter, suggesting that disc stability also play a role in the significance of diffuse ionised gas. In contrast to models that predict that ISM porosity is important in setting diffuse ionised emission fraction, we find that the compact ionised emission fraction increases with metallicity. Together these results characterise the significance of the diffuse and compact molecular and ionised gas and their dependence on environment in nine nearby galaxies.

4.1 Introduction

Emission from gas in galaxies is observed both from dense compact structures and from large-scale diffuse structure. Understanding the structure and evolution of gas in galaxies therefore requires a physical understanding of both of these phases. Diffuse hydrogen gas is observed, at least in ionised form, to be a ubiquitous feature of galaxies, with large variation in its significance observed across the galaxy population (see e.g. Lacerda et al., 2018). A fundamental question that we can ask regarding diffuse and compact gas in galaxies is: "what drives the observed variation in significance between these two components?"

The most widely used tracer of ionised gas is Hα. Hα emission from galaxies emanates both from compact regions in galaxies, such as HII regions and planetary nebulae, as well as from a large-scale diffuse hydrogen gas component known as the Diffuse Ionised Gas (DIG).[31] It is observed to be a ubiquitous feature of galaxies (Oey et al., 2007; Lacerda et al., 2018; Levy et al., 2019).

Lyman continuum radiation leakage from HII regions is often proposed as the source of the DIG (e.g. Mathis, 1986; Sembach et al., 2000; Wood et al., 2010). Observational evidence for this includes an observed spatial correlation of the DIG and HII regions (Hoopes et al., 1996; Zurita et al., 2000, 2002). Additionally, observations of the Magellanic Clouds show that a significant fraction of Lyman continuum radiation can escape from HII regions (Oey & Kennicutt, 1998; Voges et al., 2008; Pellegrini et al., 2012) and it is observed that this escape fraction varies between regions, for example Oey & Kennicutt (1998) estimate escape fractions of $0-51$ per cent for HII regions in the LMC. Observations also show that escaping Lyman continuum radiation is sufficient to account for the diffuse ionised gas in a number of galaxies (Zurita et al., 2000; Weilbacher et al., 2018).

A number of other sources have also been proposed for the DIG. These include ionising radiation emitted by post-asymptotic giant branch stars (Binette et al., 1994; Sarzi et al., 2010; Flores-Fajardo et al., 2011; Yan & Blanton, 2012), starlight scattered by dust (Seon et al., 2011; Seon & Witt, 2012) and shocks (Martin, 1997; Pety & Falgarone, 2000; Collins & Rand, 2001). Contributions from these different sources vary with the conditions of galaxies (see e.g. Collins & Rand, 2001; Voges, 2006; Sarzi et al., 2010; Lacerda et al., 2018). For example, Lacerda et al. (2018) found that ionisation from hot low-mass evolved stars dominated in the haloes of galaxies, whilst a number of different sources contribute in the discs of galaxies. Such variation is likely one cause of the variation in the total significance of the DIG observed between galaxies.

Observations of the DIG with Hα in samples of galaxies show that the significance of the DIG varies with environment. Lacerda et al. (2018) observed that the DIG fraction in galaxies of the CALIFA galaxy sample is correlated with Hubble type, with later type galaxies having less significant DIG fractions. That is to say that they found that elliptical galaxies had the highest diffuse fractions and spiral galaxies had the lowest fraction with lenticular galaxies transitional between the two. This is, however, in contrast to an earlier study by Oey et al. (2007) who found no such correlation with Hubble type.

Poggianti et al. (2019) examined the diffuse Hα-emitting gas in the tidal tails of cluster galaxies experiencing stripping via ram-pressure. They found a strong anti-correlation between the total SFR in the tail and the amount of diffuse emission. This result contrasts to the picture for galaxies more generally; Oey et al. (2007) found no correlation with SFR in their sample of 109 galaxies of a range of types. They did find, however, that starbursting galaxies in general had lower DIG fractions than non-starbursting galaxies.

Furthermore the diffuse emission fraction of Hα varies within galaxies themselves. Blanc et al. (2009) measured the fraction of diffuse emission in HII regions in M51 and found that fainter HII

[31] The DIG is also referred to as the Warm Ionised Medium (WIM) especially in the context of Milky Way studies.

regions had higher DIG fractions. Kreckel et al. (2016) found that spiral arms also play a role in observed diffuse fractions, with HII regions located in the spiral arms of NGC628 having higher DIG fractions than those situated in the inter-arm regions.

Studies of the diffuse extended component of molecular gas have thus far been far less extensive. This is in part due to the greater challenge of obtaining high-resolution, high-sensitivity observations of tracers of molecular gas such as carbon monoxide (CO), which is observed at mm wavelengths. Garcia-Burillo et al. (1992) detected an extended molecular gas component in the edge-on galaxy NGC891, which represents ~ 20 per cent of the luminosity of the thin disc of the galaxy and extends to large distances away from the plane of the thin disc. Molecular gas has subsequently been detected in the haloes of other highly-inclined galaxies, including M82 (Walter et al., 2002). Additionally, dust features, which may be associated to extraplanar molecular gas have been observed in edge on galaxies (Howk & Savage, 1999). However, studying diffuse molecular gas in edge-on and highly-inclined galaxies comes with the limitation that such studies are unable to characterise the resolved structure of the ISM and star forming regions.

It is thought in general that, within galaxies, molecular gas may only form in the cold dense regions of the ISM, such as in molecular clouds. However, after formation other processes may be able to transport molecular gas into large-scale diffuse reservoirs. Observations indicate that AGN can drive outflows of molecular gas from the disc (Walter et al., 2002; García-Burillo et al., 2014) and that these outflows may be capable of transporting significant molecular mass to the haloes of galaxies (Walter et al., 2002). Stellar feedback is also observed to drive molecular outflows, which in some cases can drive molecular gas to large scale-heights (Bolatto et al., 2013b; Geach et al., 2014, 2018).

An early study of the nearby galaxy M33 by Wilson & Walker (1994) showed that up to 60 per cent of the ^{12}CO emission in M33 could be diffuse, by comparing the ratio of ^{12}CO to ^{13}CO between single dish and interferometric observations. Other studies have investigated the fraction of flux lost between single dish and interferometric observations for a single tracer. This effect arises due to the fact that interferometers recover flux only up to a maximum angular resolution, thereby imaging flux only from structures more compact than this maximum resolution, whilst not recovering flux from large-scale structure that is recovered by single dish observations. This threshold is set by the distances between the telescopes in the interferometer array (so-called baselines) and is therefore not physically motivated. One such comparison between single dish and interferometric observations by Rosolowsky et al. (2007) of M33 found that only 20 per cent of the single dish flux was recovered. Pety et al. (2013) found that $\sim$50 per cent of CO(1-0) emission observed in single dish observations of M51 was lost in interferometric observations that did not recover flux from scales in excess of 1.3 kpc. Caldú-Primo et al. (2015) found flux recovery of $35-74$ per cent and $81-92$ per cent in interferometric observations of the spiral galaxies NGC 4736 and NGC 5055, attributing this to emission distributed across spatial scales in excess of ~ 1 kpc.

Additional evidence for large-scale diffuse molecular gas comes from comparisons of HI and CO velocity dispersions. Caldú-Primo et al. (2013) found that HI and CO velocity dispersions were very similar in the galaxies they observed. Due to the compact and diffuse HI components of nearby galaxies, CO velocity dispersion would be expected to be lower were it to contain only a compact component. This therefore indicates the presence of a thick diffuse molecular disc. A similar analysis in M33, however, indicates that M33 does not contain a significant thick molecular gas disc, suggesting that atomic gas dominated galaxies do not contain a significant thick molecular gas disc (Koch et al., 2019). In Hygate et al. (2019), we presented a method for quantifying the fraction of emission in tracer maps emanating from compact and extended (diffuse) structures. Application of this method to a signal-masked CO image of M33 found a low ($\lesssim 10$ per cent) diffuse molecular gas fraction (Hygate et al., 2019), similarly to the finding of Koch et al. (2019).

Another avenue of investigation has been to consider differences between molecular gas measurements from tracers that probe different gas densities. In the Milky way, Goldsmith et al. (2008) found that ~ 50 per cent of the molecular gas mass detected in the Taurus molecular cloud with ^{12}CO was undetected in ^{13}CO, a tracer of higher-density molecular gas. Analysis of ^{12}CO and ^{13}CO in a wider survey of the Milky Way found that the diffuse component undetected in ^{13}CO accounted for 25 per cent of the total molecular gas mass, with the fraction of mass in this diffuse phase increasing with galactocentric radius (Roman-Duval et al., 2016). Jiménez-Donaire et al. (2019) measured the ratio of hydrogen cyanide (HCN; a tracer of denser gas) to ^{12}CO in nine nearby galaxies. They similarly found that the fraction of gas not traced by HCN increases with galactocentric radius. Additionally they found that it increased with stellar surface density, molecular gas surface density, molecular gas fraction and dynamical equilibrium pressure.

The diversity of approaches, observational set-ups, methodologies and definitions of the diffuse molecular gas, presents both a challenge for the comparison of results between studies, but also the opportunity to compare physical properties of the diffuse gas. Studies, such as the one presented here, that consider the fraction of molecular gas in compact and spatially extended structures are complementary to line-ratio studies that probe the significance of molecular gas emission from different densities.

The PHANGS[32] collaboration is producing cloud-scale (~ 100 pc) molecular gas imaging for ~ 80 galaxies. Combined with similar resolution ionised gas imaging, these observations will allow us to examine the significance of diffuse and compact emission in the ionised and molecular phases of ISM in the context of environment. In this paper, we present the application of the method of Hygate et al. (2019) to an initial sample of nine nearby galaxies. We first detail the method used to separate the diffuse and compact components in Section 4.2 and summarise the observational data to which we apply the method in Section 4.3. Thereafter, we present the results of our analysis in Section 4.4. Last, we present a summary of the paper in Section 4.5.

4.2 Method

The "uncertainty principle for star formation" is a statistical method for constraining the lifecycles and spatial distribution of star-forming regions. The method was first presented by Kruijssen & Longmore (2014). Its implementation, as the Heisenberg code in IDL[33] for application to observational data was presented by Kruijssen et al. (2018). The method constrains the relative visibility lifetimes for star-forming regions in each of two stages in an evolutionary sequence, which are traced by observational images, as well as the relative timescale of overlap for regions visible in both phases. For the PHANGS-ALMA galaxies we trace molecular clouds with CO and the young massive stars that form from them with Hα. With these data the method therefore constrains the relative visibility durations of CO-visible molecular clouds ($t_{\rm CO}$), Hα-visible young massive stars ($t_{\rm star}$) and regions where young massive stars co-exist with their natal gas clouds before stellar feedback destroys or disperses them ($t_{\rm fb}$). In addition the Heisenberg code constrains the mean separation distance between independent star forming regions, λ.

Chevance et al. (2019) present the application of the Heisenberg code to the nine galaxies considered in this study along with the measured values of $t_{\rm CO}$, $t_{\rm fb}$ and λ. A number of quantities may be derived from these fitting parameters as detailed in Kruijssen et al. (2018). The feedback velocity ($v_{\rm fb}$)[34] and the star formation efficiency ($\epsilon_{\rm sf}$) are presented in Chevance et al. (2019). We

[32] Physics at High Angular Resolution in Nearby GalaxieS; http://phangs.org.

[33] Interactive Data Language http://www.harrisgeospatial.com/SoftwareTechnology/IDL.aspx

[34] We note that Kruijssen et al. (2018) presented two options for calculating the feedback velocity ($v_{\rm fb} = r_{\rm peak,CO}/t_{\rm fb}$ and $v_{\rm fb,\lambda} = \lambda/2t_{\rm fb}$). We consider $v_{\rm fb}$ in this analysis, as testing on simulated data by Hygate et al.

additionally make use of the characteristic region sizes in each tracer ($r_{\mathrm{peak,CO}}$ and $r_{\mathrm{peak,H}\alpha}$), the map filling factors (ζ_{CO} and $\zeta_{\mathrm{H}\alpha}$) and the time averaged mass loading factor (η_{fb}). These quantities are calculated, as described in Kruijssen et al. (2018), during the application of the HEISENBERG code by Chevance et al. (2019) but are not presented in that paper.

Masks were applied to the galaxies to remove foreground stars and background galaxies and to exclude regions outside the field of view of either tracer. In addition, the centres of galaxies were masked to exclude the regions of galaxies where blending between regions is most severe. These masks are shown in Chevance et al. (2019). Measurements were then made by applying the HEISENBERG code to the masked images for the whole galaxy, and in concentric annular radial "bins", with a minimum width of 1 kpc, such that the distribution of independent star-forming regions is recovered on scales in excess of their mean separation, λ (Chevance et al., 2019, typically a few hundred parsecs), to ensure good results from the HEISENBERG code.

The measurements of t_{CO} and t_{fb} depend on a reference timescale. We presented prescriptions for the characteristic visibility timescales of Hα and UV SFR tracers in the HEISENBERG framework in Haydon et al. (2018). These prescriptions provide reference timescales that allow us to calibrate the evolutionary timeline of star formation and thus recover absolute visibility lifetimes from the constrained relative lifetimes. We note, however, that the value of λ that we use to determine the boundary between diffuse and compact emission is not affected by the adopted stellar reference timescale. In this analysis we use Hα as our reference tracer, the prescription for which given by Haydon et al. (2018) is

$$t_{\mathrm{H}\alpha}[\mathrm{Myr}] = 4.32^{+0.09}_{-0.23}\left(\frac{Z}{\mathrm{Z}_{\odot}}\right)^{-0.086^{+0.010}_{-0.023}}, \tag{4.1}$$

where $Z/\mathrm{Z}_{\odot}$ is the metallicity in units of solar mass and $t_{\mathrm{H}\alpha} = t_{\mathrm{star}} - t_{\mathrm{fb}}$, i.e. the total visibility lifetime of Hα-visible young stellar regions excluding the time for which they are co-spatial with their natal gas clouds. Moreover this prescription depends only very weakly on the metallicity and thus the particular adopted value of $t_{\mathrm{H}\alpha}$ does not strongly affect the measured evolutionary timescales.

Additionally, in the analysis presented in this paper we apply a selection to the reported values of t_{fb} and derived quantities in our analysis. Specifically, we exclude measurements of t_{fb} made by Chevance et al. (2019) that do not satisfy the criterion $t_{\mathrm{fb}} > 0.05\tau$, where $\tau = t_{\mathrm{CO}} + t_{\mathrm{H}\alpha} - t_{\mathrm{fb}}$ is the total duration of the evolutionary timeline. This criterion is recommended by Kruijssen et al. (2018) on the basis of detailed testing of the HEISENBERG code on simulations.

In Hygate et al. (2019), we presented a method for decomposing images into diffuse and compact emission images by separating emission in Fourier space with a spatial wavelength criterion set by λ. The method filters emission from large spatial wavelengths through the application of a Gaussian filter in Fourier space

$$\Psi(u,v) = 1 - \exp\left(-\frac{(D(u,v))^2}{2\left(\frac{l_{\mathrm{pix}}}{n_{\lambda}\lambda}\right)^2}\right). \tag{4.2}$$

The filter defines the attenuation, $\Psi(u,v)$, which ranges from 0 (unattenuated) to 1 (totally atten-

(2019) shows that a shift in position of a region in one tracer from an originally co-spatial region in the other tracer over a distance $\sim r_{\mathrm{peak,CO}}$ is enough to cause the two to become unassociated in the context of the HEISENBERG code.

Table 4.1: The adopted value of the filter-softening parameter, n_λ. This table is reproduced from Chevance et al. (2019)

Galaxy	n_λ
NGC628	10
NGC3351	10
NGC3627	12
NGC4254	12
NGC4303	12
NGC4321	12
NGC4535	12
NGC5068	10
NGC5194	12

uated), at the spatial frequencies u,v. The amount of attenuation at a given 2D-spatial frequency co-ordinate is determined by λ, the pixel length scale $l_{\rm pix}$ (in the same physical units as λ), an attenuation softening factor n_λ, and $D(u,v)$ the spatial frequency distance of the co-ordinate from the zero-frequency "DC component". The value of n_λ is chosen so that $q_{\rm con} \geqslant 0.9$, following the recommendation of Hygate et al. (2019), based on testing with simulated datasets. The values of n_λ that we use for each galaxy are listed in Table 4.1.

After applying this filter in Fourier space, the image is transformed back into "real space" leaving an image of the emission from compact structures. We then apply a threshold to the image at twice the noise level for the image. Subsequently the HEISENBERG code is applied to the filtered images and a new set of measurements made. This filtering process is applied iteratively, with a filter determined by the most recently measured value of λ, until the measured value of λ is consistent to within five per cent with the previous four measurements of λ.

The Gaussian filter that we apply attenuates emission from the compact structures in the image in addition to the diffuse structure. Therefore to calculate the fraction of compact emission in the image, we calculate two corrective factors $q_{\rm con}$, which accounts for the flux attenuated from isolated compact regions and $q_{\rm overlap}$, which accounts for the additional flux attenuated from isolated compact regions due to overlap between them. The first corrective factor, $q_{\rm con}$, was calibrated by Hygate et al. (2019) and is defined for each tracer image as

$$q_{\rm con} = 1 + \frac{-1.016}{\left(1 + \left(\frac{n_\lambda \lambda}{\rm FWHM}/4.86\right)^{1.69}\right)}, \tag{4.3}$$

where FWHM[35] is the full-width at half-maximum of compact regions in the image. Testing on simulated datasets by Hygate et al. (2019) shows that in order to recover accurate measurements of the compact emission fraction in an image, less than 10% of the flux should be removed from isolated compact regions (i.e. $q_{\rm con} > 0.9$). We therefore select a value of n_λ for galaxies such that $\min\left(q_{\rm con,CO}, q_{\rm con,H\alpha}\right) > 0.9$ for each galaxy. This value of n_λ varies between ten and twelve (see Table 4.1)

The second corrective factor, $q_{\rm overlap}$, was calibrated by Hygate et al. (2019) and is defined for

[35] In other parts of this paper we quote region sizes measured by the HEISENBERG code as $r_{\rm peak}$. The FWHM and $r_{\rm peak}$ are related as $\mathrm{FWHM} = 2\sqrt{2\ln 2}\, r_{\rm peak}$.

each tracer image as

$$q_{\rm overlap} = 0.98 + \frac{-1.33}{\left(1 + \left(\frac{\tilde{D}_{\rm nearest/FWHM}}{1.41}\right)^{3.1}\right)}, \tag{4.4}$$

where $\tilde{D}_{\rm nearest}$ is the median nearest neighbour distance between identified emission peaks in the tracer image. Taking account of these corrective factors, the compact fraction, f, in a tracer (either Hα or CO) image is then calculated as

$$f = \frac{1}{q_{\rm con} q_{\rm over}} \frac{\sum_{m,n} \mathcal{F}'(m,n)}{\sum_{m,n} \mathcal{F}(m,n)}, \tag{4.5}$$

where $\sum_{m,n} \mathcal{F}(m,n)$ and $\sum_{m,n} \mathcal{F}'(m,n)$ are the total flux in the original ($\mathcal{F}(m,n)$) and filtered images ($\mathcal{F}'(m,n)$), respectively.

4.3 Data

We take our data from the PHANGS-ALMA survey and from archival sources. The galaxies of the PHANGS-ALMA survey are selected such that they are on or near to the Main Sequence of star formation. Further selections are then made such that they are nearby ($\lesssim 17$ Mpc) and have low inclinations ($\lesssim 75°$), which are important for sufficiently resolving the cloud-scale structure of the ISM. The survey has been undertaken in two phases: an initial survey in ALMA Cycle 3 and an expanded survey in ALMA Cycle 5. The data products of the full PHANGS-ALMA survey are presented in Leroy et al. (in prep.) and presentations of a subset of the data are given in Sun et al. (2018) and Utomo et al. (2018). The galaxies that we analyse in this paper are those that are selected by Chevance et al. (2019) as being suitable for the application of the Heisenberg code due to the current availability of cloud-scale molecular gas and Hα SFR tracer imaging. This sample comprises eight galaxies from the PHANGS-ALMA survey, namely NGC628, NGC3351, NGC3627, NGC4254, NGC4303, NGC4321, NGC4535 and NGC5068 and an additional galaxy, NGC5194, for which high-resolution archival molecular gas imaging is available.

To trace the molecular gas in these galaxies we use rotational transitions of the CO molecule. With the exception of NGC5194, we use cloud-scale CO(2-1) observations of the galaxies from the PHANGS-ALMA survey (Leroy et al., in prep.; see also Sun et al. 2018 and Utomo et al. 2018). In NGC5194, we use the CO(1-0) Plateau de Bure Interferometer dataset presented by Pety et al. (2013); Schinnerer et al. (2013). In the remainder of the paper we refer to both CO(1-0) and CO(2-1) collectively as CO.

Importantly for our analysis of the relative importance of the compact and large-scale diffuse emission components, these datasets cover all spatial scales of the galaxies by including short and zero spacing visibilities. For the PHANGS-ALMA galaxies this is achieved through the combination of the ALMA 12m, 7m and total power arrays. For NGC5194, the interferometric data are combined with single dish observations from the IRAM 30m telescope.

We use continuum-subtracted, narrow-band Hα imaging to trace the ionised gas phase. For the galaxies, NGC3351, NGC4321 and NGC5194, we use archival data from the Spitzer Infrared Nearby Galaxies Survey (Kennicutt et al., 2003). While for NGC628, NGC3627, NGC4254, NGC4303, NGC4535 and NGC5068 we make use of new images obtained with the La Silla Observatory MPG/ESO 2.2m telescope; these images are presented in Razza et al. (in prep.). A summary of

the data reduction for the Hα images used in this paper is also given in Chevance et al. (2019).

4.3.1 Auxiliary data

We make use of additional archival data for our galaxies from the HyperLEDA[36] database (Makarov et al., 2014). In order to characterise the sizes of the galaxies in our sample and to normalise their radii, we use the radius at the isophote of 25th magnitude in the B-band (r_{25}). The procedures used to calculate r_{25} by HyperLEDA are presented by Paturel et al. (1991, 1997). We also use the morphological type code $t_{\rm morph}$, which is a numerical encoding of morphological type where higher values of $t_{\rm morph}$ correspond to later galaxy classes. $t_{\rm morph}$ in HyperLEDA is calculated as a weighted mean of available determinations of each galaxy's morphological type as presented by Paturel et al. (1997).

We also use a number of parameters describing aspects of the galaxies in our sample compiled by Chevance et al. (2019). These are the azimuthally-averaged surface densities of molecular gas ($\Sigma_{\rm H_2}$), stars ($\Sigma_{\rm stars}$) and SFR ($\Sigma_{\rm SFR}$), the rotation velocity ($v_{\rm rot}$), the Toomre Q parameter, and the gas phase metallicity in terms of solar mass ($Z/{\rm Z}_\odot$). To get a value for these parameters corresponding to each bin, we interpolate the datapoints presented by Chevance et al. (2019) and take the mean of this interpolated function over the annular range of the bin.

4.4 Results

For each of the galaxies in our sample, we present the decomposition into compact and diffuse emission images for the Hα tracer maps in Figure 4.1 and for the CO tracer maps in Figure 4.2. With these decomposed images, we measure the compact fraction of Hα emission, $f_{\rm H\alpha}$, and of CO, $f_{\rm CO}$, as described in Section 4.2. We present radial profiles, for each of our galaxies, of $f_{\rm H\alpha}$ in Figure 4.3 and $f_{\rm CO}$ in Figure 4.4. With these measurements, we observe significant variations of the compact fractions between galaxies, as well as within galaxies.

In order to investigate the origin of these variations, we measure the correlations between $f_{\rm CO}$ and $f_{\rm H\alpha}$ and a number of physical quantities that we have constrained for the galaxies in our sample with the HEISENBERG code (see Section 4.2) and parameters from auxiliary datasets (see

Table 4.2: The constrained values of the compact emission fractions in Hα ($f_{\rm H\alpha}$) and CO ($f_{\rm CO}$) for the nine galaxies of our sample along with the factors $q_{\rm con}$ (see Equation 4.3) and $q_{\rm overlap}$ (see Equation 4.4). This table is reproduced from Chevance et al. (2019).

Galaxy	$f_{\rm H\alpha}$	$f_{\rm CO}$	$q_{\rm con,H\alpha}$	$q_{\rm con,CO}$	$q_{\rm overlap,H\alpha}$	$q_{\rm overlap,CO}$
NGC628	$0.69^{+0.01}_{-0.01}$	$0.82^{+0.06}_{-0.06}$	$0.89^{+0.02}_{-0.01}$	$0.89^{+0.02}_{-0.01}$	$0.74^{+0.02}_{-0.01}$	$0.52^{+0.06}_{-0.05}$
NGC3351	$0.31^{+0.01}_{-0.01}$	$0.83^{+0.06}_{-0.06}$	$0.89^{+0.01}_{-0.01}$	$0.90^{+0.01}_{-0.01}$	$0.73^{+0.02}_{-0.02}$	$0.56^{+0.05}_{-0.04}$
NGC3627	$0.42^{+0.01}_{-0.01}$	$0.81^{+0.04}_{-0.06}$	$0.91^{+0.02}_{-0.01}$	$0.91^{+0.01}_{-0.01}$	$0.70^{+0.03}_{-0.02}$	$0.49^{+0.06}_{-0.04}$
NGC4254	$0.69^{+0.01}_{-0.02}$	$0.74^{+0.06}_{-0.06}$	$0.91^{+0.01}_{-0.01}$	$0.91^{+0.02}_{-0.01}$	$0.67^{+0.03}_{-0.02}$	$0.48^{+0.06}_{-0.05}$
NGC4303	$0.68^{+0.01}_{-0.03}$	$0.82^{+0.08}_{-0.10}$	$0.89^{+0.02}_{-0.01}$	$0.90^{+0.02}_{-0.02}$	$0.62^{+0.05}_{-0.02}$	$0.46^{+0.09}_{-0.06}$
NGC4321	$0.44^{+0.01}_{-0.01}$	$0.79^{+0.05}_{-0.05}$	$0.91^{+0.01}_{-0.01}$	$0.91^{+0.01}_{-0.01}$	$0.69^{+0.02}_{-0.02}$	$0.49^{+0.04}_{-0.04}$
NGC4535	$0.93^{+0.02}_{-0.03}$	$0.98^{+0.09}_{-0.11}$	$0.89^{+0.02}_{-0.01}$	$0.90^{+0.02}_{-0.02}$	$0.68^{+0.04}_{-0.02}$	$0.44^{+0.08}_{-0.06}$
NGC5068	$0.64^{+0.01}_{-0.01}$	$1.35^{+0.04}_{-0.04}$	$0.92^{+0.01}_{-0.01}$	$0.95^{+0.01}_{-0.01}$	$0.74^{+0.04}_{-0.03}$	$0.76^{+0.03}_{-0.02}$
NGC5194	$0.37^{+0.01}_{-0.01}$	$1.05^{+0.06}_{-0.09}$	$0.90^{+0.01}_{-0.01}$	$0.91^{+0.01}_{-0.01}$	$0.71^{+0.02}_{-0.01}$	$0.45^{+0.06}_{-0.04}$

[36] http://leda.univ-lyon1.fr/

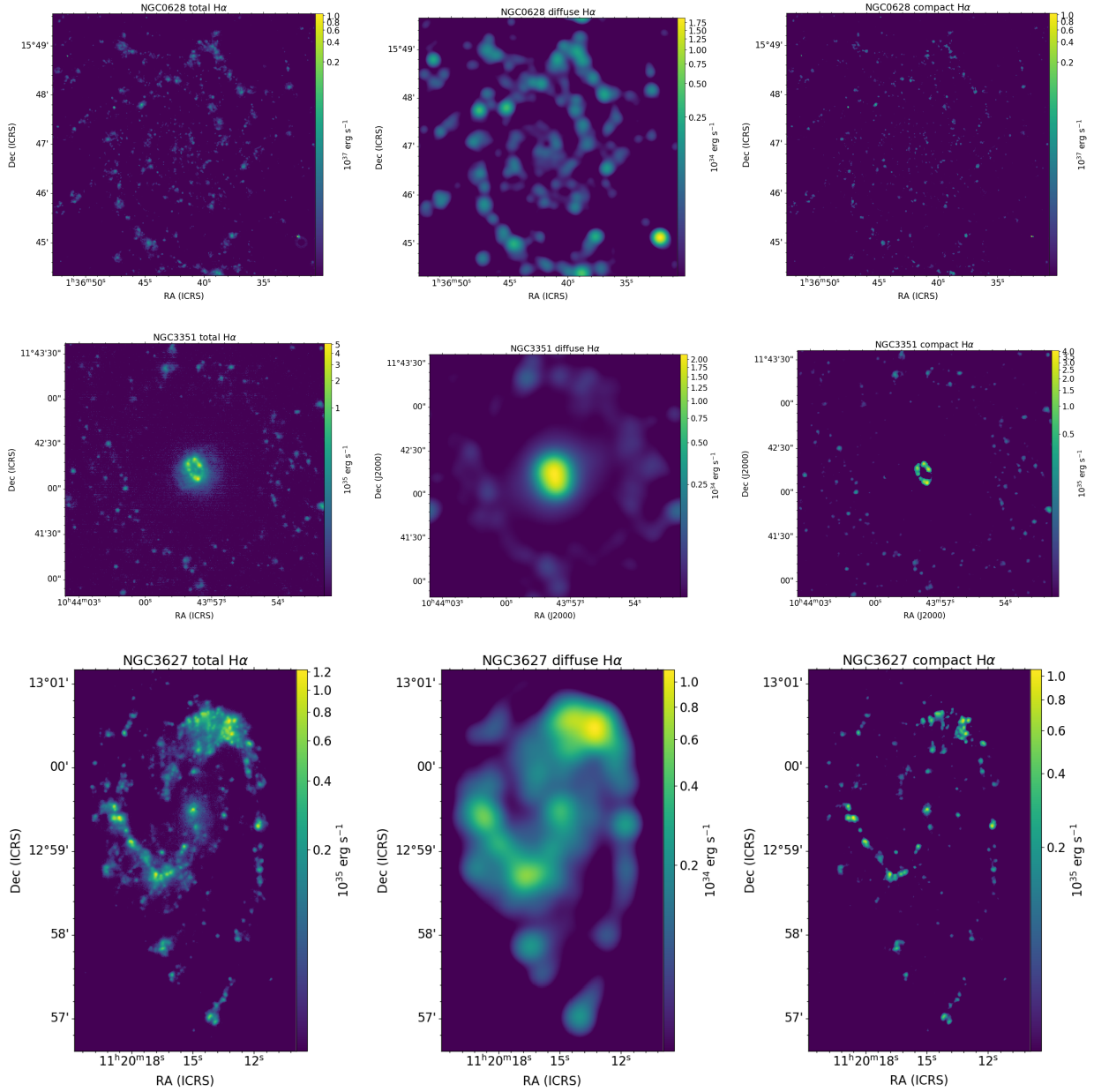

Figure 4.1: Decomposition of the Hα tracer maps of our sample of galaxies. We show the total image [left column] and its decomposition into diffuse [middle column] and compact [right column] components for each galaxy. Note the different intensity scales for each of the panels.

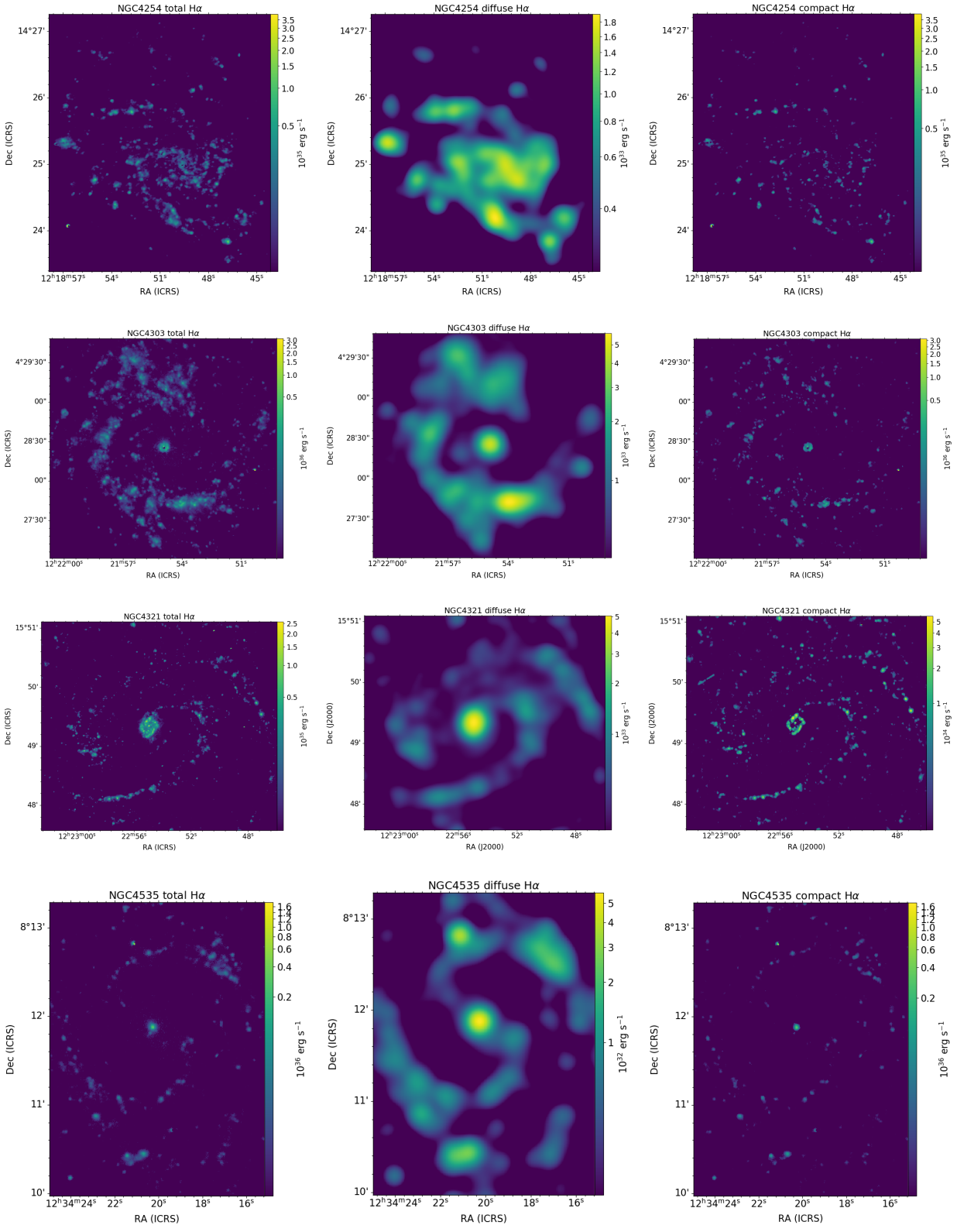

Figure 4.1: *continued*

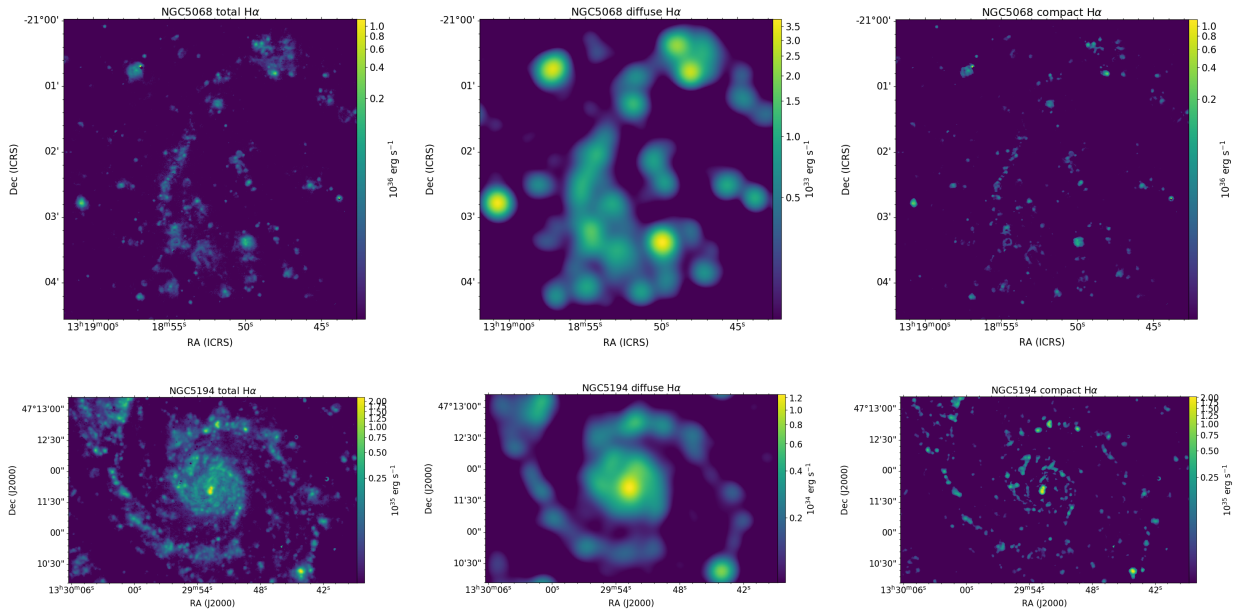

Figure 4.1: *continued*

Section 4.3.1). Together these parameters characterise a number of the properties of star forming regions, the ISM and their host galaxies.

We quantify the significance of the relationship between these parameters with the Spearman's rank correlation coefficient, ρ using the SciPy (Virtanen et al., 2019) task stats.spearmanr. This coefficient quantifies the extent to which one parameter is monotonically related to another parameter, with $\rho = 1$ indicating a perfect positive monotonic correlation, $\rho = -1$ indicating a perfect negative monotonic correlation and $\rho = 0$ indicating no correlation. We display ρ along with the two-sided p-value for each parameter that we consider in combination with $f_{\mathrm{H}\alpha}$ and f_{CO} in Table 4.3. We define the threshold for statistical significance of the correlation as $p \leqslant 0.05$. First, we find no statistically significant relationship between the fraction of compact emission in the ionised ($f_{\mathrm{H}\alpha}$) and molecular gas (f_{CO}) phases of nearby star forming galaxies (see Figure 4.5). We thus proceed to discus the statistically significant correlations and their implications for each phase individually.

We also find no statistically significant correlation between the corrective factors we apply to our measurements (See Equations 4.3 and 4.4) and the compact emission fractions, with the exception of $q_{\mathrm{con,H}\alpha}$ and f_{CO}, which we discuss further in Section 4.4.2. As $q_{\mathrm{con,H}\alpha}$ is used to correct $f_{\mathrm{H}\alpha}$ and not f_{CO}, we conclude on the basis of the high p-values for the other corrective factors and compact fraction combinations, that the corrective factors do not drive the trends and correlations that we observe with respect to f_{CO} and $f_{\mathrm{H}\alpha}$.

4.4.1 The compact fraction of Hα

We find significant variation in $f_{\mathrm{H}\alpha}$ between our galaxies, with the total emission from some galaxies dominated by emission from compact structures, whilst others are dominated by emission from diffuse structure. NGC4535 is the galaxy with the highest compact fraction of $0.93^{+0.02}_{-0.03}$ and NGC3351 has the lowest compact fraction of $0.31^{+0.01}_{-0.01}$. We measure statistically significant correlations between $f_{\mathrm{H}\alpha}$ and galactocentric radius; the surface densities of H_2, stars and SFR; the gas phase metallicity; Toomre Q parameter and the morphological type of the galaxy (see Table 4.3). For

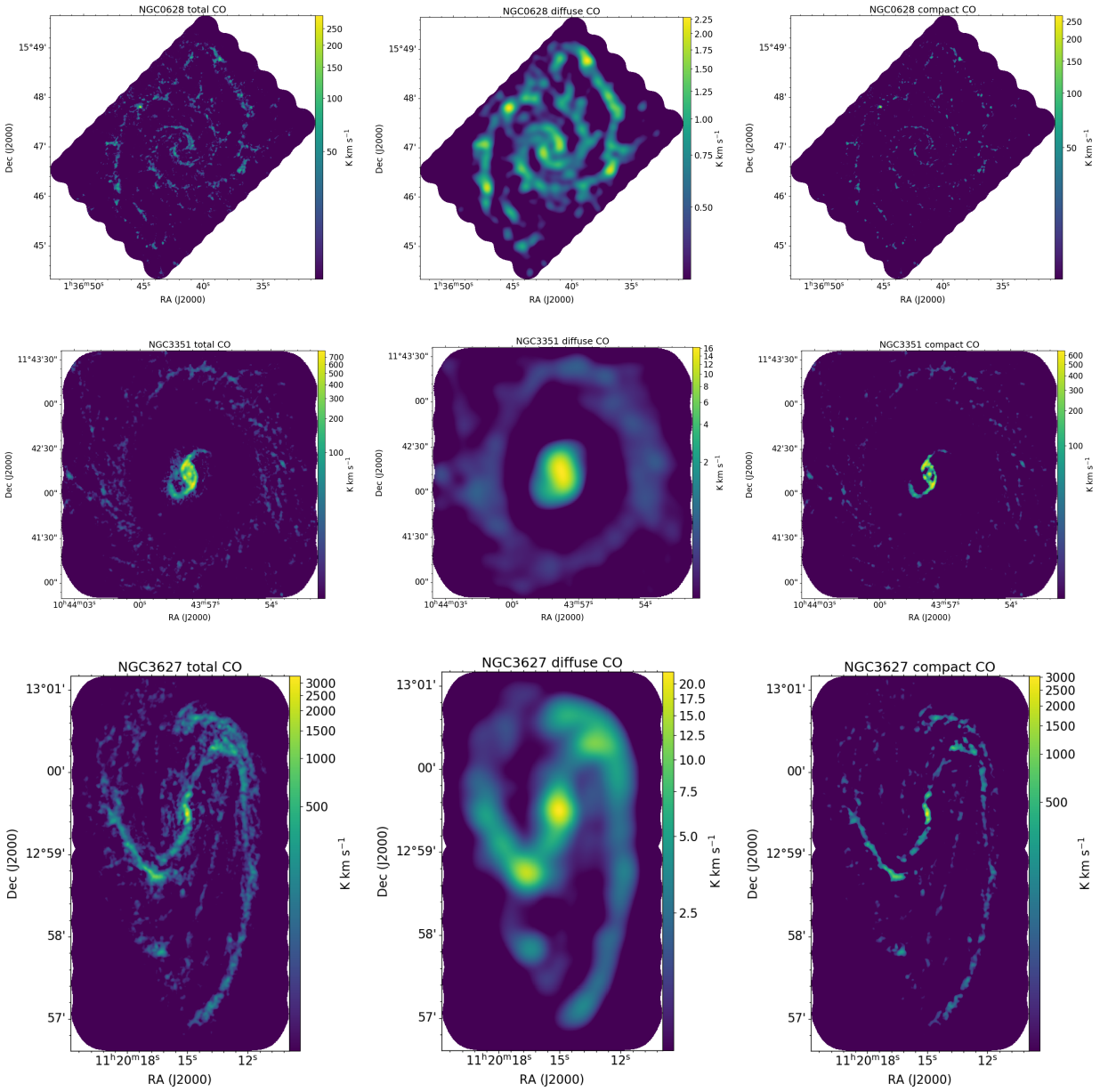

Figure 4.2: Decomposition of the CO tracer maps of our sample of galaxies. We show the total image [left column] and its decomposition into diffuse [middle column] and compact [right column] components for each galaxy. Note the different intensity scales for each of the panels. For NGC5068 and NGC5194 we do not display a diffuse CO image, as our measurement of f_{CO} indicates that there is no diffuse CO component in these two galaxies (see Table 4.2).

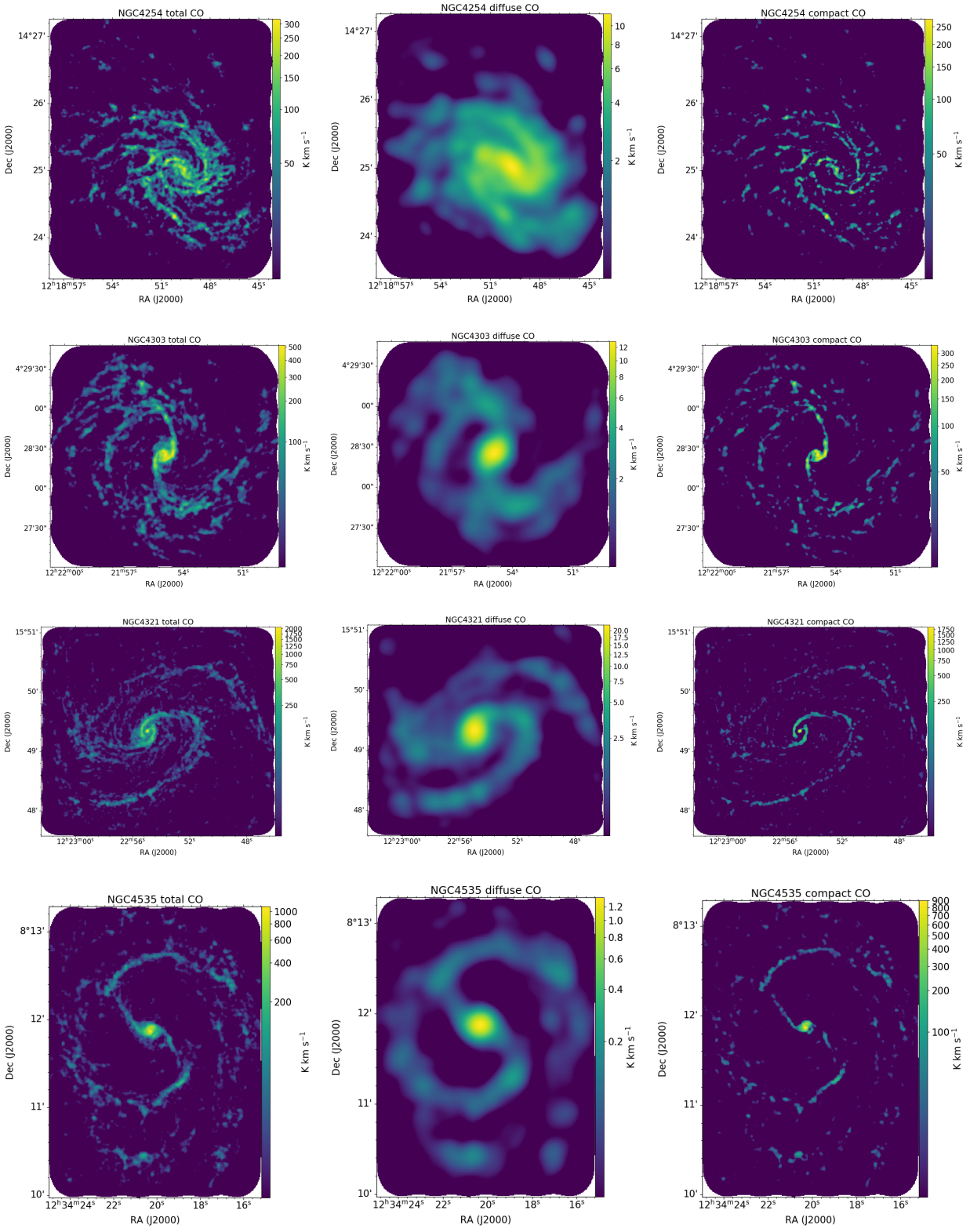

Figure 4.2: *continued*

Table 4.3: Spearman's rank correlation coefficients, $\rho_{f_{\mathrm{H}\alpha}}$ and $\rho_{f_{\mathrm{CO}}}$, along with the corresponding two-sided p-value, $p_{f_{\mathrm{H}\alpha}}$ and $p_{f_{\mathrm{CO}}}$, for $f_{\mathrm{H}\alpha}$ and f_{CO} as a function of the physical parameters considered in this analysis. p-values below 0.01 are reported as "<0.01".

Variable	$\rho_{f_{\mathrm{H}\alpha}}$	$p_{f_{\mathrm{H}\alpha}}$	$\rho_{f_{\mathrm{CO}}}$	$p_{f_{\mathrm{CO}}}$
ϵ_{sf}	-0.19	0.2	-0.01	0.96
$f_{\mathrm{H}\alpha}$	1.0	<0.01	0.17	0.26
f_{CO}	0.17	0.26	1.0	<0.01
λ	0.14	0.34	-0.52	<0.01
t_{fb}	0.16	0.27	0.05	0.73
t_{CO}	-0.11	0.44	0.11	0.46
t_{star}	0.18	0.23	0.05	0.72
v_{fb}	-0.04	0.80	-0.29	0.05
η_{fb}	0.19	0.20	0.01	0.96
$q_{\mathrm{con,CO}}$	0.04	0.79	-0.11	0.48
$q_{\mathrm{con,H}\alpha}$	0.12	0.43	-0.28	0.05
$q_{\mathrm{overlap,CO}}$	-0.00	0.98	-0.22	0.13
$q_{\mathrm{overlap,H}\alpha}$	-0.15	0.31	0.01	0.97
$r_{\mathrm{peak,CO}}$	0.18	0.21	-0.45	<0.01
$r_{\mathrm{peak,H}\alpha}$	0.20	0.17	-0.45	<0.01
$\zeta_{\mathrm{H}\alpha}$	-0.07	0.63	0.22	0.14
ζ_{CO}	0.01	0.96	0.15	0.32
Σ_{H_2}	-0.45	<0.01	-0.41	<0.01
Σ_{stars}	-0.64	<0.01	-0.38	0.01
Σ_{SFR}	-0.38	0.01	-0.38	0.01
v_{rot}	-0.18	0.21	-0.02	0.90
Q_{Toomre}	-0.51	<0.01	-0.04	0.78
$t_{\mathrm{fb}}/t_{\mathrm{star}}$	0.13	0.38	0.06	0.68
$t_{\mathrm{fb}}/t_{\mathrm{CO}}$	0.26	0.08	-0.29	0.05
t_{morph}	0.67	<0.01	0.18	0.22
Galactocentric radius/r_{25}	0.40	<0.01	0.26	0.07
Galactocentric radius	0.42	<0.01	0.13	0.37
$Z/Z_{\odot}$	-0.64	<0.01	-0.21	0.16

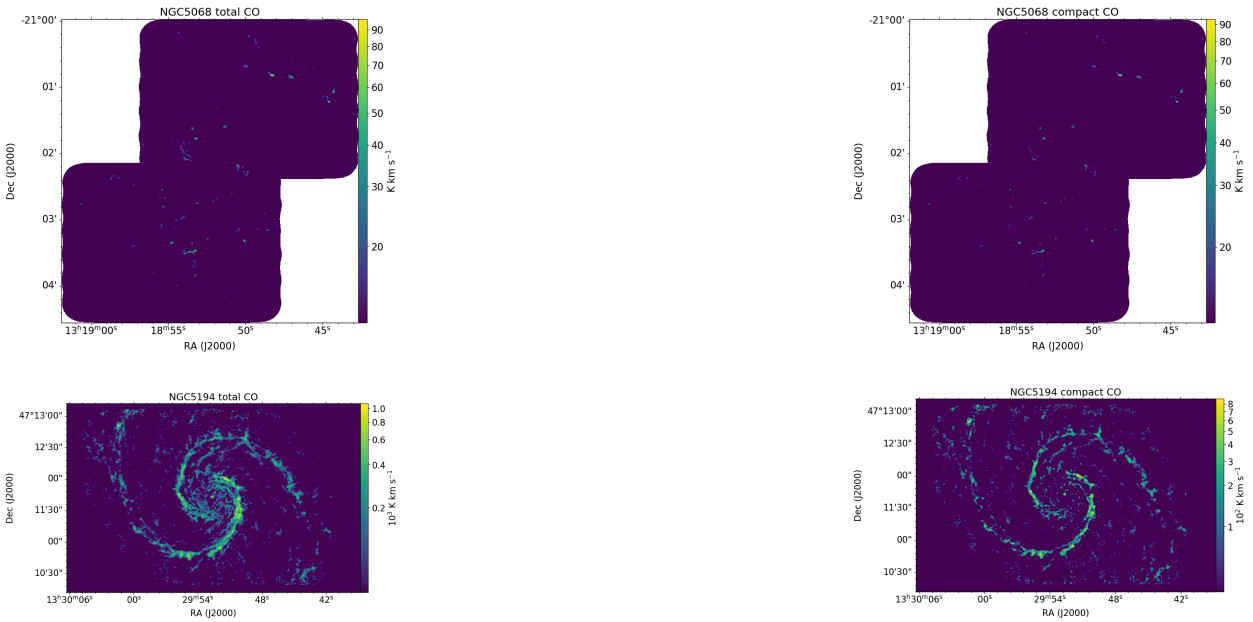

Figure 4.2: *continued*

our galaxies, we measure a mean $f_{\mathrm{H}\alpha}$ of 0.58 ± 0.19. This translates to a diffuse Hα fraction of 0.42 ± 0.19, slightly lower, but in agreement with previous measurements of 0.59 ± 0.19 (Oey et al., 2007) and 0.56 ± 0.38 (Lacerda et al., 2018). However, as we only have nine galaxies in our sample (in comparison to greater than 100 in the other two studies) a statistically relevant comparison will require application of our method to a larger sample. We find one overlapping galaxy between our sample and that of Oey et al. (2007), namely NGC5068. Oey et al. (2007) report a non-diffuse Hα emission fraction for the galaxy of 0.4, somewhat lower than our measurement of $0.64^{+0.01}_{-0.01}$. We do not find any of our galaxies in the CALIFA sample (Sanchez et al., 2018) from which the sample of Lacerda et al. (2018) is drawn.

We first consider the correlation with t_{morph}, which we plot against $f_{\mathrm{H}\alpha}$ for measurements from whole galaxies only in Figure 4.6, due to its invariance with radius. We find that $f_{\mathrm{H}\alpha}$ increases with t_{morph}. A higher type number equates to a later Hubble stage and this finding is thus in qualitative agreement with the finding of Lacerda et al. (2018) that the fraction of emission from star formation increases with Hubble Type. However, we note that we have at most three galaxies for each value of t_{morph}, in comparison to the much larger sample of Lacerda et al. (2018).

We find that the radial profiles of $f_{\mathrm{H}\alpha}$ (shown in Figure 4.3) within our galaxy sample are consistent with either being flat or increasing radially outwards. We show $f_{\mathrm{H}\alpha}$ against galactocentric radius and galactocentric radius normalised to r_{25} in Figure 4.7. We observe an overall trend of increasing $f_{\mathrm{H}\alpha}$ with radius. This is in qualitative agreement with Lacerda et al. (2018) who find that the fraction of Hα flux from star forming complexes increases in significance compared to that emanating from the DIG at higher galactocentric radii.

The question then arises as to whether it is geometry, in the form of galactocentric radius, that is the determining factor or if another galaxy property that changes with radius is the driving factor behind the radial increase in $f_{\mathrm{H}\alpha}$ that we observe. We investigate the correlations of $f_{\mathrm{H}\alpha}$ with a number of other physical parameters, which are displayed in Table 4.3 along with their correlation coeficients and p-values. First, we find no statistically significant correlations between $f_{\mathrm{H}\alpha}$ and the lifecycles of molecular clouds or characteristic size-scales of the ISM (λ, $r_{\mathrm{peak,CO}}$ and $r_{\mathrm{peak,H}\alpha}$). We

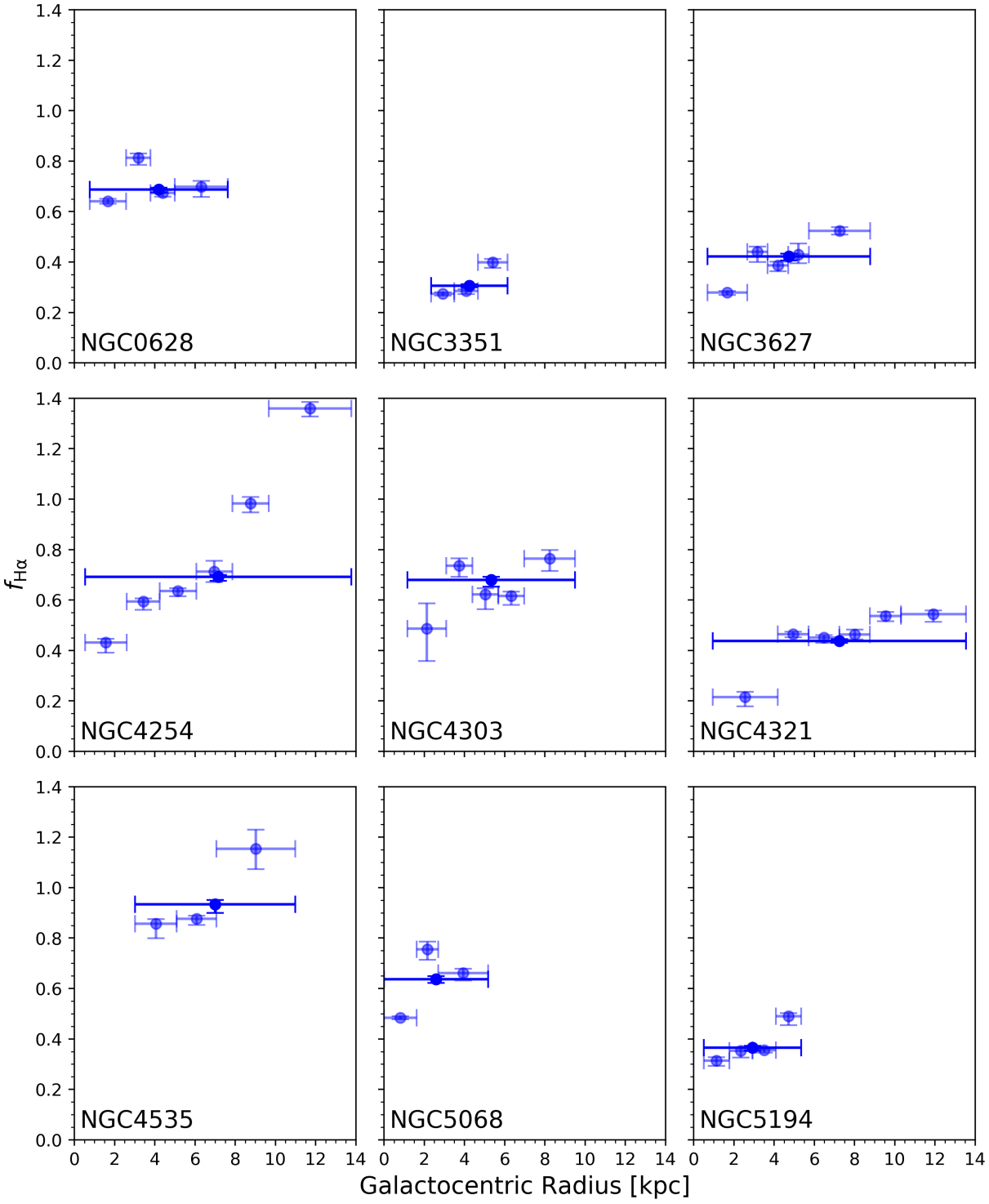

Figure 4.3: Radial profiles of the compact Hα fraction, $f_{H\alpha}$ for each individual galaxy in our sample. Dark blue datapoints show the measurement for the entire galaxy. Light blue datapoints show measurements for individual radial bins. For all datapoints, the vertical error bar shows the 1σ uncertainties on the measurement and the horizontal error bar shows the radius range of the radial bin in which the measurement was made. In general, the value of $f_{H\alpha}$ increases outwards or consistent with being flat.

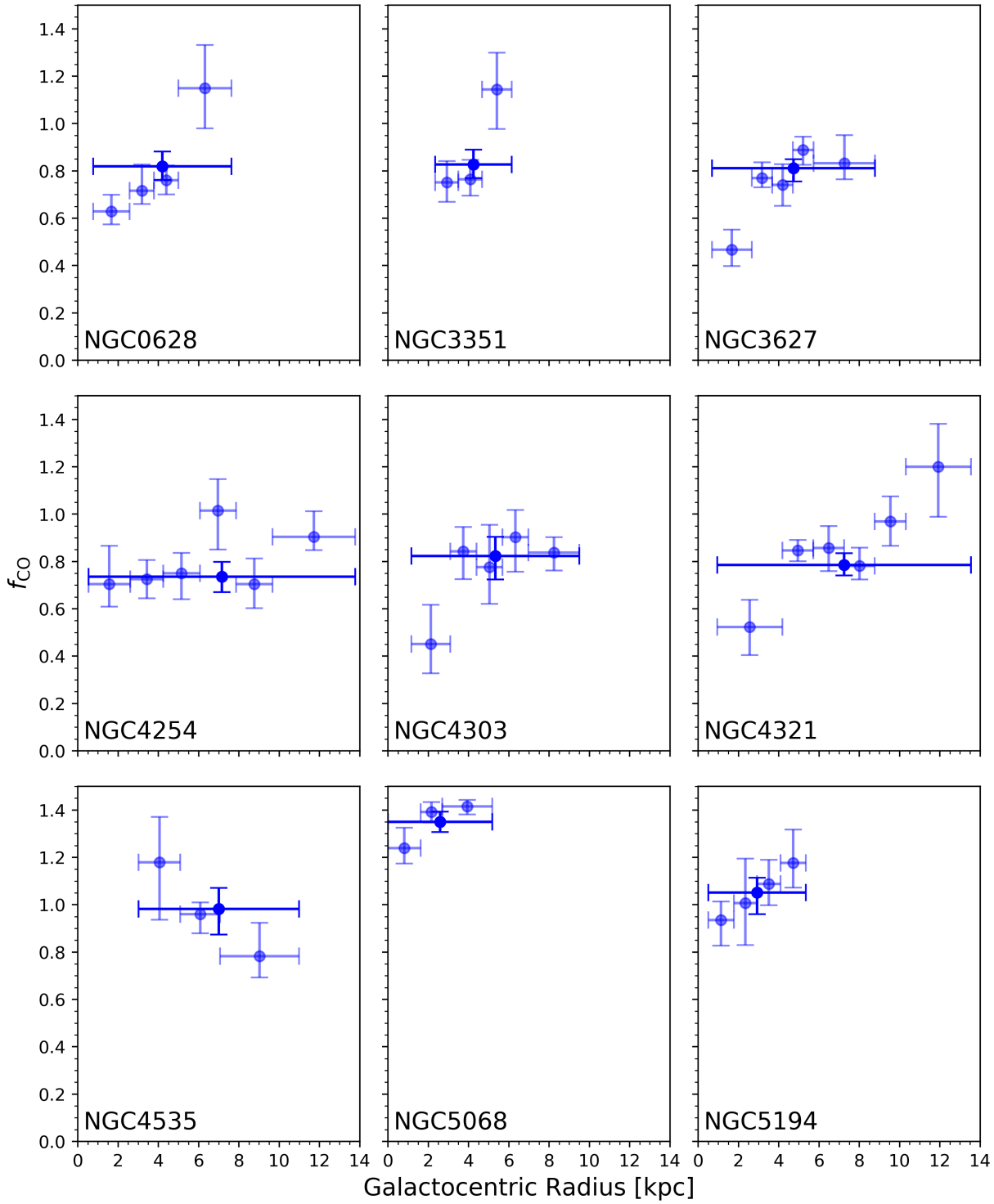

Figure 4.4: Radial profiles of the compact CO fraction, $f_{\rm CO}$ for each individual galaxy in our sample. Dark blue datapoints show the measurement for the entire galaxy. Light blue datapoints show measurements for individual radial bins. For all datapoints, the vertical error bar shows the 1σ uncertainties on the measurement and the horizontal error bar shows the radius range of the radial bin in which the measurement was made.

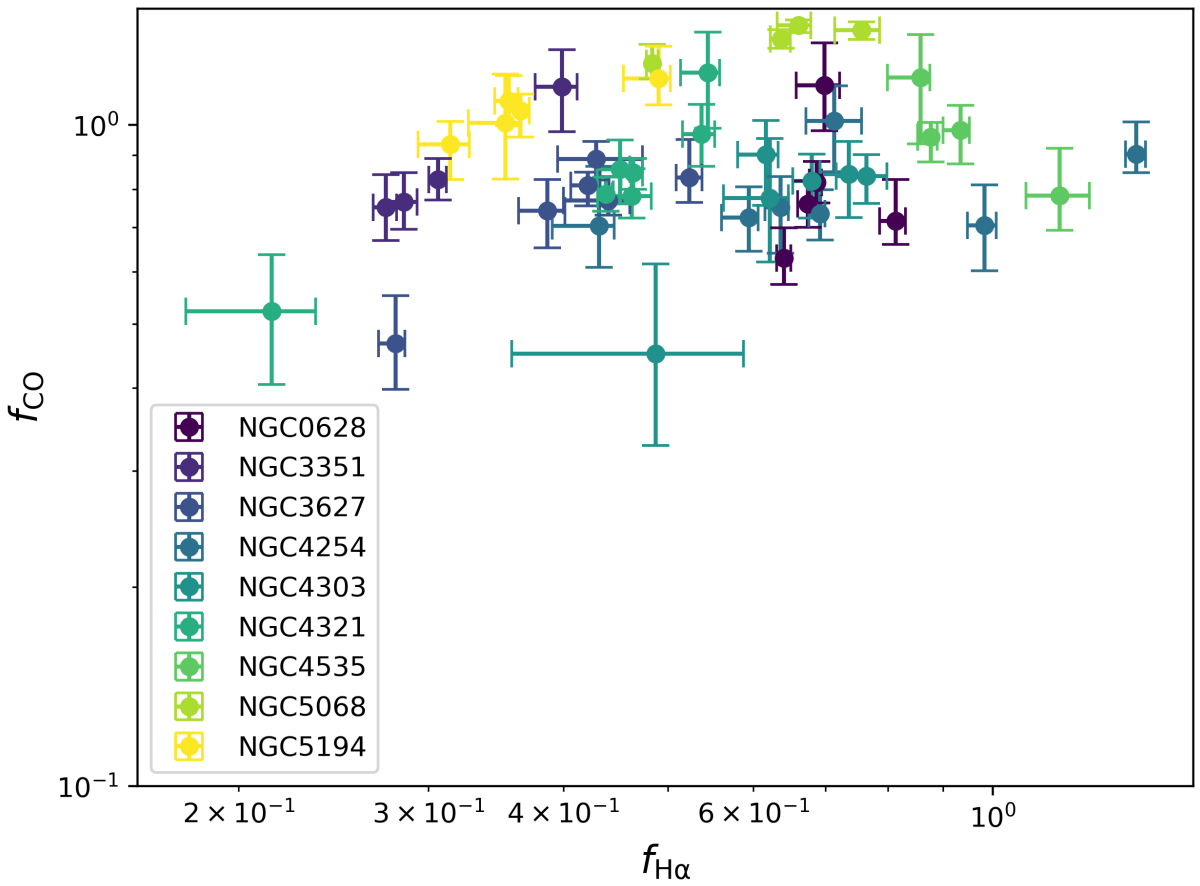

Figure 4.5: f_{CO} as a function of $f_{H\alpha}$. Measurements for each galaxy are shown with colours indicated by the legend. The horizontal and vertical error bars indicate the 1σ uncertainties.

show $f_{H\alpha}$ as a function of those parameters for which we find statistically significant correlations in Figure 4.8. In the rest of this section, we proceed to discuss each in detail.

First, we find a statistically significant anti-correlation with the gas phase metallicity. Modelling of observations of the ISM indicates that lower metallicity galaxies are observed to have more porous interstellar media than those of high metallicity galaxies (e.g. Cormier et al., 2019). This would indicate that more ionising radiation would escape HII regions to ionise the DIG. Indeed, simulations indicate that greater fractions of Lyman-continuum radiation are able to escape HII regions at lower metallicity (see e.g. Rahner et al., 2017; Kimm et al., 2019) and would thus be available to ionise the DIG. Such a scenario would lead to increasing $f_{H\alpha}$ with increasing metallicity, however, in contrast to the trend we observe. It should be noted, however, that a complication of interpreting this correlation is that measurements of metallicity and metallicity gradients can be affected by the presence of diffuse ionised gas (Zhang et al., 2017; Poetrodjojo et al., 2019; Vale Asari et al., 2019).

We find statistically significant anti-correlations with Σ_{stars}, Σ_{SFR} and Σ_{H_2}, the strongest of which is with Σ_{stars}. All the surface densities of these three components decrease with radius, however, Σ_{stars} decreases most smoothly with radius. The fact that Σ_{stars} is more significantly correlated with $f_{H\alpha}$ than Σ_{SFR} may point to the relative importance of field stars at driving variation in $f_{H\alpha}$ with respect to photons escaping from star forming regions in our sample. Lacerda et al. (2018)

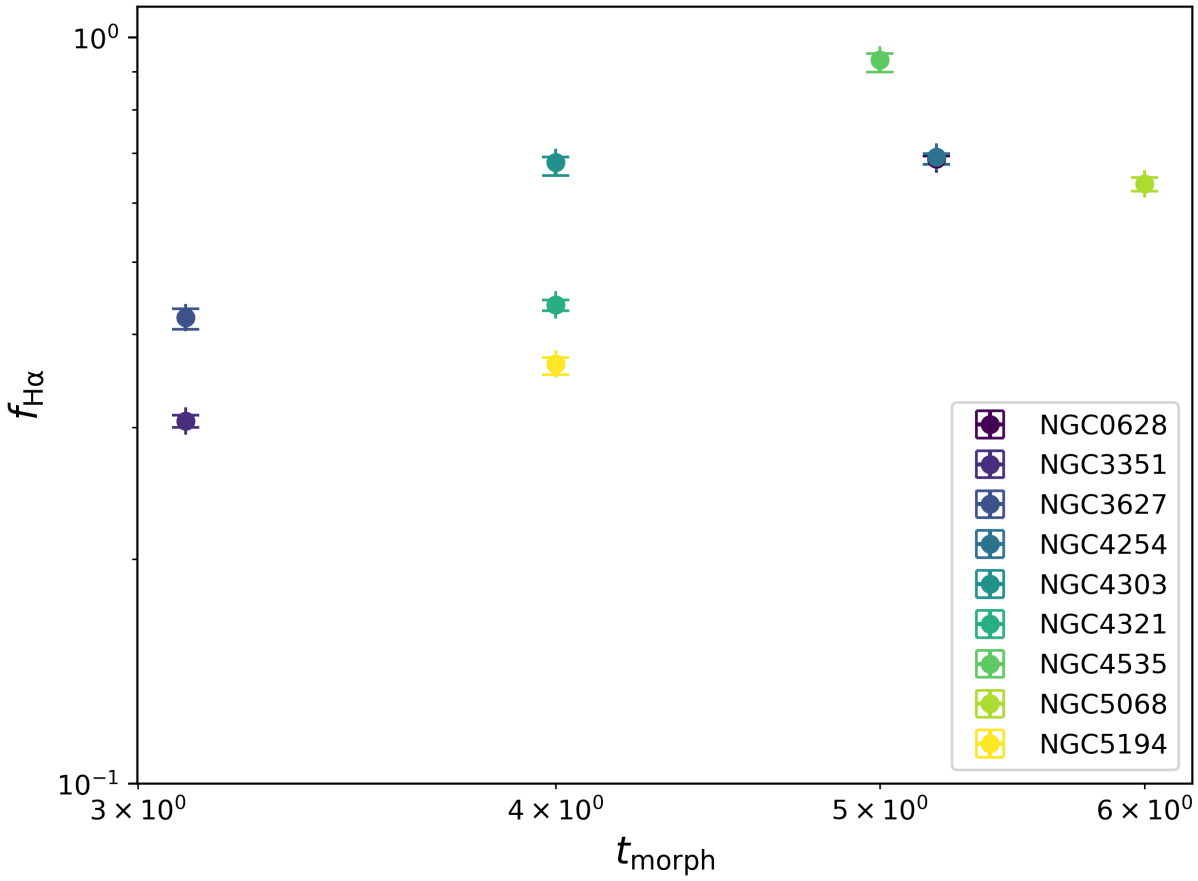

Figure 4.6: The compact Hα emission fraction as a function of morphological type. Measurements for each galaxy are shown with colours indicated by the legend. The vertical error bars indicate the 1σ uncertainty on the measurements.

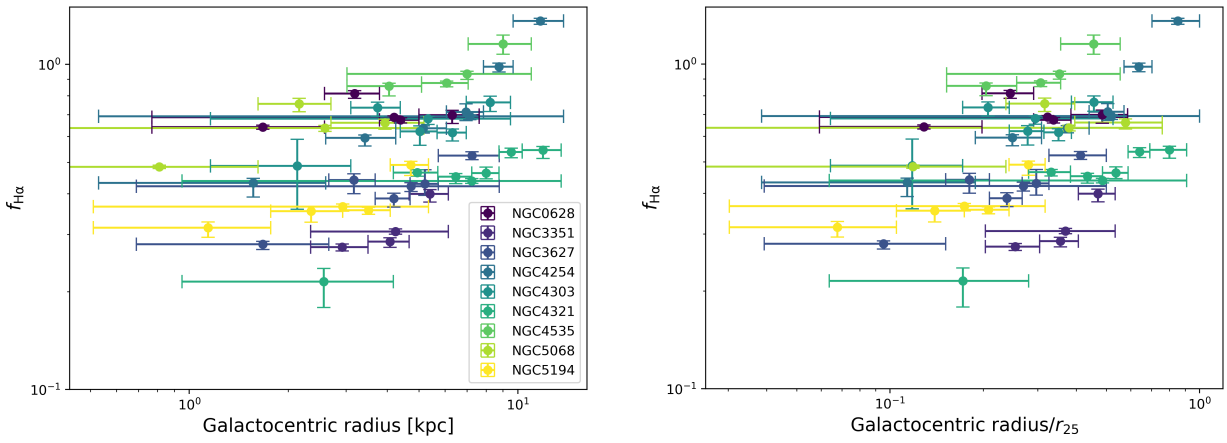

Figure 4.7: $f_{H\alpha}$ as a function of [left panel] galactocentric radius and [right panel] galactocentric radius normalised to the radius of the galaxy at the isophote of 25th magnitude in the B-band (r_{25}). The vertical error bars show the 1σ uncertainties on the measurement and the horizontal error bar shows the radius range of the radial bin in which the measurement was made. Measurements for each galaxy are shown with colours indicated by the legend on the left panel.

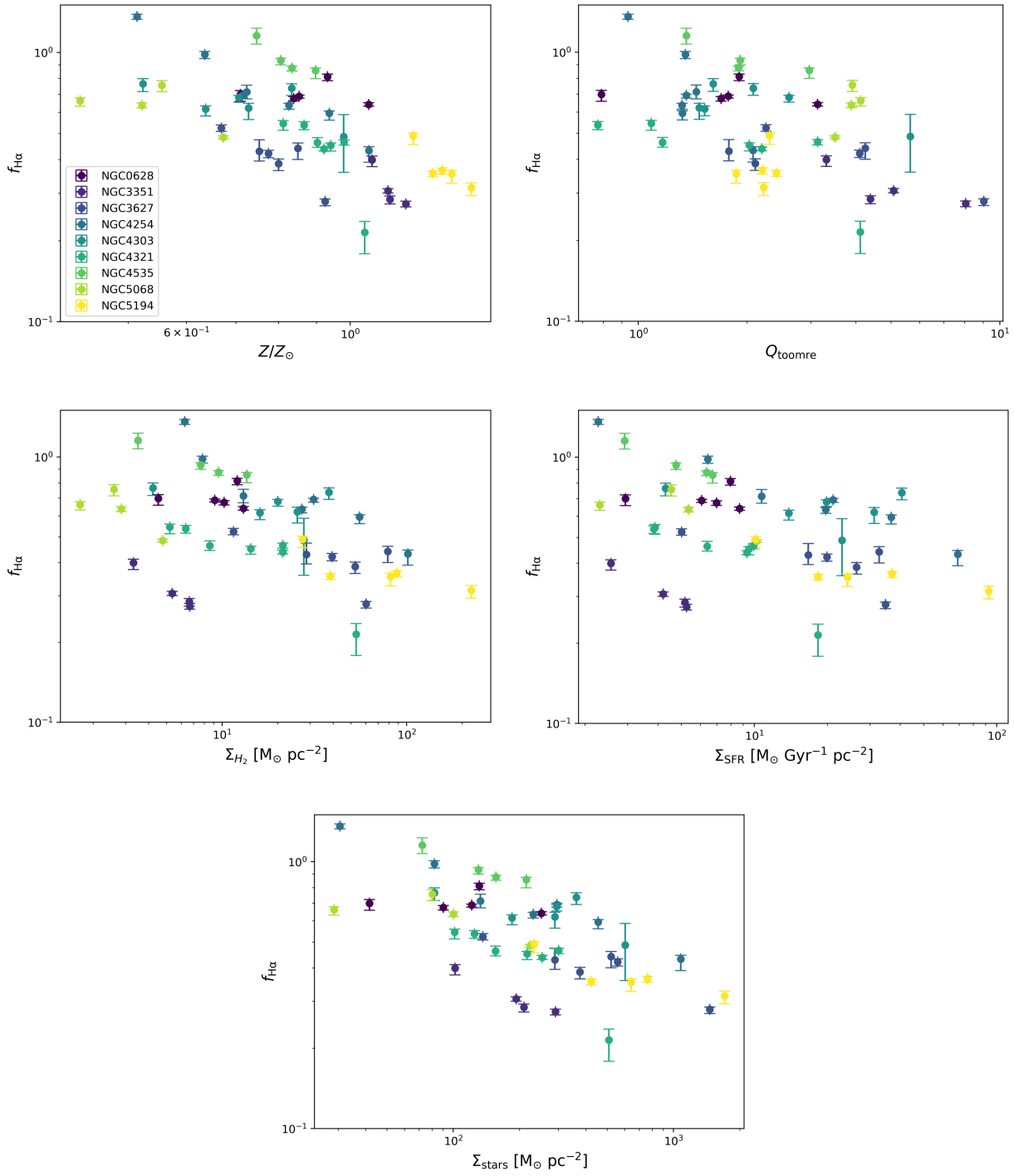

Figure 4.8: Figures showing the compact Hα emission fraction, $f_{\rm CO}$, against [top left panel] the metallicity $Z/{\rm Z}_\odot$, [top right panel] Toomre Q parameter [middle left panel] $\Sigma_{\rm H_2}$, [middle right panel] $\Sigma_{\rm SFR}$, [bottom panel] $\Sigma_{\rm stars}$. Measurements for each galaxy are shown with colours indicated by the legend on the top left panel. The horizontal and vertical error bars indicate the 1σ uncertainties.

further classified the DIG into "hDIG", ionised by hot low-mass evolved stars and "mDIG", ionised by a mixture of processes. In addition to an increase in the total significance of the DIG towards galaxy centres, they found an increase in the significance of the hDIG, indicating that this trend is partially driven by the older stellar populations towards galaxy centres in bulges.

We also find that there is an anti-correlation between the Toomre Q parameter and $f_{\mathrm{H}\alpha}$. Such a correlation could come about due to greater Toomre Q representing an increased general stability of a gas disc to collapse, reducing the possibility for the DIG to recollapse into compact structures. Toomre Q is inversely-proportional to $\Sigma_{\mathrm{H_2}}$ and we find the opposite trend to the one that we would expect if the correlation with Toomre Q were being driven by $\Sigma_{\mathrm{H_2}}$. This suggests that the molecular gas velocity dispersion and/or the epicyclic frequency to which Toomre Q are proportional drive this trend. Indeed, kinematic studies of edge-on galaxies indicate that galaxies host extraplanar, turbulence-supported, thick diffuse ionised gas discs (Levy et al., 2018, 2019). Future studies should therefore investigate the significance of $f_{\mathrm{H}\alpha}$ in terms of galactic kinematics, in particular the molecular and ionised gas kinematics.

We note that, for the correlations with $f_{\mathrm{H}\alpha}$ that we have explored, there is significant scatter between galaxies and some galaxies exhibit the opposite trend radially to the trend observed for the population of galaxies as a whole. As we explore correlation only, it is important to note that the trends we observe may well not be fundamental; there may well be other fundamental physical reasons that produce the correlations that we observe.

4.4.2 The compact fraction of CO

In general we find that the molecular gas, as traced by CO, is mostly in the form of compact structures. We measure that the majority of emission from all the galaxies in our sample comes from compact structures, however, we do find that some radial bins in our galaxies have a small majority of their emission coming from diffuse, large-scale molecular gas emission. The galaxy in our sample with the lowest compact fraction is NGC4254, with $f_{\mathrm{CO}} = 0.74^{+0.06}_{-0.06}$. At the other end of the range, we find two galaxies (NGC5068 and NGC5194) that are consistent with having no spatially-extended diffuse component.

One of the galaxies in our sample, NGC5194 (M51), has a previous measurement of the fraction of diffuse and compact emission in CO. Pety et al. (2013) determined that 50 ± 10 per cent of the emission came from size-scales larger than 1.3 kpc by comparing the flux recovered in single dish and interferometric datasets. In contrast, we determine that only 0^{+4}_{-0} per cent of the flux is diffuse, significantly lower than that reported by Pety et al. (2013). However, as noted in Chevance et al. (2019), such a measurement is similar to the process we employ of filtering diffuse emission in Fourier space, though without the application of corrective factors to account for flux loss from compact regions as a result of Fourier filtering that we apply (See section 4.2). Before applying these corrective factors, 57 per cent of the total flux is removed by the Fourier filter (i.e. would be considered diffuse emission), which agrees with the value determined by Pety et al. (2013).

We find that the most statistically significant correlations for the molecular gas compact emission fraction are with parameters relating to the structure of the ISM, in particular λ, $r_{\mathrm{peak,H}\alpha}$ and $r_{\mathrm{peak,CO}}$ and to the surface densities of $\mathrm{H_2}$, stars and SFR. We also find less significant correlations to feedback related quantities, namely v_{fb} and the ratio of the feedback timescale to the cloud lifetime ($t_{\mathrm{fb}}/t_{\mathrm{CO}}$). In addition, we observe a correlation with the corrective factor $q_{\mathrm{con,H}\alpha}$. $q_{\mathrm{con,H}\alpha}$ is an empirical corrective factor applied to measurements of $f_{\mathrm{H}\alpha}$ and does not enter into the calculation of f_{CO}. It is calculated as a function of $r_{\mathrm{peak,H}\alpha}$ and λ (see Equation 4.3). Both of these parameters exhibit stronger more statistically significant correlations with f_{CO} and we thus consider this to be the probable cause for the correlation.

The radial profiles of f_{CO} for the galaxies in our sample are displayed in Figure 4.4 and we plot

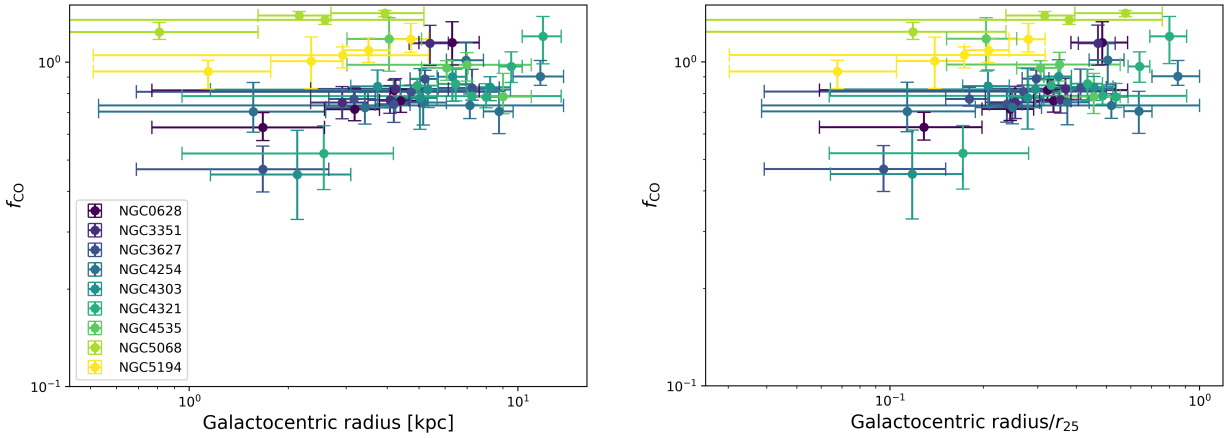

Figure 4.9: f_{CO} as a function of [left panel] galactocentric radius and [right panel] galactocentric radius normalised to the radius of the galaxy at the isophote of 25th magnitude in the B-band (r_{25}). The vertical error bars show the 1σ uncertainties on the measurement and the horizontal error bar shows the radius range of the radial bin in which the measurement was made. Measurements for each galaxy are shown with colours indicated by the legend on the left panel.

f_{CO} as a function of galactocentric radius and galactocentric radius normalised to r_{25} in Figure 4.9. We do not find a statistically significant correlation with radius, in contrast to that found for $f_{H\alpha}$, though normalising to r_{25} does increase the significance somewhat, such that it is marginally statistically significant ($p = 0.07$). We find a range of radial profiles for the galaxies. Some galaxies show either a potential increase or decrease of the compact gas fraction with radius, however, in general most of the galaxies are consistent with having a flat profile of f_{CO}. This contrasts with results from studies that compare tracers of molecular gas that probe different densities of molecular gas. These studies find that the fraction of dense gas decreases with radius (Roman-Duval et al., 2016; Jiménez-Donaire et al., 2019). A number of galaxies in the sample of Jiménez-Donaire et al. (2019) overlap with our own, namely NGC628, NGC3627, NGC4254, NGC4321 and NGC5194; we can thus compare the individual galaxies. For NGC628, Jiménez-Donaire et al. (2019) report a positive correlation between the ratio of HCN and CO intensities (I_{HCN}/I_{CO}, which traces the dense gas fraction) and radius and we likewise find that f_{CO} increases with radius. For the other galaxies Jiménez-Donaire et al. (2019) reports a negative correlation between I_{HCN}/I_{CO} and radius, whereas we find that f_{CO} increases with radius or is flat. These differences suggest that the dense gas fraction and the fraction of CO emission in compact structures are not directly correlated.

We display f_{CO} as a function of the remaining statistically significant physical parameters in Figure 4.10. The strongest correlation that we find is a negative correlation with λ, thus the larger the separation between individual star-forming regions the greater the fraction of CO emission that emanates from a large-scale, diffuse molecular gas reservoir. We note that we would expect f_{CO} to increase with increasing λ if this were simply a result of the definition of our filter. This is because an increased value of λ reduces the attenuation for a given spatial wavelength and thus results in a greater fraction of the total image flux remaining in the compact image produced as a result of the filtering process (see Equation 4.2). Thus, the fact that we find decreasing f_{CO} with increasing λ points towards this being a meaningful correlation. We also find a significant anti-correlation to the size of the star-forming regions in both tracers, $r_{peak,CO}$ and $r_{peak,H\alpha}$, further suggesting that the structure of the ISM and f_{CO} are linked.

We find statistically significant anti-correlations of f_{CO} with Σ_{H_2}, Σ_{SFR} and Σ_{stars}. This is the

opposite of what is found by studies assessing the dense gas fraction. In the Milky Way, Roman-Duval et al. (2016) find that the dense gas fraction increases with increasing Σ_{H_2} and in a sample of nearby galaxies, Jiménez-Donaire et al. (2019) find that the dense gas fraction increases with increasing Σ_{H_2} and Σ_{stars}. These contrasting trends again point towards different processes being responsible for setting the dense and compact molecular gas fractions in galaxies.

We also observe an anti-correlation with the feedback velocity $v_{fb} = r_{peak,CO}/t_{fb}$. This would suggest that both the feedback timescale and the size of the regions being dispersed are important for determining the fraction of molecular gas in a diffuse component. This would mean that galaxies with larger molecular clouds and molecular clouds that are more quickly dispersed by feedback would have a lower fraction of compact molecular gas. However, as we find a statistically significant correlation between f_{CO} and $r_{peak,CO}$, but do not find one between f_{CO} and t_{fb} and given the definition of v_{fb}, we consider that the correlation we observe between f_{CO} and t_{fb} is primarily a residual result of the correlation to $r_{peak,CO}$. Indeed we measure a larger correlation coefficient for $r_{peak,CO}$ along with greater statistical significance. We note, however, that we do observe an anti-correlation of f_{CO} with the ratio of t_{fb} to t_{gas}, which suggests that the fraction of a cloud lifetime that it is co-spatial with young, feedback-producing stars is important, with a larger fraction resulting in a greater diffuse gas fraction. If molecular outflows from molecular clouds feed a diffuse molecular gas reservoir, then longer portions of cloud lifetimes where feedback is active could drive a greater fraction of molecular material into this diffuse phase.

Finally, we note that, for the relationships that we have presented for f_{CO}, there is significant variation between the galaxies in our sample. Furthermore, some galaxies exhibit the opposite radial trend to the trend for the sample of galaxies in total. As we have measured correlation only, we note that other fundamental processes may indeed be driving the correlations that we observe.

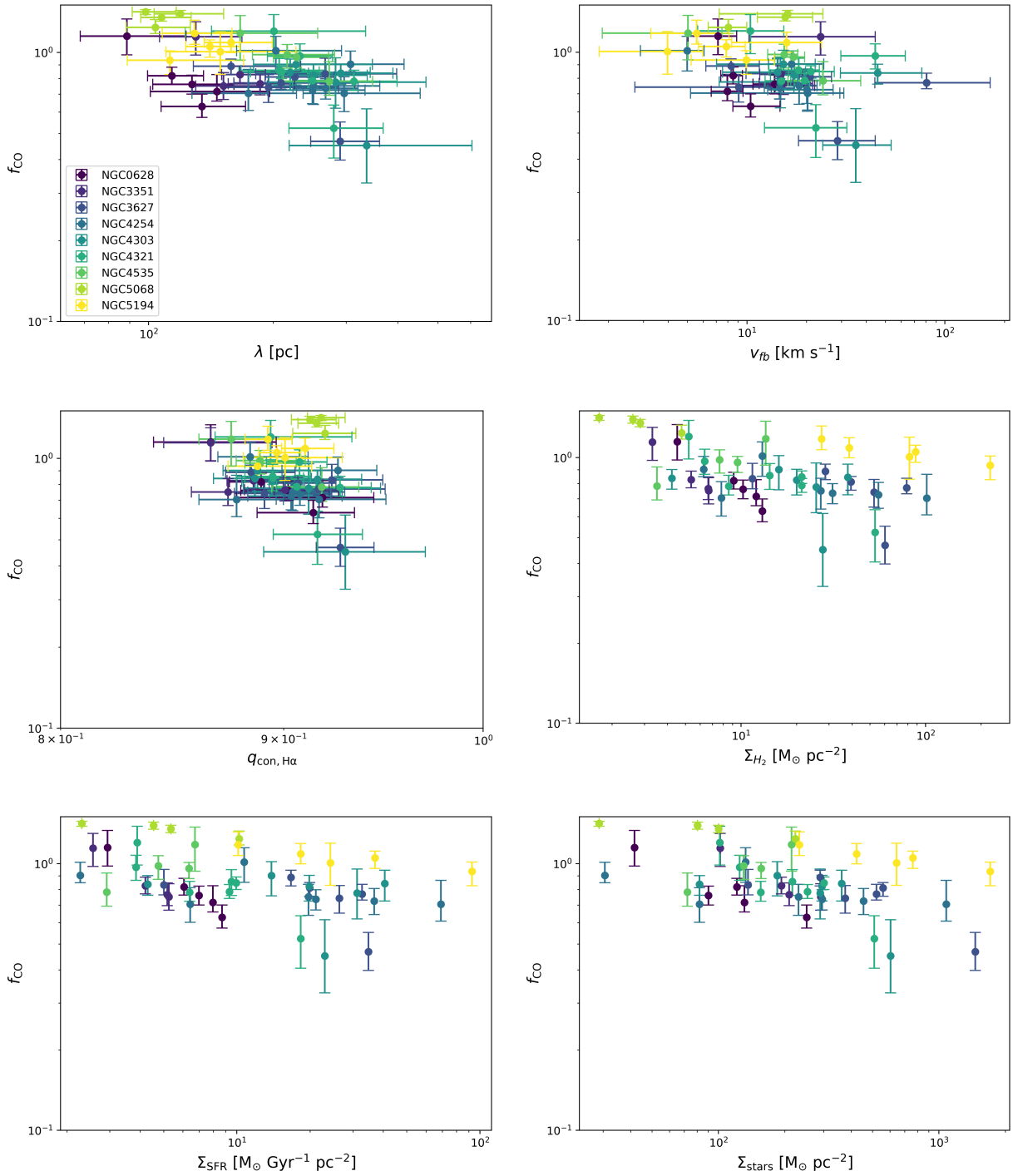

Figure 4.10: Figures showing the compact CO emission fraction, $f_{\rm CO}$, against [top left panel] λ, [top right panel] $v_{\rm fb}$, [middle left panel] $t_{\rm fb}$, [middle right panel] $\Sigma_{\rm H_2}$, [bottom left panel] $\Sigma_{\rm SFR}$, [bottom right panel], $\Sigma_{\rm stars}$, [continued, top left] $r_{\rm peak,CO}$, [continued, right left] $r_{\rm peak,H\alpha}$ and [continued, bottom] $t_{\rm fb}/t_{\rm CO}$. Measurements for each galaxy are shown with colours indicated by the legend on the top left panel. The horizontal and vertical error bars indicate the 1σ uncertainties.

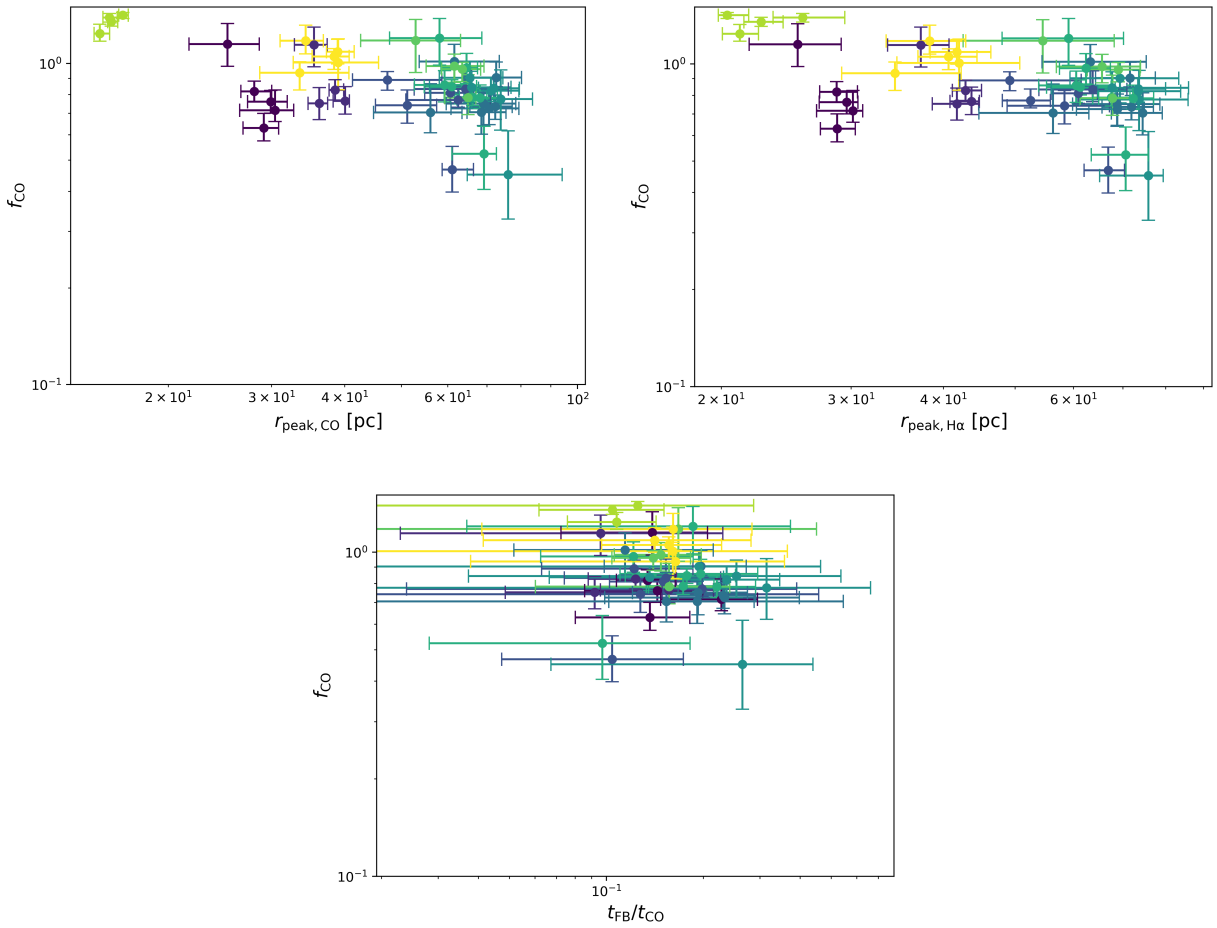

Figure 4.10: *continued*

4.5 Summary

We have measured the fractions of compact and diffuse emission in the molecular gas, as traced by CO ($f_{\rm CO}$) and ionised gas, as traced by Hα ($f_{\rm H\alpha}$) for a sample of nine nearby galaxies. We have also presented a number of statistically significant correlations between these compact fractions and other physical quantities relating to galaxy structure, the ISM, star formation and feedback. Our main conclusions are as follows:

- There is no statistically significant correlation between the fraction of compact emission in the ionised and molecular gas phases. However, both $f_{\rm H\alpha}$ and $f_{\rm CO}$ are anti-correlated with $\Sigma_{\rm H_2}$, $\Sigma_{\rm SFR}$and $\Sigma_{\rm stars}$.
- There is significant variation of $f_{\rm CO}$ and $f_{\rm H\alpha}$ between and within galaxies.
- The fraction of Hα emission in compact structures increases with or is flat with radius. This matches qualitatively the results of a study of the DIG based on an Hα equivalent-width criterion (Lacerda et al., 2018) who found that the fraction of diffuse gas decreased with radius.
- $f_{\rm H\alpha}$ is larger in galaxies with later morphological types. This matches qualitatively the results

of Lacerda et al. (2018), but is in contrast to Oey et al. (2007), who found no trend with morphological type.

- $f_{\mathrm{H}\alpha}$ is anti-correlated to the Toomre Q parameter, suggesting that increased disc stability may play a role in supporting a spatially-extended diffuse ionised gas component. Future studies should explore how $f_{\mathrm{H}\alpha}$ is related to galactic kinematics.
- $f_{\mathrm{H}\alpha}$ is anti-correlated to metallicity, which is the opposite of what would be expected if the porosity of the ISM drove the increase in the significance of the DIG. However, extra care should be taken in interpreting this result as the DIG has been shown to affect measurements of metallicity (Zhang et al., 2017; Poetrodjojo et al., 2019; Vale Asari et al., 2019).
- The majority of CO emission is contained in compact structures, presumably molecular clouds, for all of the galaxies in our sample.
- f_{CO} is correlated most strongly with parameters related to the structure of the ISM: the separation between star forming regions (λ) and the size of compact regions in both phases ($r_{\mathrm{peak,CO}}$ and $r_{\mathrm{peak,H}\alpha}$). This suggests that the same processes that regulate the structure of the ISM may also regulate the fraction of diffuse molecular gas.
- f_{CO} is also less significantly anti-correlated with v_{fb} and the ratio of t_{fb} to t_{CO} suggesting that timescales associated to feedback may play a role in setting the fraction of diffuse molecular gas.
- We do not reproduce correlations with physical parameters that are observed for the dense molecular gas fraction (see Roman-Duval et al., 2016; Jiménez-Donaire et al., 2019) when considering f_{CO}. This suggests different mechanisms regulate the fractions of dense and compact molecular gas.

We have reported a number of observed correlations between the compact emission fractions of ionised and molecular gas in nine nearby disc galaxies. These correlations suggest that different processes are responsible for diffuse emission in the two gas phases. We also observe variation between the galaxies in our sample, for example we observe both decreasing and increasing radial profiles for f_{CO}. The sample presented in this paper amounts to nine galaxies, however, the full PHANGS-ALMA survey (Leroy et al., in prep.) will enable future work to analyse the compact emission fractions in ~ 80 galaxies. This will enable us to examine the origin of such variation within the population in greater detail.

5 Conclusions and outlook

The study of cloud-scale star formation is at an exciting juncture. The high-resolution, high-sensitivity imaging now available as a result of the Atacama Large Millimeter/Submillimeter Array (ALMA; Wootten & Thompson, 2009) is transitioning us from an era where cloud-scale molecular gas observations were restricted to the Milky Way and the nearest few galaxies to one where samples with tens of galaxies are possible. These new observations combined with new observational methods such as the "uncertainty principle of star formation" are allowing us to tackle a number of important questions regarding the star formation process across a range of environments. Upcoming and proposed observational facilities such as the James Webb Space Telescope (JWST; Gardner et al., 2006), the Square Kilometre Array (SKA; Dewdney et al., 2009) and the next-generation Very Large Array (ngVLA; Selina et al., 2018) will improve upon the resolution and sensitivity of current facilities. These new capabilities will allow star formation to be characterised on the cloud-scale out to higher redshifts more routinely, as well as widening the range of galaxy components that can be traced on the cloud-scale.

In this thesis, I have contributed to the development of observational methods to constrain the structure and evolution of galaxies, as well as applying them in the Nearby Universe. In this concluding chapter, I summarise the results of this thesis as well as highlighting their links to other work. I also present a number of avenues through which the questions addressed in this thesis and by others can be advanced in the future.

5.1 The lifecycles of molecular clouds

Star formation in galaxies takes place in dense, cool formations of molecular gas known as molecular clouds. The nature and evolution of these objects is a key question in understanding the evolution of galaxies, with their lifetimes in particular being an important area of inquiry. The time-scales for molecular clouds to collapse under their own self-gravity is typically ~ 10 Myr (Schruba et al., 2019). However, galaxies in the nearby universe are observed to be inefficient at converting their molecular gas reservoirs into stars, with molecular gas depletion times of ~ 2 Gyr at current star-formation rates (e.g Bigiel et al., 2008, 2011). A key question then has been to understand whether clouds are short-lived objects with lifetimes comparable to their freefall times that are dispersed quickly by feedback after forming stars or whether they persist for a timescale equivalent or greater to that of galactic rotation or the lifetimes of hydrogen molecules ($\gtrsim 100$ Myr). Observational evidence from a number of methods points towards cloud lifetimes of a few tens of Myr in nearby star-forming late-type galaxies (Engargiola et al. 2003; Kawamura et al. 2009; Miura et al. 2012; Meidt et al. 2015; Corbelli et al. 2017; Kruijssen et al. 2019; Chevance et al. 2019 and Chapter 3 of this thesis). Some studies have, however, concluded that clouds live for 100 Myr or more based on the presence of clouds in the interarm regions of spiral galaxies (Scoville et al., 1979; Koda et al.,

2009). Extreme environments may also lead to significantly different cloud lifetimes; an analysis of cloud lifetimes in the Milky Way CMZ indicated cloud lifetimes of only ~ 1 Myr (Kruijssen et al., 2015).

The natural next question after having measured cloud lifetimes in a number of galaxies is: "how do the lifetimes of molecular clouds vary and what determines this variation?" A recent application of the "uncertainty principle of star formation" to nine nearby galaxies by Chevance et al. (2019) found that the lifetimes of molecular clouds vary within environment and identified two regimes dependent on the azimuthally-averaged molecular gas surface density within the $\sim$ kpc radial bins in which the lifetimes were determined. In the high ($\Sigma_{\rm H_2} \geqslant 8$ M$_\odot$ pc^{-2}) molecular gas surface density regime, cloud lifetimes matched timescales predicted by the analytic theory of Jeffreson & Kruijssen (2018), with the timescales for dispersal by shear (τ_β) and the ISM gravitational freefall time ($\tau_{\rm ff,g}$) dominating the predicted timescale for the majority of measurements (see Equation 1.20). In contrast, in the low ($\Sigma_{\rm H_2} \leqslant 8$ M$_\odot$ pc^{-2}) molecular surface density regime the cloud lifetimes correlate best with the cloud's internal dynamical timescales, namely the timescale of gravitational freefall (Equation 1.18) and the cloud crossing time (Equation 1.19).

Previous studies of the cloud lifetime have in general focussed on a single target and have employed a diversity of methods. The application of the same method to a sample of nine galaxies by Chevance et al. (2019) represents an important step towards a statistical analysis of the question of cloud lifetimes. The PHANGS-ALMA survey (Leroy et al. in prep.) will extend cloud-scale ($\sim 50-80$ pc), high mass sensitivity (detection of molecular clouds $\gtrsim 10^5$ M$_\odot$) imaging to a sample of ~ 80 nearby massive star forming galaxies. The resolution and sensitivity of this survey should enable the measurement of cloud lifetimes across the sample using "the uncertainty principle for star formation". Thus whilst cloud lifetimes had only been measured in a handful of galaxies at the time I commenced this thesis, a competitively large sample of molecular cloud lifetimes is within reach in the foreseeable future.

Molecular clouds do not, however, live exclusively in late-type galaxies. Indeed they have been detected in the lenticular galaxy NGC4526 (Utomo et al., 2015). However, they are observed to have different properties when compared to the Milky Way and other nearby galaxies: specifically, they found that clouds of a similar size in NGC4526 are more luminous, denser and have higher velocity dispersions. Notably, Utomo et al. (2015) found also no relationship between size and line-width[37] for molecular clouds unlike that found for the Milky Way and other nearby galaxies (see Equation 1.1). Such different properties may well lead to different cloud lifetimes to those in nearby late-type galaxies. Indeed, the analytic theory of Jeffreson & Kruijssen (2018) predicts that the typical environments of early-type galaxies will lead to a different combination of processes being important for determining cloud lifetimes as compared to late-type galaxies. A statistical comparison between late and early-type galaxies will require high-resolution molecular gas imaging of a sample of early-type galaxies. Such a survey is possible as a number of gas rich early-type galaxies have been detected (Young et al., 2011; Davis et al., 2015).

Another uncertainty with respect to molecular clouds is the timescale of their destruction or dispersal due to feedback and whether they are able to survive from the time when stars form until the onset of the first supernovae (~ 3 Myr Leitherer et al., 2014). Kruijssen et al. (2019) found that clouds continue to coexist with HII regions for only $t_{\rm fb} = 1.5^{+0.2}_{-0.2}$ Myr after they become visible Hα in the nearby galaxy NGC300. This indicates that they are dispersed or destroyed before the earliest supernovae. In contrast, application of the same method to M33 found $t_{\rm fb} = 5.2^{+0.9}_{-1.3}$ Myr (see Chapter 3), suggesting that the earliest supernovae can explode whilst their progenitor molecular cloud remains. We hypothesise that this is due to the larger, more massive molecular clouds in M33 in comparison to NGC300 (Schruba et al., 2019) resulting in a longer timescale for their dispersal

[37] an observable proxy for velocity dispersion

by photoionization. Analysis of $t_{\rm fb}$ in relation to the cloud properties in a sample of galaxies larger than two is required to determine if this correlation is significant, however. Chevance et al. (2019) has measured $t_{\rm fb}$ in nine nearby galaxies and future work will analyse these measurements in relation to other properties.

Star formation is a multi-stage process. This thesis looks at the progression from molecular clouds to young stars (see Chapter 3). A natural next step to build upon such studies is to characterise the durations of the other stages of star formation. One example of an important stage in the star formation process, is the formation of molecular clouds. Extragalactic studies indicate that molecular clouds form in dense regions of HI (e.g Engargiola et al., 2003; Wong et al., 2009). As the HEISENBERG code can be applied to any two evolutionary stages in a Lagrangian sequence, it can be used to constrain the lifetimes of these phases. Whilst the maximum obtainable resolution of HI observations is worse than that which can be obtained for molecular gas, a few galaxies in the Local Group have been imaged on the cloud-scale: the SMC (10 pc; Di Teodoro et al., 2019), the LMC (15 pc; Kim et al., 2003), IC10 (20 pc; Wilcots & Miller, 1998), M31 (50 pc; Braun et al., 2009) and M33 (80 pc; Koch et al., 2018). A survey of nearby galaxies in HI (THINGS; Walter et al., 2008) imaged 34 galaxies at resolutions ranging from ~ 100 pc for the nearest (~ 2 Mpc) galaxies to ~ 500 pc for the furthest (~ 15 Mpc) galaxies in the sample. HI imaging on the cloud-scale would become feasible in a much larger sample of galaxies with the SKA (see e.g. de Blok et al., 2015) and ngVLA (see e.g. Pisano et al., 2018). Such a survey would allow a number of important questions to be addressed as a function of environment, including the lifetimes of HI clouds and the formation timescales for molecular clouds.

5.2 The structure of the ISM

In the Milky Way, the ISM is observed to form into a number of structures. One such structure is that of molecular clouds (see Section 1.2.1.6) in which star formation takes place and bright HII regions form. A question that one can ask regarding these "star forming regions" is: "how are they distributed within galaxies and why?" One of the fitting parameters measured by the HEISENBERG code is the mean separation between independent star forming regions, λ. Kruijssen et al. (2019) found that λ is approximately the scale height of the gas disc of NGC300, arguing that this is indicative of an ISM that is "structured by feed back-driven bubbles that depressurise when they break out of the disc". Analysis in a sample of galaxies will determine if this relationship holds in galaxies with different properties or if other physical length scales such as the Toomre length, the epicyclic length scale and the turbulent driving scale are important in different environments. Chevance et al. (2019) presented measurements of λ for nine nearby galaxies; future work will be able to compare these measurements to the aforementioned length scales.

However, hydrogen gas in galaxies is not restricted to spatially compact regions such as HII regions and molecular clouds. Indeed a spatially-extended, diffuse ionised hydrogen layer has been known about in the Milky Way for many decades (e.g. Reynolds et al., 1973) and is a well established feature of external galaxies also (e.g. Oey et al., 2007; Lacerda et al., 2018). More recent observations have indicated a diffuse component of molecular hydrogen also (see e.g; Caldú-Primo et al. 2013; Pety et al. 2013; Caldú-Primo et al. 2015 and Chapter 4 of this thesis).

Properly accounting for diffuse emission is crucial for properly interpreting observational results. Unresolved integrated measurements of galaxies will necessarily include this diffuse spatially extended emission, whereas resolved measurements allow the identification of compact structures embedded in such a diffuse medium. Combining measurements on both size scales therefore can introduce uncertainty due to the significance of such a phase. For example, measuring the star formation efficiency per freefall time when combining an integrated depletion time measurement

with a cloud-scale measurements of $\tau_{\rm ff}$ introduces such an uncertainty, as increased diffuse gas will reduce the star formation efficiency (see discussion in Schruba et al., 2019).

Indeed, diffuse emission has been shown to impact measurements and interpretation of results in a wide range of scenarios. For example, the Kennicutt-Schmidt relation is a well established, correlation between the surface density of SFR and the surface density of gas in galaxies (Schmidt, 1959; Kennicutt, 1989, 1998). Subtraction of diffuse emission from SFR and gas tracers alters the slope and normalisation of this relation and has important implications for comparison to predictions from models of star formation (Kennicutt, 1998). The DIG specifically has been shown to impact the measurement of metallicity and metallicity gradients in galaxies (Zhang et al., 2017; Poetrodjojo et al., 2019; Vale Asari et al., 2019), the measurement of Hα rotation profiles and the determination of galaxy masses from these dynamical masses (Levy et al., 2018).

As new telescope facilities increasingly allow us to resolve the structure of galaxies, properly accounting for diffuse emission will play a role in the proper interpretation of observational results. In Chapter 2, applications of the HEISENBERG code to simulated datasets show that diffuse emission can significantly bias the measurements of molecular cloud lifecycles and the ISM structure. A method for separating the diffuse and compact components of the ISM in Fourier space, by using λ, the mean separation between star-forming regions, as a physical divide between compact and diffuse, spatially extended emission is presented in Chapter 2. This method allows cloud lifecycles and ISM structure to be measured with the HEISENBERG code without the biasing impact of diffuse emission. This method also quantifies the significance of the compact and diffuse, spatially-extended emission components.

Chapter 4 presents measurements, with this method, of the compact emission fractions of ionised ($f_{\rm H\alpha}$) and molecular ($f_{\rm CO}$) gas in nine nearby galaxies, along with a correlation analysis of these compact fractions with a number of other physical quantities. The correlations that are presented point towards a number of relationships. First, there is no correlation between $f_{\rm H\alpha}$ and $f_{\rm CO}$ indicating that different processes may set the significance of diffuse and compact emission in these phases.

We report that the fraction of compact ionised gas emission in later-type galaxies is higher than that in earlier-type galaxies. A number of other methods have been used to analyse the significance of the DIG in galaxies. Our result qualitatively matches the results of a study separating the flux from star-forming regions and the DIG using an Hα equivalent width criterion (Lacerda et al., 2018), but disagrees with the results of Oey et al. (2007), who seperated the DIG and star-forming region flux using an HII region identification algorithm. We also find that $f_{\rm H\alpha}$ is positively correlated with radius in our sample, in agreement with Lacerda et al. (2018).

In addition, we find that $f_{\rm H\alpha}$ is anti-correlated with the Toomre Q parameter. Such a result may suggest that an increase in disc stability may play a role in supporting the DIG. A logical future step to investigate this relationship in our galaxies is to investigate $f_{\rm H\alpha}$ in terms of galactic kinematics. We observe an anti-correlation of $f_{\rm H\alpha}$ to the gas-phase metallicity of our galaxies. Such a relationship is the opposite of the relationship we would expect if ISM porosity was the determining factor for the significance of the DIG in galaxies. The significance of this result may well be affected by previously mentioned impact that the DIG can have on metallicity measurements (Zhang et al., 2017; Poetrodjojo et al., 2019; Vale Asari et al., 2019).

We find that the majority of CO emission is in compact structures in all nine galaxies of the sample. Our results do not reproduce correlations that have been observed for the dense molecular gas fraction (see Roman-Duval et al., 2016; Jiménez-Donaire et al., 2019). Indeed we find that $f_{\rm CO}$ exhibits the strongest correlations with quantities describing ISM structure, namely λ and the sizes of compact regions in the Hα and CO maps. We also find less significant correlations to the feedback velocity, $v_{\rm fb}$ and the ratio of $t_{\rm fb}$ to $t_{\rm CO}$. These results suggest that processes that shape

the structure of the ISM, including stellar feedback, may also play a role in determining $f_{\rm CO}$.

The method presented in Chapter 2 can be applied to images across the wavelength range where suitable resolution can be obtained. Diffuse emission has been detected in a number of other commonly used astronomical tracers. This includes tracers of molecular gas mass such as C II (Kapala et al., 2015) and tracers of star formation, such as infrared wavelengths (see Leroy et al. 2012, Crocker et al. 2013 and Verley et al. 2009 for diffuse emission in 8 μm and 24 μm), UV (Pradhan et al., 2010, 2011; Thilker et al., 2005) and X-ray (Fabbiano et al., 1990; Bregman & Pildis, 1994; Strickland et al., 2004).

In Chapter 3, the method is applied to GALEX FUV and NUV images in addition to Hα and CO. We report a diffuse emission fraction in the FUV (63^{+1}_{-1} per cent) in good agreement with an earlier study of M33 by Thilker et al. (2005), who reported an FUV diffuse emission fraction of ~ 65 per cent. We find a similar diffuse emission fraction in the GALEX NUV (67^{+1}_{-1} per cent) image as for the FUV image. Targeted spectroscopic observations at FUV wavelengths indicate variation in the diffuse fraction both with wavelength and between galaxies. Such observations of regions within the LMC (Pradhan et al., 2010) and SMC (Pradhan et al., 2011) indicate that the diffuse UV fraction in the SMC is higher that the LMC. Pradhan et al. (2011) attributes this a to higher dust albedo in the SMC and a resultant increase in scattered light. It is also found that the diffuse fraction increases with wavelength across the FUV band in both galaxies (Pradhan et al., 2010, 2011). Understanding the variation of UV diffuse emission requires its analysis in a larger variety of environments and thus a survey of the significance of diffuse emission in nearby galaxies is required.

5.3 Comparisons with simulations

Comparing observations to simulations is an important step for our understanding of the physical processes that govern the star formation process. A number of different physical models are currently used for star formation and feedback in numerical simulations. These models can produce galaxies with the same integrated properties, such as SFR, however, their cloud-scale matter distributions differ (Hopkins et al., 2013; Haas et al., 2013; Scannapieco et al., 2012).

Comparing between observations and simulations in a like-for-like manner is, however, crucial for these comparisons to be meaningful. The application of observational methods, such as the Heisenberg code, to synthetic observations is a promising method of achieving this. Fujimoto et al. (2019) measured the lifecycles of molecular clouds with the Heisenberg code in a high spatial-resolution (8 pc) simulation of a disc galaxy. They measured a cloud lifetimes of 36^{+4}_{-6} Myr, which is towards the upper end of those measured observationally with the method (cf. Chevance et al., 2019). However, they measure a 23^{+1}_{-1} Myr, which is greater than four times the longest feedback timescale measured with the method ($5.2^{+0.9}_{-1.3}$ Myr; see Chapter 3). On this basis they concluded that their feedback recipe was unable to disperse molecular clouds as rapidly as observed in reality. Applications of cloud-scale diagnostics to high-resolution simulations will place further constraints on the range of plausible physical models.

5.4 Resolving the ISM at high-redshift

Large scale studies such as those that will be undertaken on the PHANGS sample will give us a snapshot of the physics of star formation on the cloud-scale in the Local Universe at $z \sim 0$ in a range of different galaxy environments. However, in order to understand how galaxies have formed and evolved, we must measure star formation and ISM physics on the cloud-scale across cosmic time. Such studies are motivated by the fact that the large-scale properties of galaxies change with

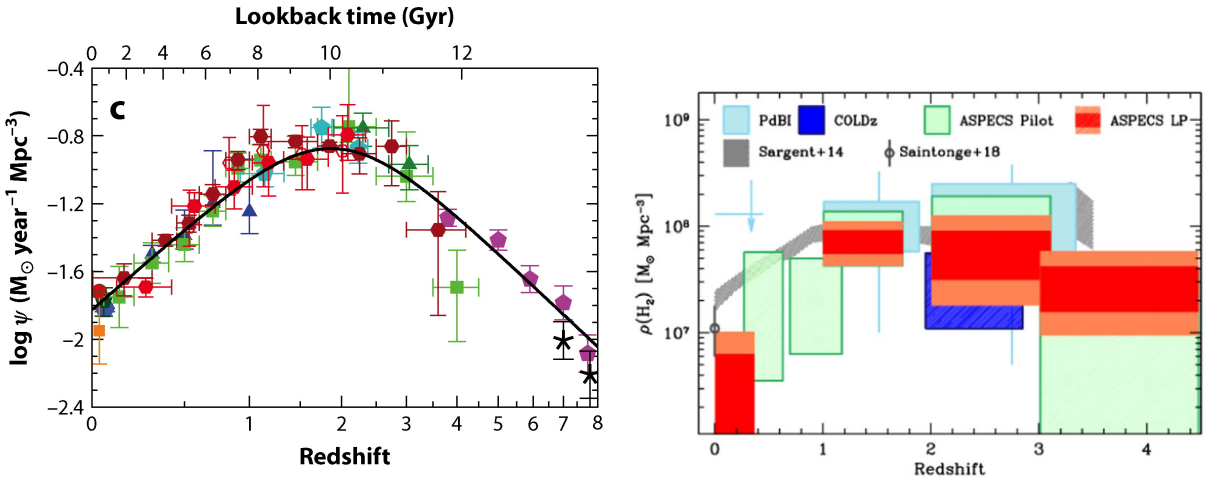

Figure 5.1: The cosmic evolution of SFR density [left panel] and molecular gas surface density [right panel]. In comparison to the present day, the universe at $z \sim 1$ is more molecular gas-rich and more star-forming. Left figure taken from Madau & Dickinson (2014). Right figure taken from Decarli et al. (2019)

redshift. For example, figure 5.1 illustrates the change of SFR and molecular gas surface density with redshift.

High-redshift star-forming galaxies are observed to have morphologies characterised by massive ($\sim 10^9$ $M_\odot$), large (diameters of $\sim 1.5-2.5$ kpc) star-forming "clumps" (Elmegreen & Elmegreen, 2005). Whilst an eventual goal must be to observe molecular gas in high-redshift galaxies at the scale of clouds in the Local Universe (~ 100 pc) in order to make direct comparisons to the Local Universe, a first step is to resolve the scale of these clumps. Molecular gas imaging at $\sim$ kpc resolution would allow measurement of a number of important quantities that describe high-redshift clumps and their host galaxies such as the clump lifetime, velocity dispersion profile, Toomre stability profile, gravitational collapse lengthscales and rotation curve. Such measurements would address several critical open questions regarding high-redshift star formation feedback, and galaxy growth. These questions include, whether clumps are gravitationally bound and how long do they live? Which feedback processes (if any) are capable of dispersing them? Do they inspiral towards galactic centres and contribute to bulge growth? Why do high-redshift galaxies host massive gas concentrations whereas Local Universe galaxies do not? Are the star formation efficiencies of these clumps high enough to enable the formation of extremely massive (globular) clusters?

The analytical model of Jeffreson & Kruijssen (2018) predicts that the lifetimes of molecular gas concentrations are set by a variety of physical mechanisms (see Equation 1.20). Jeffreson & Kruijssen (2018) also identify a number of regimes in galaxy parameter space spanned by Toomre Q and rotation curve slope where different combinations of these mechanisms dominate. High-redshift galaxies probe a lower Q, high rotation curve slope section of this parameter space than $z = 0$ targets that have been studied (Jeffreson & Kruijssen, 2018) and thus provide a critical benchmark in our understanding of star formation and feedback.

Simulations of high-redshift clumpy galaxies disagree as to whether observed clumps are short-lived and quickly dissipated by stellar feedback, with lifetimes of tens of Myr like local molecular clouds (Genel et al., 2012; Oklopčić et al., 2017) or have long (hundreds of Myr) lifetimes and spiral into the centre of galaxies to form bulges before they can be disrupted (Bournaud et al., 2014). Measuring their lifetimes would discriminate between these two cases by constraining the lifecycles and dynamical states of high-redshift clumps, providing key insight into the physics of

the high-redshift ISM and the processes that shape galaxy morphology. A tentative clump lifetime estimate in a $z \sim 2$ galaxy is 500 Myr (Zanella et al., 2015). This is significantly in excess of the (~ 10 Myr) lifetimes measured for molecular clouds in nearby galaxies (see e.g. Kruijssen et al. 2019, Chevance et al. 2019 and Chapter 3 of this thesis). However, Zanella et al. (2015) calculate this lifetime on the basis of the detection of only a single clump with age $\tau < 10$ Myr.

Current observational evidence suggests that the dynamical properties of high-redshift galaxies are somewhat different to those of local galaxies. Recent observations of Hα (Genzel et al., 2017) and CO(3-2) (Genzel et al., 2013) rotation curves at high redshift indicate decreasing velocities at large radii. This suggests that high-redshift discs are baryon-dominated, in contrast to the flat, dark matter-dominated rotation curves that are ubiquitous in Local Universe disc galaxies (also see Übler et al., 2018). Previous results from a lensed galaxy (Swinbank et al., 2011), based on indirectly-inferred molecular surface densities using Hα (Genzel et al., 2011) indicate that massive high-redshift discs are unstable to gravitational collapse on a large length scale (the Toomre length, $\sim$ kpc). Molecular gas observations at kpc-scales would allow measurement of the velocity dispersion across the disc of such a high-redshift galaxy. Thus, direct observations of the cold molecular phase would enable a Toomre stability analysis (cf. Reina-Campos & Kruijssen, 2017), measurement of the Toomre length and an assessment of the gravitational boundedness of the kpc-scale molecular gas concentrations.

CO emission (as a tracer of molecular gas emission) is now routinely detected in high-redshift galaxies (e.g Daddi et al., 2010; Tacconi et al., 2010; Genzel et al., 2010; Walter et al., 2014; Decarli et al., 2016, 2019; Riechers et al., 2019), but essentially all observations to date are spatially unresolved, or barely resolve galactic discs on 10 kpc scales. Spatially-resolved, kpc-scale observations are a requirement, however, to assess the structure of the clump-scale ISM and the lifetimes of the clumps themselves with the Heisenberg code. I note that high spatial resolution has been achieved in some studies (e.g Swinbank et al., 2011; Livermore et al., 2012; Cava et al., 2018) by observing gravitationally lensed galaxies. However, the Heisenberg code method for measuring the lifetimes of gas concentrations relies strongly on the spatial structure of the galaxy maps, implying that the uncertainties associated with the source plane reconstruction of lensed galaxies prohibit meaningful constraints.

In order to consider the feasibility of clump-scale molecular gas observations at high-redshift, I consider the case of the galaxy UVUDF22410. UVUDF22410 is a good candidate for such an assessment. First, it is a nearly face-on disc galaxy, which is required for structural measurements. The galaxy has a CO(2-1) line detection at high signal to noise from the ASPECS large programme (Decarli et al., 2019). Furthermore, UVUDF22410 has been imaged at high-sensitivity and resolution in ultraviolet, optical and NIR wavelengths (some examples are shown in Figure 5.2) with the Hubble Space Telescope (HST). This data is available through its location in the Hubble Ultra-Deep Field and includes deep broadband imaging from the HST eXtreme Deep Field (Illingworth et al., 2013), UV imaging from the UVUDF survey (Teplitz et al., 2013) and Hα from the 3D-HST survey (Nelson et al., 2016).

To validate the feasibility of such observations, I have simulated observations in CASA[38] (McMullin et al., 2007) at the requested sensitivity. UVUDF22410 has a radius of ~ 1.1" (Santini et al., 2015). It can thus be observed with two ALMA 12m configurations (C43-8 and C43-5) to reach a desired 0.13" ($\sim$ kpc) resolution (providing ~ 300 resolution elements) while recovering flux from the largest ($\lesssim 3$") scales in the galaxy. I model the spatial distribution of the molecular gas with the HST F606W image of the galaxy. As the diffuse gas fraction is unknown, but may be significant (see e.g. Caldú-Primo et al. 2015, Pety et al. 2013 and Chapter 4 of this thesis), the model conservatively estimates that $\sim 75\%$ of the flux is diffuse and not part of clumps. I scale our model

[38] the Common Astronomy Software Applications package, available at https://casa.nrao.edu/

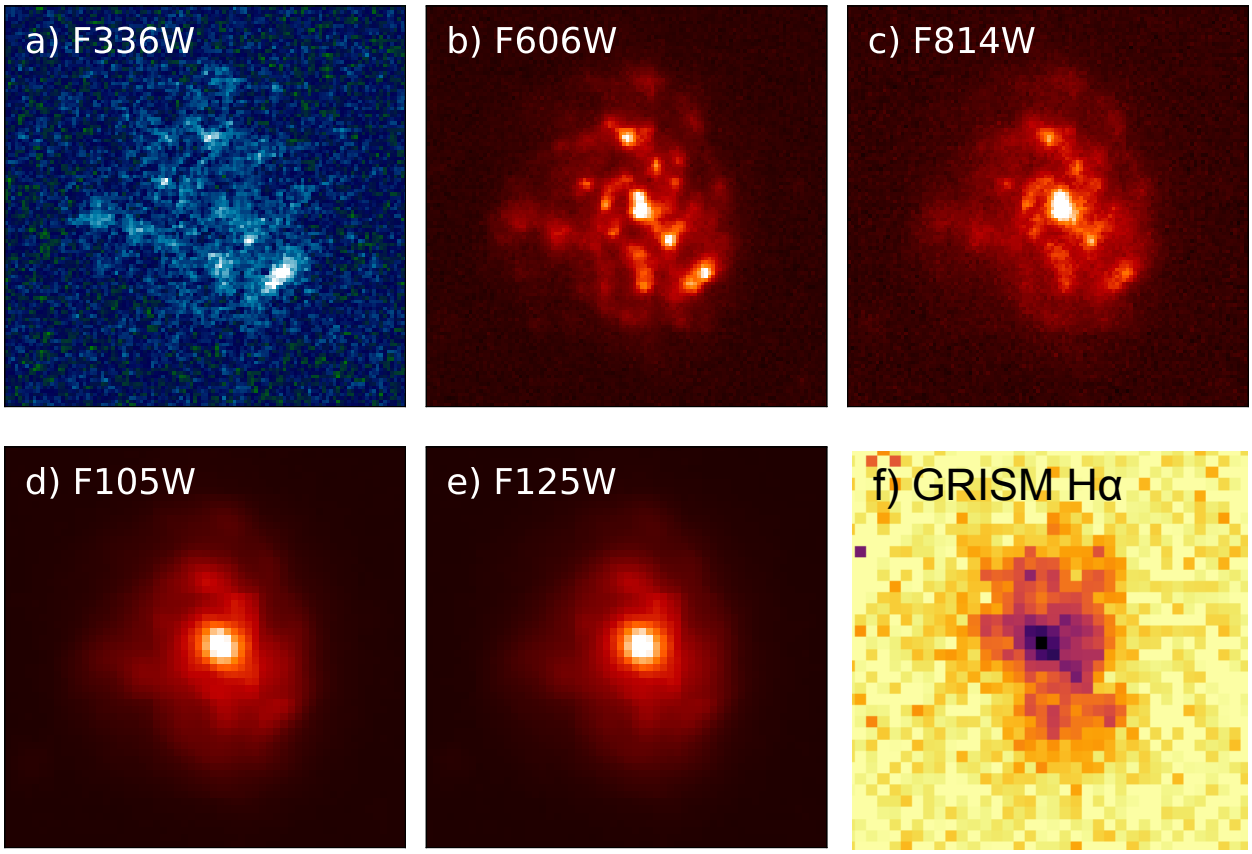

Figure 5.2: 3.5"x3.5" images of UVUDF22410 showing the wide range of imaging available for the galaxy. (a) UVUDF survey UV image (Teplitz et al., 2013) (b-e) HST eXtreme Deep Field images (Illingworth et al., 2013). f) 3D-HST Hα image (Nelson et al., 2016).

to the flux density obtained from distributing the integrated CO(2-1) ASPECS large programme line flux ($F'_{CO(2-1)} = 0.43$ Jy km s^{-1}) across a typical 40 kms^{-1} (boxcar) line width (Caldú-Primo et al., 2013). I simulate for ~ 30 hours of ALMA observing time including overheads, which is within the proposal time constraints for ALMA. The resulting simulations are shown in Figure 5.3 at the target 0.13" resolution, revealing the required > 15 gas concentrations detected at $\geqslant 3\sigma$ that are needed to apply the Heisenberg code method and measure the lifetimes of molecular clumps. At a resolution of 0.13" ($\sim$ kpc) the galaxy's disc is detected at $\geqslant 1\sigma$ in the simulations, however, convolving to 0.26" allows the disc to be detected at $\geqslant 3\sigma$.

Observations of cool molecular gas at z ~ 1.1 on kpc-scales, although challenging, are possible with current observational capabilities given a suitable target. Such observations would enable robust measurements of the lifetimes of molecular clumps and the structure and dynamical state of the high-redshift ISM. Looking beyond current facilities, the proposed next generation Very Large Array would allow such high-redshift molecular gas observations in even shorter timescales (Casey et al., 2018).

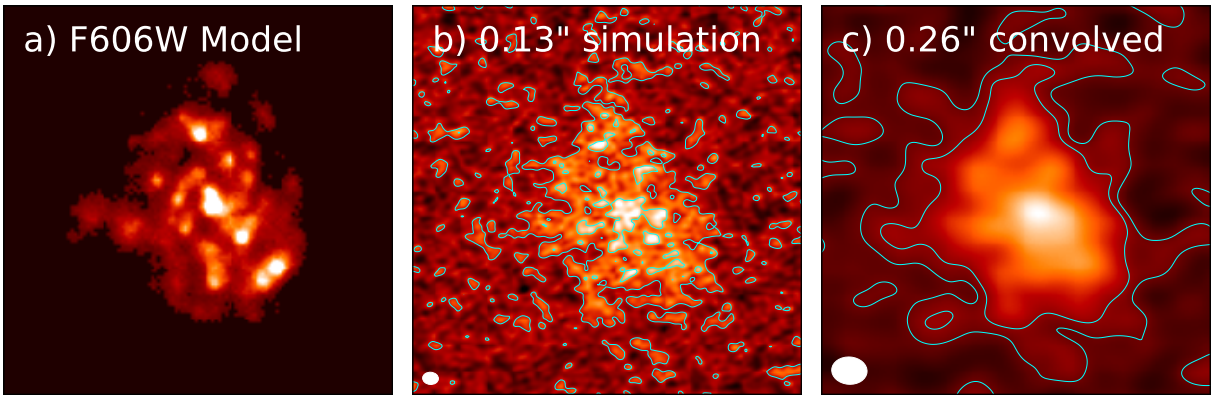

Figure 5.3: CASA simulations of $\sim$ 30 hours ALMA observations of UVUDF22410 at a target resolution of 0.13". The model used to simulate the galaxy, based on the HST F606W image of the galaxy is shown in the left panel. Simulated images generated from this model by performing simulated observations in CASA are shown at the target 0.13" resolution showing > 15 clumps detected at $\geqslant 3\sigma$ [middle panel] and convolved to 0.26" [right panel]. The white ellipse in the simulated images (bottom left) shows the ALMA beam and the cyan contours indicate the 1σ and 3σ significance levels of the images.

5.5 Concluding comments

In this chapter, I have summarised the work presented in this thesis. I presented a physically-motivated method for the separation of diffuse and compact emission using Fourier filtering of tracer images in Chapter 2. This method enables the application of the HEISENBERG code to measure cloud lifecycles and the mean separation between star-forming regions without the biasing impact of the diffuse emission present in common tracers of star formation and gas. Such an application to M33 is presented in Chapter 3. This analysis determined a cloud lifetime of $19.5^{+3.0}_{-3.2}$ Myr, on the order $\tau_{\rm ff}$, the timescale of gravitational collapse. Applications of the HEISENBERG code to a range of galaxies in the nearby universe (Kruijssen et al., 2019; Chevance et al., 2019) have found similar tens of Myr cloud lifetimes and characterised their variation in terms of environment. The analysis of M33 also measured a timescale for the dispersal of molecular clouds by feedback of $5.2^{+0.9}_{-1.3}$, longer than the earliest onset time for supernova. Measurements in other galaxies show a range of dispersal times, with clouds in some galaxies being dispersed before the first supernovae happen (Kruijssen et al., 2019; Chevance et al., 2019).

The method presented in Chapter 2 also measures the fraction of emission in two components: emission from compact structures, and emission from diffuse, extended structure. In Chapter 4, I presented such measurements for the ionised and molecular gas in nine nearby galaxies and reported a number of observed correlations with other physical parameters.

I have also presented a number of avenues for future research to build upon the results presented in this thesis and other related works. Moving forwards we will be able to characterise multiple phases of the star formation process. Furthermore, current and future observational facilities will enable us to constrain the physics of star formation and feedback outside of the nearest few galaxies and thus to measure how it changes and evolves across cosmic time.

6 Publications statement

6.1 Published first author papers appearing as a part of this thesis

Hygate, Alexander P. S., Kruijssen, J. M. Diederik, Chevance, Mélanie, Schruba, Andreas, Haydon, Daniel T. and Longmore, Steven N., 2007, "An uncertainty principle for star formation - IV. On the nature and filtering of diffuse emission", MNRAS, 488, 2800

This publication appears as Chapter 2 of this thesis. The text of this chapter was written by the author of this dissertation, which incorporated feedback received from the co-authors listed here.

6.2 Submitted and in preparation first author papers appearing as a part of this thesis

Hygate, Alexander P. S., Kruijssen, J. M. Diederik, Chevance, Mélanie, Walter, Fabian, Kim, Jenny J., Ward, Jacob L., Schruba, Andreas, Haydon, Daniel T. and Longmore, Steven N. "the molecular cloud lifecycle in M33", MNRAS, submitted

This work, appearing as Chapter 3 of this thesis has been submitted to MNRAS and will appear in a similar format in publication, subject to approval through the refereeing process. Section 3.10 of Chapter 3, along with the code to combine cloud lifetimes presented in this section was initially written by Jacob L. Ward. Figure 3.14 was also produced by Jacob L. Ward. The rest of the text of this chapter was written by the author of this dissertation, which incorporated feedback received from the co-authors listed here.

Hygate, Alexander P. S. et. al., Kruijssen, J. M. Diederik, Chevance, Mélanie (full author list to be determined), "Diffuse molecular and ionised gas in nearby galaxies", in preparation

This work, appearing as Chapter 4 of this thesis, in currently in preparation to be submitted to a scientific journal and will appear in a similar format in publication, subject to approval through the refereeing process. The text of this chapter was written by the author of this dissertation, which incorporated feedback received from the co-authors listed here.

6.3 Other papers authored during my doctoral studies on which I am a co-author

Sun, J., Leroy, A. K., Schruba, A., Rosolowsky, E., Hughes, A., Kruijssen, J. M. D., Meidt, S., Schinnerer, E., Blanc, G. A., Bigiel, F., Bolatto, A. D., Chevance, M., Groves, B., Herrera, C. N.,

Hygate, A. P. S., Pety, J., Querejeta, M., Usero, A., Utomo, D., 2018, "Cloud-scale Molecular Gas Properties in 15 Nearby Galaxies", ApJ, 860, 172.

Utomo, D., Sun, J., Leroy, A. K., Kruijssen, J. M. D., Schinnerer, E., Schruba, A., Bigiel, F., Blanc, G. A., Chevance, M., Emsellem, E., Herrera, C., Hygate, A. P. S., Kreckel, K., Ostriker, E. C., Pety, J., Querejeta, M., Rosolowsky, E., Sandstrom, K. M., Usero, A., 2018, "Star Formation Efficiency per Free-fall Time in nearby Galaxies", ApJ, 861, L18.

Kruijssen, J. M. D., Schruba, A., Hygate, A. P. S., Hu, C.-Y., Haydon, D. T., Longmore, S. N., 2018, "An uncertainty principle for star formation - II. A new method for characterizing the cloud-scale physics of star formation and feedback across cosmic history", MNRAS, 479, 1866.

Haydon, D. T., Kruijssen, J. M. D., Hygate, A. P. S., Schruba, A., Krumholz, M. R., Chevance, M., Longmore, S. N., 2018, "An uncertainty principle for star formation - III. The characteristic emission time-scales of star formation rate tracers", arXiv e-prints, arXiv:1810.10897.

Querejeta, M., Schinnerer, E., Schruba, A., Murphy, E., Meidt, S., Usero, A., Leroy, A. K., Pety, J., Bigiel, F., Chevance, M., Faesi, C. M., Gallagher, M., García-Burillo, S., Glover, S. C. O., Hygate, A. P. S., Jiménez-Donaire, M. J., Kruijssen, J. M. D., Momjian, E., Rosolowsky, E., Utomo, D., 2019, "Dense gas is not enough: environmental variations in the star formation efficiency of dense molecular gas at 100 pc scales in M 51", A&A, 625, A19.

Kruijssen, J. M. D., Schruba, A., Chevance, M., Longmore, S. N., Hygate, A. P. S., Haydon, D. T., McLeod, A. F., Dalcanton, J. J., Tacconi, L. J., van Dishoeck, E. F., 2019, "Fast and inefficient star formation due to short-lived molecular clouds and rapid feedback", Nature, 569, 519.

Schinnerer, E., Hughes, A., Leroy, A., Groves, B., Blanc, G. A., Kreckel, K., Bigiel, F., Chevance, M., Dale, D., Emsellem, E., Faesi, C., Glover, S., Grasha, K., Henshaw, J., Hygate, A., Kruijssen, J. M. D., Meidt, S., Pety, J., Querejeta, M., Rosolowsky, E., Saito, T., Schruba, A., Sun, J., Utomo, D., 2019, "The Gas-Star Formation Cycle in Nearby Star-Forming Galaxies I. Assessment of Multi-scale Variations", arXiv e-prints, arXiv:1910.10520.

Herrera, C. N., Pety, J., Hughes, A., Meidt, S. E., Kreckel, K., Querejeta, M., Saito, T., Lang, P., Jesús Jiménez-Donaire, M., Pessa, I., Cormier, D., Usero, A., Sliwa, K., Faesi, C., Blanc, G. A., Bigiel, F., Chevance, M., Dale, D. A., Grasha, K., Glover, S. C. O., Hygate, A. P. S., Kruijssen, J. M. D., Leroy, A. K., Rosolowsky, E., Schinnerer, E., Schruba, A., Sun, J., Utomo, D., 2019, "The headlight cloud in NGC 628: An extreme giant molecular cloud in a typical galaxy disk", arXiv e-prints, arXiv:1910.14311.

Chevance, M., Kruijssen, J. M. D., Hygate, A. P. S., Schruba, A., Longmore, S. N., Groves, B., Henshaw, J. D., Herrera, C. N., Hughes, A., Jeffreson, S. M. R., Lang, P., Leroy, A. K., Meidt, S. E., Pety, J., Razza, A., Rosolowsky, E., Schinnerer, E., Bigiel, F., Blanc, G. A., Emsellem, E., Faesi, C. M., Glover, S. C. O., Haydon, D. T., Ho, I.-T., Kreckel, K., Lee, J. C., Liu, D., Querejeta, M., Saito, T., Sun, J., Usero, A., Utomo, D., 2019, "The lifecycle of molecular clouds in nearby star-forming disc galaxies", arXiv e-prints, arXiv:1911.03479.

Schinnerer, E., Hughes, A., Leroy, A., Groves, B., Blanc, G. A., Kreckel, K., Bigiel, F., Chevance, M., Dale, D., Emsellem, E., Faesi, C., Glover, S., Grasha, K., Henshaw, J., Hygate, A., Kruijssen, J. M. D., Meidt, S., Pety, J., Querejeta, M., Rosolowsky, E., Saito, T., Schruba, A., Sun, J., Utomo, D., 2019, "The Gas–tar Formation Cycle in Nearby Star-forming Galaxies. I. Assessment of Multi-scale Variations", ApJ, 887, 49.

6.4 Other work appearing as a part of this thesis

Section 5.4 of Chapter 5 is based upon a series of ALMA proposals, which are listed below. The text of this section was written by the author of this dissertation, which incorporated feedback received from the co-investigators listed on these proposals.

- Alex Hygate, Melanie Chevance, Roberto Decarli, Daniel Haydon, Diederik Kruijssen, Steven Longmore, Erica Nelson, Andreas Schruba, Fabian Walter, Anita Zanella Melanie Chevance, Roberto Decarli, Daniel Haydon, Diederik Kruijssen, Steven Longmore, Erica Nelson, Andreas Schruba, Fabian Walter, Anita Zanella, 2016, "The cloud-scale physics of star formation and feedback across cosmic time" 2016.1.01414.S
- Alex Hygate, Manuel Aravena, Frank Bertoldi, Melanie Chevance, Paulo Cortes, Pierre Cox, Emanuele Daddi, Roberto Decarli, David Elbaz, Daniel Haydon, Jacqueline Hodge, Sarah Jeffreson, Diederik Kruijssen, Steven Longmore, Pascal Oesch, Gergö Popping, Marta Reina Campos, Dominik Riechers, Hans-Walter Rix, Andreas Schruba, Ian Smail, Rachel Somerville, Fabian Walter, Axel Weiss, Anita Zanella, Laura Zschaechner, Chris carilli, Elisabete da Cunha "The first kpc-scale map of the cold molecular ISM in a z=1.1 main sequence galaxy" 2017.1.00865.S
- Alex Hygate, Leindert Boogaard, Melanie Chevance, Roberto Decarli, Daniel Haydon, Sarah Jeffreson, Diederik Kruijssen, Steven Longmore, Erica Nelson, Marta Reina Campos, Hans-Walter Rix, Andreas Schruba, Fabian Walter, Anita Zanella, Laura Zschaechner, "The first kpc-scale map of the cold molecular ISM in a z=1.1 main sequence galaxy" 2018.1.01521.S
- Alex Hygate, Leindert Boogaard, Melanie Chevance, Roberto Decarli, Daniel Haydon, Sarah Jeffreson, Diederik Kruijssen, Steven Longmore, Erica Nelson, Marta Reina Campos, Hans-Walter Rix, Andreas Schruba, Fabian Walter, Anita Zanella, Laura Zschaechner "The first kpc-scale map of the cold molecular ISM in a z=1.1 main sequence galaxy" 2019.1.00742.S

6.5 Images reproduced in this thesis from the World Wide Web

Images in Figure 1.2:

- Top image credit: ESO/C. Malin. The image was downloaded from https://www.eso.org/public/images/ann13016a/ and reproduced in this thesis as allowed under the Creative Commons Attribution 4.0 International License https://creativecommons.org/licenses/by/4.0/, as specified by the ESO image copyright summary https://www.eso.org/public/outreach/copyright/.
- Bottom left image credit: NASA. The image was downloaded from https://www.nasa.gov/directorates/heo/scan/services/missions/universe/GALEX.html and is in the public domain as stated in the NASA media usage guidelines. https://www.nasa.gov/multimedia/guidelines/index.html.
- Bottom right image credit: NOAO/AURA/NSF. The image was downloaded from https://www.noao.edu/image_gallery/html/im0202.html and reproduced in this thesis as allowed by the NOAO/AURA Image Library Conditions of Use https://www.noao.edu/image_gallery/copyright.html.

Images in Figure 1.5:

- Left image credit ESO. The image was downloaded from https://www.eso.org/public/images/eso1424a/ and reproduced in this thesis as allowed under the Creative Commons Attribution 4.0 International License https://creativecommons.org/licenses/by/4.0/, as specified by the ESO image copyright summary https://www.eso.org/public/outreach/copyright/.
- Right image credit: NASA, ESA, S. Beckwith (STScI) and the Hubble Heritage Team (STScI/AURA). The image was downloaded from https://hubblesite.org/image/3913/printshop and is in the public domain as stated in the hubblesite copyright summary https://hubblesite.org/copyright.

Images in Figure 1.4:

- Top left image credit: ESO. The image was downloaded from https://www.eso.org/public/images/eso0024a/ and reproduced in this thesis as allowed under the Creative Commons Attribution 4.0 International License https://creativecommons.org/licenses/by/4.0/, as specified by the ESO image copyright summary https://www.eso.org/public/outreach/copyright/.
- Top right image credit: ESA/Hubble, NASA and Gilles Chapdelaine. The image was downloaded from https://www.spacetelescope.org/images/potw1328a/ and reproduced in this thesis as allowed under the Creative Commons Attribution 4.0 International License https://creativecommons.org/licenses/by/4.0/ as specified by the image usage summary at https://www.spacetelescope.org/copyright/.
- Bottom left image credit: NASA, ESA, and The Hubble Heritage Team (STScI/AURA). The image was downloaded from https://www.spacetelescope.org/images/opo0501a/ and reproduced in this thesis as allowed under the Creative Commons Attribution 4.0 International License https://creativecommons.org/licenses/by/4.0/ as specified by the image usage summary at https://www.spacetelescope.org/copyright/.
- Bottom right image credit: ESO/VISTA VMC. The image was downloaded from https://www.eso.org/public/images/eso1714a/ and reproduced in this thesis as allowed under the Creative Commons Attribution 4.0 International License https://creativecommons.org/licenses/by/4.0/, as specified by the ESO image copyright summary https://www.eso.org/public/outreach/copyright/.

Bibliography

Agertz, O., Teyssier, R., & Moore, B. 2011, MNRAS, 410, 1391 98

André, P., Men'shchikov, A., Bontemps, S., et al. 2010, A&A, 518, L102 20

Ann, H. B., Seo, M., & Ha, D. K. 2015, ApJS, 217, 27 13

Aristotle, Stocks, J. L. J. L., & Wallis, H. B. 1922, De Caelo (Oxford : The Clarendon Press) 9

Arzoumanian, D., André, P., Könyves, V., et al. 2019, A&A, 621, A42 20

Asplund, M., Grevesse, N., Sauval, A. J., & Scott, P. 2009, ARA&A, 47, 481 107

Bagetakos, I., Brinks, E., Walter, F., et al. 2011, AJ, 141, 23 18

Baldwin, J. A., Phillips, M. M., & Terlevich, R. 1981, PASP, 93, 5 49

Bash, F. N., Green, E., & Peters, W. L. 1977, ApJ, 217, 464 34, 35, 98

Bash, F. N., & Peters, W. L. 1976, ApJ, 205, 786 35, 98

Bastian, N., Covey, K. R., & Meyer, M. R. 2010, ARA&A, 48, 339 24

Beichman, C. A., Myers, P. C., Emerson, J. P., et al. 1986, ApJ, 307, 337 20

Bergin, E. A., & Tafalla, M. 2007, ARA&A, 45, 339 20

Bertoldi, F., & McKee, C. F. 1990, ApJ, 354, 529 112

Beuther, H., Mottram, J. C., Ahmadi, A., et al. 2018, A&A, 617, A100 20

Bigiel, F., Leroy, A., Walter, F., et al. 2008, AJ, 136, 2846 24, 26, 31, 98, 161

Bigiel, F., Leroy, A. K., Walter, F., et al. 2011, ApJL, 730, L13 24, 31, 161

Binette, L., Magris, C. G., Stasińska, G., & Bruzual, A. G. 1994, A&A, 292, 13 48, 99, 136

Blanc, G. A., Heiderman, A., Gebhardt, K., Evans, N. J., & Adams, J. 2009, ApJ, 704, 842 48, 49, 99, 136

Blitz, L., & Shu, F. H. 1980, ApJ, 238, 148 33, 98

Bolatto, A. D., Wolfire, M., & Leroy, A. K. 2013a, ARA&A, 51, 207 23

Bolatto, A. D., Warren, S. R., Leroy, A. K., et al. 2013b, Nature, 499, 450 137

Bournaud, F., Perret, V., Renaud, F., et al. 2014, ApJ, 780, 57 166

Braun, R., Thilker, D. A., Walterbos, R. a. M., & Corbelli, E. 2009, ApJ, 695, 937 163

Bregman, J. N., & Pildis, R. A. 1994, ApJ, 420, 570 48, 165

Bresolin, F. 2011, ApJ, 730, 129 101, 104

Bressan, A., Marigo, P., Girardi, L., et al. 2012, MNRAS, 427, 127 29

Brinchmann, J., Charlot, S., White, S. D. M., et al. 2004, MNRAS, 351, 1151 11

Brunthaler, A., Reid, M. J., Falcke, H., Greenhill, L. J., & Henkel, C. 2005, Science, 307, 1440 113

Bundy, K., Ellis, R. S., & Conselice, C. J. 2005, ApJ, 625, 621 13

Buta, R. J., Verdes-Montenegro, L., Damas-Segovia, A., et al. 2019, MNRAS, 488, 2175 13

Caldú-Primo, A., Schruba, A., Walter, F., et al. 2015, AJ, 149, 76 19, 49, 137, 163, 167

—. 2013, AJ, 146, 150 19, 49, 137, 163, 168

Carilli, C. L., & Walter, F. 2013, ARA&A, 51, 105 22, 23

Carruthers, G. R. 1970, ApJ, 161, L81 20

Casey, C. M., Narayanan, D., Carilli, C., et al. 2018, Science with a Next Generation Very Large Array, 517, 629 168

Cava, A., Schaerer, D., Richard, J., et al. 2018, Nature Astronomy, 2, 76 167

Chabrier, G. 2003, PASP, 115, 763 24

Chan, T. K., Kereš, D., Hopkins, P. F., et al. 2019, MNRAS, 488, 3716 10

Chen, C.-H. R., Indebetouw, R., Chu, Y.-H., et al. 2010, ApJ, 721, 1206 28

Chevance, M., Kruijssen, J. M. D., Hygate, A. P. S., et al. 2019, arXiv e-prints, arXiv:1911.03479 52, 54, 80, 82, 100, 111, 114, 138, 139, 140, 141, 142, 155, 161, 162, 163, 165, 167, 169

Churchwell, E. 2002, ARA&A, 40, 27 18

Collins, J. A., & Rand, R. J. 2001, ApJ, 551, 57 48, 99, 136

Corbelli, E., Braine, J., Bandiera, R., et al. 2017, A&A, 601, A146 34, 98, 99, 111, 161

Cormier, D., Abel, N. P., Hony, S., et al. 2019, A&A, 626, A23 152

Crocker, A. F., Calzetti, D., Thilker, D. A., et al. 2013, ApJ, 762, 79 48, 165

Daddi, E., Bournaud, F., Walter, F., et al. 2010, ApJ, 713, 686 167

Dai, X., & Guerras, E. 2018, ApJ, 853, L27 10

Dale, J. E. 2015, New Astronomy Reviews, 68, 1 98

Davis, T. A., Young, L. M., Crocker, A. F., et al. 2014, MNRAS, 444, 3427 24

Davis, T. A., Rowlands, K., Allison, J. R., et al. 2015, MNRAS, 449, 3503 162

de Blok, E., Fraternali, F., Heald, G., et al. 2015, aska, 129 163

Decarli, R., Walter, F., Aravena, M., et al. 2016, ApJ, 833, 69 167

Decarli, R., Walter, F., Gónzalez-López, J., et al. 2019, ApJ, 882, 138 13, 166, 167

DeGraaff, R. B., Blakeslee, J. P., Meurer, G. R., & Putman, M. E. 2007, ApJ, 671, 1624 13

Dettmar, R.-J. 1990, A&A, 232, L15 48

Deul, E. R., & den Hartog, R. H. 1990, A&A, 229, 362 18, 112

Dewdney, P. E., Hall, P. J., Schilizzi, R. T., & Lazio, T. J. L. W. 2009, IEEEP, 97, 1482 161

Di Teodoro, E. M., McClure-Griffiths, N. M., Jameson, K. E., et al. 2019, MNRAS, 483, 392 163

Dobbs, C. L., Burkert, A., & Pringle, J. E. 2011, MNRAS, 417, 1318 32

Dobbs, C. L., & Pringle, J. E. 2013, MNRAS, 432, 653 32

Dobbs, C. L., Pringle, J. E., & Burkert, A. 2012, MNRAS, 425, 2157 32

Dobbs, C. L., Krumholz, M. R., Ballesteros-Paredes, J., et al. 2014, Protostars and Planets VI, 3 98

Donas, J., Deharveng, J. M., Laget, M., Milliard, B., & Huguenin, D. 1987, A&A, 180, 12 29

Downes, D., & Solomon, P. M. 1998, ApJ, 507, 615 23

Draine, B. T. 2011, Physics of the Interstellar and Intergalactic Medium by Bruce T. Draine. Princeton University Press 17

Druard, C., Braine, J., Schuster, K. F., et al. 2014, A&A, 567, A118 80, 100, 101, 102, 111, 114, 188

Egusa, F., Hirota, A., Baba, J., & Muraoka, K. 2018, ApJ, 854, 90 13

Elmegreen, B. G. 1991, in The Physics of Star Formation and Early Stellar Evolution, ed. C. J. Lada & N. D. Kylafis, NATO ASI Series (Dordrecht: Springer Netherlands), 35–60 33

—. 2000, ApJ, 530, 277 31

Elmegreen, B. G., & Elmegreen, D. M. 1986, ApJ, 311, 554 13

—. 2005, ApJ, 627, 632 166

Elson, E. C., Kam, S. Z., Chemin, L., Carignan, C., & Jarrett, T. H. 2019, MNRAS, 483, 931 101

Engargiola, G., Plambeck, R. L., Rosolowsky, E., & Blitz, L. 2003, ApJS, 149, 343 19, 35, 98, 111, 161, 163

Eskridge, P. B., & Frogel, J. A. 1999, Ap&SS, 269, 427 13

Fabbiano, G., Heckman, T., & Keel, W. C. 1990, ApJ, 355, 442 48, 165

Fabian, A. C. 2012, ARA&A, 50, 455 10

Ferrière, K. M. 2001, Reviews of Modern Physics, 73, 1031 10, 17, 18

Fitzpatrick, E. L., & Massa, D. 2007, ApJ, 663, 320 101

Flores-Fajardo, N., Morisset, C., Stasińska, G., & Binette, L. 2011, MNRAS, 415, 2182 48, 49, 99, 136

Foyle, K., Rix, H.-W., Walter, F., & Leroy, A. K. 2010, ApJ, 725, 534 13

Fujimoto, Y., Chevance, M., Haydon, D. T., Krumholz, M. R., & Kruijssen, J. M. D. 2019, MNRAS, 487, 1717 32, 165

Fukui, Y., Mizuno, N., Yamaguchi, R., et al. 1999, PASJ, 51, 745 34, 99

GaiaCollaboration, Brown, A. G. A., Vallenari, A., et al. 2018, A&A, 616, A1 32, 103

Galliano, F., Galametz, M., & Jones, A. P. 2018, ARA&A, 56, 673 11

Garay, G., & Lizano, S. 1999, PASP, 111, 1049 18

Garcia-Burillo, S., Guelin, M., Cernicharo, J., & Dahlem, M. 1992, A&A, 266, 21 137

García-Burillo, S., Combes, F., Usero, A., et al. 2014, A&A, 567, A125 137

Gardner, J. P., Mather, J. C., Clampin, M., et al. 2006, Space Sci.Rev., 123, 485 161

Geach, J. E., Hickox, R. C., Diamond-Stanic, A. M., et al. 2014, Nature, 516, 68 137

Geach, J. E., Tremonti, C., Diamond-Stanic, A. M., et al. 2018, ApJ, 864, L1 137

Genel, S., Naab, T., Genzel, R., et al. 2012, ApJ, 745, 11 166

Genzel, R., Tacconi, L. J., Gracia-Carpio, J., et al. 2010, MNRAS, 407, 2091 167

Genzel, R., Newman, S., Jones, T., et al. 2011, ApJ, 733, 101 167

Genzel, R., Tacconi, L. J., Kurk, J., et al. 2013, ApJ, 773, 68 167

Genzel, R., Schreiber, N. M. F., Übler, H., et al. 2017, Nature, 543, 397 167

Gieren, W., Górski, M., Pietrzyński, G., et al. 2013, ApJ, 773, 69 98, 104

Gil de Paz, A., Boissier, S., Madore, B. F., et al. 2007, ApJS, 173, 185 101

Gillessen, S., Eisenhauer, F., Trippe, S., et al. 2009, ApJ, 692, 1075 10

Gnedin, N. Y., Tassis, K., & Kravtsov, A. V. 2009, ApJ, 697, 55 98

Gogarten, S. M., Dalcanton, J. J., Williams, B. F., et al. 2010, ApJ, 712, 858 113

Goldsmith, P. F., Heyer, M., Narayanan, G., et al. 2008, ApJ, 680, 428 138

González Delgado, R. M., Cid Fernandes, R., Pérez, E., et al. 2016, A&A, 590, A44 11

Governato, F., Willman, B., Mayer, L., et al. 2007, MNRAS, 374, 1479 98

Grasha, K., Calzetti, D., Bittle, L., et al. 2018, MNRAS, 481, 1016 34

Grasha, K., Calzetti, D., Adamo, A., et al. 2019, MNRAS, 483, 4707 34

Gratier, P., Braine, J., Rodriguez-Fernandez, N. J., et al. 2010a, A&A, 512, A68 87

—. 2010b, A&A, 522, A3 23, 100, 102, 188

Greenawalt, B. E. 1998, Ph.D., New Mexico State University, United States – New Mexico 99, 101, 116, 120

Greve, A., Panis, J.-F., & Thum, C. 1996, A&AS, 115, 379 33, 103

Guizar-Sicairos, M., Thurman, S. T., & Fienup, J. R. 2008, Optics Letters, 33, 156 103

Haas, M. R., Schaye, J., Booth, C. M., et al. 2013, MNRAS, 435, 2931 14, 98, 165

Haffner, L. M., Dettmar, R.-J., Beckman, J. E., et al. 2009, Reviews of Modern Physics, 81, 969 18

Hamden, E. T., Schiminovich, D., & Seibert, M. 2013, ApJ, 779, 180 99

Hao, C.-N., Kennicutt, R. C., Johnson, B. D., et al. 2011, ApJ, 741, 124 29

Hartquist, T. W., & Williams, D. A. 1998, The molecular astrophysics of stars and galaxies, 4 20, 21

Haydon, D. T., Fujimoto, Y., Chevance, M., et al. 2019, submitted 112, 119

Haydon, D. T., Kruijssen, J. M. D., Hygate, A. e. P. S., et al. 2018, arXiv e-prints, arXiv:1810.10897 39, 100, 107, 108, 111, 119, 131, 139

Haydon, D. T., Kruijssen, J. M. D., Hygate, A. P. S., et al. 2018, arXiv e-prints, arXiv:1810.10897 48, 50, 52, 67

Hony, S., Gouliermis, D. A., Galliano, F., et al. 2015, MNRAS, 448, 1847 28

Hoopes, C. G., & Walterbos, R. A. M. 2000, ApJ, 541, 597 101

Hoopes, C. G., Walterbos, R. A. M., & Bothun, G. D. 2001, ApJ, 559, 878 48, 99, 116, 120

Hoopes, C. G., Walterbos, R. A. M., & Greenwalt, B. E. 1996, AJ, 112, 1429 136

Hopkins, P. F., Kereš, D., Oñorbe, J., et al. 2014a, MNRAS, 445, 581 10

—. 2014b, MNRAS, 445, 581 13

Hopkins, P. F., Narayanan, D., & Murray, N. 2013, MNRAS, 432, 2647 14, 98, 165

Hopkins, P. F., Wetzel, A., Kereš, D., et al. 2018, MNRAS, 480, 800 13

Howk, J. C., & Savage, B. D. 1999, AJ, 117, 2077 137

Hubble, E. P. 1922, ApJ, 56, 162 10

—. 1926, ApJ, 64, 321 10

—. 1936, Realm of the Nebulae 10, 14

Hughes, A., Meidt, S. E., Colombo, D., et al. 2013, ApJ, 779, 46 19

Hunt, L. K., & Hirashita, H. 2009, A&A, 507, 1327 18

Hygate, A. P. S., Kruijssen, J. M. D., Chevance, M., et al. 2019, MNRAS, 488, 2800 54, 99, 100, 103, 107, 108, 114, 116, 119, 120, 121, 122, 124, 125, 127, 137, 138, 139, 140

Hygate, A. P. S., Kruijssen, J. M. D., Walter, F., et al. 2019, MNRAS submitted 52, 80, 82, 137, 140

Ilbert, O., McCracken, H. J., Le Fèvre, O., et al. 2013, A&A, 556, A55 13

Illingworth, G. D., Magee, D., Oesch, P. A., et al. 2013, ApJS, 209, 6 167, 168

Ingrosso, G., Novati, S. C., de Paolis, F., et al. 2009, MNRAS, 399, 219 10

Jeans, J. H. 1919, JRASC, 13, 215 13

Jeffreson, S. M. R., & Kruijssen, J. M. D. 2018, MNRAS, 476, 3688 31, 162, 166

Jessop, N. E., & Ward-Thompson, D. 2000, MNRAS, 311, 63 20

Jiménez-Donaire, M. J., Bigiel, F., Leroy, A. K., et al. 2019, ApJ, 880, 127 138, 156, 157, 160, 164

Kam, S. Z., Carignan, C., Chemin, L., et al. 2017, AJ, 154, 41 113

Kang, X., Zhang, F., & Chang, R. 2017, MNRAS, 469, 1636 113

Kapala, M. J., Sandstrom, K., Groves, B., et al. 2015, ApJ, 798, 24 48, 165

Karachentsev, I. D., Grebel, E. K., Sharina, M. E., et al. 2003, A&A, 404, 93 113

Kawamura, A., Mizuno, Y., Minamidani, T., et al. 2009, ApJS, 184, 1 3, 34, 36, 98, 99, 161

Kennicutt, R. C. 1989, ApJ, 344, 685 24, 164

—. 1998, ApJ, 498, 541 24, 164

Kennicutt, R. C., & Evans, N. J. 2012, ARA&A, 50, 531 25, 28, 30, 101

Kennicutt, R. C., Armus, L., Bendo, G., et al. 2003, PASP, 115, 928 141

Kim, K.-T., & Koo, B.-C. 2001, ApJ, 549, 979 18

Kim, S., Staveley-Smith, L., Dopita, M. A., et al. 2003, ApJS, 148, 473 163

Kimm, T., Blaizot, J., Garel, T., et al. 2019, MNRAS, 486, 2215 152

Kippenhahn, R., Weigert, A., & Weiss, A. 2012, Stellar Structure and Evolution, 2nd edn. (Berlin, Heidelberg: Springer) 29

Koch, E. W., Rosolowsky, E. W., Schruba, A., et al. 2019, MNRAS, 485, 2324 137

Koch, E. W., Rosolowsky, E. W., Lockman, F. J., et al. 2018, MNRAS, 479, 2505 98, 104, 163

Koda, J., Scoville, N., Sawada, T., et al. 2009, ApJ, 700, L132 32, 35, 98, 161

Kolmogorov, A. 1941, Akademiia Nauk SSSR Doklady, 30, 301 19

Kolmogorov, A. N. 1991, Proceedings of the Royal Society of London Series A, 434, 9 19

Kreckel, K., Blanc, G. A., Schinnerer, E., et al. 2016, ApJ, 827, 103 48, 49, 137

Kroupa, P. 2001, MNRAS, 322, 231 24

Kruijssen, J. M. D., Dale, J. E., & Longmore, S. N. 2015, MNRAS, 447, 1059 33, 162

Kruijssen, J. M. D., & Longmore, S. N. 2013, MNRAS, 435, 2598 33

—. 2014, MNRAS, 439, 3239 37, 49, 50, 68, 98, 100, 104, 138

Kruijssen, J. M. D., Schruba, A., Hygate, A. P. S., et al. 2018, MNRAS, 479, 1866 37, 40, 41, 42, 43, 49, 50, 52, 60, 62, 64, 67, 78, 80, 82, 87, 88, 100, 101, 104, 106, 109, 116, 119, 122, 138, 139

Kruijssen, J. M. D., Schruba, A., Chevance, M., et al. 2019, Nature, 569, 519 52, 54, 80, 82, 98, 100, 112, 113, 114, 161, 162, 163, 167, 169

Krumholz, M. R., Bate, M. R., Arce, H. G., et al. 2014, Protostars and Planets VI, 243 98

Kulkarni, S. R., & Heiles, C. 1987, Interstellar Processes, 134, 87 18

Lacerda, E. a. D., Cid Fernandes, R., Couto, G. S., et al. 2018, MNRAS, 474, 3727 48, 49, 136, 149, 152, 159, 160, 163, 164

Larson, R. B. 1981, MNRAS, 194, 809 19, 31, 33

Lee, C. W., & Myers, P. C. 1999, ApJS, 123, 233 20

Leisawitz, D., Bash, F. N., & Thaddeus, P. 1989, ApJS, 70, 731 34

Leitherer, C., Ekström, S., Meynet, G., et al. 2014, ApJS, 212, 14 27, 98, 112, 162

Leroy, A. K., Walter, F., Brinks, E., et al. 2008, AJ, 136, 2782 101

Leroy, A. K., Bigiel, F., de Blok, W. J. G., et al. 2012, AJ, 144, 3 48, 49, 99, 165

Leroy, A. K., Walter, F., Sandstrom, K., et al. 2013, AJ, 146, 19 98

Leroy, A. K., Sandstrom, K. M., Lang, D., et al. 2019, ApJS, 244, 24 113

Levy, R. C., Bolatto, A. D., Teuben, P., et al. 2018, ApJ, 860, 92 155, 164

Levy, R. C., Bolatto, A. D., Sánchez, S. F., et al. 2019, ApJ, 882, 84 136, 155

Liu, G., Koda, J., Calzetti, D., Fukuhara, M., & Momose, R. 2011, ApJ, 735, 63 48

Livermore, R. C., Swinbank, A. M., Smail, I., et al. 2012, ApJ, 758, L35 167

Lopez, L. A., Krumholz, M. R., Bolatto, A. D., et al. 2014, ApJ, 795, 121 98

Lyons, L., Gibaut, D., & Clifford, P. 1988, Nuclear Instruments and Methods in Physics Research A, 270, 110 130, 131

Madau, P., & Dickinson, M. 2014, ARA&A, 52, 415 13, 166

Madau, P., Pozzetti, L., & Dickinson, M. 1998, ApJ, 498, 106 29

Madore, B. F. 2005, The Spectral Energy Distributions of Gas-Rich Galaxies: Confronting Models with Data, 761, 331 30

Maeda, F., Ohta, K., Fujimoto, Y., Habe, A., & Baba, J. 2018, PASJ, 70, 37 13

Makarov, D., Prugniel, P., Terekhova, N., Courtois, H., & Vauglin, I. 2014, A&A, 570, A13 142

Marino, A., Bianchi, L., Rampazzo, R., et al. 2011, ApJ, 736, 154 13

Martig, M., Bournaud, F., Teyssier, R., & Dekel, A. 2009, ApJ, 707, 250 13

Martin, C. L. 1997, ApJ, 491, 561 136

Martin, D. C., Fanson, J., Schiminovich, D., et al. 2005, ApJ, 619, L1 101

Mathis, J. S. 1986, ApJ, 301, 423 48, 99, 136

—. 1990, ARA&A, 28, 37 10

McLeod, A. F., Dale, J. E., Evans, C. J., et al. 2019, MNRAS, 486, 5263 98, 112

McMullin, J. P., Waters, B., Schiebel, D., Young, W., & Golap, K. 2007, Astronomical Data Analysis Software and Systems XVI, 376, 127 167

Meidt, S. E., Hughes, A., Dobbs, C. L., et al. 2015, ApJ, 806, 72 3, 32, 35, 37, 98, 161

Miura, R. E., Kohno, K., Tosaki, T., et al. 2012, ApJ, 761, 37 34, 98, 99, 111, 161

Monnet, G. 1971, A&A, 12, 379 48

Mortlock, A., Conselice, C. J., Bluck, A. F. L., et al. 2011, MNRAS, 413, 2845 13

Murray, N. 2011, ApJ, 729, 133 33, 98

Murray, N., & Rahman, M. 2010, ApJ, 709, 424 112

Murthy, J. 2014, ApJS, 213, 32 116

Murthy, J., Henry, R. C., & Sujatha, N. V. 2010, ApJ, 724, 1389 99, 116

Naab, T., & Ostriker, J. P. 2017, ARA&A, 55, 59 14

Nelson, D., Pillepich, A., Springel, V., et al. 2018, MNRAS, 475, 624 13

Nelson, E. J., van Dokkum, P. G., Momcheva, I. G., et al. 2016, ApJ, 817, L9 167, 168

Oey, M. S., & Kennicutt, R. C., J. 1998, Publications of the Astronomical Society of Australia, 15, 141 136

Oey, M. S., Meurer, G. R., Yelda, S., et al. 2007, ApJ, 661, 801 48, 136, 149, 160, 163, 164

Oh, S., Oh, K., & Yi, S. K. 2012, ApJS, 198, 4 13

Oklopčić, A., Hopkins, P. F., Feldmann, R., et al. 2017, MNRAS, 465, 952 166

Onodera, S., Kuno, N., Tosaki, T., et al. 2010, ApJ, 722, L127 24, 98, 101

Paturel, G., Fouqué, P., Buta, R., & Garcia, A. M. 1991, A&A, 243, 319 142

Paturel, G., Andernach, H., Bottinelli, L., et al. 1997, A&AS, 124, 109 142

Pellegrini, E. W., Oey, M. S., Winkler, P. F., et al. 2012, ApJ, 755, 40 136

Pety, J., & Falgarone, É. 2000, A&A, 356, 279 48, 99, 136

Pety, J., Schinnerer, E., Leroy, A. K., et al. 2013, ApJ, 779, 43 19, 49, 80, 137, 141, 155, 163, 167, 188

Pisano, D., Walter, F., & Stanimirović, S. 2018, Science with a Next Generation Very Large Array, 517, 471 163

Poetrodjojo, H., D'Agostino, J. J., Groves, B., et al. 2019, MNRAS, 487, 79 152, 160, 164

Poggianti, B. M., Gullieuszik, M., Tonnesen, S., et al. 2019, MNRAS, 482, 4466 136

Pradhan, A. C., Murthy, J., & Pathak, A. 2011, ApJ, 743, 80 165

Pradhan, A. C., Pathak, A., & Murthy, J. 2010, ApJL, 718, L141 165

Putman, M. E., Peek, J. E. G., Muratov, A., et al. 2009, ApJ, 703, 1486 113

Rahner, D., Pellegrini, E. W., Glover, S. C. O., & Klessen, R. S. 2017, MNRAS, 470, 4453 152

Rand, R. J., Kulkarni, S. R., & Hester, J. J. 1990, ApJ, 352, L1 48

Rathborne, J. M., Johnson, A. M., Jackson, J. M., Shah, R. Y., & Simon, R. 2009, ApJS, 182, 131 19

Reina-Campos, M., & Kruijssen, J. M. D. 2017, MNRAS, 469, 1282 167

Relaño, M., & Kennicutt, R. C. 2009, ApJ, 699, 1125 18

Reynolds, R. J., Scherb, F., & Roesler, F. L. 1973, ApJ, 185, 869 48, 163

Richings, A. J., & Schaye, J. 2016, MNRAS, 460, 2297 32

Riechers, D. A., Pavesi, R., Sharon, C. E., et al. 2019, ApJ, 872, 7 13, 167

Roman-Duval, J., Heyer, M., Brunt, C. M., et al. 2016, ApJ, 818, 144 138, 156, 157, 160, 164

Rosolowsky, E., Keto, E., Matsushita, S., & Willner, S. P. 2007, ApJ, 661, 830 99, 101, 117, 137

Rosolowsky, E., & Leroy, A. 2006, PASP, 118, 590 100

Rubin, V. C., Burstein, D., Ford, W. K., & Thonnard, N. 1985, ApJ, 289, 81 10

Salaris, M., & Cassisi, S. 2005, Evolution of Stars and Stellar Populations (Chichester [u.a.]: Wiley) 29

Salpeter, E. E. 1955, ApJ, 121, 161 24

Sanchez, S. F., Garcia-Benito, R., Zibetti, S., et al. 2018, VizieR Online Data Catalog, J/A+A/594/A36 149

Santini, P., Ferguson, H. C., Fontana, A., et al. 2015, ApJ, 801, 97 167

Sarzi, M., Shields, J. C., Schawinski, K., et al. 2010, MNRAS, 402, 2187 48, 99, 136

Sasseen, T. P., Lampton, M., Bowyer, S., & Wu, X. 1995, ApJ, 447, 630 99

Scannapieco, C., Wadepuhl, M., Parry, O. H., et al. 2012, MNRAS, 423, 1726 14, 98, 165

Schawinski, K., Urry, C. M., Simmons, B. D., et al. 2014, MNRAS, 440, 889 13

Schaye, J., Crain, R. A., Bower, R. G., et al. 2015, MNRAS, 446, 521 13

Schiminovich, D., Friedman, P. G., Martin, C., & Morrissey, P. F. 2001, ApJ, 563, L161 99

Schinnerer, E., Meidt, S. E., Pety, J., et al. 2013, ApJ, 779, 42 141, 188

Schlegel, D. J., Finkbeiner, D. P., & Davis, M. 1998, ApJ, 500, 525 101

Schmidt, M. 1959, ApJ, 129, 243 24, 164

Schruba, A., Kruijssen, J. M. D., & Leroy, A. K. 2019, ApJ, 883, 2 19, 20, 30, 31, 111, 113, 114, 161, 162, 164

Schruba, A., Leroy, A. K., Walter, F., Sandstrom, K., & Rosolowsky, E. 2010, ApJ, 722, 1699 24, 98, 99, 106, 116, 120

Scoville, N. Z., & Hersh, K. 1979, ApJ, 229, 578 31, 98

Scoville, N. Z., Solomon, P. M., & Sanders, D. B. 1979, The Large-Scale Characteristics of the Galaxy, 84, 277 31, 35, 98, 161

Scoville, N. Z., & Wilson, C. D. 2004, The Formation and Evolution of Massive Young Star Clusters, 322, 245 31, 98

Selina, R. J., Murphy, E. J., McKinnon, M., et al. 2018, ASPC, 517, 15 161

Sembach, K. R., Howk, J. C., Ryans, R. S. I., & Keenan, F. P. 2000, ApJ, 528, 310 48, 99, 136

Seon, K.-I., Witt, A., Kim, I.-J., et al. 2011, ApJ, 743, 188 136

Seon, K.-I., & Witt, A. N. 2012, ApJ, 758, 109 48, 99, 136

Sheffer, Y., Rogers, M., Federman, S. R., et al. 2008, ApJ, 687, 1075 21

Skibba, R. A., Masters, K. L., Nichol, R. C., et al. 2012, MNRAS, 423, 1485 13

Smith, N., Povich, M. S., Whitney, B. A., et al. 2010, MNRAS, 406, 952 27

Soderblom, D. R. 2010, ARA&A, 48, 581 28

Solomon, P. M., Rivolo, A. R., Barrett, J., & Yahil, A. 1987, ApJ, 319, 730 19

Somerville, R. S., & Davé, R. 2015, ARA&A, 53, 51 14

Spitzer, L. 1956, ApJ, 124, 20 17

—. 1990, ARA&A, 28, 71 17

Strickland, D. K., Heckman, T. M., Colbert, E. J. M., Hoopes, C. G., & Weaver, K. A. 2004, ApJS, 151, 193 48, 165

Sullivan, M., Treyer, M. A., Ellis, R. S., et al. 2000, MNRAS, 312, 442 29

Sun, J., Leroy, A. K., Schruba, A., et al. 2018, ApJ, 860, 172 141

Swinbank, A. M., Papadopoulos, P. P., Cox, P., et al. 2011, ApJ, 742, 11 167

Tacconi, L. J., Genzel, R., Neri, R., et al. 2010, Nature, 463, 781 167

Tachihara, K., Gratier, P., Sano, H., et al. 2018, PASJ, 70, S52 109

Teplitz, H. I., Rafelski, M., Kurczynski, P., et al. 2013, AJ, 146, 159 167, 168

Thilker, D. A., Braun, R., & Walterbos, R. A. M. 2000, AJ, 120, 3070 48, 49

Thilker, D. A., Walterbos, R. A. M., Braun, R., & Hoopes, C. G. 2002, AJ, 124, 3118 48, 49

Thilker, D. A., Hoopes, C. G., Bianchi, L., et al. 2005, ApJ, 619, L67 48, 99, 101, 116, 117, 120, 165

Togi, A., & Smith, J. D. T. 2016, ApJ, 830, 18 20

Tosaki, T., Kuno, N., Onodera, S. M., et al. 2011, PASJ, 63, 1171 99, 101, 103, 117

Tüllmann, R., Pietsch, W., Rossa, J., Breitschwerdt, D., & Dettmar, R.-J. 2006, A&A, 448, 43 17

Übler, H., Genzel, R., Tacconi, L. J., et al. 2018, ApJ, 854, L24 167

Utomo, D., Blitz, L., Davis, T., et al. 2015, ApJ, 803, 16 162

Utomo, D., Sun, J., Leroy, A. K., et al. 2018, ApJ, 861, L18 20, 141

Vale Asari, N., Couto, G. S., Cid Fernandes, R., et al. 2019, MNRAS, 489, 4721 152, 160, 164

van der Walt, S., Schönberger, J. L., Nunez-Iglesias, J., et al. 2014, PeerJ, 2, e453 103

van Dishoeck, E. F., Glassgold, A. E., Guelin, M., et al. 1992, Astrochemistry of Cosmic Phenomena, 150, 285 21

van Dokkum, P. G. 2005, AJ, 130, 2647 13

Veilleux, S., Cecil, G., & Bland-Hawthorn, J. 2005, ARA&A, 43, 769 98

Verley, S., Corbelli, E., Giovanardi, C., & Hunt, L. K. 2009, A&A, 493, 453 101, 112, 165

Virtanen, P., Gommers, R., Oliphant, T. E., et al. 2019, arXiv, arXiv:1907.10121 145

Vogelsberger, M., Genel, S., Springel, V., et al. 2014, Nature, 509, 177 13

Voges, E. S. 2006, Ph.D. Thesis 136

Voges, E. S., Oey, M. S., Walterbos, R. a. M., & Wilkinson, T. M. 2008, AJ, 135, 1291 136

Walter, F., Brinks, E., de Blok, W. J. G., et al. 2008, AJ, 136, 2563 163

Walter, F., Weiss, A., & Scoville, N. 2002, ApJ, 580, L21 137

Walter, F., Decarli, R., Sargent, M., et al. 2014, ApJ, 782, 79 167

Ward, J. L., Kruijssen, J. M. D., Chevance, M., et al. 2020, to be submitted 52, 54, 80, 82

Weilbacher, P. M., Monreal-Ibero, A., Verhamme, A., et al. 2018, A&A, 611, A95 136

Weiß, A., Downes, D., Neri, R., et al. 2007, A&A, 467, 955 23

Welch, G. A., & Sage, L. J. 2003, ApJ, 584, 260 13

Westmeier, T., Braun, R., & Koribalski, B. S. 2011, MNRAS, 410, 2217 113

Westmeier, T., Koribalski, B. S., & Braun, R. 2013, MNRAS, 434, 3511 113

Wilcots, E. M., & Miller, B. W. 1998, AJ, 116, 2363 163

Willett, K. W., Schawinski, K., Simmons, B. D., et al. 2015, MNRAS, 449, 820 13

Williams, J. P., Blitz, L., & McKee, C. F. 2000, Protostars and Planets IV, 97 20

Williams, J. P., de Geus, E. J., & Blitz, L. 1994, ApJ, 428, 693 108, 125

Williams, T. G., Baes, M., De Looze, I., et al. 2019, MNRAS, 487, 2753 112

Williams, T. G., Gear, W. K., & Smith, M. W. L. 2018, MNRAS, 479, 297 101

Wilson, C. D., & Walker, C. E. 1994, ApJ, 432, 148 49, 99, 137

Wilson, R. W., Jefferts, K. B., & Penzias, A. A. 1970, ApJ, 161, L43 21

Wilson, T. L., Rohlfs, K., & Hüttemeister, S. 2016, Tools of Radio Astronomy, 6th edn., Astronomy and Astrophysics Library (Berlin [u.a.]: Springer) 22

Wong, T., Hughes, A., Fukui, Y., et al. 2009, ApJ, 696, 370 19, 163

Wood, K., Hill, A. S., Joung, M. R., et al. 2010, ApJ, 721, 1397 48, 99, 136

Wootten, A., & Thompson, A. R. 2009, IEEE Proceedings, 97, 1463 161

Yamaguchi, R., Mizuno, N., Mizuno, A., et al. 2001, PASJ, 53, 985 34, 99

Yan, R., & Blanton, M. R. 2012, ApJ, 747, 61 48, 99, 136

Young, L. M., Bureau, M., Davis, T. A., et al. 2011, MNRAS, 414, 940 11, 13, 162

Zanella, A., Daddi, E., Le Floc'h, E., et al. 2015, Nature, 521, 54 167

Zasov, A. V., & Khoperskov, S. A. 2015, MNRAS, 452, 4247 31

Zhang, K., Yan, R., Bundy, K., et al. 2017, MNRAS, 466, 3217 49, 152, 160, 164

Zurita, A., Beckman, J. E., Rozas, M., & Ryder, S. 2002, A&A, 386, 801 136

Zurita, A., Rozas, M., & Beckman, J. E. 2000, A&A, 363, 9 136

Acknowledgements

I would firstly like to thank my thesis advisers Diederik Kruijssen and Fabian Walter for selecting me to undertake this PhD thesis and for your support, guidance and training throughout my studies.

I would like to thank Diederik Kruijssen and Hans-Walter Rix for agreeing to referee this thesis, thank you for taking the time to do so.

I would like to thank my scientific collaborators, in particular the co-authors on the papers I prepared as a part of this thesis: Mélanie Chevance, Daniel Haydon, Steven Longmore, Jenny (Jaeyeon) Kim, Diederik Kruijssen, Andreas Schrubam, Fabian Walter and Jacob Ward.

I would like to thank Melanie Kaasinen, Sarah Leslie, Matthias Samland and Georgina Hygate for proof-reading parts of this thesis.

I would like to thank my thesis advisory committee: Diederik Kruijssen, Fabian Walter and Hans-Walter Rix for support during the thesis.

I would like to thank the directors of MPIA (Hans-Walter Rix and Thomas Henning) and ARI (Eva Grebel and Joachim Wambsganß) for leading scientifically stimulating and positive institutes. I would also like to thank the the staff and students at these institutes for working towards creating such environments.

I would like to thank my officemates at ARI and MPIA for providing a fun and positive working environment.

I would like to thank the members of Fabian Walter's group (Roberto Decarli, Alyssa Drake, Emanuele Farina, Carl Ferkinhoff, Roger Ianjamasimanana, Melanie Kaasinen, Nico Krieger, Chiara Mazzucchelli, Mladen Novak, Marcel Neeleman, Masafusa Onoue, Jan-Torge Schindler, Bade Uzgil, Bram Venemans and Laura Zschaechner) and members of Diederik Kruijssen's group (Mélanie Chevance, Jindra Gensior, Daniel Haydon, Sarah Jeffreson, Benjamin Keller, Jenny (Jaeyeon) Kim, Meghan Miholics, Jacob Nieswand, Maya Petkova, Marta Reina-Campos, Sebastian Trujillo-Gomez, Jacob Ward and Theodora Xylaki) in Heidelberg for your welcoming attitudes and the many discussions about science and other things we have had.

I would also in particular like to warmly thank Bram Venemans for discussions regarding astrometric offsets in relation to Chapter 3.

I would like to thank my master's thesis supervisor, Anne-Marie Weijmans for your support in applying for this PhD position.

I would like to thank the IMPRS-HD doctoral school of which I have been a member along with Christian Fendt, the scientific co-ordinator of the programme. I have been happy to be a member of the 11th generation of students and would like to thank all the students of this generation and the other generations.

I would also like to thank my friends and family for their support during my thesis.

I thank the anonymous referee for comments that improved the presentation of the paper that appears a Chapter 2 of this paper.

I gratefully acknowledge funding from the European Research Council (ERC) under the European Union's Horizon 2020 research and innovation programme via the ERC Starting Grant MUSTANG (grant agreement number 714907)

I thank IRAM for making the data products of the M33 CO Large Program (Gratier et al., 2010b; Druard et al., 2014) available.

This work made use of PAWS, 'The PdBI Arcsecond Whirlpool Survey' (Schinnerer et al., 2013; Pety et al., 2013).

I wish to thank the PHANGS collaboration, data from whom is used in Chapter 4.
This work makes use of the following ALMA data: ADS/JAO.ALMA #2012.1.00650.S, ADS/JAO.ALMA #2015.1.00925.S, ADS/JAO.ALMA #2015.1.00956.S. ALMA is a partnership of ESO (representing its member states), NSF (USA) and NINS (Japan), together with NRC (Canada), NSC and ASIAA (Taiwan), and KASI (Republic of Korea), in cooperation with the Republic of Chile. The Joint ALMA Observatory is operated by ESO, AUI/NRAO and NAOJ. The National Radio Astronomy Observatory is a facility of the National Science Foundation operated under cooperative agreement by Associated Universities, Inc.

This research has made use of NASA's Astrophysics Data System.

I acknowledge the usage of the HyperLeda database (http://leda.univ-lyon1.fr)